The impact of faults on fluid flow in porous carbonate rocks

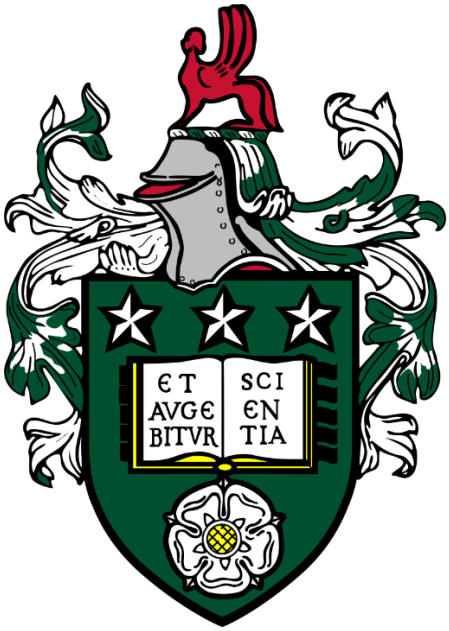

Andrew Philip Cooke

Submitted in accordance with the requirements for the degree of
Doctor of Philosophy

The University of Leeds
School of Earth and Environment

September 2019

The candidate confirms that the work submitted is his/her own, except where work which has formed part of jointly-authored publications has been included. The contribution of the candidate and the other authors to this work has been explicitly indicated below. The candidate confirms that appropriate credit has been given within the thesis where reference has been made to the work of others. Contributors to jointly-authored publications are outlined below.

Chapter Three

A.P. Cooke: principal investigator, collected and analysed all structural and microstructural data, main author.

Q.J. Fisher: fieldwork assistance, discussion, manuscript review.

E.A.H. Michie: fieldwork assistance, discussion, manuscript review.

G. Yielding: fieldwork assistance, discussion, manuscript review.

Chapter Four

A.P. Cooke: principal investigator, collected and analysed all petrophysical data, main author.

Q.J. Fisher: discussion, manuscript review.

E.A.H. Michie: discussion, manuscript review.

G. Yielding: discussion, manuscript review.

Chapter Five

A.P. Cooke: principal investigator and main author.

Q.J. Fisher: discussion, manuscript review.

E.A.H. Michie: discussion, manuscript review.

G. Yielding: discussion, manuscript review.

Acknowledgements

First and foremost I would like to thank my principal supervisor, Professor Quentin Fisher, for his help throughout this thesis, timely replies to emails despite being in far flung corners of the world, and many entertaining nights during fieldwork and beyond; my secondary supervisors at Badley Geoscience; Dr Emma Michie, who has been extremely helpful throughout the last 4 years, both in the field and over my continual pestering emails, and Dr Graham Yielding, for lending his expert structural knowledge. I would also like to thank the staff in the Wolfson Lab, Dr Sam Allshorn, Dr Carlos Grattoni, and Phil Guise, all of whom have steered me from potentially useless results on many occasions, and consistently reminded me that Darcy's Law does not apply to a core plug composed almost solely of vugs and fractures; my various field assistants, Ieva Kaminskaite, Grace Cosgrove, and Sam Tobiss; Harry Wyn Williams, for the continual assistance making thin sections; all the staff at Badley Geoscience, for making me feel very welcome during my time in Lincolnshire and ensured my structural model was up to scratch; John Martin and Kirk Handley, for their assistance in the drilling shed; Frauke Schaefer, for helping to organise fieldwork in Germany and access to core samples; and the many others who have aided me throughout my PhD.

Most of all, I would like to thank my family, without whom I certainly would not have made it this far. Their unwavering support throughout the various ups and downs of the last four years has been nothing short of a life saver.

Finally, to all those I am lucky enough to call friends, on the Wirral, from UCL, Leeds, and beyond; all those who have resided in office 7.131; all my housemates, past and present; and last, but not least, Scarborough North Bay, for those rare dreamy North Sea lefts.

Abstract

Faults may impact subsurface fluid flow over production and geological timescales. Predicting fault permeability is crucial for understanding subsurface fluid flow, which is required for a number of subsurface industries. Fault permeability is determined by the micro-fabric and distribution of fault rocks, which are influenced by the deformation mechanisms exhibited during faulting, fault-related diagenesis, and fault zone architectural evolution. Non-uniform strain distributions along fault zones lead to heterogeneous fault cores, therefore, predicting fault permeability is difficult. Empirical relationships linking lithological parameters to the petrophysical properties of different fault rocks are commonly utilised to predict fault permeability in clay-bearing sequences. However, no such relationships exist for carbonate rocks. A better understanding of these controls, in addition to the characterisation of fault rock permeability is required to establish predictive relationships for fault rock permeability. This thesis combines structural, microstructural and petrophysical data from a series of carbonate-hosted fault zones in Malta. Thereby enabling an understanding of the fault zone permeability structures in various lithofacies, whilst highlighting the heterogeneity on all scales of carbonate-hosted fault zones. The continuity of fault rock is shown to increase with displacement, and displacement thresholds for both a continuous fault core and cataclasite are established for fault zones in Malta. Only fault rocks derived from high porosity host rocks have the potential to retard fluid flow over reservoir scales. Lithological heterogeneity is retained within fault cores, whereby the heterogeneity of the faulted lithofacies is linked to the variability in fault rock petrophysical properties. Novel methods of upscaling fault permeability and implementing fault rock continuity relationships to fault property modelling are presented. The results provide an example of how porosity of the host carbonate can impact fault rock permeability under low stresses. Combined with similar studies from different lithofacies and structural settings, this thesis contributes towards a generalised understanding of the controls on fault permeability in porous carbonate rocks.

Contents

List of tables

List of figures

CHAPTER 1.

Introduction

1.1. Rationale

A considerable amount of research has been directed towards determining the conditions in which faults act as conduits, barriers or partial barriers to flow. This understanding can help to reduce uncertainty when estimating the hydraulic properties of fault zones in the subsurface for industrial applications, such as oil and gas production, CO_2 storage, and nuclear waste disposal. This research has been primarily directed towards siliciclastic hydrocarbon reservoirs (e.g. Knipe 1992; Yielding *et al.* 1997; Fisher & Knipe 1998; Sperrevik *et al.* 2002). However, a growing amount of recent research has focussed on the impact of faults on fluid flow in carbonates (e.g. Billi *et al.* 2003; Agosta *et al.* 2007; Tondi 2007; Bastesen *et al.* 2009; Dimmen *et al.* 2017; Michie *et al.* 2017; Kaminskaite *et al.* 2019), owing to their importance in global hydrocarbon reserves; around 60% of global oil reserves and 40% of global gas reserves are stored in carbonates (Schlumberger 2007). There are numerous published case studies of fault behaviour in carbonate reservoirs, of which there are no examples of carbonate-hosted faults sealing over geological timescales and the majority suggest that faults have either no impact, or behave as fluid conduits (e.g. Richter 1967; Trocchio 1990; de Medeiros *et al.* 2007). However, several examples exist that interpret faults to be sealing over production timescales, which are almost exclusively from porous carbonate reservoirs (Acevedo 1980; Kosters *et al.* 1989; Hussain 1993; Jakobsen *et al.* 2005; Barkved *et al.* 2016). This mixture of the hydraulic behaviours of carbonate-hosted faults, combined with a poor understanding of what controls these behaviours, means that carbonate-hosted fault zones carry a great deal of uncertainty to numerous industries. Thus, highlighting the importance in ascertaining the key controls on fault behaviour in porous carbonates.

To assess the across-fault fluid flow potential of porous carbonate-hosted fault zones, both the structural characteristics and the petrophysical properties of fault rocks must be determined (Caine *et al.* 1996; Evans *et al.* 1997; Rawling *et al.* 2001). This understanding allows for predictions of fault core properties, based upon parameters that can be obtained from the subsurface, thereby allowing geological realistic upscaling of fault zones to reservoir simulations (Manzocchi *et al.* 1999; Harris *et al.* 2007; Yielding *et al.* 2010). However, with the exception of fault rock thickness, there are currently no empirical relationships that can be used to estimate

structural and petrophysical parameters in carbonate-hosted fault zones. The following section outlines how these problems will be addressed in this research.

1.2. Aims and objectives

The main aim of this research is to better understand how fault zones in porous carbonates impact fluid flow. In particular, the controls on the distributions and permeability of fault rocks in carbonate-hosted fault zones must be understood in order to parameterise bulk fault permeability in carbonates. Towards this goal, fault zone outcrops in the Maltese Islands of Malta and Gozo were chosen as study sites for this research, from which detailed field mapping and sample collection could take place. Malta is selected based upon the excellent exposure of faulted carbonate rocks, which have relatively simple tectonic and diagenetic histories. The rocks from the Maltese stratigraphy are all porous, but have a range in porosities, which allows investigations in to how the pore space in carbonates controls fault zone deformation. Additionally, fault zones in Malta have been subject to a number of studies, which provides a good background to help build on current understandings on fault permeability and structure. Previous studies have investigated the structure of the large displacement Il-Maghlaq fault (Bonson *et al.* 2007), the control of host facies on fault rock microstructures, fault zone architecture, and permeability (Michie *et al.* 2014; Michie 2015), the permeability heterogeneity across several Maltese fault zones (Haines *et al.* 2016; Michie & Haines 2016), and the growth processes of deformation bands (Rotevatn *et al.* 2016). These studies highlight the heterogeneity within fault zone structures, fault rock microstructures, and fault rock permeability. Heterogeneous fault cores are interpreted to be a product of the juxtaposition of host rocks that exhibit contrasting styles of deformation, or the linkage of fault segments during fault growth. However, empirical relationships between host rock properties and fault zone properties, such as fault rock thickness, fault rock continuity, and fault rock permeability, are limited. Therefore, this research aims to address the following questions:

Research question 1

What are the key controls on the thickness and continuity of fault rock in shallowly buried porous carbonate rocks?

Research question 2

How does the host rock texture impact the fault rock texture and permeability in shallowly buried porous carbonates?

Research question 3

Can the bulk fault core permeability be predicted from lithological parameters in shallowly buried porous carbonates?

1.3. Thesis outline

Answering each of these research questions enables predictions of bulk fault permeability in similar carbonate lithofacies; thereby providing a starting point for a generalised predictive algorithm for fault seal analysis in porous carbonate rocks. The following section outlines the chapters in this thesis, through which these research questions are addressed.

Chapter two

Chapter 2 provides a review of our current understanding of faults by outlining the fundamental fault seal mechanisms, the current understanding of the structural characteristics of carbonate-hosted fault zones, the microstructural and petrophysical properties of carbonate fault rocks, and finally a brief overview of the current workflows that are used for fault seal analysis, thereby highlighting the need for workflows directly applicable to carbonate reservoirs.

Chapter three

Chapter 3 has been published in the Journal of Structural Geology (Cooke *et al.* 2018). The chapter provides a detailed investigation in to 3 fault zones in the Qala Point area of eastern Gozo, detailing and comparing the structural and microstructural features in each fault zone. Fault rock thickness measurements are presented for different fault rock types, and fault rock continuity is estimated from each fault zone. The continuity of cataclasite from a total of 8 fault zones is estimated from field measurements, showing how continuity varies with fault throw.

Chapter four

Chapter 4 has been accepted for publication in Petroleum Geoscience (Cooke *et al.* 2019). This chapter presents a method of quantifying the relative textural heterogeneity of core plugs within a sample set, using macroscale X-ray tomography. This is used to link textures of host rocks to the textures of fault rocks. The permeability of host, damage zone, and fault rocks are presented, which enables relationships between host properties and fault rock permeability. Permeability contrasts between host and fault rocks are used as an indicator of how different fault rocks are likely to impact fluid flow.

Chapter five

Chapter 5 has not been submitted to a journal, but is ready for submission. This chapter links chapters 3 and 4 by upscaling both the structural and petrophysical fault zone measurements to predictive algorithms for fault permeability and thickness. These algorithms are implemented within a reservoir simulation of the Island of Gozo, which is used to show the predicted flow properties of the studied fault zones. The effect of fault core fracturing is investigated by simulating a fault cut by fractures, varying fracture spacing.

Chapter six

Chapter 6 provides a discussion of chapters 3-5, linking the results in to previous research and comparing results to fault zones in different carbonate lithologies.

Chapter seven

Chapter 7 provides overall conclusions of this thesis, together with suggestions for future work.

CHAPTER 2.

Literature review

Faults can impact fluid flow over geological and production timescales, thereby being a *fault seal, fault barrier* or a *conduit* to fluids. A sealing fault relies on capillary pressures along a fault being sufficient to prevent the flow of fluids, whereas a fault barrier exists when fluid pressures overcome the threshold capillary pressure of the fault and the permeability of the fault determines the rate of flow across the fault. If this permeability is greater than the surrounding host rock, then the fault may behave as a conduit to fluids either across the fault or along the fault. Faults may also be conduit/barrier systems, in which regions of the fault zone have increased permeability and others have reduced permeability (e.g. Caine *et al.* 1996; Aydin 2000). To determine the sealing capacity or permeability of faults in the subsurface, the petrophysical properties of the fault rocks and their distribution in the fault zone must be predicted. Thus requiring an understanding of the structural, microstructural, and petrophysical characteristics of carbonate fault zones, in addition to workflows to implement fault property predictions in to reservoir models. The following sections outline the current understanding of these topics.

2.1. Fault seal mechanisms

Fundamentally, there are two mechanisms by which faults can act as barriers to fluid flows in the subsurface. First, faults can juxtapose high permeability strata against low permeability rocks such as shale or evaporites (Figure 2-1); these are known as *juxtaposition seals* (e.g. Schowalter 1979; Watts 1987; Allan 1989). Secondly, the fault rock itself can act as the barrier to fluid flow (Figure 2-1); these are known as fault rock or fault seals sensu stricto (e.g. Watts 1987; Yielding *et al.* 1997; Fisher & Knipe 1998). Regardless of the type of seal, the factors that contribute to sealing or leakage of hydrocarbons across a fault are linked to the rock properties (e.g. clay content, pore size, permeability, thickness, mechanical strength, and displacement), the formation water (pore pressure), and the hydrocarbons (e.g. buoyancy, viscosity, and charge rate). These factors are predominantly static (i.e. do not change with time), with the exception of water pressures and hydrocarbon charge rates, which are dynamic (i.e. time dependant) (Heum 1996). Additionally, diagenesis can change fault permeability and pore sizes over time.

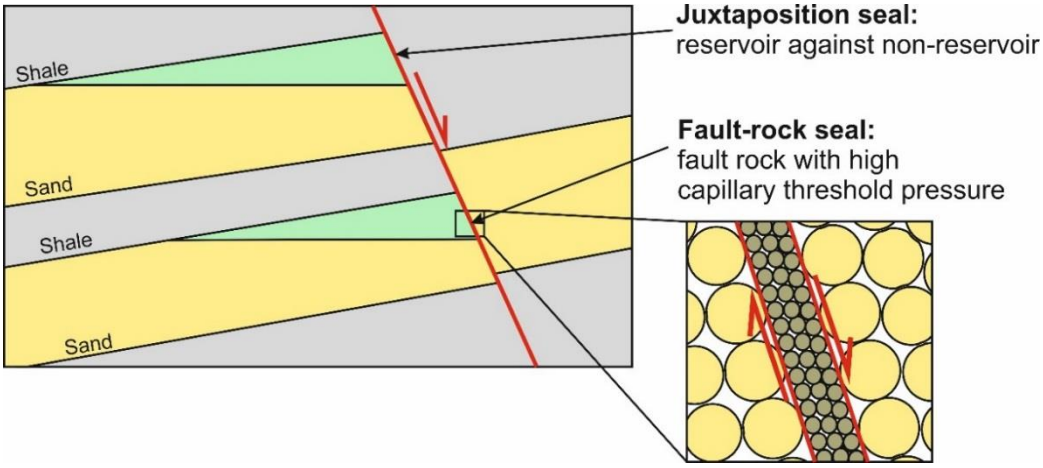

Figure 2-1: Schematic to show the difference between a juxtaposition seal and a fault rock seal (after Yielding et al. *2010).*

The mechanisms that enable a fault to seal hydrocarbons are similar for both juxtaposition seals and fault rock seals, and are analogous to membrane cap-rocks tilted to the angle of the fault (Watts 1987). These mechanisms are namely *capillary seals* and *hydraulic resistance seals*. Capillary (or membrane) seals occur when two immiscible fluids are present and the capillary threshold pressure of the sealing unit (either juxtaposing formation or the fault plane) exceeds the capillary pressure in the reservoir rock (Schowalter 1979; Watts 1987). Hydraulic resistance seals occur when either a single fluid phase is present or when two immiscible fluids are present and the capillary pressure exceeds the threshold pressure of the fault. In either system, a hydraulic resistance seal occurs when the rate of petroleum recharge exceeds the rate of leakage across the fault, such that the petroleum column at the fault is not compromised (Heum 1996).

The following subsections are aimed at providing an overview of the processes governing capillary seals, and the controls on across-fault leakage once the capillary pressure exceeds the threshold pressure of the fault.

2.1.1. Capillary/membrane seals

In a system containing two immiscible phases (e.g. oil-water, gas-water), the capillary pressure represents the difference between the buoyancy pressure of the wetting and non-wetting phases (Schowalter 1979). Under the assumption of a water-wet rock, the threshold capillary pressure, P_{Th} (psi), refers to the pressure required for hydrocarbons to enter the largest interconnected

pore throat of a rock (Watts 1987). Therefore, if the threshold pressure of a fault exceeds the capillary pressure, it can support a hydrocarbon column of height, *H* (ft), given by:

Equation 2-1

$$\boldsymbol{H = \frac{P_{Th}\gamma \cos\theta}{0.4335[\rho_w - \rho_p]}}$$

where γ (dynes/cm) is the petroleum-water interfacial tension, θ (°) is the contact angle for the hydrocarbon-water-rock system, ρ_w and ρ_p (g/cm^3) are the densities of the water and hydrocarbons, respectively, and 0.4335 is a conversion factor so that *H* is calculated in field units (ft). The buoyancy pressure of the hydrocarbon leg is directly related to the difference between ρ_w and ρ_p, meaning larger density differences and larger contact angles will reduce the hydrocarbon column height that a fault can support, whilst larger threshold pressures and interfacial tensions will increase the column height that can be supported. If the threshold capillary pressure does not exceed *H*, then the permeability of the fault is effectively zero to the non-wetting phase. Therefore, in the case of fault rock seals, the potential for a fault to support a hydrocarbon is essentially a product of three components: (i) the *in-situ* fluid densities, (ii) the hydrocarbon-water interfacial tension at reservoir conditions, and (iii) the pore size and wettability of the fault plane material (i.e. capillary threshold pressure) (Watts 1987). Figure 2-1 highlights how the juxtaposition of a reservoir unit against a sealing unit, or a reduction in pore size along a fault, can generate a capillary seal.

Wettability

It is important to note that wettability has a major impact on hydrocarbon flow within a rock, particularly the threshold pressures of a seal. Wettability refers to the preference of one fluid phase to be in contact with a solid relative to another. The phase that preferentially adheres to the surface is referred to as the wetting phase. The most universal measure of the wettability of a surface is the contact angle (θ) that is generated between the non-wetting phase and the solid surface that is already in contact with the wetting phase (Morrow 1990). Figure 2-2 illustrates wettability in the case of a two phase system, in which rocks are termed oil-wet or water-wet. It is worth noting that a rock may also be intermediate-wet (no wetting preference) or mixed-wet (variable wetting preference). The contact of a surface with a non-wetting phase may change the wettability of that rock (e.g. Morrow *et al.* 1986).

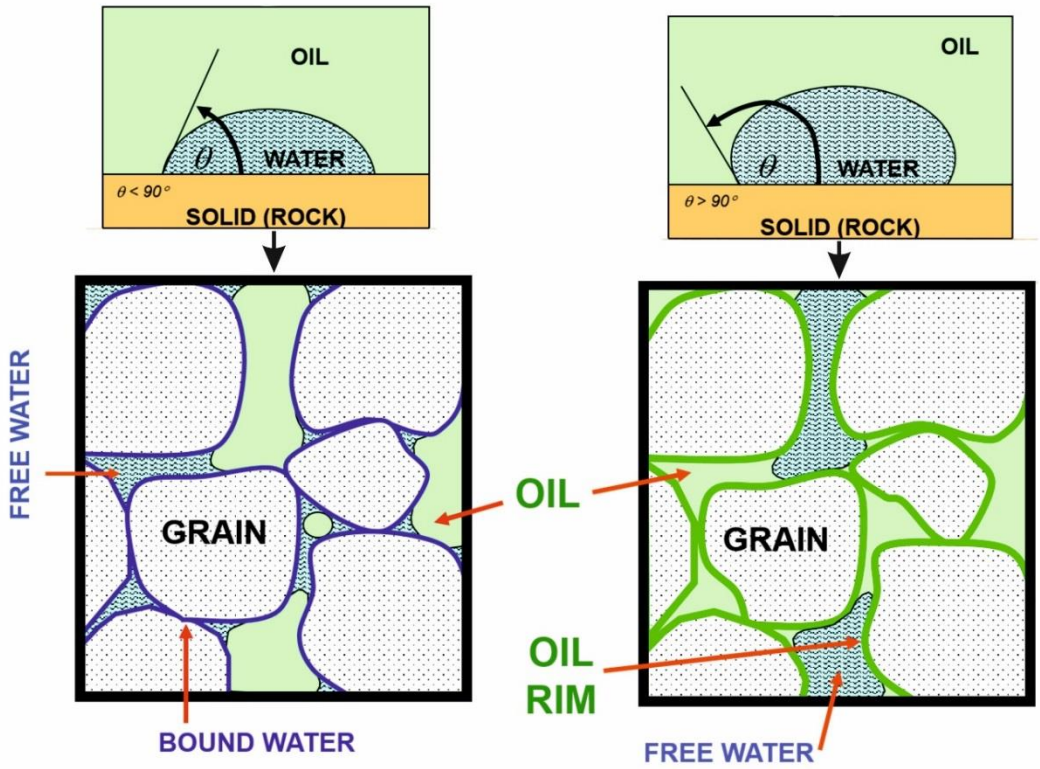

Figure 2-2: Illustration of wettability showing the contact angles for a water wet (left) and oil wet (right) rock. The images below show the impact this has on the bound oil or water.

A variety of studies have been undertaken to determine the wettability of reservoir rocks (e.g. Treiber *et al.* 1972). In general, it is thought that siliciclastic reservoir rocks are either strongly water-wet or have mixed wettability. However, a review of carbonate wettability conducted by Chilingar & Yen (1983), suggests that wettability tended to be oil or have mixed wettability; from a total of 161 limestone, dolomitic limestone, calcitic dolomite, and dolomite cores, 15% were strongly oil wet (θ = 160-180°), 65% were oil wet (θ = 100-160°), 12% had intermediate wettability (θ = 80-100°), and 8% were water wet (θ = 0-80°). An oil-wet rock will have a lower threshold pressure for oil to enter the rock than for a water wet rock. Therefore, the likelihood that a carbonate is oil-wet indicates that leakage across a fault can occur at any capillary threshold pressure, such that faults leakage will occur via two-phase flow (Ingram *et al.* 1997).

2.1.2. Across-fault leakage

In the case that the buoyancy pressure exerted by the hydrocarbon column exceeds the capillary threshold pressure of the sealing material, the non-wetting phase will begin to leak across the fault and the fault will become a permeability barrier rather than a capillary seal (Fulljames *et al.* 1997). The rate of leakage is controlled by a number of factors (absolute and relative permeability behaviour, pressure gradient, and phase saturation) and will vary at different depths along the fault due to variations in capillary pressures, assuming the fault has uniform properties across the fault surface; across-fault fluid flow is expected at the shallowest points of the fault, where capillary pressures are highest due to large hydrocarbon columns (Heum 1996; Fisher *et al.* 2001; Brown 2003). Towards the free-water level (FWL), capillary pressures are so low that the relative permeability of oil becomes zero and the fault behaves as a capillary seal (Fisher *et al.* 2001). Where the capillary seal is overcome by the capillary pressure, the rate of across-fault fluid flow can be calculated according to Darcy's Law for multi-phase flow:

Equation 2-2

$$\boldsymbol{Q = \frac{k.k_r}{\mu}\left(\frac{\Delta P}{\Delta L}\right)}$$

where Q is the rate of flow per unit area, k is the absolute permeability, k_r is the relative permeability of the phase in question, A is cross sectional area, μ is viscosity, and $\Delta P/\Delta L$ is the pressure gradient across the fault. For fault rock seals, ΔL refers to fault thickness, and the permeabilities are that of the fault rock. It is clear from this relationship that for the case of a fault rock seal, the inability to directly quantify fault rock permeability and fault rock thickness generates a great deal of uncertainty regarding the determination of across-fault fluid flow (Hesthammer & Fossen 2000).

2.2. Structural and microstructural characteristics of carbonate-hosted fault zones

It is evident that for the hydraulic behaviour of faults to be characterised, their structural characteristics must be understood. These structural characteristics include the number of fault planes present within the fault zone, how these fault planes are interconnected, and how fault rock is distributed throughout the fault zone; together, these characteristics comprise the fault

zone architecture. Therefore, both the fault zone architecture and microstructures, which govern petrophysical characteristics, determine the hydraulic behaviour of fault zones. The following sections aim to provide a review of the different structural and microstructural elements of carbonate-hosted fault zones, together with fault rock distribution parameters that are critical in establishing potential across-fault fluid flow: fault zone thickness and continuity of fault rock on the fault plane.

2.2.1. Fault zone architecture

Faulting in the shallow crust is a form of brittle failure that occurs when stresses overcome the frictional strength of a rock, generating a planar discontinuity that hosts some measurable shear displacement. Through this displacement, the adjacent rock mass is subject to deformation via processes such as fracturing and mechanical attrition. Rocks that are subject to this deformation, or subsequent alteration via fault related mineralization, are termed *fault rocks*, and comprise the *fault core* (e.g. Higgins 1971; Sibson 1977). Typically, a zone of deformed rock is generated surrounding a fault, known as a *damage zone*. The fault core and damage zone combined are known as the *fault zone*.

The structure of fault zones has been subject to a great deal of research, through which a number of conceptual models have been developed. A commonly adopted architectural model, first proposed by Chester & Logan (1986) and later developed by a number of authors (Caine *et al.* 1996; Faulkner *et al.* 2003; Micarelli *et al.* 2006), consists of a localised *fault core*, or several strands of fault core, surrounded by a *damage zone*, in which damage decreases in to the undeformed protolith. In general, the fault core is composed of high strain products (fault rocks), that destroy the protolith fabric. The surrounding damage zone typically contains a high fracture density whilst mostly preserving the protolith fabric (Chester & Logan 1986; Chester *et al.* 1993; e.g. Antonellini & Aydin 1994; Evans *et al.* 1997; Fisher & Knipe 2001; Faulkner *et al.* 2003; Wibberley & Shimamoto 2003; Micarelli *et al.* 2006) (Figure 2-3). However, depending on factors such as the porosity, grainsize and stress conditions at the time of faulting, the damage zone may host features such as deformation bands (Fossen *et al.* 2007). This architectural model has been shown to be consistent with carbonate-hosted fault zones (Agosta & Kirschner 2003; Billi *et al.* 2003; Agosta *et al.* 2007; Jeanne *et al.* 2012; Michie *et al.* 2014), despite studies being primarily focussed on siliciclastic and crystalline rocks.

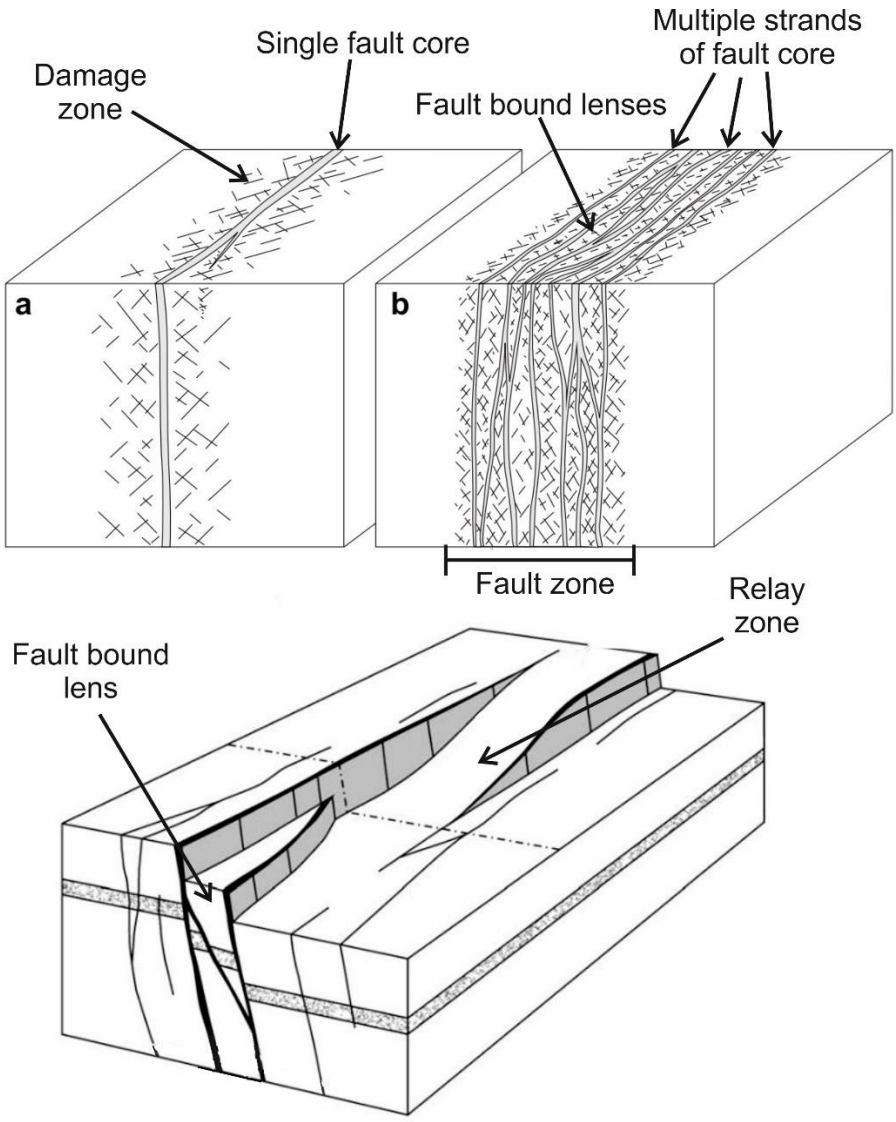

Figure 2-3: Top) Conceptual model of a fault core composed of a single slip surface (a), and a fault zone with multiple slip surfaces, creating multiple strands of fault rock which combine in to a wider fault core (b) (after Faulkner et al. *2010). Bottom) Three dimensional model of fault zone architecture, highlighting the structural variations along strike and down dip (after Childs* et al. *2009).*

As fault zones are inherently three dimensional structures, additional models have been developed to account for structural variations along their length. Childs *et al.* (1996) recognized the heterogeneity of fault zones in three dimensions, attributing this to fault zone evolution processes and the linkage of smaller faults. These findings have since been incorporated in to a

conceptual model representing fault zone complexity in three dimensions (Figure 2-3). This model proposes that fault growth occurs through the linkage of arrays of irregular fault segments. Lenses of fault bound rock are formed when relay zones formed between fault segments become breached, or asperities along the fault surface are sheared off. Further fault displacement increases the amount of deformation within these fault bound lenses. Asperities on fault surfaces can be generated by a number of processes, including changes in fault dip, which may be a product of contrasting mechanical properties in the faulted sequence (e.g. Childs *et al.* 2009; Loveless *et al.* 2011), and bed parallel slip (Figure 2-4).

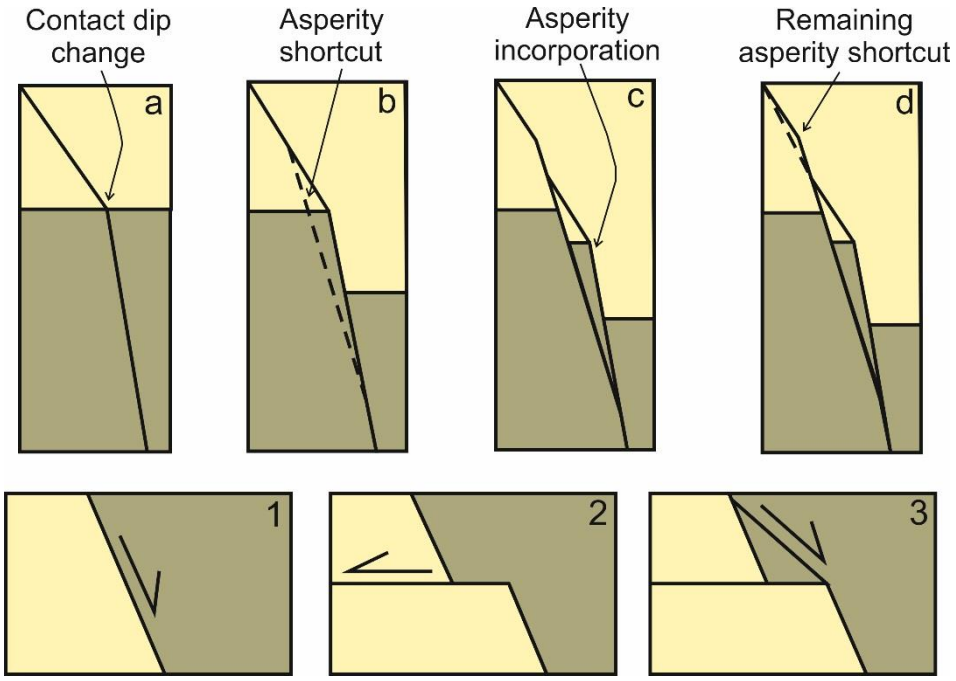

Figure 2-4: Examples fault bound lens formation through fault asperity shearing, due to contrasting competencies across bedding planes (top; after Childs et al. *2009), or as a result of bed parallel slip (bottom; after Watterson* et al. *1998).*

Fault core

The generalized model of a fault core in shallow crustal settings consists of a slip plane containing or bounding a granular material formed by shear-enhanced compaction, such as fault gouge and/or a fracture-generated dilatant material, such as cataclasite (Rutter 1986; Faulkner *et al.* 2003; De Paola *et al.* 2008; Wibberley *et al.* 2008). The deformation mechanisms involved in fault core generation can be either be cataclastic or crystal-plastic (Rutter 1986); *cataclasis* refers to the accommodation of strain through fracturing, fragmentation, and comminution of rock by

frictional sliding of grains. Crystal-plastic deformation refers to the accommodation of strain through intracrystalline plasticity and diffusive mass transfer. Depending on the conditions at the time of faulting, both of these mechanisms can generate either a discrete, localised fault core (e.g. Chester & Logan 1986; Chester *et al.* 1993) or a ductile zone of deformation (e.g. Faulkner *et al.* 2003; Wibberley & Shimamoto 2003). It is also common to observe both brittle deformation and crystal-plasticity within the same fault core (e.g. Hadizadeh 1994; De Paola *et al.* 2008).

Fault cores are rarely homogeneous planar features; fault cores commonly host multiple anastomosing slip surfaces, have variable thicknesses, are discontinuous, and/or incorporate lenses of damage zone wall rock. For example, Wibberley & Shimamoto (2003) reported a complex large scale fault zone comprised of multiple strands of highly localized fault core. The high degree of fault zone complexity was suggested to be a product of contrasting mechanical properties of the juxtaposed lithologies. Multiple authors report entrained lenses of either undeformed host rock, fractured damage zone rock, or fault rock within the fault core, often referred to as *horses* (e.g. Childs *et al.* 1996; Faulkner *et al.* 2003; Berg & Skar 2005; Gabrielsen *et al.* 2016).

Fault cores are not always present within the fault zone, in which case the footwall and hanging wall rocks are in direct contact with one another (Figure 2-5a). However, along strike variations in the thickness of fault cores means that fault lenses of fault core may still be present in these cases (see section 2.2.3 for a review of fault core continuity).

Damage zone

The damage zone accommodates the remainder of strain within the fault zone, through the generation of secondary features, such as fractures and lower displacement faults. A number of authors have studied damage zones in a variety of lithologies, showing that fracture intensities are highest immediately adjacent to the fault core, and reduce with distance from the fault (e.g. Childs *et al.* 1996; Shipton & Cowie 2001; Riley *et al.* 2010; Faulkner *et al.* 2011; Savage & Brodsky 2011; Michie *et al.* 2014). Fault zones with multiple linking fault cores can lead to overlapping damage zones, in which fracture intensities are further increased (Savage & Brodsky 2011). Billi *et al.* (2003) studied the damage zone-fault core transition in low porosity carbonate rocks, finding that orthorhombic clasts of rock characterise the damage zone, originating from intersections of fault-related fracturing with pre-existing bedding planes and joints. The transition

between damage zone and fault core is marked by the reduction in particle size, towards the generation of a fine grained cataclastic fault core (Figure 2-5c).

Damage zone complexity arises from processes such as fault-related folding, fault bends, fault linkage, and damage surrounding fault tips. Fault-related folds accommodate portions of the total fault displacement (drag folds), act as linkage features between separate fault segments (relay ramps), or form via the bending of fault blocks over non-planar fault surfaces (e.g. Suppe 1983; Erslev 1991; Schlische 1995; Khalil & Mcclay 2002). Fault tips commonly have complex fault/fracture splay systems, relating to high stress concentrations in their vicinity (Cowie & Scholz 1992). Features within these damage zones include wing cracks, horsetails fractures, synthetic faults and antithetic faults, all of which can be accompanied by block rotation (e.g. Mcgrath & Davison 1995; Kim *et al.* 2004). Similar features are observed in regions of fault linkage.

Micarelli *et al.* (2006) recognises two further structural elements within the damage zone of carbonate-hosted faults, based upon the degree of fracture connectivity observed in several fault zones within carbonate rocks of the Hyblean Plateau, Sicily. These are the intensely deformed damage zone (IDDZ), characterised by a dense network of synthetic and/or antithetic fractures that connect to form lenticular geometries, and the weakly deformed damage zone (WDDZ), characterised by less frequent sub-vertical fractures (Figure 2-5d). Depending upon the mechanical properties of the rock, not all architectural domains may be present (e.g. Michie *et al.* 2014).

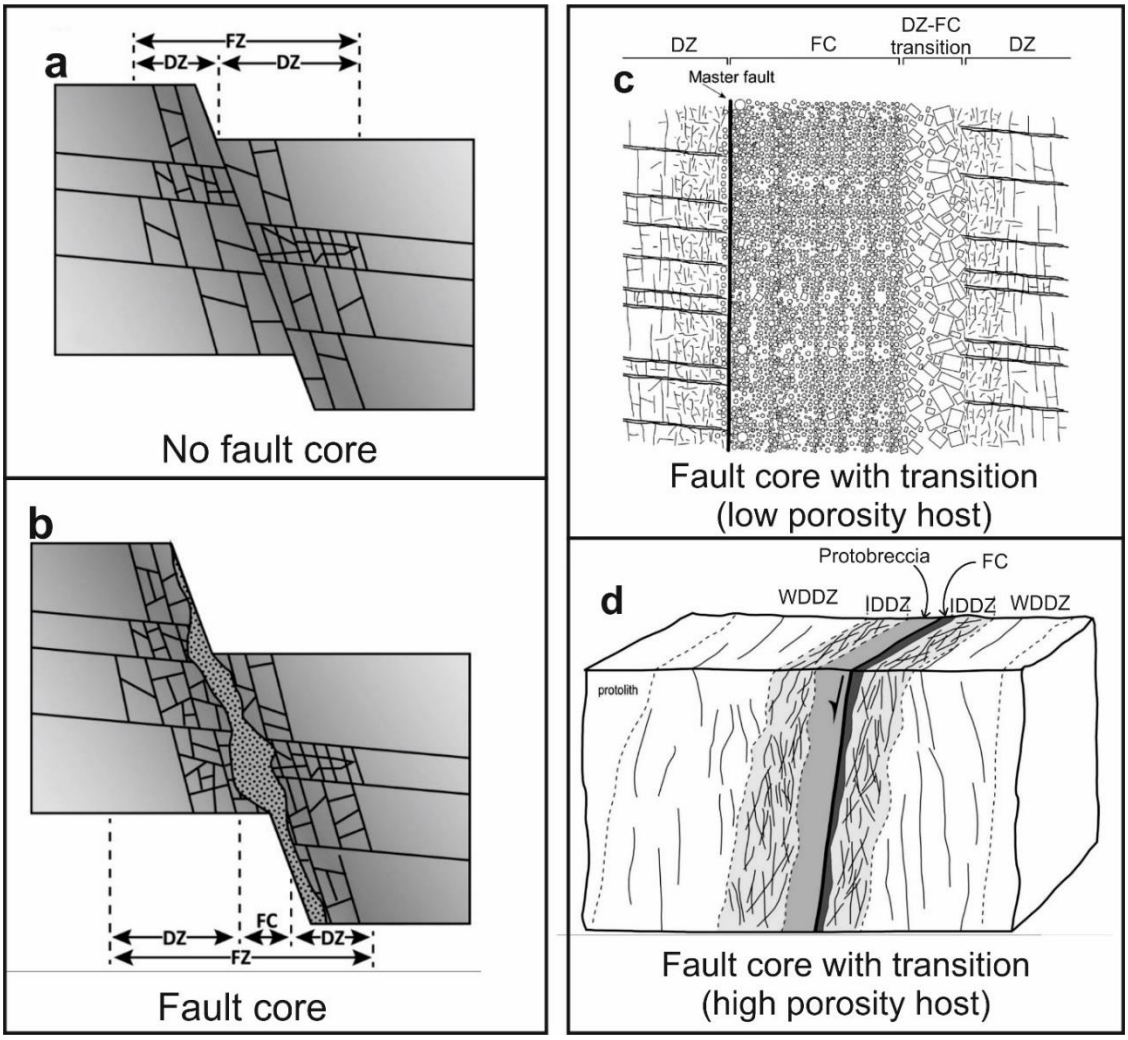

Figure 2-5: Schematic diagrams from studies of carbonate-hosted fault zones: a) Fault zone with no fault core; b) fault zone with a fault core and fractured damage zone (a & b after Solum & Huisman 2017); c) fault zone composed of increasingly small clasts towards the master fault, generating a gradual damage zone-fault core transition (after Billi et al. *2003); d) fault zone with a cataclasite fault core surrounded by a damage zone divided in to the intensely and weakly deformed damage zones (after Micarelli* et al. *2006). FZ = fault zone; DZ = damage zone; FC = fault core.*

2.2.2. Microstructural characteristics

The microstructures of fault rocks reveal the deformation mechanisms that have taken place during faulting and the resultant rock fabric, which is key in governing how faults impact fluid flow. A variety of fabrics can be generated, allowing the division of fault rocks into different categories, as first outlined by Sibson (1977). This classification differentiated between

incohesive and cohesive fault rocks and included the percentage of the rock matrix, the proportion of matrix, and whether the rock fabric is foliated to distinguish between different fault rock types. The fault rocks referred to as incohesive are fault gouge or fault breccia, which contain <30% and >30% visible fragments, respectively. However, it has since been noted by numerous authors that fault breccia can be either cohesive or incohesive (Woodcock & Mort 2008 and references therein). Therefore, a revised classification scheme by Woodcock & Mort (2008) only uses cohesion to distinguish fault gouge from other fine grained fault rocks, in addition to the inclusion of a subdivision of fault breccia and criterions for clast and matrix grainsizes (Figure 2-6). This classification scheme defines fault breccia as being composed of >30% large (>2 mm) clasts. The subdivision specifies three types of fault breccia, which represent increasing clast rotation and percent matrix. In order of increasing clast rotation and matrix component, these are crackle, mosaic, and chaotic breccia. Cohesive fault rocks with <30% large clasts are part of either the cataclasite series (non-foliated) or the mylonite series (foliated).

The deformation observed in carbonate fault cores differs to those in siliciclastics, principally due to the capacity of carbonate minerals to deform by crystal-plasticity and physico-chemical processes at very shallow depths. Additionally, the reactivity of carbonate rocks means that early diagenetic alteration can have profound impacts on the host rock mechanical properties and, therefore, the potential deformation mechanisms during faulting. It has been shown that the key controls on the deformation mechanisms observed in fault cores include the mechanical properties of a rock, grain size and porosity (e.g. Sibson 1977; Hugman III & Friedman 1979; Heynekamp *et al.* 1999; Přikryl 2001; Chester *et al.* 2004; Vajdova *et al.* 2004; Berg & Skar 2005; Jeanne *et al.* 2012).

The following sections will outline the macro and microscale structures observed in fault rocks derived from low porosity, high porosity, and clay-bearing carbonate rocks.

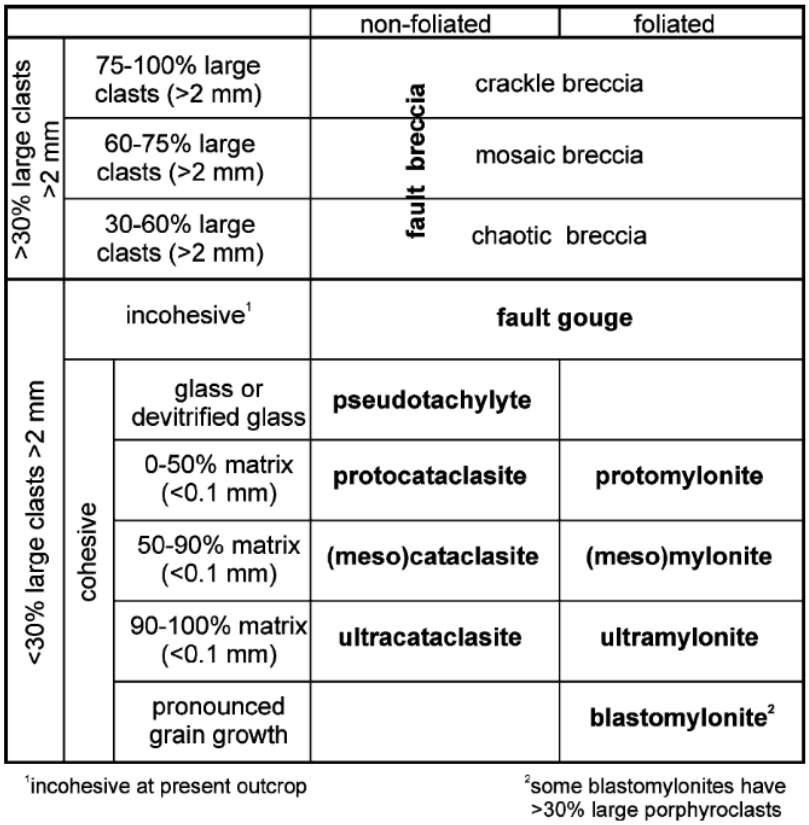

Figure 2-6: Fault rock classification series proposed by Woodcock & Mort (2008).

Fault rocks in low porosity carbonates

Fault zones in low porosity carbonate rocks are typically dominated by brittle cataclastic processes on the macro scale, accompanied by crystal-plastic deformation on the microscale. This leads to highly fragmented cores, intense damage zone fracturing and lenses of fault rock (Billi *et al.* 2003; Agosta *et al.* 2007; Schröckenfuchs *et al*. 2015; Ferraro *et al.* 2018). Principal slip surfaces often feature slickensides, which can produce highly polished fault surfaces in mature fault zones, known as fault mirrors (Jackson & Mckenzie 1999; Fondriest *et al.* 2013; Siman-Tov *et al.* 2013).

Fluids can play a key role in fault deformation, either through physical processes, by reducing the strength of the rock and raising pore pressures, or chemical processes, by providing the medium for solution transfer on the grain-scale (Fitz-Diaz *et al.* 2011). Grain size reduction due to cataclasis in carbonates can be accompanied by pressure solution (Billi 2010), mechanical twinning (Burkhard 1993), and dynamic recrystallization (Kennedy & Logan 1998; Kennedy & White 2001; Molli *et al.* 2011), even under low pressure and temperature conditions. The

morphology of crystal twinning is dependent upon pressure and temperature conditions and are, therefore, often used as palaeopiezometers (e.g. Burkhard 1993; Ferrill *et al.* 2004). Dynamic recrystallization is a form of intracrystalline plasticity, in which sub-grain rotation and grain boundary migration lead to the formation of smaller grains along relict twin and grain boundaries, overlaying the original rock texture (Kennedy & White 2001). Agosta & Aydin (2006) highlight how the shearing of pre-existing features, such as pressure solution seams, can lead to fault initiation.

The brittle nature of faulting in lower porosity carbonates means that fault geometries can be key to fault rock formation and distributions. Dilation sites, such as fault jogs, are often filled with brittle fault rock (e.g. Tarasewicz *et al.* 2005; Bauer & Decker 2010) or mineral precipitates (e.g. Lee *et al.* 1997; Ferrill & Morris 2003; Agosta *et al.* 2015); commonly, fault rocks are cohesive and damage zone fractures are filled with calcite cements. The formation of fault breccia in these locations has multiple mechanisms of generation, including hydraulic implosion due to large differences in pressure between the void space and the wall rock (Sibson 1986), the sedimentary filling of void space (e.g. Woodcock *et al.* 2006; Wright *et al.* 2009), or in-situ shattering due to high-strain rate seismic deformation (e.g. Demurtas *et al*. 2016; Schröckenfuchs *et al*. 2015). Agosta *et al.* (2015) documented faulting in heterogeneously layered carbonates, highlighting how releasing jogs are formed around the stiffer limestone beds, which are subsequently filled with calcite cements. Similarly, the formation of distributed fracturing and subsequent brecciation may occur where slip is impeded along a fault, such as anti-dilatational jogs or restraining stepovers (Sibson 1986).

Bauer *et al.* (2016) compared the difference between fault rocks from low porosity limestones and dolomites from the Hochschwab massif, Austria. In limestone fault zones, lenses of dilatational fault breccia occur along secondary slip surfaces surrounding a principal cataclastic fault core, which enables fault zone fluid circulation and subsequent karstification. Additionally, they report cemented fault breccia immediately adjacent to the principal cataclastic fault core, in which pressure solution leads to calcite precipitation within cracks and veins. For the dolostone-hosted fault zones, they report multiple complex cataclastic fault cores surrounded by wide zones of dilatational fault breccia. Ferraro *et al.* (2019) found differences in the diagenetic evolution of dolomite and calcite-rich fault rocks from high-angle extensional faults in the central and southern Apennines; physical compaction was prominent in dolomite-rich fault rocks, whereas chemical compaction coupled with dissolution was prominent in calcite-rich fault rocks. Additionally, they

found that calcite cement precipitation was widespread in calcite-rich fault rocks and virtually absent in dolomite-rich fault rocks, due to the high chemical stability of dolomite crystals, which prevents dissolution at the burial depths in question (<1.5 km).

Fault rocks in moderate to high porosity carbonates

The deformation of high porosity carbonates is achieved by different mechanisms than are observed in low porosity carbonates. The presence of void space within the rock means that strain can be accommodated, at least initially, by compaction processes (pore collapse, grain rotation, and grain fracturing).

High porosity granular rocks often accommodate strain by dilation, compaction, or shear-enhanced compaction, forming arrays of narrow bands, known as deformation bands (Figure 2-7). There are different types of deformation bands depending on the deformation mechanisms present, which are documented in both clastic rocks (e.g. Aydin & Johnson 1978; Antonellini & Aydin 1994; Flodin *et al.* 2005; Fossen *et al.* 2005, 2007; Rotevatn *et al.* 2008; Ballas *et al.* 2015) and carbonates (Tondi *et al.* 2006; Tondi 2007; Agosta *et al.* 2010; Rath *et al.* 2011; Cilona *et al.* 2012; Antonellini *et al.* 2014; Rotevatn *et al.* 2016; Kaminskaite *et al.* 2019). In rocks with low cohesive strength, tensile stress is principally accommodated through granular flow, which is the governing process of sediment disaggregation. These mechanisms enable the generation of *dilation bands* (Du Bernard *et al.* 2002). Granular flow accompanying compaction forms *compaction bands*. Under shear stress, grains will move past each other to accommodate offset, forming either a *compactive* or *dilatant shear band* (Fossen *et al.* 2007). In compaction and shear bands, granular disaggregation is often accompanied by cataclasis, whereby intragranular fracturing occurs at grain-grain contacts (Herzian impingement microcracks). Grain-grain contacts also provide sites for pressure solution (e.g. Tondi *et al.* 2006; Cilona *et al.* 2012; Rotevatn *et al.* 2016). The presence of micritic peloid grains in carbonates allows further plastic deformation, due to their preference for smearing and mixing (Antonellini *et al.* 2014; Kaminskaite *et al.* 2019).

Deformation band formation is generally a strain-hardening process (Aydin & Johnson 1978; Woodcock & Underhill 1987; Cilona *et al.* 2012), in which the strength of the rock increases with deformation. This prevents localisation along a single slip surface and results in the formation of deformation band arrays (Schultz and Siddharthan, 2005). However, it has been argued that cataclastic deformation bands are a strain-weakening process that may form during the migration

of shear strains at fault irregularities as part of slip localisation (Nicol *et al.* 2013). However, fault cores of large displacement faults suggest that once enough cataclasis has occurred, deformation becomes strain-softening, a process which reduces the rock strength with deformation. This leads to a plane of weaker material than the surrounding host rock, thereby enabling localisation of strain along a single fault core during subsequent fault movement (Wibberley *et al.* 2007). Deformation results in further grainsize reductions of the material through mechanical comminution (cataclasis) with this additional fault movement. However, strain localisation along the fault core can occur without the formation of deformation bands (e.g. Micarelli *et al.* 2006; Matonti *et al.* 2012). Instead, a single localised cataclastic fault core can be formed, hosting lenses of dilatational fault breccia or regions of highly cemented host rock, potentially relating to extensive pressure solution even at shallow burial depths (Matonti *et al.* 2012).

Fault rocks in clay-bearing sequences

The presence of clay minerals either in the deformed rock or in beds within the faulted sequence has further consequences for the style of deformation observed. Microstructural analyses of clay-bearing fault rocks reveals that large portions of strain can be accommodated by the ductile deformation of phyllosilicate minerals. This includes the alignment and smearing of phyllosilicate minerals along slip planes, enabling frictional sliding, the formation of *phyllosilicate framework fault rocks* (Knipe 1997; Fisher & Knipe 1998), and extensive pressure solution, forming interconnected pressure solution seams that are aligned with fault slip (Viti et al., 2014). In impure carbonates containing clay minerals, pressure solution and can lead to the accumulation of clay minerals along pressure solution seams, leading to the formation of fault breccia or cataclasite with clay rich matrices (Bauer *et al.* 2016). Smeraglia *et al*. (2016) document a fault zone containing a phyllosilicate-rich fault core, formed by the injection and concentration of phyllosilicates along the fault core from overlying formations.

The ductile deformation of clay-rich layers in any faulted sequence often leads to the formation of clay smears. The importance of clay smears to hydrocarbon accumulations means that they are well documented, including in carbonate dominated sequences (e.g. Færseth 2006; Bonson *et al.* 2007). Clay smears will be discussed further in Section 2.4.

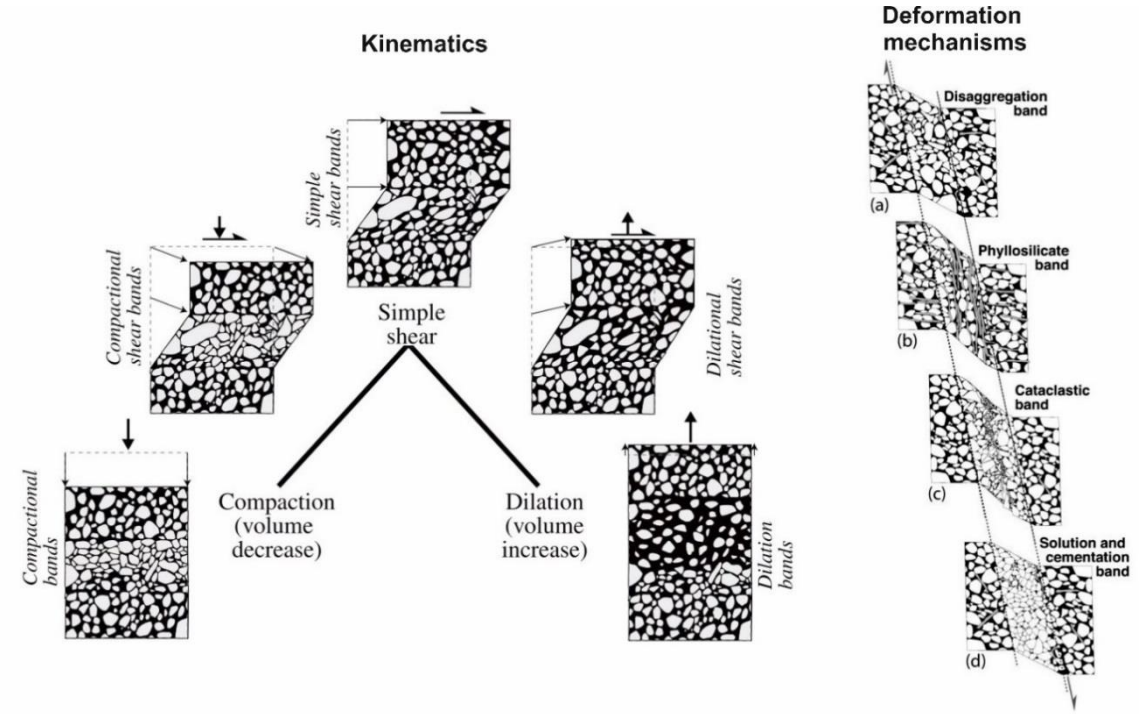

Figure 2-7: Kinematic classification of deformation bands and principal deformation mechanisms that occur within deformation bands (after Fossen et al*. 2007).*

2.2.3. Fault rock thickness

Fault zone thickness has been shown to be correlated with fault displacement (Engelder 1974; Hull 1988; Evans 1990; Shipton & Cowie 2001; Shipton *et al.* 2006; Bastesen & Braathen 2010). This is generally considered to be a result of continuous mechanical attrition of the fault walls, widening the zone of deformation (e.g. Scholz 1987). However, this correlation shows considerable scatter within log-log space, such that there are extremely large variations in fault rock thickness for any given displacement. Solum & Huisman (2017) compiled all published data for fault zone and fault core width, according to the faulted lithology (carbonate, mixed carbonate/other, or non-carbonate). They note that of all studies that differentiate fault core from fault damage zone, the fault core is commonly defined as the width of a zone of cataclasite, gouge, or breccia (i.e. fault rock thickness). This data highlights a general increase in both fault zone and fault core thickness with increasing fault displacement, but shows there to be up to five orders of magnitude variation in fault core thickness for a given displacement (Figure 2-8). There are multiple reasons for this scatter, which include variations in the host lithology, the mechanical

properties of the host rock, the fault zone architectural evolution, and the stress and temperature conditions at the time of faulting.

Wibberley *et al*. (2008) notes that high damage zone fracture intensities, as are typical in lower porosity rocks, lead to changes in the rheology adjacent to the fault core. This may enhance fault core thickness in the initial stages of fault development, because of the continuation of fracturing towards cataclasite formation (Billi *et al.* 2003). After a certain amount of deformation, the majority of strain can be accumulated along the fault core, thereby inhibiting further growth in fault core thickness. However, the incorporation of fault zone complexities (as outlined in section 2.2.1) can lead to extreme variability in the thickness of different fault zone elements (Figure 2-8). In some sections of a fault there may be a single narrow fault core, whilst there may be additional structural elements in regions of fault linkage, which increase the width of the fault core (Shipton & Cowie 2001; Childs *et al.* 2009). For example, a breached relay zone subject to coseismic deformation can be preserved within the fault core as a lens of deformed rock. This is highlighted by Childs *et al*. (2009), who compiled thickness data of different fault zone architectural elements. Those being: fault rocks, deformation bands, fault zones, breached relay zones, intact relay zones, and damage zones. These data suggests that the breaching of relay zones can significantly increase fault zone thickness. However, it must also be noted that two small faults that join to become one large fault would be thinner than a single slip surface of the same length, assuming linkage processes did not contribute to fault thickness (Dawers & Anders 1995; Walsh *et al.* 2002; Kim & Sanderson 2005).

Shipton *et al*. (2006) uses fault core and damage zone thickness data from the Big Hole normal fault in central Utah, cutting the high porosity Navajo Sandstone. The data shows how fault core thickness can vary by an order of magnitude at any point along a single fault and the mean fault core thickness does not change with displacement. However, there is a positive correlation between the damage zone thickness and displacement. Studies of a similar nature that focus on carbonate lithologies are limited, however the thickness of fault zone elements are noted in many carbonate-hosted fault zone outcrop studies (Billi 2005; Micarelli *et al.* 2006; Bastesen & Braathen 2010; Michie *et al.* 2014). Bastesen & Braathen (2010) studied a series of extensional faults cutting fine grained carbonates, finding significant architectural variability between fault zones. They note that fault core thickness-displacement distributions can be represented by two distinct power law functions, representing thin localized fault cores and thicker, more complex fault cores with additional architectural elements such as overlap structures and fault lenses.

Solum & Huisman (2017) uses binned data of carbonate fault core width and displacement to suggest the probability of a fault core width at a given displacement. Figure 2-9 shows this data converted to fault displacement ranges of <10 m, 10-100 m, and >100 m. The data shows that the most common fault core thickness for a <10 m displacement fault is 0.01-0.1 m (49% probability), the most common fault core thickness for a 10-100 m displacement fault is 0.1-1 m (56% probability), and the most common fault core thickness for a >100 m displacement fault is 1-10 m (40% probability).

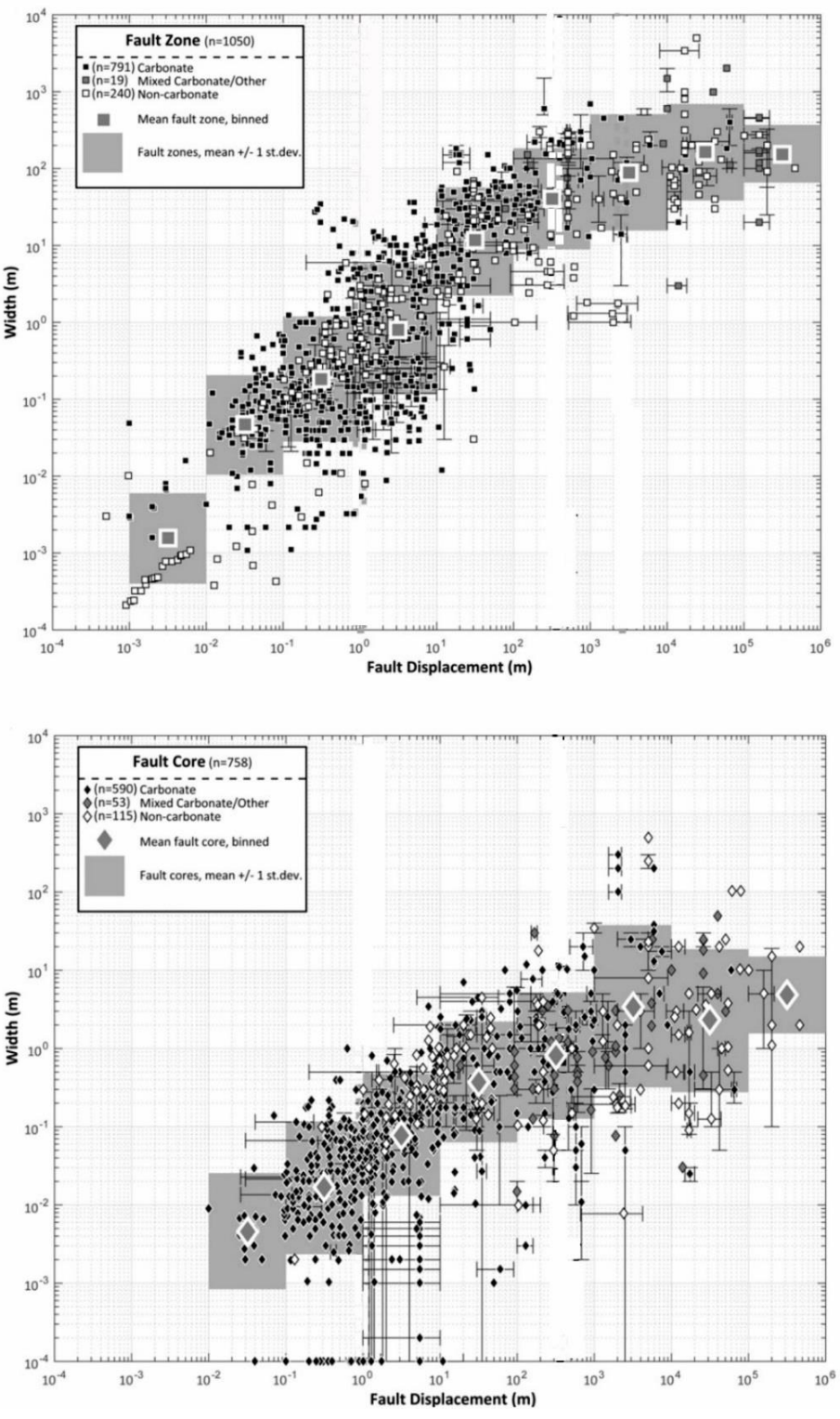

Figure 2-8: Compilaton of fault zone and fault core width data reported for carbonates (black), mixed carbonate/non-carbonate (grey) and non-carbonate lithologies (white) (after Solum & Huisman 2017).

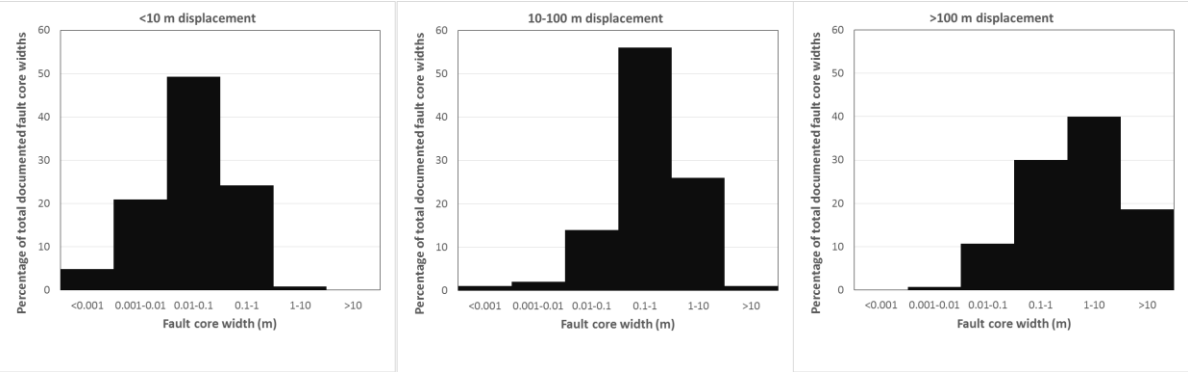

Figure 2-9: Percentage of fault cores within binned fault widths from all published data. Data collected from Solum & Huisman (2017).

2.2.4. Fault rock continuity

The continuity of fault rock is a key parameter to bulk fault permeability, which has gained little consideration. A number of studies comment on whether fault rocks are continuous (Færseth 2006; Micarelli *et al.* 2006; Michie *et al.* 2014; Bauer *et al.* 2016; Ferraro *et al.* 2018), however, none so far have attempted to derive a global scaling relationship between fault displacement and fault rock continuity.

According to the database presented by Solum and Huisman (2017), fault zones without a fault core altogether only occur at displacements <100 m (Figure 2-8). Micarelli *et al*. (2006) investigated a number of low displacement fault cores from vertical sections in high porosity carbonates in the Hyblean Plateau, Sicily, finding that fault core continuity was achieved for all faults with >5 m displacement. Michie *et al*. (2014) investigated a number of fault zones cutting shallow burial, high porosity limestones in Malta, finding that a continuous fault cores only occurred at displacement of >60 m. Bauer *et al*. (2016) reports wide zones of distributed deformation, hosting multiple strands of discontinuous cataclastic fault rock, along faults cutting low porosity dolostones. Contrastingly, they report localised and continuous cataclastic fault cores occur along faults cutting low porosity limestones with more than a 'few tens of meters' displacement. Ferraro *et al.* (2018) also investigated several limestone and dolostone-hosted fault zones, finding that cataclastic fault rocks are continuous at all studied displacements (tens to hundreds of meters). However, with greater displacement, there becomes greater continuity of 'matrix-supported' fault rocks, defined as cataclasite predominantly composed of a fine grained

matrix (>50% matrix), and fault gouge (>75% matrix). These fault rocks are shown to require hundreds of meters displacement to achieve continuity.

Current literature suggests that carbonate fault rock continuity is achieved in the range of 10-100 m. However, it is important to note that the along strike and dip variability in fault core thickness that is typical is most fault zones (Shipton *et al.* 2006; Sosio De Rosa *et al.* 2018) means that observations of fault core continuity over the scale of accessible outcrops may not be representative of the fault core as a whole. Solum & Huisman (2017) argue that fault rock thickness is a better proxy for fault rock continuity, which itself varies over multiple orders of magnitude for a given displacement (Figure 2-8). The degree of variability in continuity estimates suggests that displacement is not the only controlling factor controlling the continuity of carbonate fault rocks; factors such as the mechanical stratigraphy of the faulted sequence, depth and temperature conditions at the time of faulting, and fluid histories are likely to also influence the fault rock continuity.

2.3. Petrophysical characteristics of carbonate-hosted fault zones

The petrophysical properties of carbonate-hosted fault rocks has been reported by a number of authors (Géraud *et al.* 2006; Micarelli *et al.* 2006; Agosta *et al.* 2007; Rath *et al.* 2011; Matonti *et al.* 2012; Antonellini *et al.* 2014; Ran *et al.* 2014; Tondi *et al.* 2016; Bauer *et al.* 2016; Michie & Haines 2016; Williams *et al.* 2017; Kaminskaite *et al.* 2019). The following sections outline the published data for fault rocks derived from low porosity (<5%) and moderate to high porosity (>5%) host rocks.

2.3.1. Fault rocks from low porosity host rocks

Agosta *et al*. (2007) studied normal faults cutting low permeability (6.9 x 10^{-4} mD) and porosity (0.8%) platform carbonates. They reported permeability in the fractured damage zone of 8-20 mD and cataclasite and breccia permeability of 0.1 mD and 2-5% porosity, reducing to <10^{-5} mD and 0.6% porosity where cemented. Additionally, mercury injection capillary pressure (MICP) tests showed that uncemented fault rocks can support a 6-80 m hydrocarbon column for gas and a 10-140 m hydrocarbon column for oil (4-50 psi entry pressure). Géraud *et al*. (2006) report data from tight pelagic limestone with minor clay content (<1% porosity) and a very low permeability (10^{-4} mD). Their data indicate an asymmetric porosity profile across the fault zone, with rapid increase in porosity to the fault core in the footwall, and a gradual increase in porosity towards the fault

core in the hanging wall. Fault core porosity is measured as 5-6%. A fault core permeability of 10^3-10^4 mD is inferred from mercury injection data. Bauer *et al.* (2016) studied faults cutting low porosity limestone and dolostones, but do not quantify the host rock properties. Measurements of fault zone samples show permeability of 0.01 – 1 mD for fractured rock, >1000 mD for dilation breccia, 0.1 mD for dissolution breccia, and 100-1000 mD for cataclasite, reducing to 0.01-1mD with increased cataclasis. Porosity increased towards the fault core, from 1% in rocks with least fracturing to 6% in cataclasite samples.

Overall, these measurements indicate that the properties of fault rocks from low porosity carbonates are highly dependent upon the degree of diagenesis, whereby cemented fault rocks may have reduced permeability relative to host rocks, but porosity and permeability exhibits an increase when fault rock is uncemented.

2.3.2. Fault rocks formed from moderate to high porosity host rocks

Deformation bands often develop in porous carbonates and typically have reduced permeability relative to their protolith. Antonellini *et al*. (2014) studied deformation bands in platform limestones, Italy, with an average permeability in the undeformed host rock of *c.*100 mD and a host porosity of 17-27%. Deformation bands have a porosity of 2-5%, permeability normal to the slip surface is 7.8 mD, and parallel to the slip surface is 48.2 mD. Kaminskaite *et al*. (2019) studied deformation bands in high porosity (40-50%) carbonates, from a variety of carbonate lithologies. They report deformation band porosities as low as 5%, but more typically 10-30%. Permeability reductions of up to 6.5 orders of magnitude relative to host are reported, but data is extremely scattered. Some deformation bands in chalk have negligible impact on permeability, whereas cemented deformation bands in grainstones exhibit permeability as low as 10^{-3} mD. Similarly, Rath *et al*. (2011) studied deformation bands in grainstones, which exhibit a reduced porosity from 22-35% host porosity down to 2-5% deformation band porosity as a result of deformation band cementation. Deformation band permeability reduced up to three orders of magnitude relative to the host rock. Tondi *et al*. (2016) measured in-situ permeability of compactive shear bands in porous grainstones from Majella Mountain, Italy, and Favignana Island, Sicily. Host rocks at Majella Mountain have a porosity of 20% and permeability of 0.45 mD, reducing to a porosity of 0.5% and permeability of 0.008 mD in the deformation bands. In Favignana, the average host rock porosity is 30% and permeability is 70 mD, reducing to a porosity of 0.5 % and permeability of 0.5 mD in the deformation bands.

In the fault core, permeability reductions relative to the host rock are common, but not wholly observed. Matonti *et al.* (2012) does not report permeability values, but shows how moderate porosity carbonate rocks (5-16%) can contain fault rocks with very low porosity (<2%), attributing this entirely to cementation due to fault induced pressure solution. Micarelli *et al*. (2006) studied normal faults cutting high porosity carbonates in Sicily, with a host rock permeability of 20-40 mD. They report average fault rock permeability values of 0.6 mD for discontinuous, 1-5 m displacement fault cores and 0.15 mD for continuous, >5 m displacement fault cores, respectively. Michie & Haines (2016) show how permeability varies throughout a fault zone in pelagic and coralline limestones from Malta. They report permeability variations of up to 3 orders of magnitude variability along a single 11.7 m displacement fault segment, and 6 orders of magnitude along a single 90 m displacement fault segment. In grain-dominated lithofacies with an average host porosity of 25% and permeability of 100 mD, lowest fault rock permeability measurements correspond to cataclasite and composite fault breccia (10^{-1}-10^{-4} mD), which are both highly cemented. In micrite-dominated lithofacies with an average host porosity of 38 % and permeability of 1 mD, lowest fault rock permeability measurements correspond to indurated chaotic breccia and recrystallised fault rocks, ranging from 10^{-2}-10^{-3} mD.

2.4. Current fault seal workflows

Current fault seal workflows rely upon an understanding of the behaviour of shale-rich layers during faulting and empirical relationships in siliciclastic rocks, neither of which are applicable to carbonate sequences void of shales. In a sequence containing shale-rich layers, the formation of a clay smear within the fault can be predicted using algorithms such as the clay smear potential (Weber *et al.* 1978), shale smear factor (Lindsay *et al.* 1992), and shale gouge ratio (Yielding *et al.* 1997). These algorithms relate parameters such as the thickness of the offset shales, the distance between to the shale layer at a point on the fault, and the total fault offset, enabling a prediction of the likelihood of a continuous clay smear. The sealing capacity of fault rocks from siliciclastic rocks is estimated based upon empirical relationships between host rock properties, fault rock permeability, and capillary threshold pressure, measured from outcrop and core samples (e.g. Fisher & Knipe 1998; Sperrevik *et al.* 2002). These host properties are namely clay content, burial history, time of faulting. These relationships are used to predict permeability at different points along the fault, which can then be implemented within reservoir simulations. Manzocchi *et al*. (1999) introduced a method of representing faults as transmissibility multipliers between the

faces of two faulted cells in a reservoir model, requiring predictions of fault permeability and fault thickness as input parameters.

For carbonate reservoirs, the prediction of transmissibility is hindered by the lack of a predictive tool for fault permeability. Michie *et al*. (2017) presented upscaled fault zone permeability values from 3 fault zones in Malta, through which a predictive algorithm was generated, specific to the studied sequence. This algorithm considered the juxtaposing lithofacies at any point along the fault, and assigned a fault permeability based upon trends between upscaled permeability and displacement. However, no current generalised predictive tool for fault permeability in carbonate rocks exists.

2.5. Summary

Faults can either be sealing to fluids over geological timescales, barriers to fluids over production timescales, or be conduits to fluid flow. For a sealing fault, the capillary threshold pressure of the fault is greater than the buoyancy pressure of the non-wetting phase in a two-phase system. For a fault barrier, the buoyancy pressure is greater than the capillary threshold pressure of the fault and across-fault fluid flow is determined by either the juxtaposed formation or the permeability of the fault itself. For a fault to be a conduit, the fractured damage zone or fault core exhibit increased permeabilities relative to the host rock, promoting up-fault fluid flow. The hydraulic behaviour of a fault depends on a combination of the fault zone architecture, which determines fault rock distributions, and petrophysical characteristics of those fault rocks. Carbonate-hosted fault zones are often highly complex, comprised of a variety of complexities, such as fault bound lenses, relay zones, fault bends, jogs, and splays, all of which influence fault rock thickness. Currently, the role of these complexities on fault rock continuity has not been well documented.

Fault cores are dominated by both cataclastic and plastic deformation mechanisms, which both enable the formation of various fault rock fabrics. In porous carbonates, cataclasis, compaction, and crystal-plastic mechanisms are common, acting to generate potential low permeability fault rocks. The permeability of these fault rocks is highly variable, but they are typically reported as having reduced permeability relative to host rock permeability. In contrast, fault rocks derived from low porosity carbonates typically experience permeability increases relative to their host rock. To predict the permeability of fault rock for a given fault zone, empirical relationships between host rock properties and fault rock permeability must be established. These relationships can then be upscaled to estimate bulk fault permeability, when combined with

an understanding of the fault rock distribution, and applied to reservoir simulations to predict the permeability and thickness of fault cores; thereby leading to the calculation of transmissibility multipliers for fluid flow simulations.

CHAPTER 3.

Investigating the controls on fault rock distribution in normal faulted shallow burial limestones, Malta, and the implications for fluid flow

Cooke, A.P., Fisher, Q.J., Michie, E.A.H. & Yielding, G. 2018. Investigating the controls on fault rock distribution in normal faulted shallow burial limestones, Malta, and the implications for fluid flow. *Journal of Structural Geology*, **114**, 22–42, https://doi.org/10.1016/j.jsg.2018.05.024.

3.1. Abstract

The spatial distribution and fabric of carbonate fault rocks observed at outcrop are often highly heterogeneous. Therefore, petrophysical properties of fault rock samples may not be representative of the overall sealing capacity of the fault zone. By quantifying the fault rock distributions (i.e. fault rock thickness and fault rock continuity) of several fault zones in Malta, juxtaposing shallow burial limestones, this work investigates the relationship between fault zone architecture, deformation mechanisms, and fault rock distribution. Results from microstructural analyses indicate that high porosity (>15 %) grain-dominated limestones deform via grain scale deformation, as opposed to fracture-derived cataclasites often observed in tight carbonates. Low porosity (<15 %) grain-dominated limestones and high porosity micrite-dominated limestones deform in a more distributed manner, through extensional fracturing and brecciation. Fault rock continuity estimates suggest throws of 50-200 m are required to form a continuous low-permeability cataclasite veneer in the studied sequence. However, greater throws may be required when a distributed damage zone is present, in which strain is accommodated over multiple slip surfaces. This work highlights the heterogeneity in the distribution and fabric of carbonate fault rocks within fault zones hosting tens of meters throw, and the importance of considering fault rock thickness and continuity when estimating the sealing capacity of a carbonate-hosted fault zone.

3.2. Introduction

Faults have been documented to impact fluid flow in the subsurface, (Smith 1980; Taylor & Dietvorst 1991; Knai & Knipe 1998; Wiprut & Zoback 2000; Fisher & Knipe 2001; Jolley *et al.* 2007). Although there are documented examples of carbonate-hosted fault zones acting as barriers to fluid flow (e.g. Bockel-Rebelle *et al.* 2004; Birkle & Angulo 2005; Vega Riveros *et al.* 2011; Corona *et al.* 2012), their impact on flow is poorly understood, despite the global importance of carbonate reservoirs in hydrocarbon reserves; around 60% of global oil reserves and 40% of global gas reserves are stored in carbonates (Schlumberger 2007). Past research into the sealing potential of faults has been primarily directed towards siliciclastic hydrocarbon reservoirs (e.g. Knipe 1992; Antonellini & Aydin 1994; Caine *et al.* 1996; Evans *et al.* 1997; Fulljames *et al.* 1997; Yielding *et al.* 1997; Fisher & Knipe 2001; Crawford *et al.* 2002; Flodin *et al.* 2005; Færseth *et al.* 2007). These studies indicate that fault zone structure can provide useful insights into the potential for across-fault fluid flow within the subsurface (Caine *et al.* 1996; Evans *et al.* 1997; Rawling *et al.* 2001).

Fault rock distributions and observed deformation mechanisms are controlled by a number of factors, including fault zone architecture and host rock properties (Mitchell & Faulkner 2009; Michie *et al.* 2014). Fault zone studies in both siliciclastic and crystalline rocks have enabled the development of a conceptual model for fault zone architecture. Slip along a fault commonly produces a localised fault core, or several strands of fault core, surrounded by a damage zone in which damage decreases exponentially into the undeformed protolith (Aydin & Johnson 1978; Chester & Logan 1986; Caine *et al.* 1996; Shipton & Cowie 2001; Kim *et al.* 2004; Mitchell & Faulkner 2009; Riley *et al.* 2010). In general, the fault core is composed of high strain products that destroy the protolith fabric and are often characterised by a low permeability that may act as barriers or baffles to flow. The surrounding damage zone, typically containing a high fracture density whilst mostly preserving the protolith fabric, is commonly considered a conduit to flow (e.g. Chester & Logan 1986; Chester *et al.* 1993; Antonellini & Aydin 1994; Fisher & Knipe 2001; Wibberley & Shimamoto 2003; Mitchell & Faulkner 2009). However, depending on the porosity, texture and stress conditions at the time of faulting, the damage zone may act as a barrier to flow, particularly in clastic reservoirs (Fossen *et al.* 2007).

This fault zone model has been shown to also be broadly applicable to carbonate-hosted fault zones (Agosta & Kirschner 2003; Storti *et al.* 2003; Micarelli *et al.* 2006); continuous low permeability fault cores, likely to act as a barrier or partial barrier to flow, and fractured damage zones, likely to have enhanced permeability, are documented in carbonate rocks (e.g. Micarelli *et al.* 2006; Agosta *et al.* 2007; Agosta 2008). However, carbonate-hosted fault zones are commonly documented to have a variety of additional structural elements. These include fault cores consisting of discontinuous lenses of fault rock exhibiting a variety of fabrics and petrophysical properties (e.g. Michie & Haines 2016), fault zones with permeable deformation products, such as fracturing and fault breccia, likely to allow up- and along-fault fluid flow (e.g. Lee *et al.* 1997; Matonti *et al.* 2012), and fault zones that host a fracture splay zone, whereby fractures and subsidiary slip surfaces are generated at a point of strain accumulation, relating to the mechanical stratigraphy imposed by juxtaposing two lithofacies with contrasting mechanical properties (Michie *et al.* 2014). The variable architectures associated with these examples control the distribution of fault rock and, ultimately, the fluid flow throughout the fault zone. Therefore, it is important to consider how these architectures are generated with respect to the host rock and fault kinematics.

Understanding fault rock distributions requires quantifiable physical parameters, such as fault rock thickness (FRT) and fault rock continuity (FRC). Empirical relationships between fault displacement and FRT, recorded from a combination of field and subsurface core studies, enables the prediction of FRT for any fault of known throw (Hull 1988; Wibberley *et al.* 2008; Childs *et al.* 2009; Solum & Huisman 2017). This data is directly applicable to the estimation of fault sealing potential over production timescales through the use of transmissibility multipliers (Manzocchi *et al.* 1999). However, empirical data varies over several orders of magnitude for any given displacement (e.g. Hull 1988) due to the architectural heterogeneity between fault zones. This method of thickness estimation also assumes a continuous fault core, which is often not observed at outcrop (e.g. Micarelli *et al.* 2006; Joussineau & Aydin 2007; Bauer *et al.* 2016).

Several studies consider the continuity of shale smear within siliciclastic hosted fault zones (e.g. Yielding *et al.* 1997; Færseth 2006). However, there is limited research into the spatial heterogeneity of fault rock distributions in carbonate rocks (e.g. Bonson *et al.* 2007). Studies of high porosity carbonate-hosted fault zones have suggested that fault rock becomes continuous after 5 m displacement based upon thickness measurements along vertically exposed fault zone cross sections (Micarelli *et al.* 2006). Studies of low porosity carbonate-hosted fault zones have

suggested that cataclastic fault rocks only become continuous at high displacements. However, portions of impermeable cataclasite are not considered continuous enough to have a regional impact on flow (Bauer *et al.* 2016). Studies of fault zones in Malta have suggested that fault cores are continuous at displacements greater than 30 m, due to fault rock being distributed across multiple slip surfaces generated within weaker layers (Michie & Haines 2016). Despite the importance of a continuous fault core, to the authors' knowledge, no quantified carbonate-hosted FRC measurements have previously been published.

This research aims to improve the understanding of fault rock distribution in shallow water limestones by investigating the architectural controls on fault rock formation and by providing a quantified study of FRT and FRC in faulted Oligo-Miocene limestones. Accordingly, this study presents results from the analysis of three fault zones outcropping in eastern Gozo, Malta, from which fault zone mapping and outcrop structural data are used to interpret the fault zone architecture and the distributions of fault rock. The deformation mechanisms observed within each fault zone are characterised using microstructural analysis, thereby providing an understanding of the architectural and lithological controls on fault rock fabric. FRT measurements and FRC estimates are presented from 6 Maltese fault zones, investigating the control of fault throw, host rock lithofacies, and fault zone architecture on fault rock distribution. This study highlights the importance of considering FRT heterogeneity and FRC within carbonate-hosted fault zones when estimating their hydraulic behaviour.

3.2.1. Geological setting

Field analysis was undertaken from 6 fault zones within the islands of Malta (Figure 3-1C). Detailed fault zone architecture and microstructural investigations were undertaken for three of these fault zones located on the eastern tip of the island of Gozo (Figure 3-1C, Faults A-C). Malta is characterised by well exposed, faulted Oligo-Miocene reef limestones with limited post deformation diagenesis. The studied faults offset the simple sequence with throws ranging from several meters to hundreds of meters. Faulted outcrops often enable a study of faulting in either, or both, cross sectional and map views due to the morphology of the islands, which includes raised beaches, limited vegetation, and prominent cliffs. Fault surfaces often form cliff faces themselves, such as the Il Maghlaq Fault (IMF) (Figure 3-1B & C), due to a resistance to weathering or the poor preservation of the hanging wall damage zone, allowing along strike fault rock measurements to be undertaken.

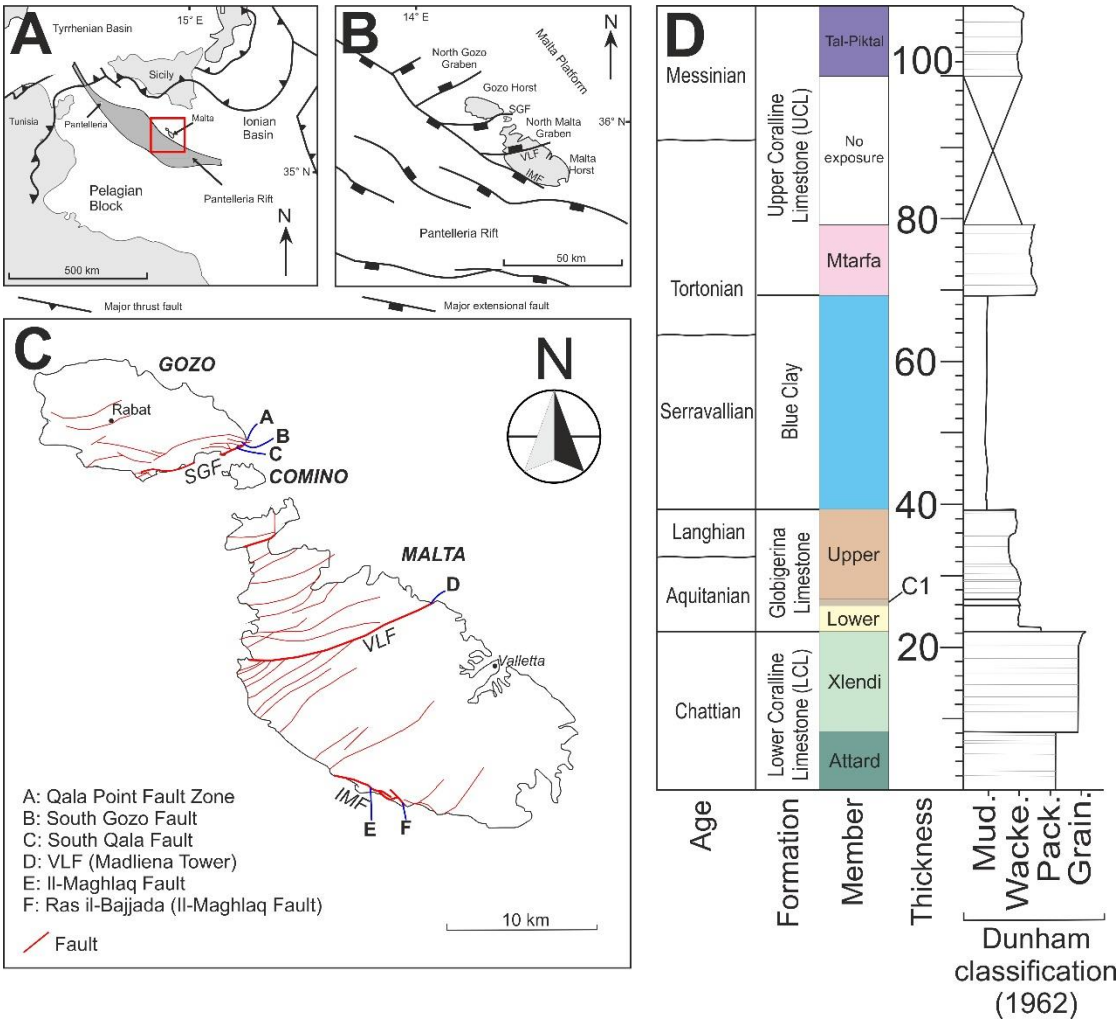

Figure 3-1: A) The location of the Maltese islands, on the northern shoulder of the Pantelleria Rift system, in the foreland of the Apennine-Maghrebian thrust system. B) Main structures of the Maltese island, oriented ENE-WSW and WNW-ESE, where the majority trends ENE-WNW (after Dart et al. 1993). SGF = South Gozo Fault; VLF = Victoria Lines Fault; IMF = Il–Maghlaq Fault. C) Overview map of the Maltese Islands showing the locations of study sites (A-F). D) Stratigraphic log for the Qala point study area, eastern Gozo.

3.2.2. Tectonic framework

The Maltese Islands (Malta, Comino, and Gozo) are located on the northern flank of the Pantelleria rift (Illies 1981; Boccaletti *et al.* 1987) (Figure 3-1A). The Pantelleria rift comprises a series of elongated, fault controlled rift basins of Miocene-Pliocene age situated at the centre of the Pelagian block (Reuther & Eisbacher 1985), a shelf bridge connecting the Hyblean Plateau of Southern Sicily and the Tripolitanian platform of northern Libya. Rifting began simultaneously with mountain belt formation in the Oligocene, forming a complex sequence of horst and grabens, including the Maltese graben system which dominates the faulting in Malta (Reuther & Eisbacher 1985; Jongsma *et al.* 1987; Dart *et al.* 1993) (Figure 3-1B). There are 2 intersecting fault trends within this system, ENE-WSW and WNW-ESE, resulting from N-S extension (Pedley *et al.* 1976; Reuther & Eisbacher 1985; Dart *et al.* 1993) (Figure 3-1B). The dominant onshore fault trends (ENE-WSW) are related to the North Malta Graben, which is bound by 2 major normal faults: the Victoria Lines Fault (VLF) and the South Gozo Fault (SGF) which crosscut Malta and outcrop along the south coast of Gozo, respectively (Figure 3-1C).

Gozo, located to the North of Malta, has a gentle regional dip to the NE and is dominated by normal faults roughly parallel to the SGF (Pedley *et al.* 1976). A series of narrow, asymmetric graben or tilt blocks extend inland from the SGF at an angle of c. 50° (Figure 3-2A), interpreted as en echelon structures relative to the dextral shear pattern of the SGF (Illies, 1981). This series of faults includes 2 of the studied fault zones, namely the Qala Point Fault Zone (QPFZ) and the South Qala Fault (SQF) (Figure 3-2B).

3.2.3. Stratigraphic framework

Carbonate lithofacies has previously been shown to exert some control on the deformation microstructures; micrite-dominated rocks (mudstones – wackestones) typically deform in a distributed manner, whereas grain-dominated rocks (packstone – grainstones) deform in a more localised manner on the grain scale (Michie *et al.* 2014). Therefore, the dominant lithofacies of each formation is noted for simplification.

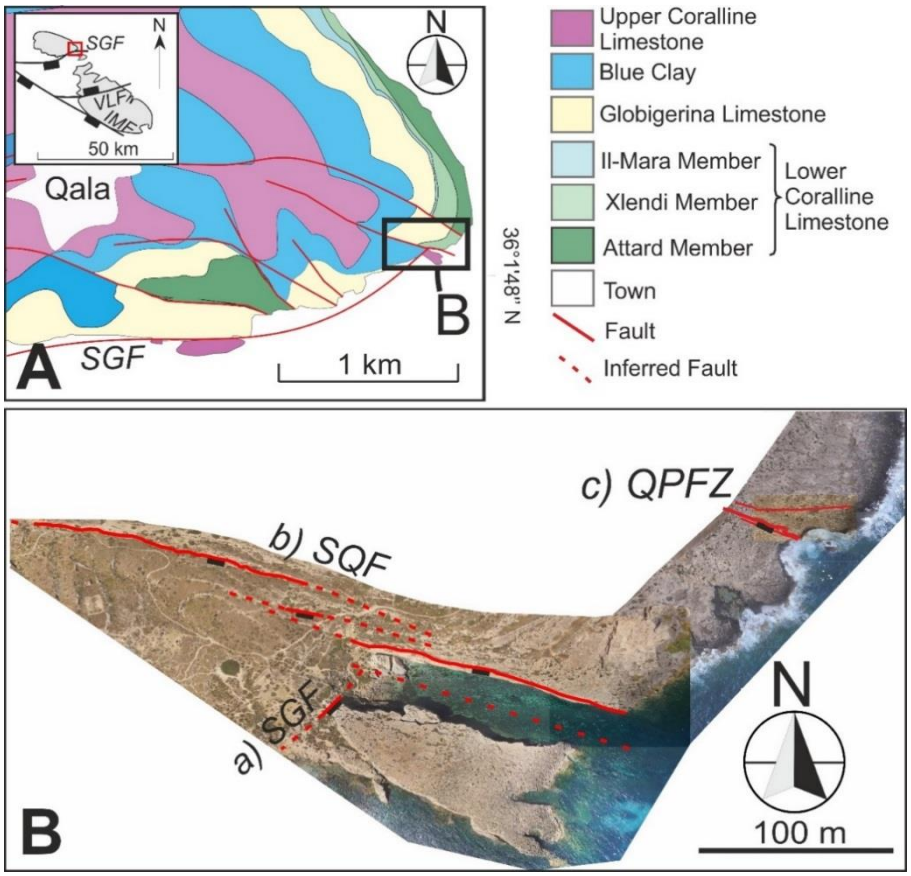

Figure 3-2: A) Geological map of the Eastern tip of Gozo (inset: map of Malta showing map location. Black box: location of the Qala Point study area). B) Drone map of the Qala Point study area with principal slip surfaces annotated. SGF = South Gozo Fault; SQF = South Qala Fault; QPFZ = Qala Point Fault Zone.

The Maltese sequence consists of a simple 'layer cake' succession of Oligocene – Miocene, shallow burial carbonates (Figure 3-1D). The oldest exposed units consist of a series of shallow water reef limestones (Lower Coralline Limestone, Figure 3-3), succeeded by pelagic foraminiferal wackestones (Globigerina Limestone, Figure 3-3), a carbonate rich clay layer (Blue Clay), and finally additional reef limestone successions (Upper Coralline Limestone, Figure 3-3).

Lower Coralline Limestone (grain-dominated)

The base of the exposed succession on Malta is formed by the Chattian (Oligocene) Lower Coralline Limestones (LCL) (Figure 3-1D & Figure 3-3). The LCL is primarily composed of grainstones and packstones. A maximum of 140 m of LCL is exposed onshore, despite its thickness

reaching up to 1000 m offshore (Pedley *et al.* 1976; Bonson *et al.* 2007). The LCL varies from pale yellow biomicrites at its base, to massively bedded coralline algal limestones, and finally coarse bioclastic limestones displaying cross bedding at the top (Pedley *et al.* 1976; Pedley 1978; Brandano *et al.* 2009). Pedley (1978) divided the LCL into 4 members that are non-uniformly distributed across the islands, these are (oldest to youngest): the Maghlaq Member, the Attard Member, the Xlendi Member and the Il-Mara Member. The Attard and Xlendi members are the only members present within the principal study areas, therefore are the only members discussed:

- The Attard member is a rhodolitic algal packstone containing coral, red algae and larger benthonic foraminifera, deposited on the inner and middle ramp (Pedley 1978; Brandano *et al.* 2009) (Figure 3-3). The Attard member has a porosity of 10 – 15%.
- The Xlendi member is a succession of bioclastic packstone units, including the Scutella beds, displaying upwards shallowing and cross bedded biosparites (Figure 3-3). Depositional setting is interpreted as a shoal environment (Pedley 1978; Brandano *et al.* 2009). It often occurs laterally to and above the Attard member. The Xlendi member has a porosity of 25 – 30%.

Globigerina Limestone (micrite-dominated)

The LCL is capped by a hardground, which in turn is overlain by the Globigerina Limestone Member (GL) pelagic carbonates of Aquitanian to Serravallian age (Pedley *et al.* 1976; Dart *et al.* 1993) (Figure 3-1D). The GL is a succession of fine-grained biomicritic wackestones and marls containing primarily planktonic foraminifera (*Globigerina*) (Figure 3-3), representing a deepening to an outer shelf environment (Pedley 1978; Bonson *et al.* 2007). Two hardgrounds, overlain by phosphoritic conglomeratic layers (<0.7 m in thickness), separate the formation into the Lower, Middle and Upper Globigerina Limestone members (LGL, MGL and UGL respectively) (Pedley 1978; Pedley & Bennett 1985; Bonson *et al.* 2007) (Figure 3-3). The LGL consists of pale cream to yellow packstones becoming wackestones just above the base and are cut by neptunian dykes, hence marking the onset of rifting (Dart *et al.* 1993). The MGL is a sequence of massive white carbonate mudstones and marls. The UGL comprises cream wackestones with a central pale grey marl. The thickness of the GL formation varies from 40 – 75 m (Pedley *et al.* 1976; Dart *et al.* 1993). However, the MGL and C2 thin southward across Gozo until they become absent, resuming in northern Malta (Figure 3-1D). The GL has a porosity of 30 – 36%.

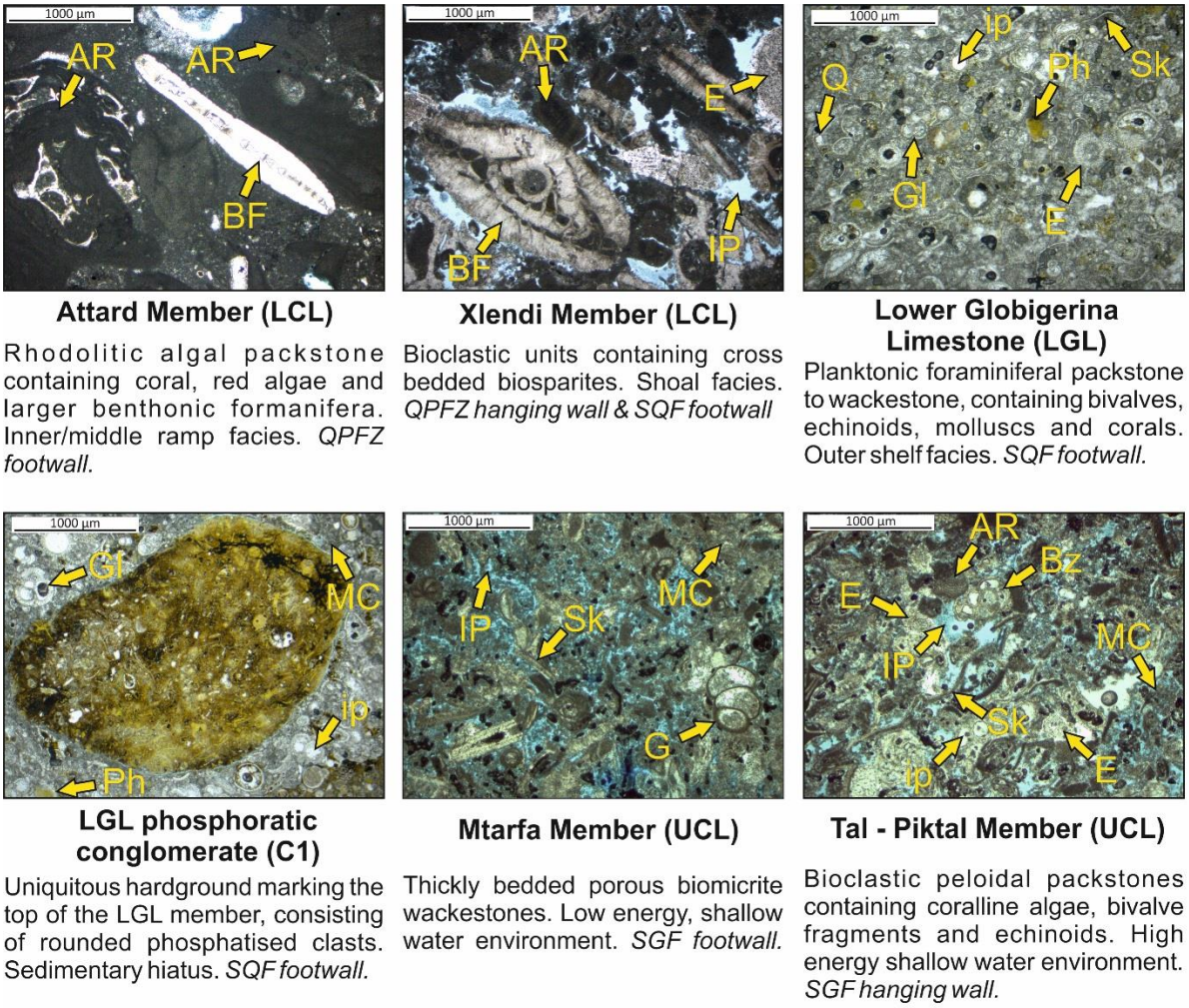

Figure 3-3: Host textures for the members of the Lower Coralline Limestone (LCL), the Lower Globigerina Limestone (LGL), and the Upper Coralline Limestone (UCL) present at outcrop. Optical micrographs in PPL with blue dyed epoxy resin used to highlight pore spaces. AR = Algal rhodolith; BF = Benthic foraminifera; Bz = Bryozoan; E = Echinoid; G = Gastropod; Gl = Globigerina; IP = Intergranular porosity; ip = Intragranular porosity; MC = Micrite cement; Ph = Ca-Phosphate; Q = Quartz; Sk = Skeletal fragments.

Blue Clay (marl/clay)

The Blue Clay formation (mid to late Serravalian) consists of light and dark grey banded marls, in which lighter colours contain greater proportion of carbonate. The Blue Clay is rich in kaolinite, glauconite, and contains up to 30% carbonate with a *c.*75 % phyllosilicate content (John *et al.*

2003). Formation thickness varies from a maximum of 65 m to areas of absence along rift margins in eastern Malta (Pedley *et al.* 1976; Dart *et al.* 1993).

Upper Coralline Limestone (micrite/grain-dominated)

The youngest outcropping unit within the Maltese sequence is the Upper Coralline Limestone (UCL), of Late Tortonian to Messinian age (Bosence & Pedley 1982; Bonson *et al.* 2007) (Figure 3-1D). The lowermost part of the UCL consists of coralline algal biostrome facies, known as the Mtarfa member, moving upward into a coral and algal patch reef facies, known as the Tal-Piktal member (Bosence & Pedley 1982; Dart *et al.* 1993). The upper part of the UCL is characterized by significant fault controlled facies distributions, areas of non-deposition, and major growth faults characterized by divergent fanning strata (Dart *et al.* 1993). The 2 members present within the study zone are the Mtarfa member, containing thickly bedded mudstones and wackestones, and the Tal-Piktal member, a pale grey wackestone to packstone (Figure 3-1D & Figure 3-3). Both members have porosities in the range of 25 – 35%.

3.3. Methodology

3.3.1. Sample collection

Oriented hand specimen sized samples were collected for microstructural and petrophysical property analysis. Sample collection aimed to represent any heterogeneity present within the fault zone whilst collecting undeformed host samples for comparison.

3.3.2. Fault zone mapping

Georeferenced orthomosaic maps were created to enable accurate fault zone mapping. To produce the maps, georeferenced aerial photos were taken with a DJI Phantom 3 Professional drone along automated flight paths. Flight elevation was selected based upon the resolution required at each outcrop; elevations ranged from 10-50 m for high and low resolution requirements, respectively. The front and side image overlap was >65 % to ensure successful photo stitching. Maps were combined with structural field data to produce accurate geological maps of each locality.

Fault rock thickness (FRT) measurements were taken along fault strike at regular intervals (0.5-1 m) for each fault zone with accessible exposure. Thickness measurements were

differentiated according to fault rock fabric, allowing for the thickness of each fault rock fabric to be compared. Fault rock continuity (FRC) was estimated as a ratio of total fault rock length to the total exposed length of the fault segment. Cataclasite FRT measurements and FRC estimates were taken at all fault zones highlighted in Figure 3-1. However, only 3 fault zones are suitable for along strike FRT measurements and FRC estimates for the entire fault zone width (i.e. well exposed and accessible fault zones, thereby allowing FRT measurements), namely the QPFZ (30 m throw), the Ras il-Bajjada (RiB) fault strand of the Il-Maghlaq fault (IMF) (50 m throw), and the Victoria Lines Fault (VLF) at Madliena Tower (90 m throw).

3.3.3. Scan Lines

Circular window scan lines were used to determine the intensity of planar features (i.e. fractures and deformation bands) (Mauldon & Dershowitz 2000; Mauldon *et al.* 2001; Rohrbaugh *et al.* 2002). Circular scan lines are best suited to avoid sampling bias relating to orientation of fracture traces. Scan lines were applied along transects perpendicular and parallel to principal slip surfaces at different spacing along strike to capture variation in such parameters. One transect was used to measure fracture intensities across the QPFZ and three scan lines were used to measure deformation band intensities in the accessible portion of the SGF hanging wall.

3.3.4. Microstructural analysis

Resin-impregnated polished thin sections were analysed using an optical microscope and a CAMSCAN CS44 scanning electron microscope. Fault rock samples were oriented in planes parallel and perpendicular to fault dip, whereas host rock samples were oriented relative to bedding. Samples were impregnated with low viscosity resin containing a blue dye to make pore spaces more apparent. Where core plugs could not be obtained, image analysis of BSE-SEM images was undertaken to estimate the sample porosity. Image analysis was also used to measure grain orientations within deformation bands. To do so, the long axis of grains was superimposed to the image and the grain Feret angles were calculated (orientation of grain Feret diameter).

3.3.5. Porosimetry

To measure host porosity, 1 inch and 1.5 inch core plugs were drilled from the collected samples (see Appendix 1 for core plug data). Core plugs were cleaned to remove salts using deionised water saturated with carbonate sediment of the same composition as the sample. Once clean, core

plugs were dried at 60° for >4 days. The bulk volume of the core plugs was calculated using calipers to measure core plug length and diameter, with a precision of 0.01 mm. Sample grain volumes were then calculated according to Boyle's Law using a double cell helium porosimeter. Porosity was calculated using the calculated grain and bulk volumes.

3.4. Results

3.4.1. Fault zone architecture

South Gozo Fault (SGF)

The SGF is a 65° SE dipping normal fault, juxtaposing the Tal-Piktal member of the UCL (hanging wall) against the top of the Blue Clay and base of the UCL Mtarfa member (footwall) (Figure 3-4D). Based upon the thickness of the Mtarfa and Tal-Piktal members, 16 m and >25 m respectively, fault throw is at least 25 m. The SGF at Qala Point intersects and terminates against the SQF (Figure 3-2B), however there is no obvious preserved interaction between these 2 intersecting fault traces. A second slip surface, parallel to the SQF, is interpreted within the coastal inlet, between which the Blue Clay formation is entrained in a clay smear (Figure 3-2B). The smearing of the Blue Clay formation is common throughout all Maltese fault zones with similar stratigraphic juxtapositions (i.e. where the Blue Clay is visibly offset).

The hanging wall and the footwall both contain intense deformation band arrays surrounding the SGF. Deformation bands appear as light ridges on the weathered surface as they are more resistant to weathering than the host rock. Figure 3-4 shows their dominant trends (*c.*030-060° dominant trend and *c.*150-170° conjugate trend), which reflect the trend of the SGF. Scan line measurements taken >2 m from the principal slip surface show that hanging wall deformation band density and intensity do not appear to correlate with distance from the principal slip surface over the scale that scan lines were undertaken (average intensity is *c.*11 m^{-1} and average density is *c.*21 m^{-2}). However, closer to the principal slip surface (<2 m), intensities observed from hand specimens and core plugs drilled perpendicular to faulting show intensity increasing rapidly towards the principal slip surface within both the hanging wall and footwall (Figure 3-4E). Although no footwall scan lines were undertaken, footwall hand specimen samples at *c.*5 m from the principal slip surface show deformation band intensities that correlate with the scan line and core plug data recorded in the hanging wall.

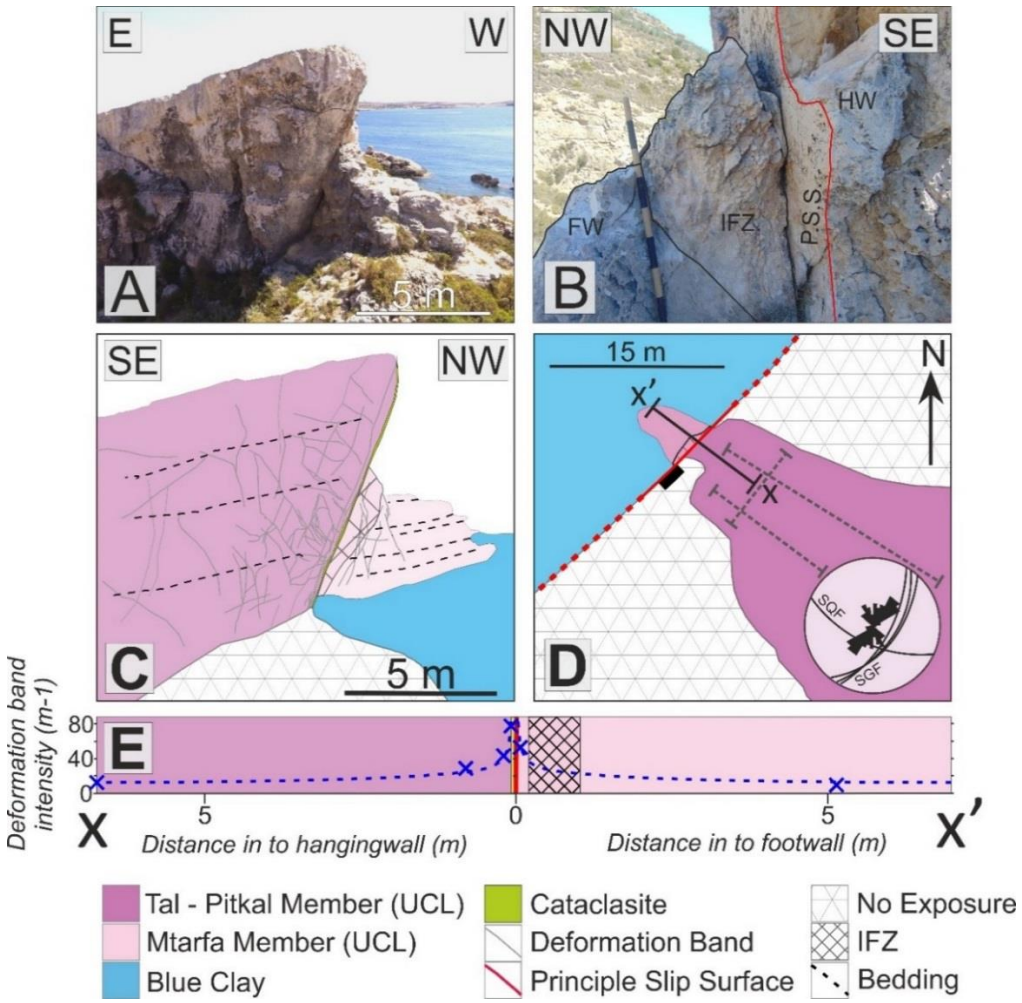

Figure 3-4: A) Cross sectional photo of the SGF outcrop at Qala Point. B) Close up photo (reverse view from A) of the SGF showing the intensely fractured zone (IFZ) of the footwall (FW) adjacent to the principal slip surface (PSS) and hanging wall (HW) hosting a cataclasite veneer. C) Geological cross section of the SGF at Qala Point (similar view to A). D) Map view of the SGF at Qala Point showing a lower hemispherical projection of the SGF and SQF faults together with deformation band orientations. Grey dashed lines represent scan line transects. E) Cross section (see D for location) showing deformation band intensity across the principal slip surface derived from field measurements and from individual samples (samples represented by crosses).

The hanging wall principal slip surface contains a cataclasite veneer which is pale brown or grey in colour, cohesive, contains some fracturing, and <30 cm thick. In addition to the anastomosing deformation band array, the footwall consists of a region of intensely fractured wall

rock up to 1 m thick. The intense fracturing has brecciated the wall rock into angular fragments ranging from 1 cm to 10 cm in size. These fragments do not appear to reduce in size towards the principal slip surface.

South Qala Fault (SQF)

The South Qala Fault is a normal fault with 2 well exposed slip surfaces, striking WNW-ESE, dipping *c.*61° SSW, with a minimum of 50 m throw (Figure 3-5). The footwall stratigraphy at outcrop consists of the LCL Xlendi member, LGL, UGL, and the Blue Clay. The hanging wall consists of the Blue Clay formation. However, there is no preserved hanging wall damage zone, thus the entire damage zone width cannot be determined. The 2 fault traces form a right stepping relay zone, with a bridge fault in between (Figure 3-5A). The exposed LGL beds forming a relay ramp (Figure 3-5D) are immediately adjacent to the Blue Clay formation, such that the UGL is absent. This geometry suggests the relay has become breached, with >30 m on the breaching fault itself which is not clearly exposed. The lowermost LGL beds within the relay ramp have an increased fracture intensity and have increasing dip towards the southern fault strand (Figure 3-5D). These beds eventually become fault parallel and entrained within the fault zone, at which point they exhibit intense microfracturing and brecciation to form a lens of preserved GL fault rock, elongated in the direction of dip.

The western fault trace is entirely composed of a polished, micrite-dominated, GL slip surface, with rake varying from 80-90° SW (Figure 3-5B). The micrite-dominated slip surface is populated by a number of fault splays, parallel slip surfaces, and lenses of intensely fractured and brecciated GL (Figure 3-5E). There is >1 slip surface along the majority of the fault strand length; a subsidiary slip surface runs parallel to the principal slip surface along the entire fault length, <5 cm into the footwall. The GL is recrystallized or cemented between these slip surfaces in certain areas, behind which fault parallel fractures extend into the footwall. At regions of fault corrugations and when the fault strand is right-stepping, additional slip surfaces are present with 0.1 – 1 m separation. Whilst the GL in the footwall damage zone has an increased fracture intensity, the matrix remains intact. Fractures are open with no fracture cements.

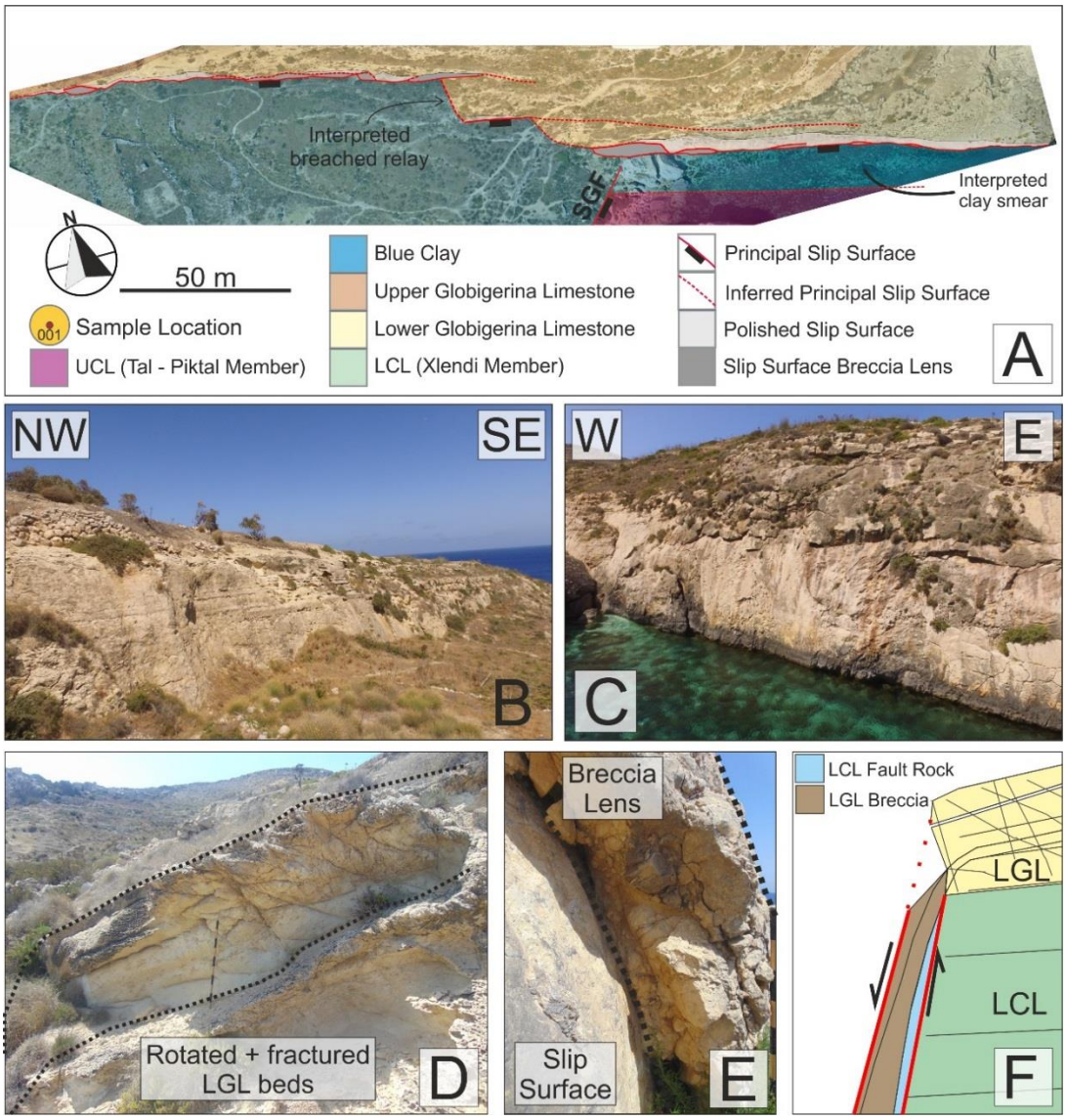

Figure 3-5: A) Geological map of the South Qala Fault (SQF) overlain on aerial drone map. B & C) photographs of the western Globigerina Limestone (GL) slip surface and eastern Lower Coralline Limestone (LCL) fault segments, respectively. D) Rotated and fractured GL bedding in the breached relay zone. E) Lens of brecciated GL bound by parallel slip surfaces, typical of the western fault segment. Here, the fault steps right and the 2 slip surfaces coalesce at the breccia lens tip. F) Schematic model of breccia formation; GL beds become increasingly fractured towards the fault, where they become rotated and entrained between parallel slip surfaces.

Breccia clasts are rounded to subrounded within the fault core with a matrix composed of disaggregated GL. Intact clasts are composed of fractured GL and range in diameter from small cm scale clasts up to 20 – 30 cm blocks. These discrete fault breccia lenses often contain multiple localised coalescing slip surfaces displaying slickensides in a variety of directions, including strike slip or low angle (< 20°) normal slip movement. The locations of breccia lenses correlate with regions where the fault is undulating or right stepping.

The SE fault segment is composed of a polished, grain-dominated, Xlendi slip surface with vertical slickensides (Figure 3-5C). Several breccia lenses can be seen along the Xlendi slip surface, though their composition is unknown due to inaccessibility. The lateral tips of the lenses correspond to splays from the slip surface, creating multiple subsidiary slip surfaces through the lens. However, these lenses are generally thinner and occur less frequently along fault strike than the GL fault breccia lenses. Unlike the NW fault segment, the SE segment does not appear to be as right stepping in its geometry.

Qala Point Fault Zone (QPFZ)

The Qala point fault zone (QPFZ) is the northernmost en echelon shear structure of the SGF (Figure 3-2). The QPFZ is a south dipping high angle (> 80°) dextral oblique normal fault zone with *c.*30 m throw, and an undetermined strike slip component, distributed over several slip surfaces. At outcrop, the principal slip surface juxtaposes the Xlendi member of the LCL (hanging wall) against the Attard member of the LCL (footwall). Both members are grain-dominated carbonates, however mechanical properties may vary due to the reduced porosity of the Attard member relative to the Xlendi member (ϕ = *c.*10-15 % and 25-30 %, respectively). A complex zone of fracturing and subsidiary slip surfaces extends to the north of the principal slip surface, with numerous additional fault strands that appear to host offset (Figure 3-6). However, individual fault strand displacements cannot be determined due to the lack of marker beds and the strike slip component to slip. Several right-stepping pull-apart structures are present within the fault zone (Figure 3-6 & Figure 3-12), in agreement with the dextral oblique faulting trend of the SGF shear structure (Figure 3-2). The pull-apart structures contain cross cutting Riedel shear slip surfaces of small offset and an increased fracture intensity. Larger scale Riedel shear fractures can be interpreted across the entire fault zone exposure.

Fracture intensity measurements were recorded along a transect oriented perpendicular to faulting (Figure 3-6), showing how fracture intensity increases from a background level of < 5 m^{-}

$^{-1}$ up to >15 m^{-1} within the fault zone. The largest fracture intensities correlate to a region of several meters surrounding the principal slip surface, and to 5 m into the footwall. These fractures are often filled with an orange-brown cemented core that other fractures often terminate against.

Fault throw is distributed across the entire zone, leading to a wide, discontinuous fault rock distribution. Fault breccia and cemented fault cores dominate fault rock fabrics within the QPFZ. Fault breccia occurs as discrete lenses bound by fault splays, and within dextral pull apart structures. Breccia lenses exhibit sharp contacts with the protolith.

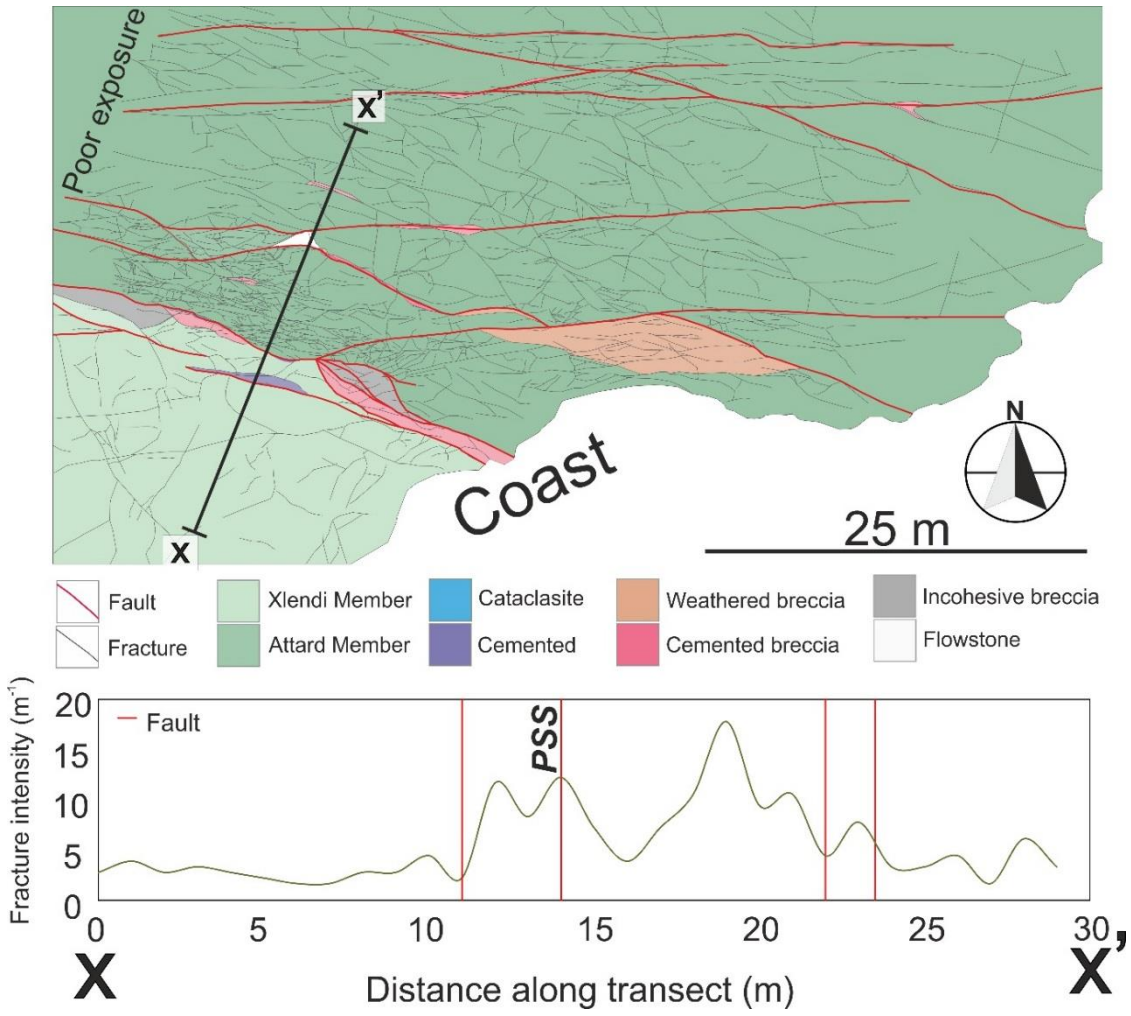

Figure 3-6: Top) Geological map of the Qala Point Fault Zone (QPFZ), showing fault rock distributions. Bottom) Linear transect across the QPFZ showing fracture intensity and the locations of slip surfaces (vertical red lines).

3.4.2. Fault rock microstructures

South Gozo Fault (SGF)

The footwall and hanging wall (Mtarfa and Tal-Piktal members of the UCL) both show similar deformation and diagenetic microstructures. However, at outcrop, well developed cataclasite is limited to a veneer along the hanging wall (Figure 3-7). Hand specimens show there to be a sharp contact between host rock and cataclastic rock (Figure 3-7A), best developed where the

cataclasite is thickest. BSE-SEM images show the cataclasite to have a low porosity, with pore sizes in the microporosity range (<30 μm) and the sharp contact showing a contrast between medium and low porosity rock (Figure 3-7B). Grain size within the cataclasite is reduced relative to the host rock; however, remnant 'survivor' bioclasts that have not been subject to cataclasis are distributed throughout the fine grained matrix. Minor pressure solution seams and sutured grain boundaries around individual fossil clasts are present within the cataclasite rock (Figure 3-7C & D). Remnant bioclasts within the cataclasite have been subject to aggrading neomorphism in the areas of highest deformation, formed of sparry calcite cement (Figure 3-7D). Survivor bioclasts are predominantly echinoderms, benthic foraminifera, and planktonic foraminifera, whereas other skeletal fossils present within the host rock appear to have been subject to preferential deformation through pore collapse and comminution.

The deformation bands present throughout the fault zone contain intact fossil clasts that have undergone little grain comminution or fracturing (cataclasis). However, the fine grained matrix between these grains indicates preferential cataclasis of the weakest grains has occurred. Quantitative image analysis of grain orientations (grain Feret diameter orientations) shows alignment of grains from bedding orientations to deformation band parallel (Figure 3-8). BSE-SEM imagery shows a reduction in porosity from *c.*20-25 % down to *c.*5-10 % from the host sediment surrounding deformation bands to the sediment within the deformation bands (Figure 3-8B).

Intergranular microspar cements are present within the host rock but are not pore filling, maintaining good intergranular porosity and pore connectivity. However, these cements occlude remnant porosity in the cataclasite and deformation bands, such that the primary porosity consists of intragranular pore spaces within fossil structures and microporosity between microspar crystals. Overall, pore connectivity appears far lower in the fault rock than within the host rock.

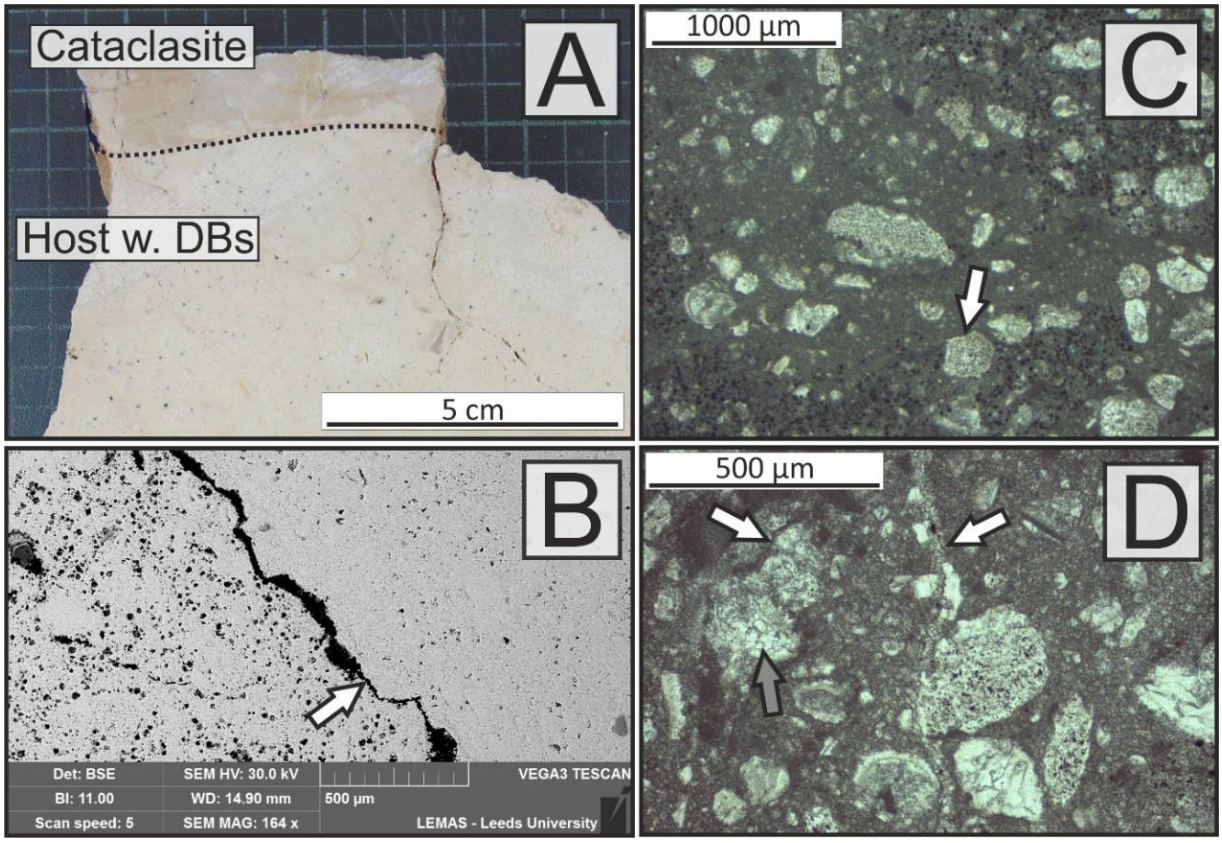

Figure 3-7: A) Hand specimen containing contact between cemented cataclasite and host rock containing deformation bands. B) BSE-SEM image of cemented cataclasite showing boundary between medium porosity and low porosity fault rock. Arrow indicates open pressure solution seam. C) Optical micrograph of a clast within cataclasite exhibiting reduced microporosity due to grain comminution. Bioclast boundary (arrow) shows a sutured grain boundary of an echinoderm at the contact with the clast, evidence of minor grain boundary pressure solution. Preferential bioclast deformation (e.g. mollusc and planktonic foraminifera fossils) has increased cryptocrystalline cement and reduced porosity (fossils such as echinoderms appear to be more resistant to deformation and have remained mostly intact). D) Optical micrograph of cemented cataclasite showing pressure solution seams (white arrows) and recrystallized bioclasts with sparry cements (grey arrow).

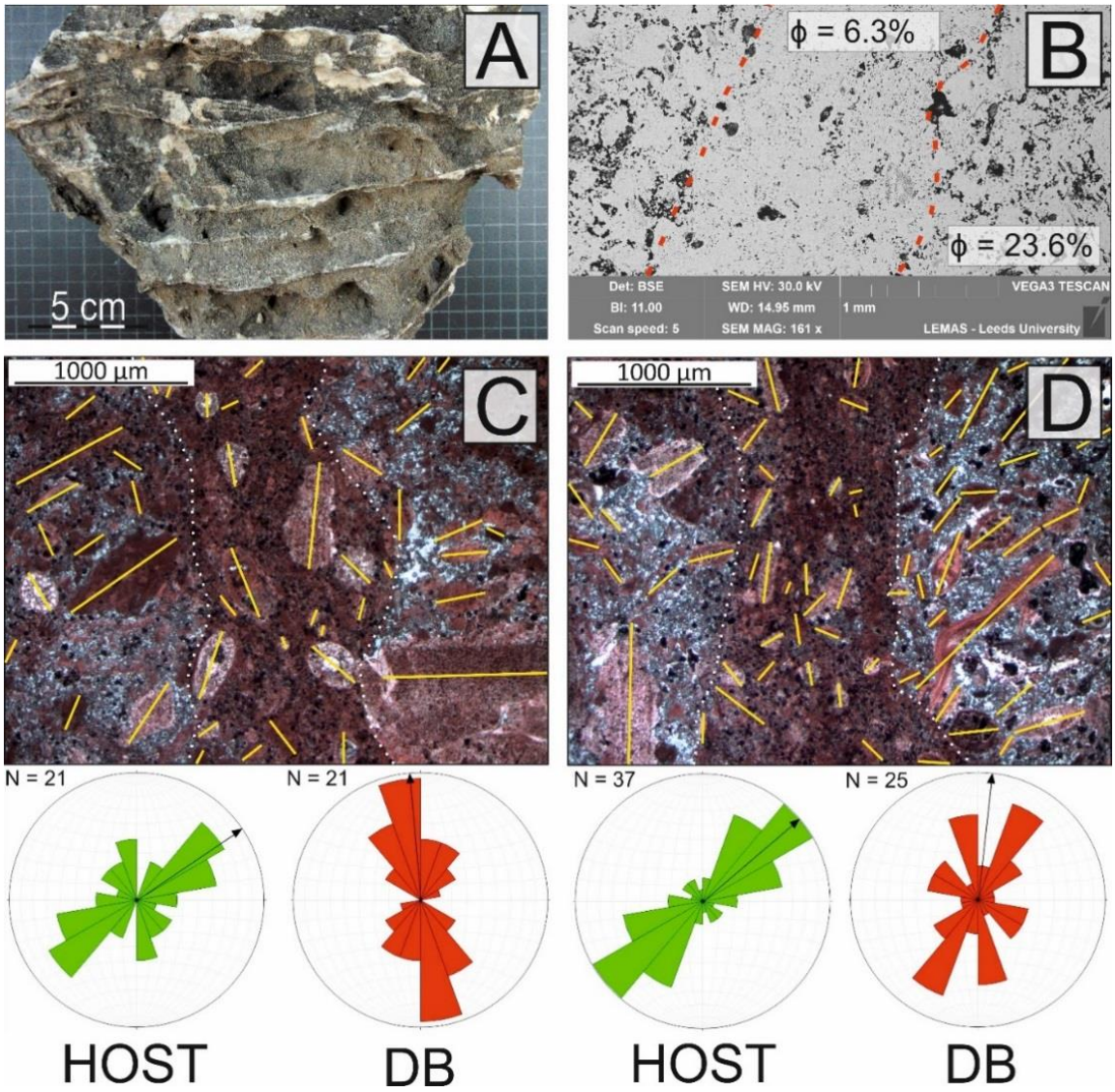

Figure 3-8: A) Hand specimen containing anastomosing deformation bands from the immediate SGF footwall. Deformation bands are less prone to weathering, hence form weathered ridges. B) BSE-SEM image of a deformation band from the sample shown in A. Red dashed line indicates the deformation band boundaries. Porosity estimated from image analysis is shown for the deformation band and surrounding sediment. C & D) Polished optical micrographs of deformation bands in the UCL, stained with Alizarin red S and potassium ferricyanide. Principal grain axes are shown by yellow lines, and their orientations are shown below for both the host and deformation band grains. The black arrows on the grain orientation plots indicate the mean orientation. Grains have been rotated and aligned parallel to the deformation band orientation. Increased micrite and microspar cements have reduced deformation band porosity.

South Qala Fault (SQF)

Along the western, micrite-dominated fault trace of the SQF, the most widespread change in texture between host and fault rock is related to fluid rock interactions. Increased cementation is commonly observed in the region between parallel slip surfaces. The calcite cements occlude both inter- and intra-granular porosity and appear to be formed of an early microcrystalline calcite followed by a later microspar calcite (Figure 3-9C). Cementation is relatively continuous along the length of the exposure.

Fault breccia is characterised by clasts of host rock within a fracture mesh, typically composed of intact globigerina grains, and fragments of cataclased bioclasts (predominantly skeletal fragments). Open fractures are common, often within a localised region of grain size reduction, indicating localised cataclasis along minor slip planes (Figure 3-9E). Breccia clasts are also commonly bound by open fractures, containing cements in certain regions (Figure 3-9A & D), along with minor calcite twinning (Figure 3-9B).

Beds that have higher proportions of coarser grained bioclasts, such as benthic foraminifera and bivalves, exhibit more cataclasis (grain fracturing and comminution) than those dominated by globigerina fossils. However, more pervasive cataclasis only occurs within several millimetres of the principal slip surface (Figure 3-9F).

The Xlendi member of the LCL along the eastern fault segment shows a more typical cataclasite veneer, bound by parallel slip surfaces, in which grain size is reduced relative to the host rock through grain comminution (Figure 3-10A). Calcite cements have occluded the majority of the pore spaces immediately adjacent to these slip surfaces, behind which pore spaces remain open. Regions of the slip surface exhibit brecciation, in which individual coarse grained bioclasts, or large bioclast fragments, behave as host clasts within a comminuted fracture mesh (Figure 3-10B). At the western tip of the slip surface is a *c.*10-30 cm thick band of deformed Xlendi member that is fine grained and composed of comminuted grains fitting the description of an uncemented cataclastic fault rock.

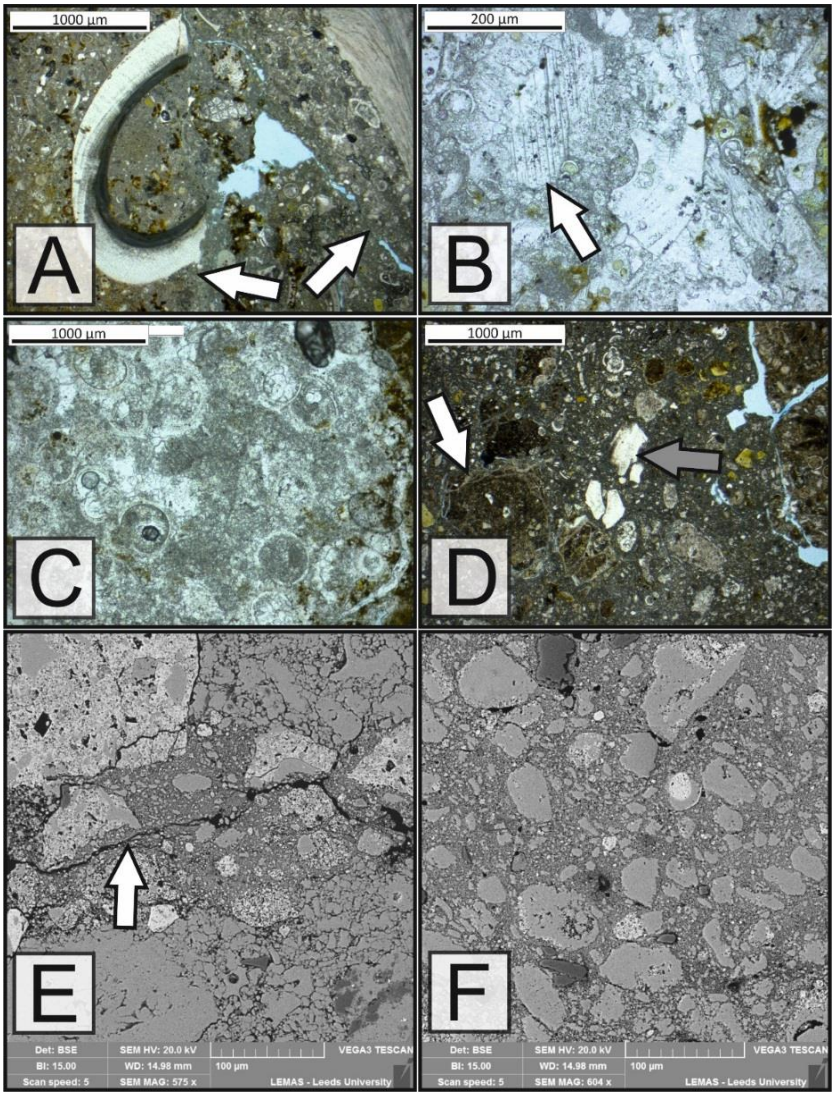

Figure 3-9: Polished optical photomicrographs (A-D) and BSE-SEM (E-F) images of fault rock from the micrite-dominated SQF slip surface. A) Fault breccia consisting of undeformed clasts surrounded by a finer grained fracture mesh. Arrows indicate clast – matrix boundaries, between which is finer grained, clay rich material. Clasts are often bound by open fractures, as indicated by the arrow to the right. B) Cemented fault rock exhibiting some calcite twinning (arrow). C) Undeformed LGL with calcite cements occluding inter- and intra-granular cements. D) Breccia containing fractured phosphatised nodules (white arrow), skeletal fragments (grey arrow), and fine grained muddy matrix. E) BSE-SEM image showing open fractures (arrow) surrounded by fine grained material, including angular fragments of phosphatised nodules. F) BSE-SEM image showing cataclasis at the PSS. Globigerina grains resist cataclastic deformation, however other skeletal fragments are more prone to comminution and grain fracturing.

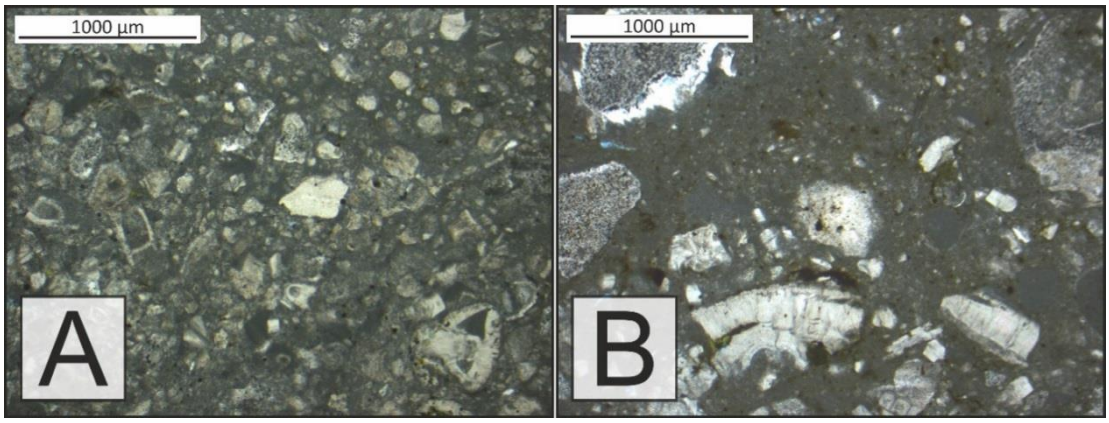

Figure 3-10: Polished optical photomicrograph images of fault rock from the grain-dominated LCL slip surface of the SQF. A) Grain scale deformation derived cataclasite immediately adjacent to the principal slip surface, consisting of grain fragments and micritic cements. B) Fracture derived cataclasite with fine grained matrix and clasts of bioclast fragments.

Qala Point Fault Zone (QPFZ)

Despite the grain-dominated fabric of the host rocks, there is limited cataclastic fault rock development within the QPFZ. A short section of the principal slip surface contains a thin hanging wall veneer of fine grained Xlendi fault rock, behind which are regions of increased cementation (Figure 3-11B). The fine-grained veneer contains clasts of low porosity cataclased bioclasts (Figure 3-11E) and a matrix consisting of intact bioclasts, or 'survivor bioclasts', surrounded by 2 generations of calcite cement (Figure 3-11E); an initial Fe-rich cryptocrystalline micrite cement surrounds the clasts and a sparry calcite cement fills the remaining voids. Dolomite cements are observed within intragranular pore spaces (Figure 3-11E). These dolomite cements are only observed within principal slip surface fault rocks. Additionally, the southern bounding slip surface contains a thin (*c.*1 cm) veneer of cataclasite (Figure 3-11A & D), in which cataclasis and cementation has resulted in a reduced porosity and a reduction in grain size (Figure 3-11D). Fossil bioclasts have become rounded during faulting and are surrounded by a matrix of fine grained clastic fragments or cements that appear dark in optical micrographs (Figure 3-11D). However, unlike the principal slip surface cataclasite veneer, there is no cemented matrix.

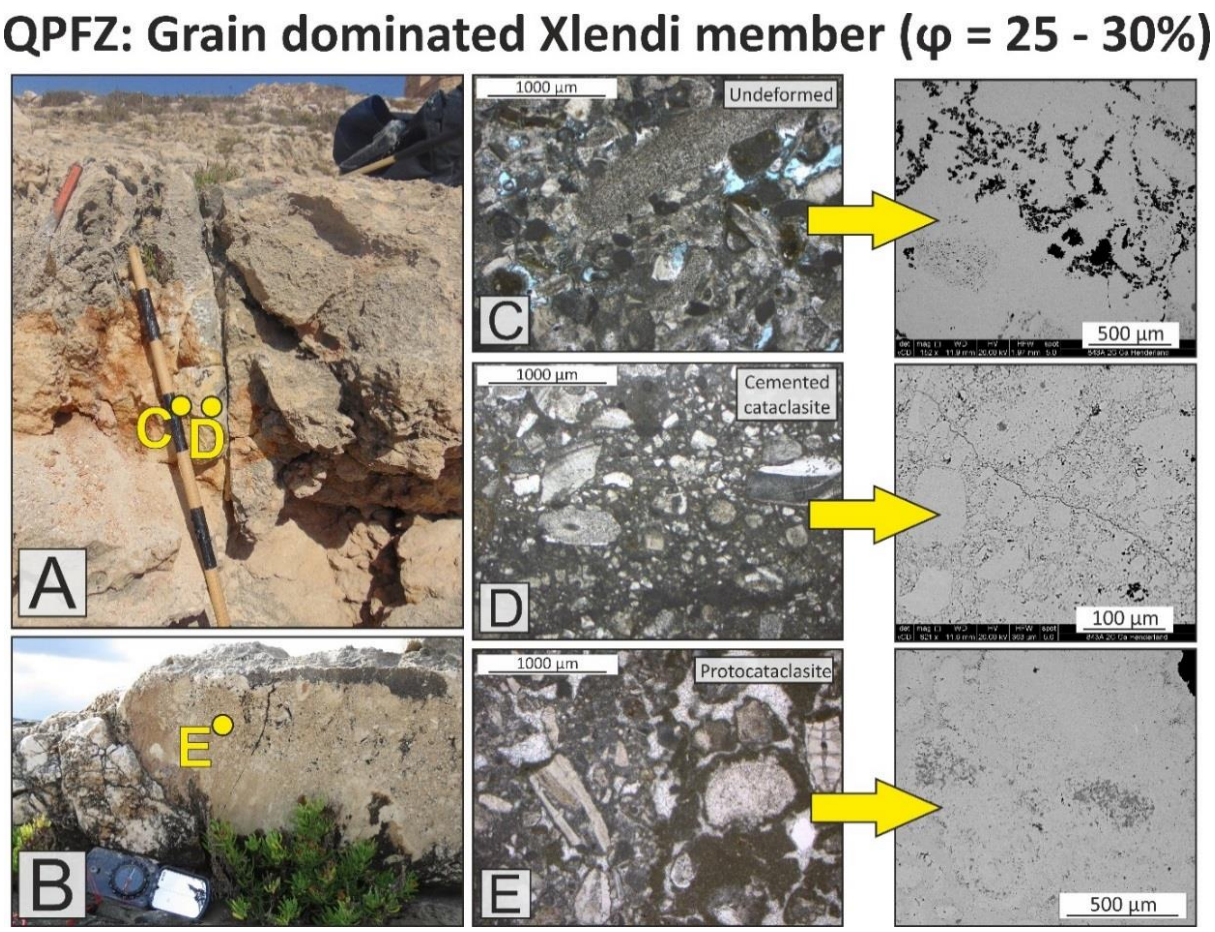

Figure 3-11: A) Southern bounding slip surface (unknown offset) of the QPFZ. B) Polished slip surface of the QPFZ principal slip surface. C) Xlendi member c.*5 cm from southern bounding slip surface. D) Cemented cataclasite immediately adjacent to the southern bounding slip surface. Less rounded fossil clasts have become sub-rounded due to grain boundary dissolution and comminution. E) Protocataclasite from the principal slip surface with cemented matrix exhibiting 2 generations of cement (red micritic cement and later sparry calcite cement). Note the darker grey intragranular dolomite cements in the BSE-SEM image.*

In contrast to the Xlendi member, the Attard member does not appear to exhibit grain scale cataclastic deformation. However, fault breccia is widespread along the principal slip surface and subsidiary slip surfaces. Breccia clasts are subrounded to subangular, range in size from mm scale up to 50 cm, and are poorly sorted with highly heterogeneous microstructures (Figure 3-12C). Two primary forms of fault breccia can be observed within the fault zone; fault breccia consist of either undeformed clasts of host rock, often with cemented pore spaces, or clasts that exhibit recrystallization. A fine grained fracture mesh, typical of cataclastic fault breccia, is not observed.

Instead, diagenetic features and palaeosol features are commonly present between breccia clasts; breccia matrices are composed of Fe-rich cements, some of which have cemented pore spaces and show evidence of rhizogenic (root formed) microstructures (Figure 3-12C). Fractures are commonly filled with local scale brecciation, or contain regions of recrystallization (Figure 3-12D). A dark brown fault core, up to 7 cm thickness, is present between the Attard and Xlendi members along the principal slip surface. Optical micrographs show this core to be composed of pedogenic calcrete with rhizogenic microstructures.

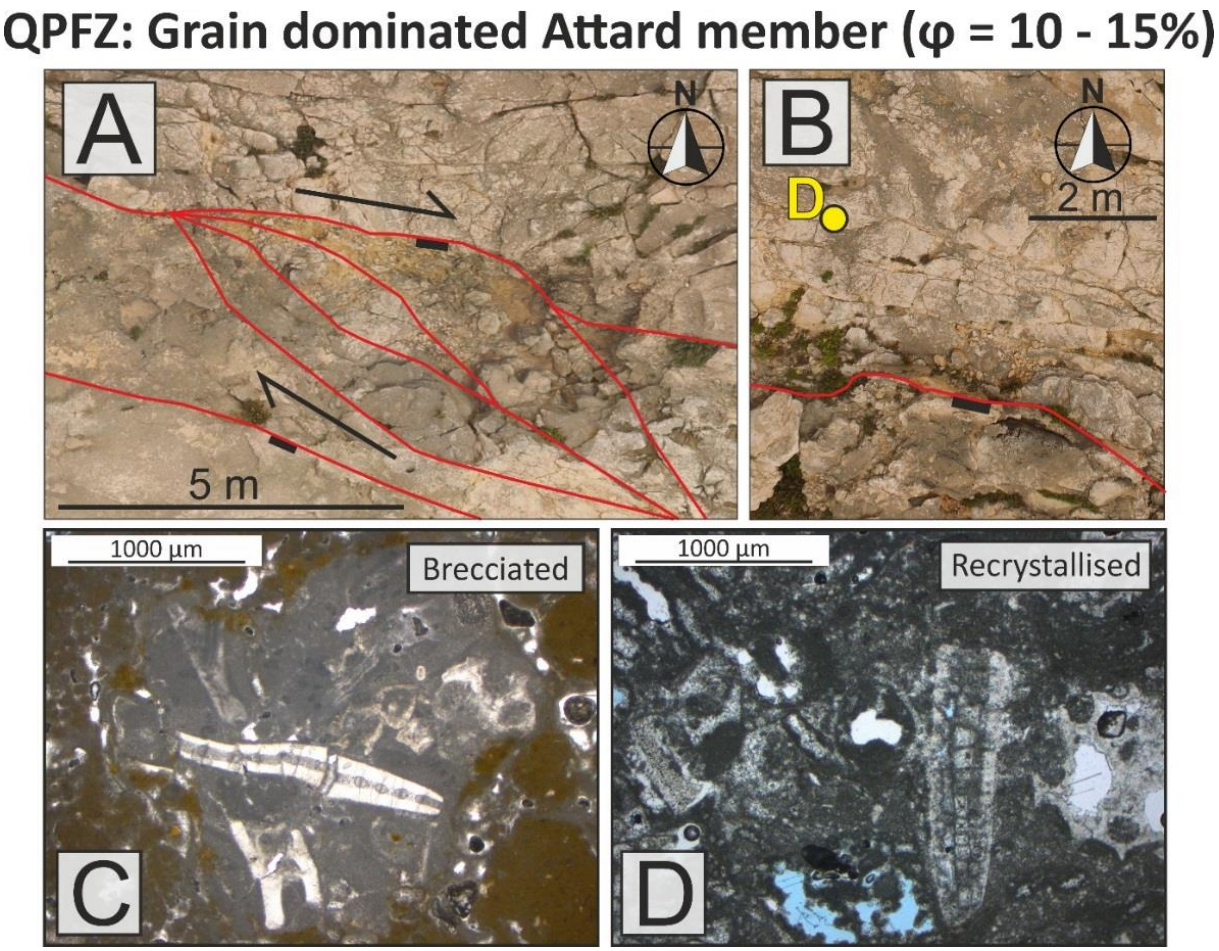

Figure 3-12: A) Releasing fault step over along the QPFZ principal slip surface indicating a dextral component to fault slip, with fault breccia. B) Anastomosing fractures/subsidiary slip surfaces in the QPFZ footwall, filled with a cemented and recrystallized core. C) Optical photomicrograph a clast of the Attard member within a Fe-rich cemented matrix. D) Recrystallized Attard member within FW fractures/subsidiary slip surfaces.

3.4.3. Fault rock thickness and continuity

The ability to quantify fault rock distribution can be aided by 2 key metrics: fault rock thickness (FRT) and fault rock continuity (FRC). Fault rock thickness is highly variable over local scales (Figure 3-13). Thickness variability is particularly evident for fault breccia, due to the lensoidal geometries and fault zone architecture complexities (i.e. fault breccia is thicker at slip surface junctions). Therefore, fault breccia is characterised by poor FRC and thicknesses ranging from areas of absence to several meters. This is best observed along the 30 m and 90 m throw faults (QPFZ and VLF, respectively). Cemented fault rocks and cataclasites have a reduced FRC, mean FRT, and thickness range relative to fault breccia. Although these fault rocks still occur in lensoidal geometries, they are generally <0.5 m in thickness, thus reducing the range of thickness values. Cataclasite is relatively uniform in thickness with poor continuity at low throws (Figure 3-14 & Figure 3-15). Although individual fault rock types have poor continuity, the total fault core continuity is relatively high for each of the 3 fault zones shown in Figure 3-13. FRC is approximately 1 along the principal slip surface, as shown by the FRC value for the combined principal slip surface measurements from all 3 fault zones (Figure 3-13). In these examples, although overall continuity of fault rock appears lowest on the highest (90m) throw fault (VLF, Figure 3-13 bottom right), this is principally due to the distributions of fault breccia on both principal and subsidiary slip surfaces in the increasingly complex fault zones. Hence it does not indicate a more general trend with fault throw.

Cataclasite continuity appears be significantly lower for the 90 m throw fault relative to the 50 m throw fault (Figure 3-13). However, cataclasite FRT and FRC measurements from all 6 fault zones show there to be a positive correlation with increasing throw for both metrics (Figure 3-15). The throw hosted by just the principal slip surface of the fault zones with highly complex, distributed damage zones (30 m and 90 m throw) is less than the total fault zone throw. Therefore, the cataclasite FRC values appear to lie to the right of the trend, such that the values are closer to the trend when considering only the throw across the principal slip surface (highlighted by black arrows in Figure 3-15).

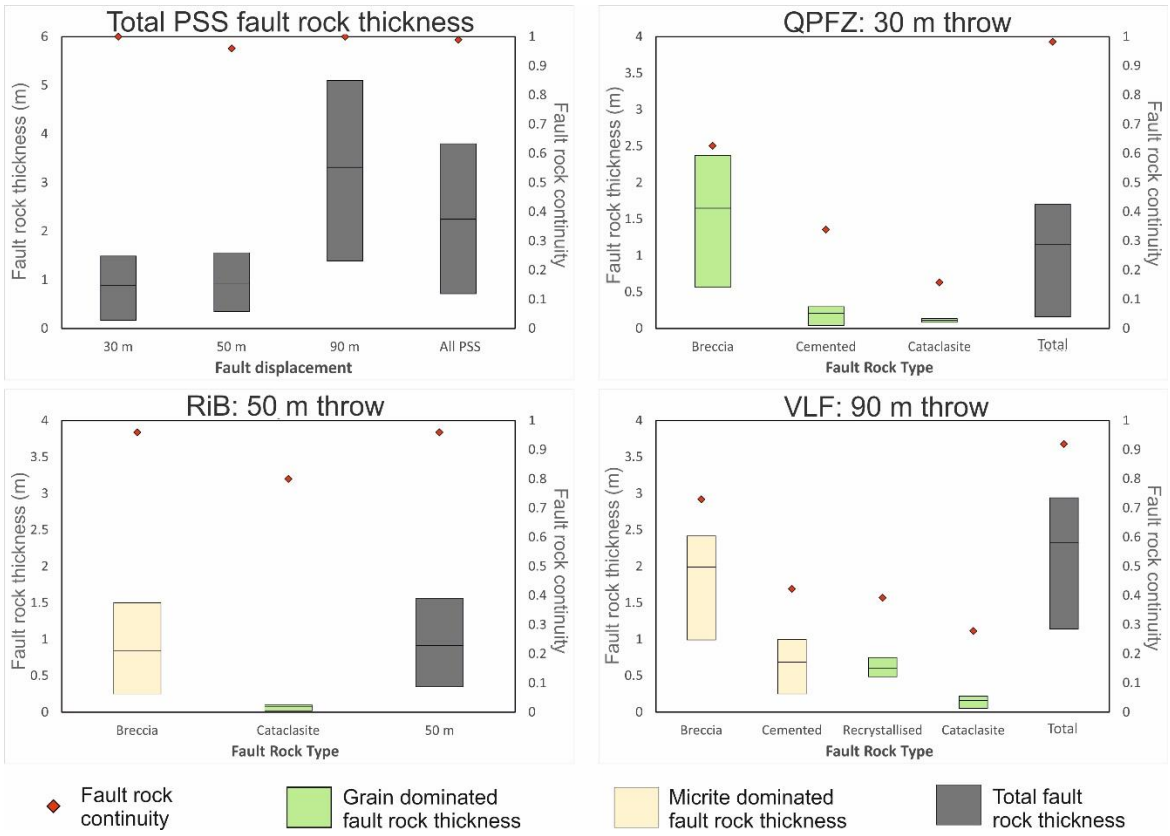

Figure 3-13: Plots of FRT and FRC measurements along fault strike for each fault rock type present at 3 Maltese fault zones. Box plots represent the interquartile range and arithmetic mean of fault rock thickness (FRT) measurements and are coloured according to lithology. Red data points represent the fault rock continuity (FRC). Top left: measurements of total fault rock thickness/continuity for each studied fault zone principal slip surface and all combined principal slip surface measurements. Other 3 plots show measurements of specific fault rock types at each specific fault zone, including along subsidiary slip surfaces (RIB = Ras il-Bajjada segment of the Il-Maghlaq Fault).

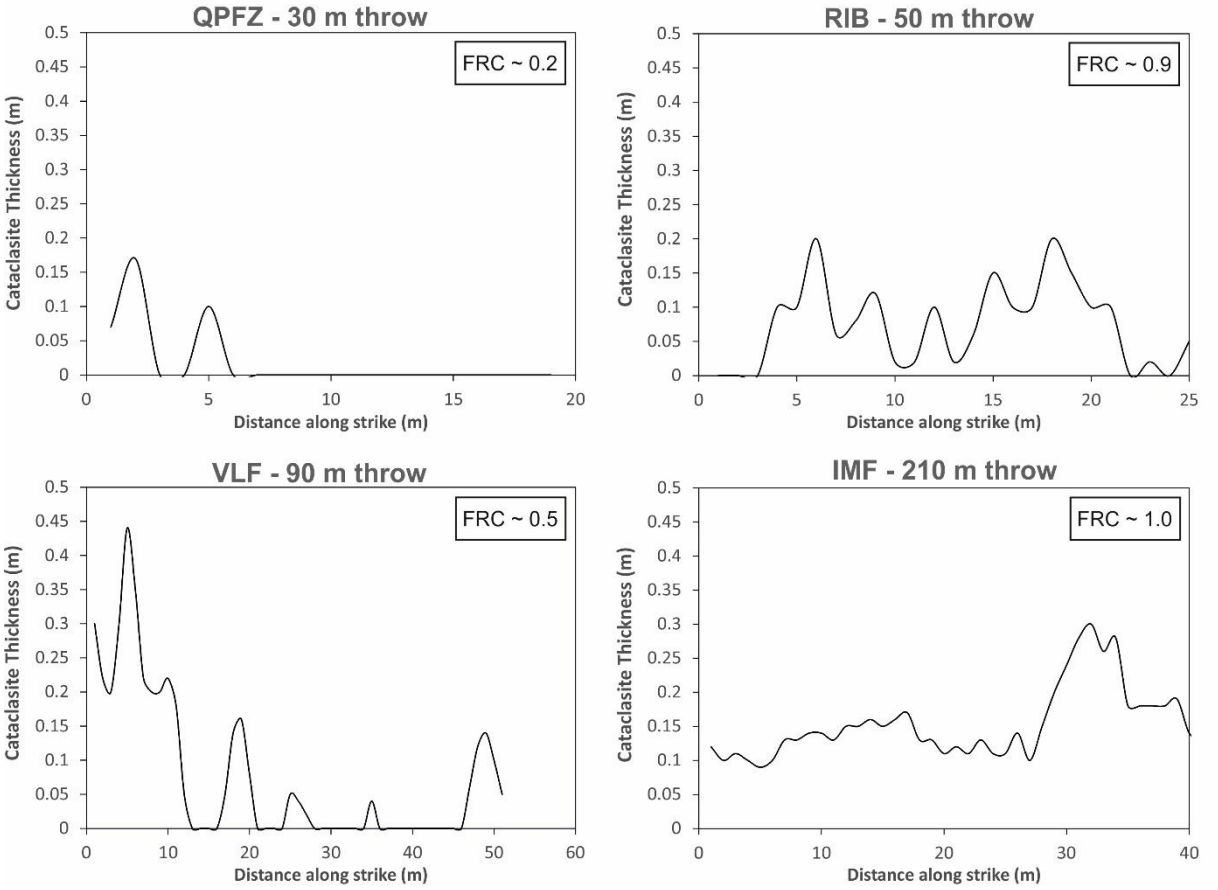

Figure 3-14: Cataclasite fault rock thickness within the grain-dominated LCL formation along strike of 4 fault zones. Clockwise from top left: Qala Point Fault Zone, Il-Maghlaq Fault (Ras il-Bajjada segment), Il-Maghlaq Fault, Victoria Lines Fault.

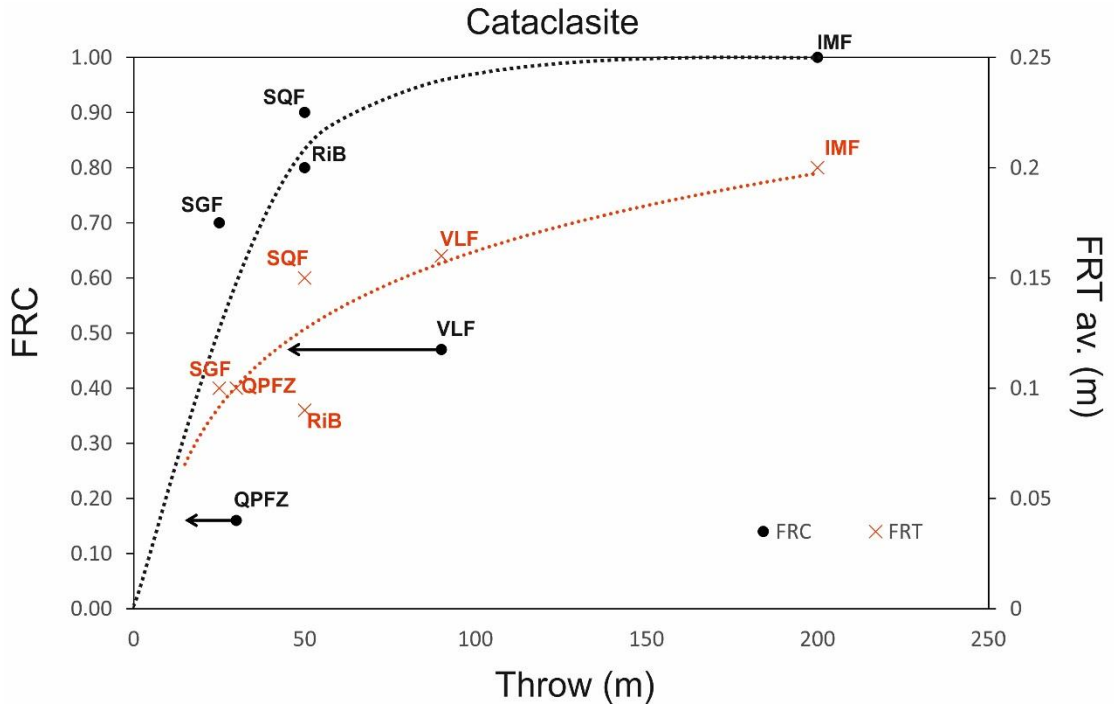

Figure 3-15: Estimated 2D fault rock continuity (FRC) and the arithmetically averaged fault rock thickness (FRT av.) for cataclastic fault rock, plotted against total fault throw. Curves are hand drawn to highlight the data trend. All Maltese fault zones suitable for sufficient along strike thickness measurements are included. Black arrows highlight how the throw across the principal slip surface is lower than the total fault zone throw for fault zones with a distributed damage zone (QPFZ and VLF). Note that FRC values are a minimum estimate, as weathering may have removed some cataclasite exposure.

3.5. Discussion

3.5.1. Controls on deformation

Fault zone architecture is highly variable throughout the studied fault zones. At the QPFZ, the dextral component to slip combined with the complex nature of the fault zone architecture, comprising of multiple slip surfaces sub-parallel to the principal slip surface, multiple pull apart structures, and Riedel shear fractures, suggests that the fault zone is likely part of a dextral flower structure or fault stepover (e.g. Mcclay *et al.* 2001). This architecture promotes distributed deformation, with several slip surfaces accommodating a portion of the strain, and encourages discontinuous fault rock distribution. Dilatational fault jogs also lead to a discontinuous fault rock distribution (primarily fault breccia). This indicates that the tectonic setting of the QPFZ (30 m

throw) is likely to have some control over fault rock distribution, whereby the small scale en echelon wrench system within the larger scale structure of the SGF leads to a distributed damage fault zone, characterised by poor FRC (Figure 3-13). Further to this, the host rock porosity also influences the architecture; in the QPFZ, subsidiary slip surfaces are primarily located within the low porosity footwall of the fault zone, where deformation is more prone to extensional and shear fracturing relative to the higher porosity hanging wall.

In contrast to the distributed damage zone of the QPFZ, the SGF and LCL slip surface of the SQF have a more typical fault zone architectures (e.g. Chester & Logan 1986; Caine *et al.* 1996), hosting localised fault cores surrounded by a damage zone. The host porosity for both the Xlendi member (LCL) and the UCL is relatively high, making them more prone to granular flow and cataclasis on the grain scale, which promotes localised deformation along a single principal slip surface.

The architectures described are intrinsically linked to the observed deformation mechanisms. Widespread fault breccia formation is limited to the micrite-dominated footwall of the SQF and to the low porosity Attard member hanging wall of the QPFZ. Whilst breccias consistently occur in discrete, discontinuous lenses, there appears to be numerous mechanisms by which they form. At the SQF, lenses of fault breccia correlate with fault irregularities or corrugations. This suggests that fault breccia lenses may be the result of either dilation, due to void spaces created from fault geometries, creating hydraulic implosion breccia (Sibson 1986; Woodcock *et al.* 2007), or increased strain during fault linkage (Fossen *et al.* 2005; Joussineau & Aydin 2007); during the initial stages of fault growth, overlapping or right stepping fault segments link to form lenses of increased dilation or strain in which fault breccia can form (Figure 3-7E). Further breccia formation appears to occur due to the entrainment of beds along the fault zone, whereby the entrained GL beds have been subject to mechanical abrasion from frictional sliding, thus resulting in intense fracturing and brecciation (Figure 3-5F) (Sibson 1986). At the QPFZ, through going slip surfaces and sharp contacts between breccia and host rock suggest fault breccia is formed via either the coalescence of multiple slip surfaces or through the creation of void space relating to fault geometries. However, the rhizogenic structures present within the breccia matrix either overprints any initial fault related fracture mesh or suggests breccia has formed via karst collapse processes (e.g. Kerans 1993; Wright *et al.* 2009). Ultimately, the mechanical weathering potential of root wedging means the extent of fault related brecciation is difficult to determine at the QPFZ.

In contrast to fault breccia formation, cataclastic deformation is limited to specific lithologies. In general, cataclastic fault rock is poorly developed within both the high porosity micrite-dominated SQF slip surface and within the low porosity grain-dominated QPFZ footwall. Within the QPFZ, cataclasis is only observed in the higher porosity grain-dominated Xlendi member. However, there is no extensive cataclasite observed at outcrop. Conversely, cataclasis is common and well developed in high porosity grain-dominated wall rocks, such as the SGF and the Eastern fault trace of the SQF. This indicates that the high initial host rock porosity is a key factor in determining whether cataclasis will occur, as has been suggested in previous literature (Wong *et al.* 1997; Billi *et al.* 2003). However, the micrite-dominated GL does not exhibit cataclastic deformation, despite the high initial porosity (>30%), indicating that there are additional controls on which deformation mechanisms occur. The GL is weaker, finer grained, and more homogeneous than the grain-dominated lithologies. This leads to dispersed deformation within the GL, through fracturing and brecciation (Michie 2015). This indicates that the presence of large, high strength bioclasts within the Xlendi member (LCL) and the UCL also plays a part in allowing them to deform via granular flow and cataclasis.

The cataclasite fault rocks observed on Malta commonly have surviving bioclasts within a fine-grained matrix of fractured fossils and microcrystalline cements (Figure 3-7, Figure 3-9 & Figure 3-11). The surviving grains show less apparent grain fracturing or comminution than the surrounding fine grained matrix. Bioclasts that deform more readily appear to consist of planktonic foraminifera and skeletal fragments with large intragranular pore spaces. Conversely, bioclasts that are more resistant to deformation appear to consist of fossils such as echinoderms, which have stronger radial cell walls and little intragranular pore space. Preferential bioclast deformation is also commonly observed in the Attard Member, in which red algae (rhodolith) fossils appear to resist deformation, due to their fine scale cellular internal structure that prevents large intragranular pores, thus increasing the fossils resistance to pore collapse. This selective deformation implies that fossil content (i.e. carbonate age and facies) may have a control on deformation style within a fault zone, hence controlling fault permeability.

In addition to lithological controls, the extent to which cataclasis occurs, and its distribution, is partially controlled by the fault zone architecture. For example, the cataclasite veneer along the QPFZ hanging wall slip surface is poorly continuous due to the distributed damage zone (Figure 3-15). The proximity to the intersection between the SGF and the SQF indicates a region of increased strain at the fault junction, which may contribute to deformation band formation; single

tip fault intersections have been shown to exhibit complex and extensive subseismic deformation (Fossen *et al.* 2005). The timing of faulting relative to deposition may also have influenced deformation band formation at the SGF. Faulting occurred early during deposition of the UCL (Dart *et al.* 1993), therefore sediments had undergone limited diagenesis, had a higher initial porosity, and were likely poorly lithified. Therefore, granular flow can easily occur, leading to a high intensity of deformation bands that exhibit a reduced porosity, reduced grain-size and grain translation (Figure 3-8). Minor pressure solution seams and sutured grain boundaries around individual fossil clasts suggest increased cementation within the deformation bands is partly a result of diffusive mass transfer in addition to the preferential disaggregation of the weakest bioclasts. Deformation bands increase in intensity towards the principal slip surface, where a fault core of several centimetres thick is produced by similar processes.

3.5.2. Controls on FRT and FRC

The continuity of fault rock is important when considering any across-fault fluid flow. For clay bearing siliciclastic rocks, shale gouge ratio and shale smear factor (Yielding *et al.* 1997) provide a first order approach to this. However, for carbonate rocks this is not applicable. Utilising field studies to draw relationships between fault rock continuity, fault rock thickness, host texture, and fault zone architecture can aid the better prediction of FRC, FRT and thickness variability in the subsurface. The data shown in this study indicates that throws in the range of 50 – 200 m are required for continuous grain scale cataclasite fault rock to form within high porosity carbonate-hosted fault zones. Whilst other forms of fault core may also restrict fluid flow, carbonate-hosted cataclasites have been shown to exhibit low permeability values (e.g. Micarelli *et al.* 2006; Agosta *et al.* 2007; Bauer *et al.* 2016; Michie & Haines 2016). Hence, is important to be able to predict when a cataclastic fault core may become continuous.

Although a FRC value <1 may impact flow over production timescales, it is highly unlikely to impact fluid flow over geological time. However, the uncertainty regarding FRC estimates from the methods used in this study means determining whether a fault core is fully continuous from outcrop data alone is unrealistic. Hence, determining FRC from field measurements can only be used as a first order approach to considering fault rock distributions. The limitations of this method of quantifying FRC are as follows (highlighted by Figure 3-16):

- The total recorded fault rock length assumes that all fault rock is mappable (i.e. fault rock has not been subject to sufficient weathering to either remove fault rock or make it poorly visible).
- The scale of fault zone exposure may be too small to capture patterns of fault rock distribution (Figure 3-16C).
- Fault rock may appear to be laterally continuous when studying fault zones that are exposed in map view (or only accessible along strike), however, the vertical distribution may be discontinuous. Therefore, a 3D fault exposure is ideal for calculating FRC.
- When studying a fault zone exposed in 3 dimensions, measuring the total fault rock length from a 2D map view may misrepresent FRC. This can be avoided by calculating FRC as a ratio of the area of fault rock coverage relative to the area of exposed fault surface (Figure 3-16D). If the exposure is not suitable for this, a horizontal plane can be projected across the fault surface, along which the total fault rock length can be measured. However, it is clear that the height of the plane on the slip surface will vary the estimated FRC value.
- It is often difficult to determine the fault rocks present behind a fault surface. Hence, a core plug drilled perpendicular to the fault surface is useful in determining FRC and FRT.

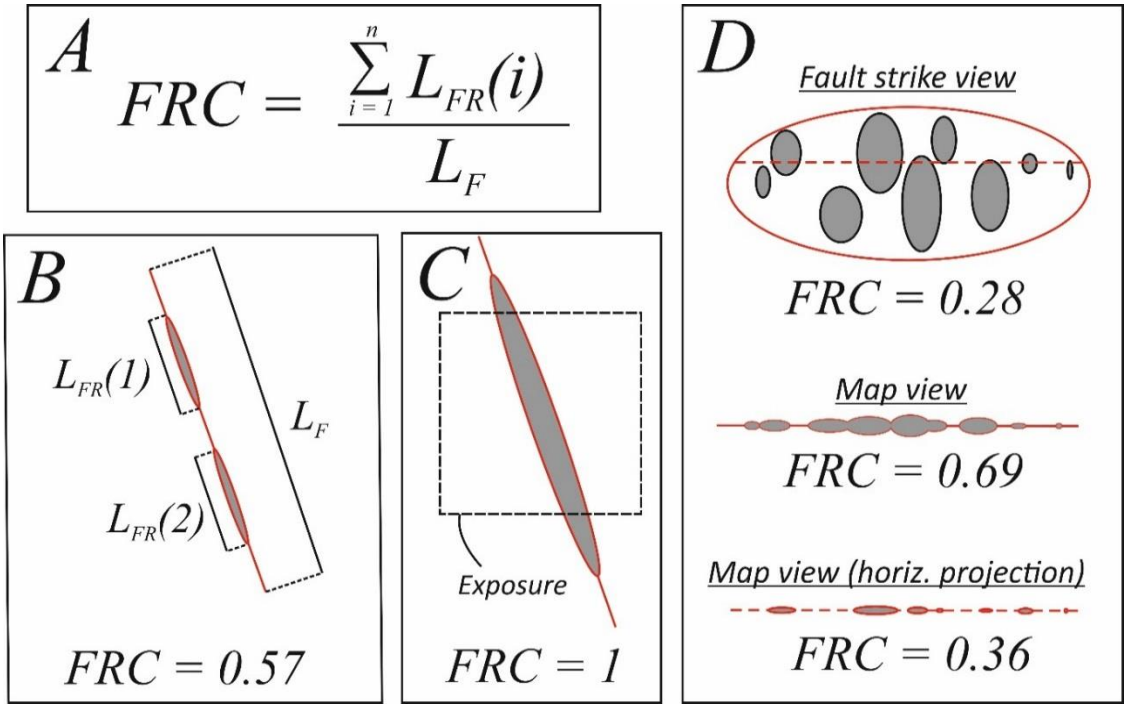

Figure 3-16: A) Equation used in calculating fault rock continuity (FRC). B) Example FRC calculation for a schematic map view of a fault zone with fault rock distributions (grey). C) Example of how a small exposure area relative to the size of fault distribution patterns can impact FRC calculations. Fault rock appears continuous (FRC = 1) from exposure, however the exposure does not account for the entire fault length, thus does not provide an accurate estimate of FRC. D) Schematic fault surface (observed from fault strike view) with a fault rock distribution. FRC is calculated for the entire fault surface based upon the area of fault rock coverage (0.28). Using the entire fault surface to calculate FRC in map view, based upon 2D length measurements, overestimates FRC (0.69). Projecting a horizontal plane across the fault surface (red dashed line) to simulate a map view exposure produces a more realistic FRC estimate (0.36).

The QPFZ (30 m throw), VLF (90 m) and the IMF (210 m) have apparently continuous fault cores. However, the fault cores are composed of multiple fault rock types which, when considered on their own, are often discontinuous (Figure 3-13 & Figure 3-14). Due to the different fabrics of each of these fault rocks, they will each have different impacts on fluid flow. According to permeability data from the VLF (Michie & Haines 2016), cataclastic fault rock has a far greater sealing potential than any other fault rocks present within Maltese fault zones. As such, the continuity of cataclasite would likely be a key factor in determining whether a fault will behave as a barrier to fluid flow.

FRC data shows that for the fault zones exhibiting a distributed damage zone, namely the QPFZ and the VLF (30 m and 90 m, respectively), fault breccia is more continuous than cataclastic fault rock. Cataclasite is poorly developed within these fault zones (FRC = *c.*0.1 – 0.5) relative to the 50 m throw fault at RiB (FRC = *c.*0.8) and the 210 m throw IMF (FRC = *c.*1). The poor FRC of cataclasite within a distributed damage zone relates to the multiple slip surfaces that accommodate displacement and reduce the amount of strain localised along the principal slip surface. Therefore, a distributed damage zone can act as a buffer to cataclasite formation. This is further highlighted by Figure 3-14, from which it is evident that increasing throw leads to better developed (i.e. thicker, more continuous) cataclasite, whilst a distributed damage zone is characterized by poor cataclasite continuity (i.e. the 30 m and 90 m throw faults). The 50 m throw fault has a similar architecture to the SQF, with a single localised Xlendi member slip surface. However, the lithofacies juxtaposition is the same as for the VLF; a GL hanging wall juxtaposed against an Xlendi footwall. The lack of a distributed damage zone may be due to strain accommodation via the formation of an intense array of deformation bands in the hanging wall, as described by Rotevatn *et al.* (2016), combined with the junction with a series of conjugate slip surfaces that are parallel to the principal orientations of this deformation band array. Due to there being no distributed damage zone, cataclasite at the 50 m throw fault zone is more continuous than for the 30 m and 90 m throw fault zones (FRC = 0.8, 0.15, and 0.47 respectively).

FRT clearly exhibits significant variability over the scales recorded in this study. However, average thicknesses show a trend of increasing thickness with increasing throw. Fault breccia is consistently the thickest fault rock fabric present within the fault zones. The nature of fault breccia distribution explains the large variability in thicknesses; fault breccia occurs in lenses, the thickness of which corresponds to whether breccia is formed via shearing of fault surface asperities, the filling of fault jogs, or fault linkage. Cataclasite FRT falls below the interquartile range of the total fault rock thickness for all 3 fault zones shown in Figure 3-13. Thicknesses appear to become less variable with increasing throw where cataclasite is present (Figure 3-14). This may be explained by a more variable strain distribution along a slip surface during the initial stages of faulting, or greater localisation of strain over larger throws.

3.5.3. Comparisons with other fault zones

To determine whether the relationships between host rock, deformation mechanisms and architectural characteristics of the studied fault zones are applicable to fault zones within different carbonate sequences, comparisons with previous field-based studies are highly valuable. A number of studied fault zones exhibit some similarities to faulting in Malta, despite larger fault displacements, more complicated tectonic histories, and greater burial (e.g. Agosta *et al.* 2007; Fondriest *et al.* 2015; Bauer *et al.* 2016; Demurtas *et al.* 2016; Tondi *et al.* 2016). These fault zones commonly have continuous cataclastic fault cores, as would typically be expected along kilometre scale displacement faults. However the deformation mechanisms by which cataclasis occurs, and therefore the resulting cataclasite textures, often differs to that of Malta. Cataclasites in these fault zones tend to result from pervasive fracturing, creating lithons that reduce in size down to the millimetre scale at the principal slip surface. Often there is little-no evidence of shearing, indicating that deformation is a result of in-situ coseismic shattering (Fondriest *et al.* 2015; Demurtas *et al.* 2016). Architectural observations of these fracture-derived cataclasites (e.g. Bauer *et al.* 2016), and their absence from Malta, suggests that greater burial depths or greater fault displacements are required to form an extensive, continuous unit.

More porous dolomite clasts within the Foiana Fault Zone (Fondriest *et al.* 2015) display grain scale deformation through pore collapse and compaction, similar to that of the high porosity, grain-dominated deformation that occurs in Malta. Grain scale deformation within high porosity carbonates is further documented in fault zones with burial depths from 2 km (Tondi *et al.* 2006) down to <50 m (Tondi 2007). This indicates that high porosity carbonates will likely deform through grain-scale cataclasis, independent of burial depth. Faulted high porosity calcarenites in southern Sicily (Micarelli *et al.* 2006) show there to be continuous fault core after 5 m. This is in contrast with fault zones in Malta, in which fault cores are not continuous until greater displacements (*c*.30 m throw for continuous fault rock (Michie & Haines 2016) and 50 – 200 m for a continuous cataclastic fault core). This difference can likely be attributed to the lack of mechanical juxtapositions along the Sicilian faults, such that strain localization can occur along the cataclastic fault core at low displacements and create a continuous band of fault rock. Contrastingly, the juxtaposition of different lithofacies with differing mechanical and textural properties in Malta tends to produce more distributed deformation, thus inhibiting FRC until greater displacements.

Cataclasis in carbonate rocks is commonly accompanied by grain boundary pressure solution, documented at a variety of burial depths (e.g. Cilona *et al.* 2012; Viti *et al.* 2014; Rotevatn *et al.* 2016). Additionally, the presence of phyllosilicate material within the faulted stratigraphy have been shown to produce alternative fault rock textures to those observed in Malta. For example, the Pietrasecca Fault, central Apennines, hosts a 14 m thick fault core consisting of discontinuous lenses of fault breccia and cataclasite, both of which host a clayey matrix, and a central phyllosilicate-rich layer. The phyllosilicate material is suggested to have been injected into the fault zone from the overlying clay formations during seismogenic activity (Smeraglia *et al.* 2016). Although the Maltese stratigraphy hosts clay rich units, this is not observed within the studied fault cores, as the injection of soft rocks along fault zones is only possible at depth, when the ratio of rock strength to effective strength is sufficiently low to allow fluid into voids (van der Zee *et al.* 2003; van der Zee & Urai 2005).

3.5.4. Impacts on fluid flow

Although fault cores are relatively continuous, it is clear that sub-seismic structures, such as restraining or releasing stepovers, breached relay zones, flower structures etc. are important when considering across-fault fluid flow; these structures are likely to be characterised by a distributed damage zone. In cases where a low permeability cataclastic fault core is predicted (e.g. 100 m throw fault juxtaposing two high porosity grain-dominated carbonates), such structures may in fact act as cross fault leakage points that prevent reservoir compartmentalisation, assuming other fault rock products have negligible permeability variations relative to the host rock. However, other fault rock fabrics may also be associated with low permeability that could make up fault core and impede flow. The most notable of these fault rocks are recrystallized fault rocks and cemented fault breccia, in which the host pore network is occluded, thus characterized by a low permeability (Michie & Haines 2016).

Based upon the fault rock microstructures observed, it is apparent that there is a variety of complex factors determining the fault rock fabric within carbonate fault zones. For high porosity grain-dominated units, such as the Xlendi member (LCL) and the UCL members, grain scale deformation is key in fault rock formation. This suggests that the high intergranular porosity at the time of faulting allows granular flow within the rock and cataclasis of individual grains, as opposed to pervasive fracturing that leads to fracture-derived cataclasite rocks. This is most likely to be the case at throws >50 m, at which point continuous cataclastic veneers may be present

(Figure 3-15). In contrast, lower porosity grain-dominated limestones, such as the Attard member (LCL), are likely to deform in a brittle manner, leading to fracture-derived fault rocks such as fault breccia and, potentially, fracture derived cataclasite. The variety in fault breccia microstructures indicates there to be a variety in their corresponding petrophysical properties. However, poor continuity of fault breccia formations means the most likely impact on fluid flow is where lenses of permeable fault breccia link two reservoir formations, allowing cross or up fault leakage.

3.5.5. Implications for transmissibility multipliers

The prediction of a geologically realistic FRT value is of great importance for estimating fault transmissibility multipliers. Figure 3-17 shows the impact of fault rock thickness on the estimated transmissibility multiplier for the 90 m throw VLF. Host permeability data is taken from Michie *et al.* (2017) and fault permeability (k_f) values of 0.001 mD – 1 mD (at each order of magnitude in between) are used to show the sensitivity of FRT for different k_f values. Typically, the determination of FRT is based upon empirical scaling relationships between FRT and fault displacement. The empirical database of Solum & Huisman (2017) is used to determine the global mean for both fault core and fault zone thickness for a 90 m displacement fault. Based upon the FRT measurements along strike of the VLF (Figure 3-13), the arithmetic mean of all field measurements (1.15 m) gives a FRT that is 0.65 m thicker than the mean fault core thickness for a 10-100 m displacement fault. According the empirical database, the fault core thickness range based on +/- 1 standard deviation for a 10-100 m displacement fault is 0.06 – 2 m, with 56 % of all documented fault cores being 0.1 – 1 m thick. The entire fault zone thickness for the VLF is >50 m (Michie *et al.* 2014), which is over 5 times thicker than the fault zone thickness value from the empirical database (10 m), but still falls within range for a 10-100 m displacement fault based on +/- 1 standard deviation of 2-55 m. Therefore, the thickness of the VLF falls at the upper end of carbonate-hosted faults documented globally, due to the presence of a distributed damage zone. For this example, a 0.75 m variation in thickness value between the global mean fault core thickness and the field derived FRT results in a maximum of *c.*0.24 variation in transmissibility multiplier. However, from the shape of the curves it is apparent that for a low displacement fault zone in which a thin fault core (< 0.3 m) is predicted, a slight variation in FRT results in a significant variation in transmissibility multiplier (Figure 3-17). In accordance with the global database, this example highlights how a generalised displacement- fault rock thickness scaling relationship may not be appropriate for the estimation of transmissibility multipliers.

For a fault core with a very low permeability (< 10^{-3} mD), even a thin core of several centimetres may be sufficient to impact flow over production timescales (Figure 3-17). However, for a fault zone exhibiting a heterogeneous FRT, the regions with the thinnest FRT may act as leakage points over production timescales if permeability is not sufficiently low, even if the fault core is continuous. On a local scale, the mean transmissibility multiplier may be sufficiently low to suggest a barrier or partial barrier to fluid flow, but the thinnest regions may have transmissibility multipliers approaching 1, such that the fault has little or no impact on fluid flow, yet a compartmentalizing fault was predicted. This would prevent reservoir compartmentalisation over geological time. Similarly a heterogeneous fault zone with a FRC < 1 may act in a similar manner due to individual leakage points along the length of the fault. Along with the variability in documented FRT values (Solum & Huisman 2017), this highlights the importance in considering FRC and FRT variations within fault zones. Utilising existing relationships between carbonate lithofacies juxtapositions, fault zone architecture, and the resultant fault rock style (Michie *et al.* 2014), the ability to predict a distributed damage zone may enable better predictions of fault zone heterogeneity and ultimately better predictions of fault permeability within faults hosting displacements on the order of meters to tens of meters.

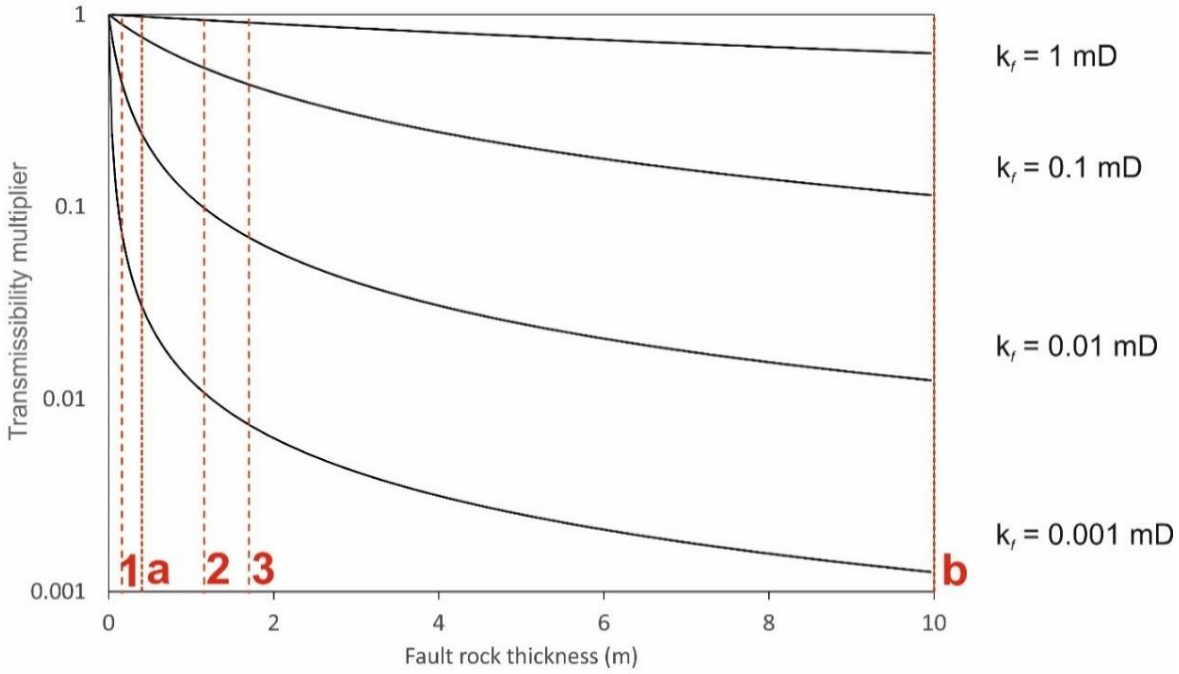

Figure 3-17: The impact of fault rock thickness on the calculated Transmissibility multiplier, for a range of fault permeability values (k_f). Host rock permeability values are taken from the 90 m displacement VLF: k_i = 2 mD, k_j = 200 mD (Michie et al*. 2017). The dashed lines represent fault rock thickness values recorded from the VLF outcrop (lower quartile (1), arithmetic mean (2), and upper quartile (3)) and estimated fault core (a) and fault zone thickness (b) values for a 90 m displacement fault, extracted from empirical data presented by Solum & Huisman (2017).*

3.6. Conclusions

Three fault zones from the Qala Point region of Gozo, Malta, show a variety of fault rock fabrics and fault zone architectures, largely controlled by host lithofacies. Fault zones with high porosity wall rock (>15%), such as the SGF and the grain-dominated SQF segment, exhibit a single localised slip surface with well-developed cataclasite veneers, as well as often forming deformation bands within the damage zone surrounding the principal slip surface. However, the presence of a distributed damage zone acts as a buffer to cataclastic deformation, such as the Xlendi member at the QPFZ, in which cataclastic fault rock is poorly developed. Cataclasite fault rocks and deformation bands form primarily by grain scale cataclasis, granular flow and grain translation. Pressure solution and cementation act to occlude remnant cataclasite porosity. Cataclasites found in Malta are typically grain scale cataclasites, in contrast to fracture derived cataclasites commonly observed in low porosity carbonates. This is attributed to the high porosity at the time

of faulting, the coarse grained nature of some lithofacies, and shallow burial. Deformation appears to have been aided by poorly lithified sediments at the time of faulting, promoting deformation band formation. Grain scale cataclasis promotes preferential bioclast deformation, whereby weaker grains or fossils deform more readily than stronger grains. However, increased displacements may lead to the addition of other deformation mechanisms.

Fault zones with low porosity, grain-dominated wall rock (<15%), such as the Attard member at the QPFZ, or high porosity, micrite-dominated rocks, such as the GL member at the SQF, are less prone to cataclastic deformation at low displacements, favouring distributed deformation through extensional fracturing and the formation of fault breccia. Fault breccia formation mechanisms include hydraulic implosion breccia mechanisms related to lithofacies type, the filling of void spaces relating to fault geometries, the shearing of fault asperities, coalescence of slip surfaces and fault stepover linkage resulting in zones of increased internal strain.

Estimating fault rock continuity (FRC) in any fault zone is key to determining the sealing capacity of the fault. Although fault core is commonly continuous over outcrop scales, low permeability cataclastic fault rock in high porosity, shallow burial granular limestones only become continuous at 50-200 m throw in this setting. The presence of a distributed damage zone appears to create a buffer in cataclastic rock formation, hence greater fault displacements are required to achieve a continuous cataclasite veneer. For example, the QPFZ shows a distributed damage zone due to the complex dextral wrench system creating numerous slip surfaces, whereby deformation is distributed across multiple sip surfaces. However, these observations are only valid for faults with <90 m throw. Fault breccia is often more continuous than cataclastic fault rocks in low displacement faults or where there is a distributed damage zone. Further to FRC impacting across-fault fluid flow, FRT estimates can be used towards creating more realistic and site specific calculations of transmissibility multipliers to be used in reservoir models.

3.7. Acknowledgements

We thank Wintershall, ENI and ADMA for project funding and support. Partial project funding was also provided by NERC. The authors would also like to thank Andrea Billi and an anonymous reviewer for providing constructive reviews, which helped to improve the quality of this manuscript.

CHAPTER 4.

Permeability of carbonate fault rocks: a case study from Malta

Cooke, A.P., Fisher, Q.J., Michie, E.A.H. & Yielding, G. 2019. Permeability of carbonate fault rocks: a case study from Malta. *Petroleum Geoscience*.

(Accepted for publication in August 2019)

4.1. Abstract

The inherent heterogeneity of carbonate rocks suggests that carbonate-hosted fault zones are also likely to be heterogeneous. Coupled with a lack of host-fault petrophysical relationships, this makes the hydraulic behaviour of carbonate-hosted fault zones difficult to predict. Here we investigate the link between host and fault rock porosity, permeability and texture, by presenting data from series of host rock, damage zone and fault rock samples from normally faulted, shallowly buried limestones from Malta. Core plug X-ray tomography indicates that texturally heterogeneous host rocks lead to greater variability in the porosity and permeability of fault rocks. Fault rocks derived from moderate to high porosity (>20%) formations experience permeability reductions of up to six orders of magnitude relative to the host; >50% of these fault rocks could act as barriers to fluid flow over production timescales. Fault rocks derived from lower porosity (<20%) algal packstones have permeabilities that are lower than their hosts by up to three orders of magnitude, which is unlikely to impact fluid flow on production timescales. The variability of fault rock permeability is controlled by a number of factors, including the initial host rock texture and porosity, the magnitude of strain localisation, and the extent of post-deformation diagenetic alteration. Fault throw has no obvious control over fault rock permeability. The results enable better predictions of fault rock permeability in similar lithotypes and tectonic regimes. This may enable predictions of fault zone sealing potential when combined with data on fault zone architecture.

4.2. Introduction

Fault cores are characterized by one or more slip surfaces, which typically bound lenses of fault rock, that have been subject to either mechanical or diagenetic alteration, such as cataclasite, fault gouge and fault breccia (Sibson 1977; Chester & Logan 1986; Scholz *et al.* 1993; Caine *et al.* 1996; Faulkner *et al.* 2003). A region of less deformed rock surrounds the fault core, known as the damage zone (e.g. Billi *et al.* 2003; Haussegger *et al.* 2010; Faulkner *et al.* 2011). Together, the fault core and the damage zone comprise the fault zone. Fault cores commonly become thicker and more continuous as fault zones mature (e.g. Micarelli *et al.* 2006; Faulkner *et al.* 2011; Cooke *et al.* 2018). Some studies report an increase in strain localisation along the fault core with increased displacement (e.g. Chester *et al.* 1993; Wibberley *et al.* 2007; Bauer & Decker 2010). Other studies report an increase in fault zone heterogeneity, whereby strain is distributed over one or more texturally and structurally heterogeneous fault cores (Childs *et al.* 1997; Faulkner *et al.* 2003; Chester *et al.* 2004; Shipton *et al.* 2006; Bastesen & Braathen 2010, Loveless *et al.* 2011), particularly in carbonated hosted fault zones (e.g. Ferrill & Morris 2008; Bauer & Decker 2010; Hausegger *et al*. 2010; Jeanne et al. 2012; Michie *et al*. 2014; Cooke *et al*. 2018).

The deformation mechanisms by which fault rocks are formed depend on several factors, including the stress and temperature conditions at the time of faulting, as well as the physical and textural properties of the host rock (Fulljames *et al.* 1997; Knipe 1997; Fisher & Knipe 1998; Sperrevik *et al.* 2002; Childs *et al.* 2009; Michie 2015). Deformation mechanisms may also vary along strike or down dip within a given fault zone as a result of heterogeneous strain localisation and variation in the juxtaposed lithofacies. In addition, diagenetic alteration may vary throughout the fault zone, owing to rates of cementation or dissolution that may vary as a function of composition and thermal history (Laubach *et al.* 2014). This variation leads to fault zones being comprised of a range fault rocks that may impact fluid flow in differing ways. It should, however, be noted that there is no reason why faults that are very different in terms of the type and/or distribution of fault rocks might not have similar up-scaled flow properties.

Several studies have demonstrated that initial host porosity is one of the principal controls on deformation (e.g. Zhang *et al*. 1990; Wong *et al*. 1997; Baud *et al*. 2000). For example, the unconfined compressive strength and the critical stress required for the onset of pore collapse (i.e. the transition between brittle deformation and cataclastic flow) decreases with increasing porosity (Wong *et al.* 1997; Vajdova *et al.* 2004). This observation suggests that low porosity rocks

tend to favour a dilatant style of deformation, whereas high porosity rocks favour a compactional style of deformation (Groshong 1988; Rutter & Hadizadeh 1991; Rawling & Goodwin 2006; Ballas *et al.* 2015). Fracture intensity increases during progressive brittle deformation of low-porosity rocks, with extensional fractures accommodating dilation. Fracture-bound clasts of undeformed rock are reduced to smaller sizes with increasing damage and strain localisation, forming a fine-grained, cataclastic fault rock in which the grain fragments often become cemented (e.g. Billi *et al.* 2003; Demurtas *et al.* 2016). Faulting of higher porosity rocks is commonly associated with the formation of deformation bands as a result of grain fracturing and/or pore collapse (Schultz & Siddharthan 2005; Tondi 2007; Cilona *et al.* 2012; Rotevatn *et al.* 2016; Kaminskaite *et al.* 2019), or through dilation in poorly lithified sediments under low stress (Du Bernard *et al.* 2002). Deformation bands within carbonates have predominantly been observed in shallowly buried formations. Fault rocks from low permeability carbonate formations have been shown to have enhanced permeability relative to the host rock, due to the brittle nature of deformation (Géraud *et al.* 2006; Ran *et al.* 2014). Fault-core cementation following brittle deformation has also been shown to impact permeability. For example, Agosta (2008) documented cemented cataclasite in low porosity and permeability platform carbonates that have a permeability of 10^{-4} mD, compared with 10^{-1} mD for the uncemented counterparts. Fault rock in high permeability formations has been shown to often have reduced permeability relative to the host rock (e.g. Micarelli *et al.* 2006; Haines *et al.* 2016; Kaminskaite *et al.* 2019). Studies focussing on fault zones in Malta have recorded permeabilities as low as 10^{-4} mD (up to six orders of magnitude reduction from the host rock) as a result of both mechanical and diagenetic processes (Haines *et al.* 2016; Michie and Haines 2016). These studies have also shown how the heterogeneity within Maltese fault zones is a product of the juxtaposing lithofacies; a relatively homogeneous fault core can be expected where low displacement faults juxtapose the same lithofacies. A heterogeneous composite fault core can be expected, with fault rock contributions from either side of the fault arranged in a complex manner, with increasing displacement and consequent juxtaposition of contrasting lithofacies (Michie 2015). However, the link between microscale textural heterogeneity and permeability in both the host and fault rock have not been quantitatively investigated.

The following work provides a study of the permeability of different fault zone deformation products in shallowly buried (<1 km) limestones from Maltese Islands. The porosity and permeability of core plugs taken from seven Maltese fault zones are presented. In addition, macroscale computerised tomography (CT) imaging and optical microscopy are used to

characterise the textural characteristics of these rocks. This information is then used to link host characteristics and fault displacement to the potential range of fault rock permeabilities. Finally, based upon differences in permeability between host and fault rocks, the potential impact of these fault rocks on fluid flow is assessed. The results have potential to improve the modelling of subsurface fluid flow by enabling a probabilistic approach to fault rock permeability prediction within similar lithologies that were faulted under similar stress conditions.

4.3. Geological background

The Maltese islands are composed of a series of well exposed and highly faulted Oligo-Miocene age carbonates providing a useful location for the analysis of fault zone development and fault rock permeability in carbonate-hosted fault zones. The geomorphology of the islands is characterised by a series of horst and graben structures, which are a product of north-south extension in the foreland of the Maghrebian-Apennine fold and thrust belt (Dart *et al.* 1993). Major extensional faulting began in the late Miocene and generated two fault trends in Malta, those being ENE-WSW, which is the dominant trend onshore, and WNW-ESE, reflecting the nearby Pantelleria Rift (Figure 4-1). Fault throws range from centimetre-scale up to hundreds of meters and are syn-depositional in the younger, Miocene formations. Faulting is predominantly normal, with a minor dextral component to slip in Gozo. Faults in the eastern tip of Gozo (Qala Point Fault and the South Qala Fault) are part of a series of en echelon structures, extending inland from the easternmost exposure of the South Gozo Fault (Illies 1981).

Sampling took place at four localities in Malta and three localities in Gozo (Figure 4-2). Two of the sampled faults comprise the bounding faults of the North Malta Graben, namely the South Gozo Fault and the Victoria Lines Fault, and the Il-Maghlaq Fault represents the only major onshore fault trending WNW-ESE. The studied faults range in throw from 11 m to >200 m.

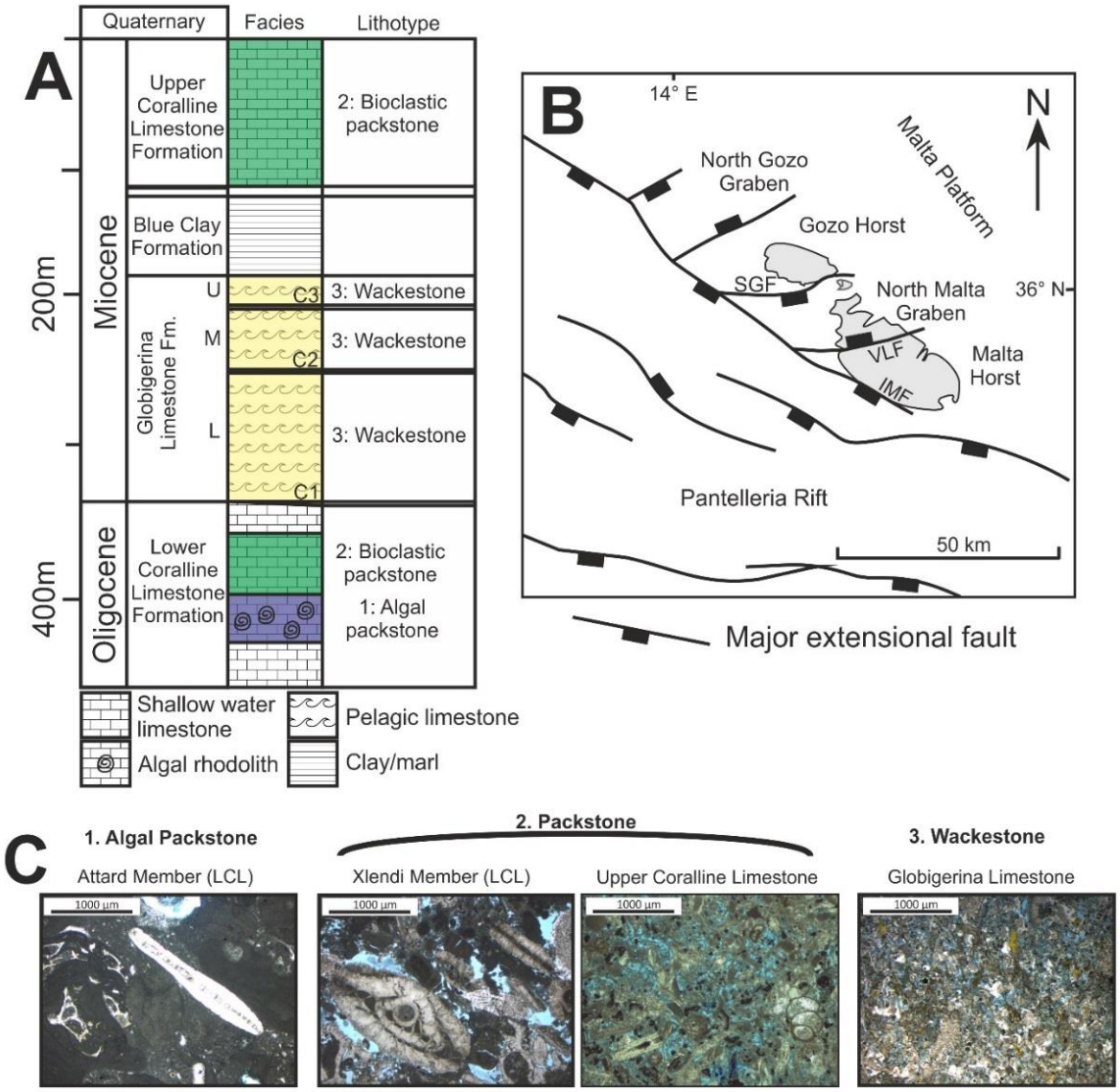

Figure 4-1: A) Generalised geological log of Malta, showing the maximum thickness of each stratigraphic unit (after Gatt 2007). C1 to C3 correspond to conglomeratic hardgrounds between the upper, middle, and lower Globigerina Limestone Fm. B) Tectonic setting of Malta, highlighting the major faults in the area (after Dart et al. 1993). C) Representative microstructures from the 4 studied facies which are assigned to 3 lithotypes (after Cooke et al. 2018).

From oldest to youngest, the stratigraphic sequence consists of the Lower Coralline Limestone (Chattian), the Globigerina Limestone (Aquitanian to the Seravallian), the Blue Clay (Seravallian), and the Upper Coralline Limestone (Messinian) formations (Figure 4-1). The Lower Coralline Limestone is a shallow water bioclastic limestone dominated by coralline algae in areas. The formation is 300 to 1000 m thick, however less than 140 m are exposed onshore (Pedley *et*

al. 1976). The Attard member of the Lower Coralline Limestone contains the highest concentrations of coralline algae and may be considered as a boundstone in some areas, leading to a lower porosity (5 to 20%) relative to the bioclastic Xlendi member (>20%). The Globigerina Limestone is represented by a succession of biomicritic, yellow-cream pelagic limestones dominated by *Globigerina* foraminifera. It reaches a thickness of >200 m (Pedley 1978) and is divided into three units (Lower, Middle and Upper), which are each underlain by thin hardgrounds and phosphoritic conglomerate layers (Pedley & Bennett 1985). The Blue Clay is a carbonate-rich (up to 30% carbonate) marl, with a thickness of 0 m to 65 m (Pedley 1978; John *et al.* 2003). The Upper Coralline Limestone is a shallow water limestone that varies from coralline algal biostrome facies to patch reefs and platform and slope facies at the top (Bosence & Pedley 1982). The sediments have experienced limited diagenetic alteration due to their shallow burial depth of 300 m to 1000 m (Dart *et al.* 1993; Kim *et al.* 2003; Haines *et al.* 2016).

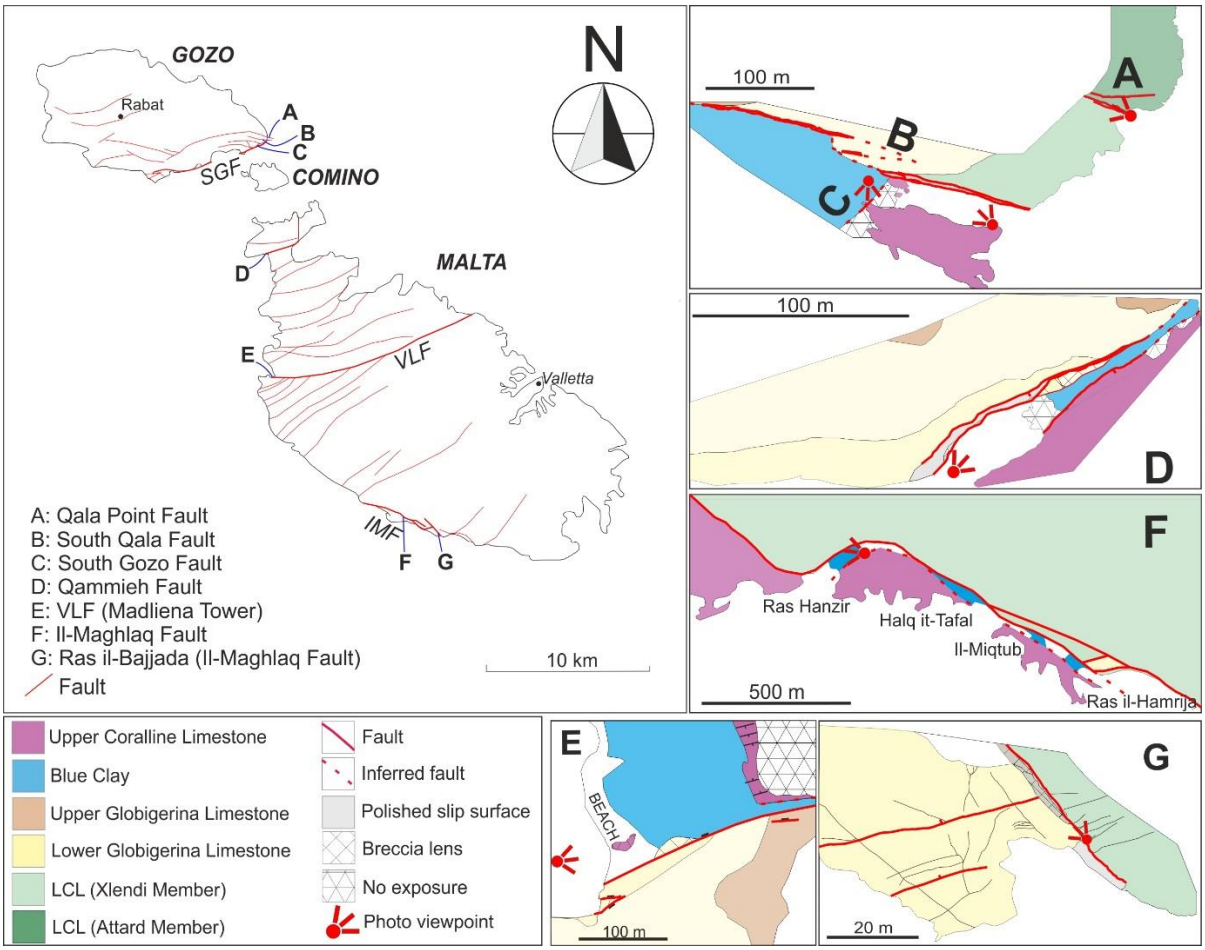

Figure 4-2: Map of Malta showing the seven study sampled localities and geological maps of each locality. All maps are oriented to the north arrow.

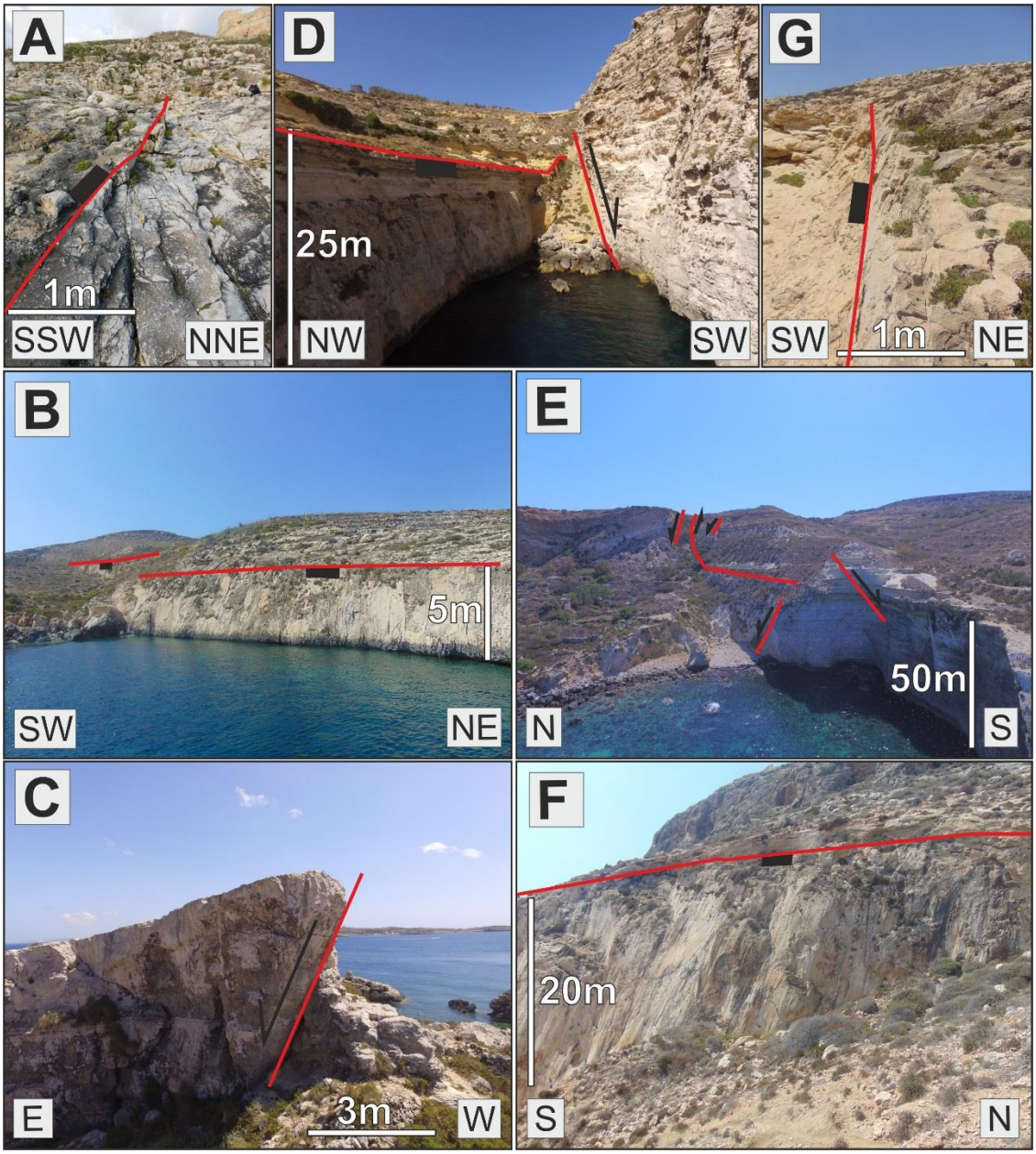

Figure 4-3: Photographs of each studied fault zone. See Figure 4-2 for location of photos and view directions.

The sampled formations are broadly simplified into 3 lithofacies, those being packstones from the Xlendi member of the Lower Coralline Limestone and the Upper Coralline Limestone, wackestones from the Globigerina Limestone, and algal packstones from the Attard member of the Lower Coralline Limestone (Figure 4-1). The largest studied faults juxtapose the Upper Coralline Limestone against the Lower Coralline Limestone, with the Blue Clay forming a thick (up to 10 m) clay smear between the hanging wall and footwall slip surfaces (faults D, E & F; Figure

4-2 & Figure 4-3). Smaller faults either self-juxtapose the Upper Coralline Limestone or the Lower Coralline Limestone, or juxtapose the Globigerina Limestone against the Lower Coralline Limestone (faults A, C & G; Figure 4-2 & Figure 4-3).

4.4. Methodology

Samples were collected from Malta to capture representative portions of fault rock and undeformed host rock. However, polished slip surfaces with no fault rock are generally not represented because they were too thin to collect and analyse. Core plugs with diameters of 25 mm (1 inch) and 38 mm (1.5 inch) were drilled for sample analyses and polished thin sections were produced for optical microscopy (see Appendix 1 for core plug info). Fault rock core plugs and thin sections were oriented at 90° to the fault plane and host rock core plugs were drilled in three orientations relative to bedding (along strike, up dip, and at 90° to bedding planes; Figure 4-4) to observe any permeability anisotropy. A total of 158 core plugs were drilled, from which 77 were from fault rocks, 48 were from damage zones, and 33 were from host rock samples (Table 4-1 & Table 4-2). Deformation bands were considered to be a feature of the damage zone rather than the fault core.

All core plugs were cleaned using carbonate saturated deionised water to remove salts that were likely to impact the petrophysical property measurements by occluding pore space. Cleaned core plugs were then placed in an oven and heated to 60° until dry.

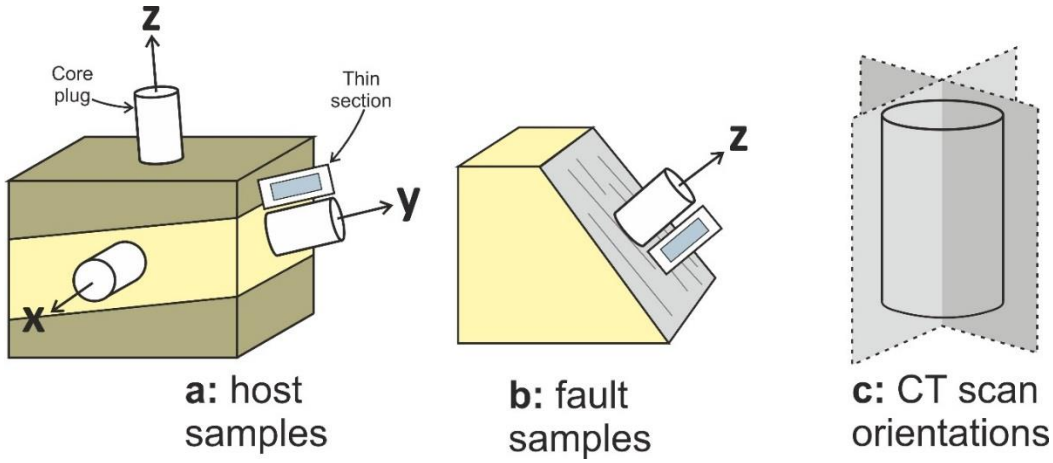

Figure 4-4: A) Orientation of host rock core plugs and thin sections relative to bedding. B) Orientation of fault rock core plugs and thin sections relative to fault plane. C) Orientation of CT scan images relative to core plug.

4.4.1. CT imaging

Core plugs were scanned using a GE Bravo 385 medical style CT scanner to locate any heterogeneities that might affect results. Core plugs were scanned in two perpendicular orientations about their length (Figure 4-4), ensuring all planar features could be visualised. Samples with open fractures formed during either the exhumation of sediments or sample preparation which, therefore, might be unrepresentative of the rock in the subsurface were ignored.

Each of the acquired CT images contains 512 x 512 pixels, with a pixel size of 200 x 200 μm^2. The CT imaging assigns a CT number to each pixel. The CT number corresponds to the density of the imaged material, and is expressed in Hounsfield units (HU) of X-ray absorption. The mean HU and the standard deviation (σ_{HU}) for each CT image was obtained using a region of interest that excludes edge effects from beam hardening. The two perpendicular scans were used to obtain average HU values for each sample. The sample density, and therefore the mean HU, is inversely correlated with porosity (Figure 4-5). Accordingly, σ_{HU} provides a proxy for porosity heterogeneity which is used as a quantitative measure of relative textural heterogeneity between samples (Figure 4-6; Maas & Hebing 2013).

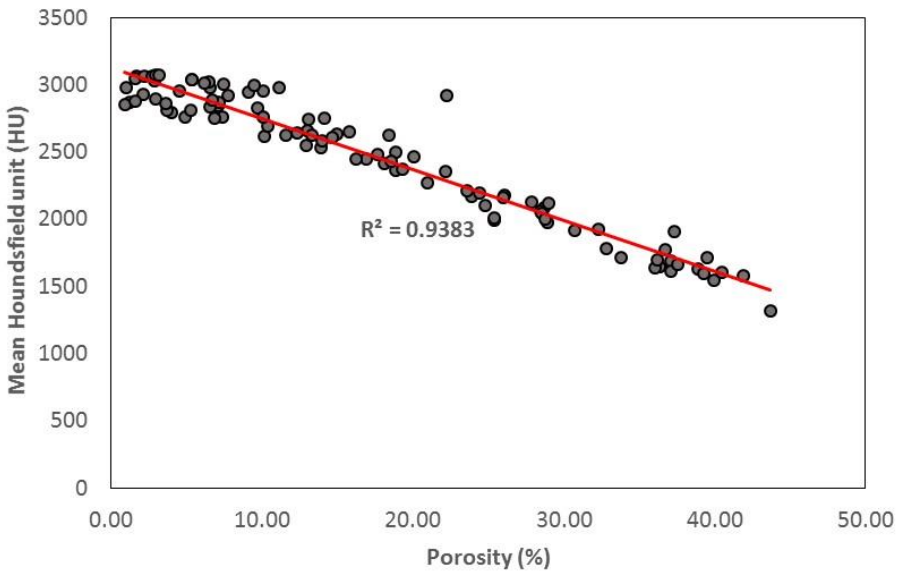

Figure 4-5: Mean Hounsfield values for all samples. Negative correlation between the mean HU and porosity shows that the HU can be used as a proxy for porosity.

CT numbers have an instrument error of ±6 HU, which corresponds to <0.5% of the total range in HU that are used to create the images. Additional errors may occur through beam-hardening effects, which increases the HU values around the edges of an image. To account for this, a region of interest that excludes the outermost area of the image is used when measuring the mean HU and σ_{HU}.

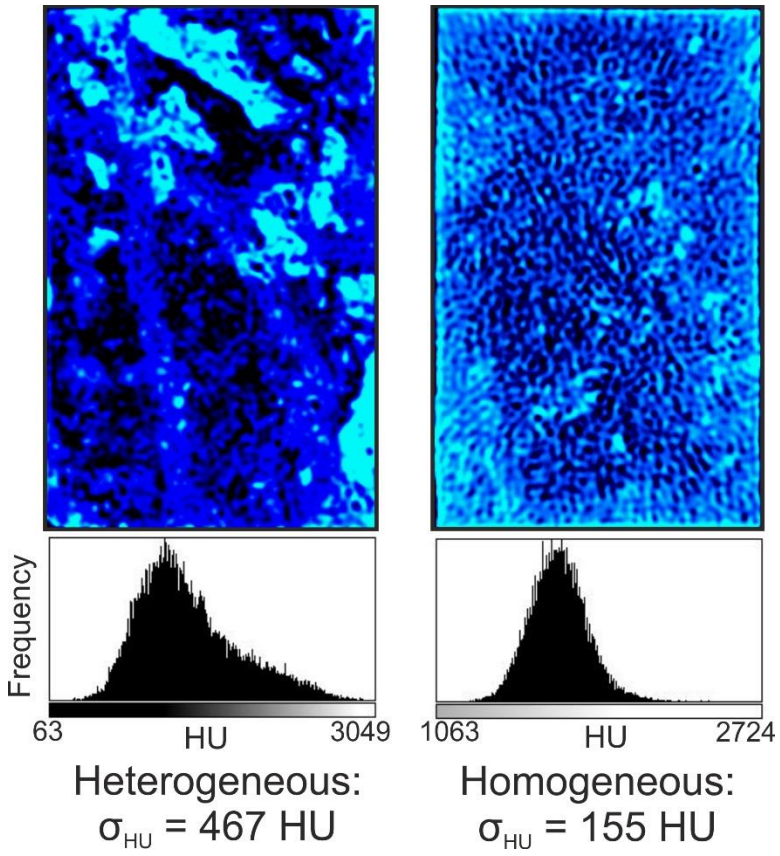

Figure 4-6: Example of processed CT images for two 1.5 inch diameter core plugs. Images are coloured according to normalized density, not absolute density. Lighter colours are high density regions, darker colours are low density regions. Histograms correspond to the HU distribution for each sample, from which the standard deviation (σ_{HU}) is used as an estimate of sample heterogeneity.

4.4.2. Petrophysical analysis

Porosity

The porosity of each core plug was calculated by measuring the bulk volume and grain volume. Bulk volume was calculated using length and diameter measurements made with a digital calliper. Grain volume was measured using Boyle's Law Double-Cell method with helium gas (API 1998).

Porosity was recorded four times for each core plug and the arithmetic average taken to reduce experimental error.

Permeability

Single phase gas permeability measurements were acquired using steady-state and pulse-decay methods for high (>1 mD) and low (<1 mD) permeability samples, respectively. In all cases, samples were loaded into a rubber sleeve inside a core holder, to which a confining pressure was applied. Tests were carried out at 20.7 MPa (3000 psi) confining pressure and up to 6.2 MPa (900 psi) pore pressure. These confining pressures were used to simulate subsurface conditions; 20.7 MPa corresponds to c.1 km burial depth, assuming an overburden density of 2 g/cm^3 (average density of all host rock samples). Helium gas was used for all tests.

To account for gas slippage effects at low pressures, permeability measurements were corrected by determining the Klinkenberg permeability (Klinkenberg 1941). The Klinkenberg permeability was determined by measuring apparent permeability at several mean pore pressures (≥ 4 data points). A plot of apparent permeability against the reciprocal of the mean pore pressure, 1/P, was produced and a regression line fitted to the data. Extrapolating the regression to infinite pore pressure (1/P = 0) gives the Klinkenberg corrected permeability.

For pulse decay permeability tests, the pore pressure within the system was increased and allowed to equilibrate across the sample. A differential pressure was induced across the sample and the absolute and differential pore pressures are monitored using pressure transducers until the pressure re-equilibrates. The apparent permeability was then calculated according to Darcy's Law. A constant upstream gas pressure was applied during steady state permeability tests, whilst the downstream was vented to ambient pressures through a flowmeter. The differential pressure across the sample was monitored until it stabilised, at which point the flow rate, the differential pressure and the pore pressure were recorded to calculate absolute permeability at a given pore pressure, according to Darcy's Law.

4.4.3. Microstructural analysis

Thin sections were produced from areas of the sample that were close to core plug locations, to ensure sampling of a similar rock material. Thin sections were oriented in a similar manner to core plugs; fault rock thin sections were in a plane normal to the fault plane (Figure 4-4), host thin

sections were in a plane normal to bedding planes. A low viscosity resin containing blue dye was used to make pore spaces more apparent when viewed in plane polarized light. Optical images from the thin sections were analysed to assess the deformation mechanisms in each sample based on documented deformation and/or diagenetic microstructures. These observations enabled were used to divide samples into different fault rock categories and to interpret how different deformation mechanisms might govern the petrophysical properties of fault rocks (Table 4-2).

4.5. Deformation mechanisms

A variety of different deformation mechanisms are observed in Malta, the majority of which are brittle. These include extensional fracturing, intragranular-extensional fracturing (Herzian impingement microcracks), grain chipping, and sediment disaggregation leading to grain translation, comminution, and pore collapse. Plastic deformation mechanisms consist of calcite twinning and pressure solution.

The principal deformation features observed within each of the samples were used to assign each sample to one of six fault rock groups, according to the evolutionary paths for grain-dominated and micrite-dominated fault rocks as outlined by Michie (2015). Several fault rock types were combined to more generalised categories to simplify the grouping. The cataclasite series, consisting of protocataclasite, composite chaotic breccia, and cataclasite, are all referred to here as cataclasite. Following the classification of Woodcock & Mort (2008), the fault breccia series are all termed fault breccia. The fault rock types used in this study are as follows:

(1) Cataclasites: fault rocks that have a fine grained matrix, with clasts of less deformed sediment or individual survivor grains. Mechanisms creating cataclasites include disaggregation (grain translation/particulate flow), intra-grain fracturing, comminution during grain rolling, and pore collapse. Cataclasites in this study are typically grain-scale cataclasites, formed by the mechanical breakdown of individual grains, as opposed to fracture-derived cataclasite, formed by more distributed fracturing that generates progressively finer grained clasts (e.g. Billi *et al.* 2003).

(2) Fault breccia: fault rocks with a rock volume composed of >30% large (>2 mm) clasts of intact host rock, surrounded by a finer grained or cemented fracture mesh Woodcock & Mort (2008). Mechanisms creating fault breccia include pervasive fracturing, mechanical attrition accompanied by dilation, and filling of void spaces within the fault zone.

(3) Cemented: fault rocks exhibiting little evidence of mechanical deformation, however, pore networks are altered by the precipitation of calcite cements. Minor apatite and dolomite cements are observed within the Globigerina Limestone. These rocks are defined as fault rocks where their occurrence correlates with fault zone lineations (i.e. cementation along the fault core).

(4) Deformation bands: similar to those observed in cataclasites, however, deformation bands are often thinner (<1 cm), hosting either small (<1 cm) or no displacement (compaction bands), and form anastomosing arrays within the damage zone.

(5) Damage zone: samples from within the damage zone and have little-no obvious macro-scale deformation. For example, these samples may be located in between deformation bands or within the damage zone between two nearby slip surfaces. Host rock texture may be altered by processes such as minor compaction, cement precipitation and extensional fracturing.

Host samples are defined as those that are outside of the fault damage zone, and have therefore not been subject to any fault-related damage or diagenesis, retaining the original texture. The number of samples assigned to each fault rock group are shown in Table 4-2. Combining the microstructural observations and interpretations of the fault rock deformation history of Michie (2015), a generalized deformation series has been created to document the fault rock products of each of the 3 lithotypes (Figure 4-7).

Grain scale cataclasis is limited to regions containing higher porosities and lower contents of algal rhodolith grains, which appear to resist cataclastic deformation. The lower porosity regions exhibit higher frequencies of extensional fractures and subsidiary slip surfaces. Coalescence of these slip surfaces accompanied by pervasive fracturing leads to the formation of fault breccia (Figure 4-7). Veneers of grain scale cataclasis are common along packstone slip surfaces (Figure 4-7). Anastomosing arrays of deformation bands are observed in packstone damage zones at 3 localities, namely the SGF, the IMF at Ras il-Bajjada, and in lenses along the main segment of the IMF. These arrays result from disaggregation and minor cataclasis (Bonson *et al.* 2007; Rotevatn *et al.* 2016; Cooke *et al.* 2018). Extensional fractures and subsequent formation of fault breccia are also observed in packstones, but to a lesser extent than the lower porosity algal packstones. The wackestone lithofacies exhibits similar characteristics to those of the packstones, with the exception that grain scale cataclasis is less commonly observed (Table 4-2). This is because of the

resistance of the fine-grained *Globigerina* foraminifera to cataclasis (Michie 2015). All fault rocks are cemented, however slip surfaces in wackestones commonly consist of a thin (<2 cm) layer of low porosity, highly cemented rock (Figure 4-7).

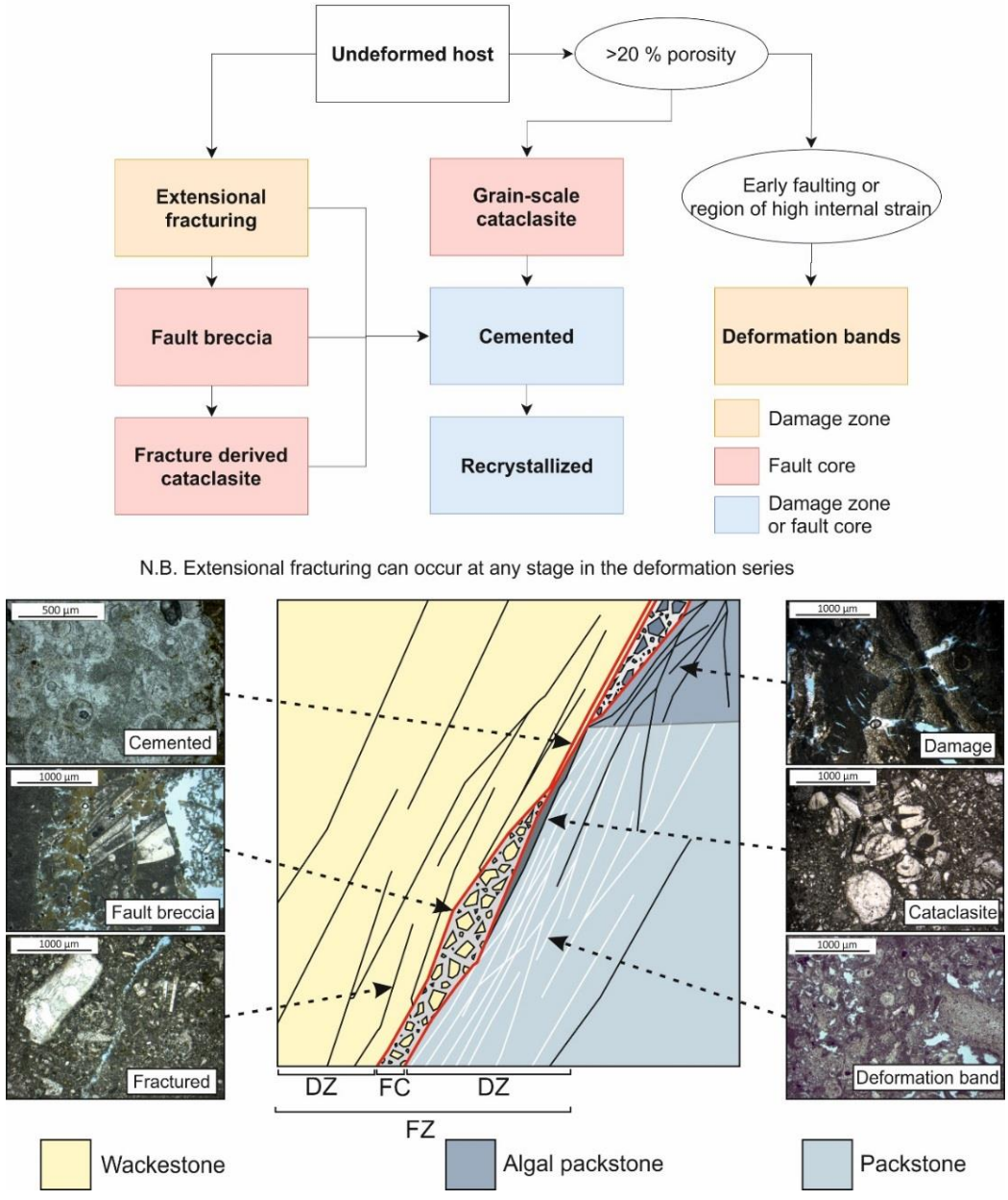

Figure 4-7: Deformation series for the studied lithotypes (after Michie 2015); moving through the deformation series broadly represents increasing deformation. Photomicrographs show typical microstructures for the different fault rock types and the schematic fault zone shows their distribution in a generic Maltese fault zone.

4.6. Results

4.6.1. Host rocks

The permeability data obtained from all samples is summarised in Table 4-1 & Table 4-2 and Figure 4-8. The geometric mean host permeability is lowest for algal packstones (1.4 mD, ranging from 0.07 mD to 9.7 mD), followed by wackestones (16.2 mD, ranging from 7.3 mD to 34.6 mD) and packstones (51.8 mD, ranging from 20.3 mD to 107.8 mD). The standard deviation of the logarithm of permeability (σ_{logK}) indicates the relative heterogeneity within different sample groups. In contrast to mean permeability, σ_{logK} is lowest for the packstones (σ_{logK} = 0.24), followed by wackestones (σ_{logK} = 0.26) and algal packstones (σ_{logK} = 0.87). Texturally, the packstones are the most heterogeneous (σ_{HU} = 401.0 HU) followed by the algal packstones (σ_{HU} = 325.2 HU) and wackestones (σ_{HU} = 177.6 HU).

Textural heterogeneity is interpreted to influence the heterogeneity in porosity and permeability data; the high average σ_{HU} of algal packstones indicates a heterogeneous texture, which is reflected by the high σ_{logK} value and the scatter in porosity (Figure 4-8A). Similarly, the wackestone samples exhibit a low average σ_{HU}, indicating that they are texturally homogenous, which is reflected by the low σ_{logK} value and the low degree of scatter in porosity (Figure 4-8A). Packstones are characterised by a heterogeneous texture and a broad range of porosity values, but have a low σ_{logK} value.

4.6.2. Damage zone

The geometric mean permeability for damage zone rocks in all lithotypes is around one order of magnitude less than the host rock (Table 4-1). In the wackestone damage zone samples these reductions are almost entirely due to deformation bands (eight of 10 samples). In contrast, the heterogeneity between sample permeability, σ_{logK}, increases from host to damage zone in all lithotypes (Figure 4-8C), as recorded by their σ_{logK} values. This increase is a result of the variety in damage zone products, including zones of increased fracturing, deformation bands, and areas of increased cementation. Packstone damage zone samples have the highest heterogeneity between sample permeability (σ_{logK} = 1.91) compared to algal packstone (σ_{logK} = 1.35) and wackestone (σ_{logK} = 0.48) damage zones samples. However, there is a greater frequency of packstone samples relative to others. On the core plug scale, σ_{HU} reduces relative to the host rock in the packstones, but increases in algal packstones and wackestones.

Lithology	Architectural unit	No. of samples	Geometric average perm (mD)	σ_{logK}	Arithmetic average σ_{HU} (HU)
Algal Packstone	Host	8	1.40	0.87	325.2
	Damage	6	0.13	1.35	355.6
	Fault	22	0.050	1.40	305.5
Packstone	Host	17	51.8	0.24	401.0
	Damage	25	1.69	1.91	298.2
	Fault	28	0.0082	2.26	186.5
Wackestone	Host	8	16.18	0.26	177.6
	Damage	10	2.67	0.48	205.2
	Fault	34	0.0046	1.39	174.6

Table 4-1: Summary of permeability data collected for each fault zone architectural unit.

Lithology	Fault rock type	No. of samples	Geometric average perm (mD)	σ_{logK}	Arithmetic average σ_{HU}
Algal Packstone	Cataclasite	3	0.035	0.86	333.8
	Fault breccia	14	0.12	1.56	339.3
	Cemented	11	0.032	1.25	265.3
Packstone	Cataclasite	19	0.00074	1.43	148.0
	Fault breccia	7	3.6	1.55	348.9
	Cemented	3	0.00050	0.68	347.9
	Deformation band	12	3.8	1.22	330.8
Wackestone	Cataclasite	7	0.000049	1.15	71.9
	Fault breccia	11	0.034	1.34	278.12
	Cemented	16	0.0057	0.87	135.32
	Deformation band	8	2.2	0.47	195.2

Table 4-2: Summary of permeability data collected for each fault rock type

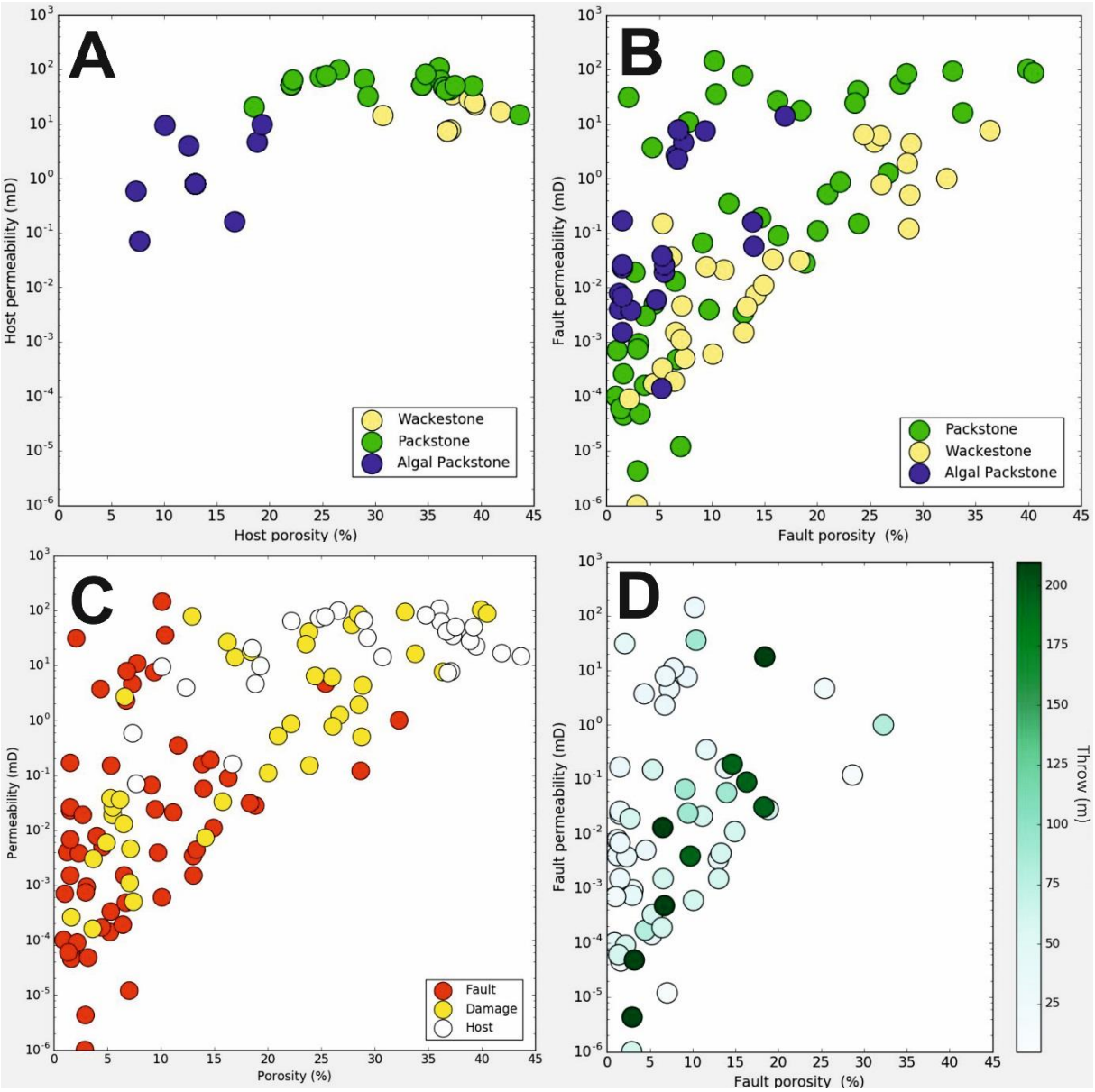

Figure 4-8: A) All poroperm data obtained from undeformed host samples. B) Poroperm data obtained from all samples within the damage zone (damage and fault samples) coloured according to host lithofacies. C) Poroperm data obtained from all samples, coloured according to architectural unit of the fault zone. D) Poroperm data from all fault rock samples, coloured according to fault throw.

4.6.3. Fault rocks

Fault rock permeabilities range from 10^{2} mD to 10^{-6} mD (Figure 4-8B). The lowest sample permeabilities are recorded in wackestone samples, which have a range of 10 mD to 10^{-6} mD.

Similarly low permeabilities are recorded in packstones, which have a range of 10^2 mD to 10^{-6} mD. Algal packstone samples have a narrower range of 10 mD to 10^{-3} mD. The geometric mean permeability reduces from host and damage zone to fault rock in all three lithotypes. The geometric mean permeability of wackestone fault rocks is the lowest of all lithotypes (0.005 mD), but packstones have a similarly low permeability (0.008 mD). These values correspond to permeability reductions from host to fault rock of almost four orders of magnitude. Geometric mean fault rock permeability in algal packstones is an order of magnitude larger than for the other lithotypes (0.05 mD), despite exhibiting the lowest average host rock permeability, corresponding to a host to fault permeability reduction of almost two orders of magnitude.

Permeability heterogeneity increases from host to fault rock for all lithofacies (Table 4-1 & Figure 4-8B). The largest increase in permeability heterogeneity is recorded in the packstone samples ($\sigma_{logK} = 2.26$), which have an almost tenfold increase in σ_{logK}. Wackestone fault rocks show a greater than fivefold increase ($\sigma_{logK} = 1.39$), and algal packstone fault rocks show less than twofold increase ($\sigma_{logK} = 0.87$). Whilst this trend highlights the increasing heterogeneity between core plugs (outcrop scale), the opposite is the case for the core plug scale; σ_{HU} decreases from host rock to fault rock in all lithotypes (Table 4-1 & Figure 4-9).

There is a lack of a clear relationship between fault throw and fault rock permeability; permeability values from the largest and smallest throw faults are not distinct (Figure 4-8D). However, the lower throw faults record more samples that have a low porosity but relatively high permeability. The majority of these samples correspond to algal packstone and a small number of packstone fault rocks. Algal packstone fault rocks are not sampled at throws greater than 60 m, such that this distribution is an artefact of sampling and does not indicate a global trend between porosity, permeability and throw.

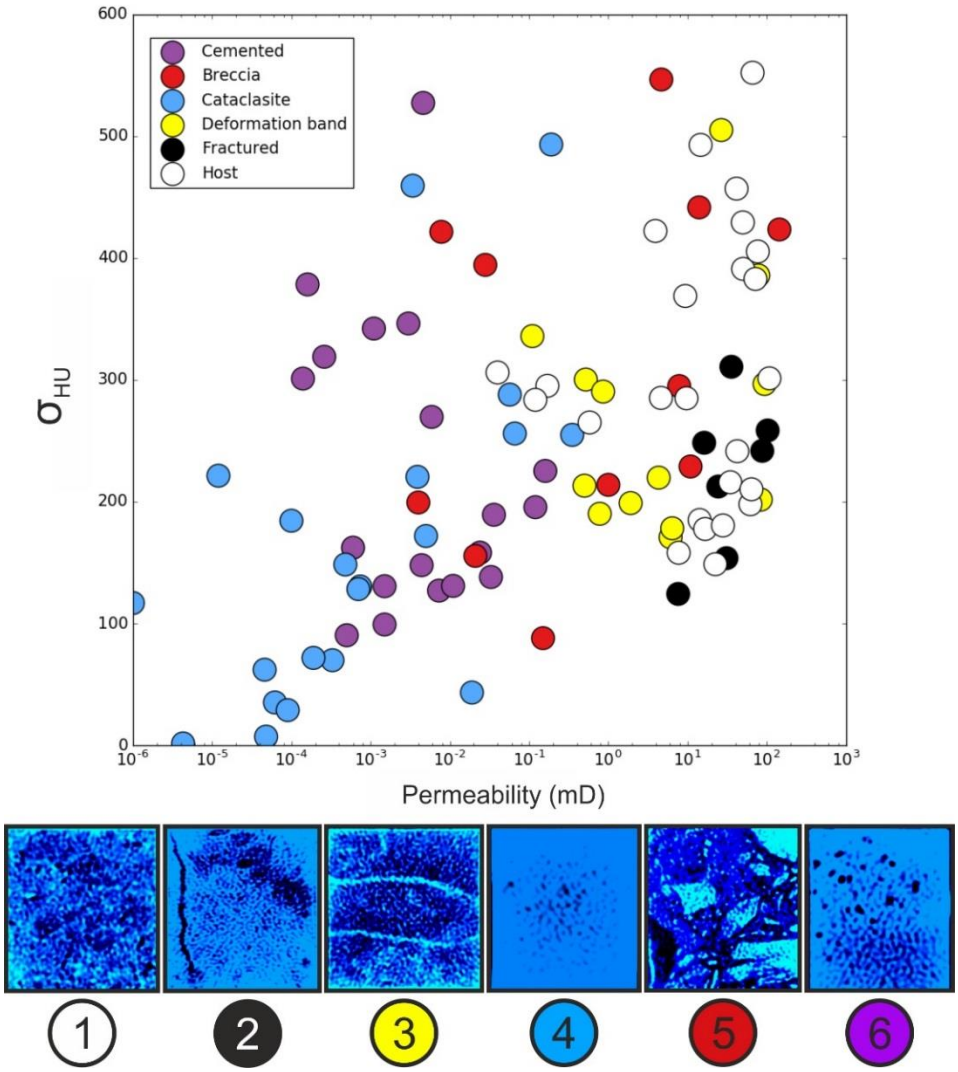

Figure 4-9: HU standard deviation (σ_{HU}) for each core plug plotted against the measured permeability, coloured according to rock type. The CT images below are examples of rock types.

Table 4-2 summarises the data grouped by different fault rocks. The frequency of sampled fault rocks from each lithotype gives an indication of the prevalence of that fault rock type. Despite efforts to sample representative portions of each fault zone, the effect of sampling bias on the frequency of each sampled fault rock means that this observation carries no quantitative value. Nevertheless, it is useful to note the prevalence of different fault rock types, which provides an insight to the dominant deformation mechanisms occurring in each lithotype. Packstones contained the most cataclasites (19 samples, 46% of packstone fault rock), over twice that of the wackestone (7 samples, 17% of wackestone fault rock) and over four times that of the algal packstone (3 samples, 11% of packstone fault rock), as a proportion of samples collected.

Cemented fault rocks are most prevalent within the wackestone. Fault breccias are most prevalent within algal packstones, which contain no deformation bands.

Cemented and cataclasite fault rocks have the lowest geometric mean permeability values, reaching as low as 10^{-4} mD and 10^{-6} mD, respectively (Figure 4-10). However, both fault rock types have a broad range of permeabilities, such that permeability varies over three orders of magnitude between cemented samples and over five orders of magnitude between cataclasite samples (Figure 4-9 & Figure 4-10). The permeability of fault breccia and deformation bands are reduced compared to the host rock permeability by a lesser degree, with the geometric mean for both fault rock types exhibiting host rock to fault rock permeability reductions of only one to two orders of magnitude. The pore destruction and occlusion that occurred during cataclasis and cementation are reflected in the HU distribution data; cataclasite in high porosity lithotypes have the lowest σ_{HU} of fault rocks within that lithotype. Cemented fault rocks have a larger σ_{HU} due to variations in the extent of cementation. In contrast, the extensional fracturing associated with fault breccia formation results in a σ_{HU} that is larger than other fault rocks and larger than the corresponding host rocks in algal packstones and wackestones.

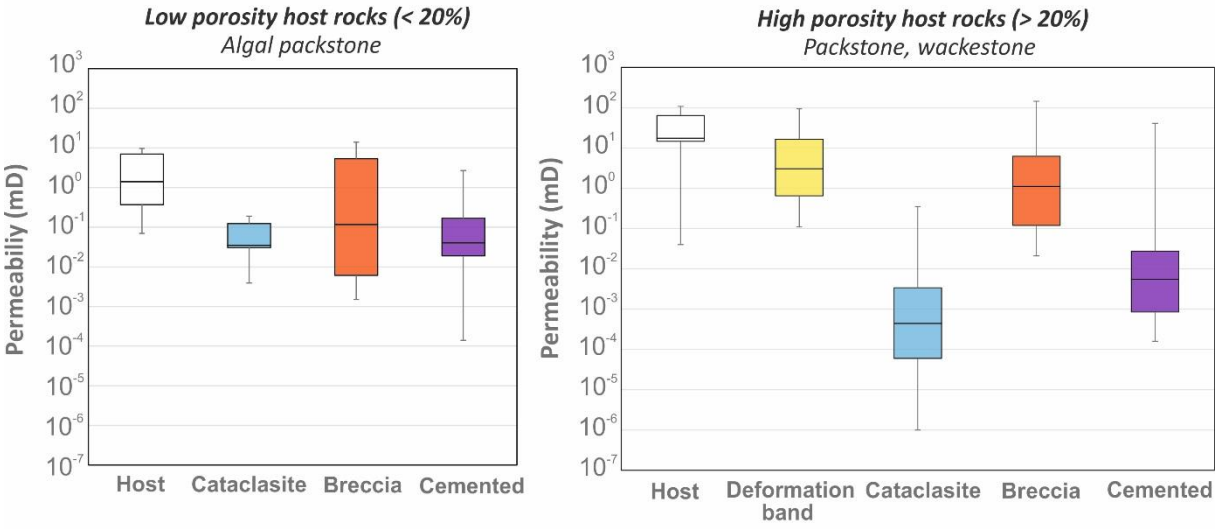

Figure 4-10: Box and whisker plots showing the permeability of each fault rock type studied in Malta derived from low porosity (<20%) host rocks (left) and high porosity (>20%) host rocks (right). The boxes represent the upper quartile, geometric mean, and lower quartile of the sampled data. The whiskers represent the minimum and maximum values from the sampled data.

Cemented samples within high porosity (>20%) lithotypes (packstones and wackestones) have the least permeability heterogeneity (σ_{logK}) of all fault rock types, which is largest in cataclasites. The heterogeneity in permeability between different cataclasite samples can be investigated by grouping each sample according to extent of cataclasis (Figure 4-11). Samples were visually grouped as follows:

(C1) minimum cataclasis, i.e. some grain fracturing, grain rotation, but overall host texture still discernible;

(C2) moderate cataclasis, i.e. fine grained matrix with large portion of survivor clasts, host texture mostly destroyed;

(C3) maximum cataclasis, i.e. minimum remnant porosity, fine grained matrix with some rounded survivor clasts. Overall host texture destroyed.

A clear relationship exists between increasing visually interpreted intensity of deformation and a reduction in both porosity and permeability, thus explaining the variability in cataclasite permeability data. The majority of C2 and C3 samples within the dataset are from low-medium throw faults (<100 m), however there is a data gap between 100 m and 200 m throw. At larger throws (>200 m), only two C2 samples and one C3 sample are recorded. In contrast, the number of C1 samples increases with increasing throw, with four samples recorded at around 200 m throw, only two samples recorded at <100 m throw, and none at <40 m throw.

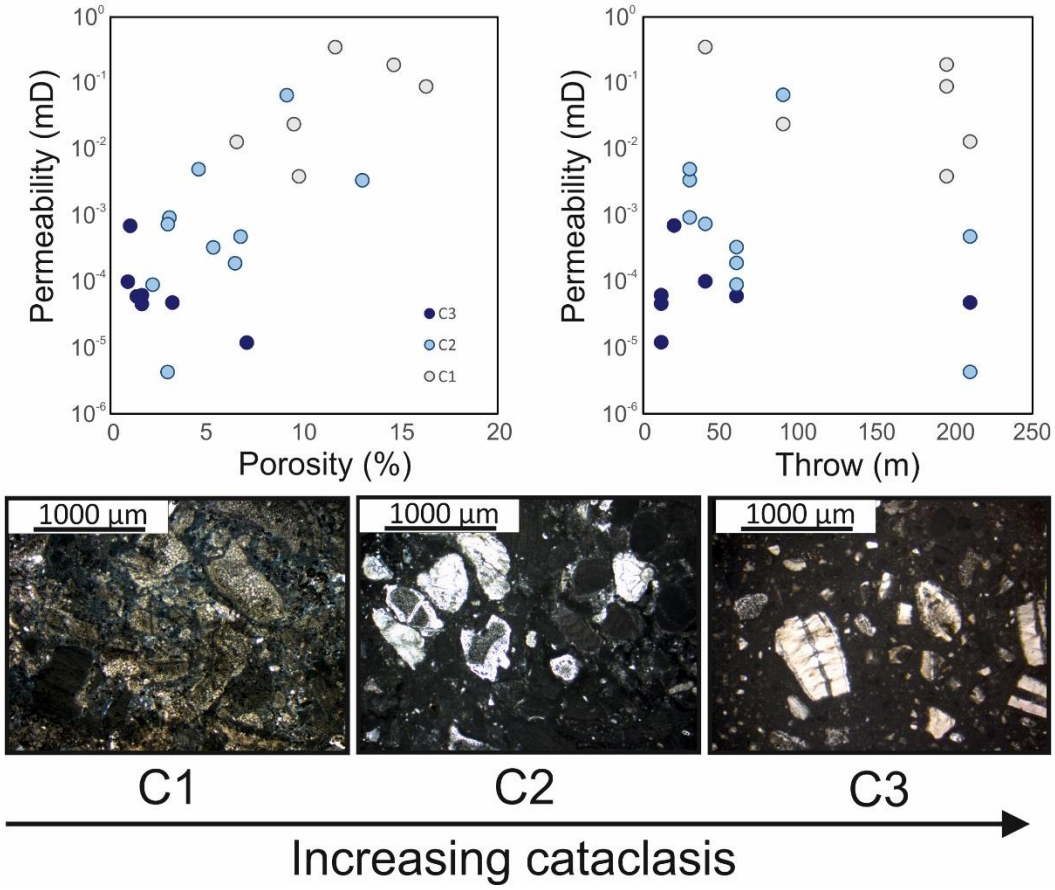

Figure 4-11: Porosity and permeability data for cataclasite samples, divided up in to 3 groups corresponding to the degree of cataclasis, increasing from C1 to C3.

4.7. Discussion

4.7.1. Fault rock heterogeneity

The fault rocks sampled within this study show variation in both textural and petrophysical properties. This is a common observation (e.g. Wibberley & Shimamoto 2003; Agosta & Aydin 2006; Michie & Haines 2016) owing to different styles of mechanical deformation throughout the fault zone (e.g. Michie *et al*. 2014) and/or differential diagenesis, which can cause fault zones to change from transmissive to sealing along strike (Laubach *et al*. 2014).

Strain is not accommodated uniformly throughout fault zones, which leads to heterogeneity in both fault rock textures and flow properties (Caine *et al.* 1996). This is in agreement with the CT and permeability data presented above, which shows that whilst fault rocks are more

texturally homogeneous than their host (Table 4-1). The permeability of fault rock is more heterogeneous than their host (Figure 4-8, Figure 4-9 & Figure 4-10), owing to the wide variety in the extent of deformation within each fault rock type. These observations indicate that fault-related deformation reduces textural heterogeneity over the core plug scale, via grain size reductions and pore occlusion, but over larger scales, fault zones are highly heterogeneous and contain a variety of different fault rock textures with different flow properties.

The heterogeneity in permeability experienced by fault rocks may be influenced by the heterogeneity of their hosts. The host packstone facies (including algal packstone) are more heterogeneous in pore size and grain size than the sampled wackestones, due to lateral stratigraphic and diagenetic variations that are typical of coralline rocks relative to pelagic sediments (Lucia 1995; Pomar & Ward 1999). This is reflected on the core plug scale, as evidenced by the high σ_{HU} recorded for host packstones relative to wackestones (Table 4-1), and is consistent with the large variation in porosity of the host packstones (Figure 4-8A). This textural and petrophysical heterogeneity appears to be retained within the fault core, with faulted packstones having greater variation in porosity and a poorer porosity-permeability correlation relative to the faulted wackestones (Figure 4-8B). This may relate to variations in the porosity and facies of packstone host rocks along individual fault zones or between different fault zones, as deformation is influenced by the host rock porosity (e.g. Zhang *et al*. 1990; Wong *et al*. 1997; Baud *et al*. 2000). Additionally, cataclasites are predominantly derived from packstones, which exhibit a large degree of porosity and permeability variation (Figure 4-11), thereby enhancing the overall packstone fault rock heterogeneity.

In general, the reduction in grain size that occurs as a result of cataclasis produces a more texturally homogenous rock, due to the destruction of pore space. Cataclasites observed in Malta are also often highly cemented, whereby the creation of freshly broken surfaces act as loci for cement precipitation, further homogenising the sample and reducing permeability by filling residual pore space (Haines *et al.* 2016). However, in some instances, fault rocks undergo a grain size reduction through cataclasis yet retain open intergranular pore space (Figure 4-11). This may be a result of varying intensities of cataclasis, the dissolution of intergranular cements, or differential fault zone cementation (Agosta & Kirschner 2003; Agosta 2008). It has been argued that differential fault zone cementation may occur when the rate of fracturing exceeds twice the rate of cement growth (Lander & Laubach 2015; Ukar & Laubach 2016), providing a potential mechanism for the lack of cementation in some cataclasites and fault breccias.

As is the case with all fault rocks, extensional fracturing may overprint the deformation related textures; fracturing may occur during later fault reactivation or through uplift and exhumation of sediments, and lead to increased permeability (Figure 4-9). Exhumation could potentially lead to the formation of fractures that could limit the extent to which outcrop samples can be used to assess how faults impact fluid flow in the subsurface. However, these effects are far less than in core samples from petroleum reservoirs, which are brought to the surface extremely rapidly resulting in sudden changes in stress and temperature (Fisher *et al.* 2018). Additionally, outcrops are subject to weathering that can alter fluid flow properties of the rock, and may not be representative of similar rocks within the subsurface. Core plug measurements are taken over a length scale of centimetres, which bypasses important flow structures within the host rock and fault zone, such as karsts, fractures, large vugs, or lateral facies variations that have broad scale controls over the permeability of a formation. The sampling method aims to address the issue of facies variation, by sampling several different areas of host rock and multiple regions of fault rock within a single fault exposure. However, it is not possible to address issues relating to the presence of void space within a rock mass. Therefore, porosity and permeability are likely underestimates of the true values, as the contribution of large vugs to porosity and the contribution of fractures to permeability in the subsurface cannot be accounted for in core analysis, even though these features may be closed at subsurface pressures. There is also likely to be a sampling bias within the core plugs, as more fractured, friable material is difficult to obtain a core plug from. Over the entire dataset, a combination of all the above factors produces greater heterogeneity on the outcrop scale and make relationships between host and fault rock properties less apparent.

4.7.2. Controls on fault rock permeability

Microscale homogenisation of rock texture through faulting and fault-zone diagenesis results in an overall reduction in permeability (Figure 4-9). Fault-zone diagenesis refers to cement accumulation that could be derived locally (Hadizadeh 1994) or as a result of fault-related fluid flow (Agosta & Kirschner 2003). The potential for this textural homogenisation is inherently a product of the initial host rock texture; high host porosities and permeabilities at the time of faulting (e.g. packstones) often allow for cataclasis and resulting pore collapse, which results in textural homogenisation and permeabilities as low as 10^{-6} mD (Figure 4-10). These low permeabilities correspond to permeability reductions from host to fault rock of up to eight orders of magnitude, but reductions of three to four orders of magnitude are more typical (Figure 4-12).

In the high porosity wackestone lithofacies, changes in the pore structure from host to fault rocks are principally related to cementation, as cataclasis is not a prevalent deformation mechanism in these rocks. This may relate to the initial composition of the host rock (Table 4-1); the sediment is composed of fine grained, rounded *Globigerina* foraminifera, which are resistant to grain-scale cataclasis at such shallow burial depths (Michie *et al.* 2014). Therefore, faulting favours the generation of extensional fractures, in addition to lenses of fault breccia that creates dilation sites for cement precipitation. Despite the lack of cataclasis, permeabilities of 10^{-6} mD are also recorded in these samples, corresponding to host to fault permeability reductions of up to seven orders of magnitude, but reductions of three to four orders of magnitude are more typical (Figure 4-12).

In contrast, host rocks with lower porosity (<20%) have little potential for pore destruction under the relatively low effective stresses that these rocks experienced during faulting. These rocks tend to favour brittle failure through extensional fracturing and brecciation. Diagenetic alteration may occlude pore spaces, which reduces permeability to as low as 10^{-4} mD, but the potential for permeability reductions is less than for rocks with a high initial porosity. Therefore, the resultant fault rocks examined within this study do not exhibit permeability reductions of over four orders of magnitude, and typically permeability is only reduced by around one order of magnitude (Figure 4-12).

The data collected during this study indicate that the potential for low permeability fault rocks in shallow, extensional settings is more likely a result of the initial host rock properties than the amount of throw; high and low permeability fault rocks can occur at a range of fault throws (Figure 4-8D). In this study, cementation is one of the key factors that influences fault rock permeability. Cements that are externally derived through fault zone fluid flow are likely to be independent of displacement, such that fault rock permeability can be reduced at any displacement. However, all faults included in this study had >10 m displacement. At throws below this, throw may play more of a control on the extent of cataclasis. However, displacement has been shown to be an important control on architectural parameters such as fault rock thickness (Shipton *et al.* 2006) and fault rock continuity (e.g. Micarelli *et al.* 2006; Cooke *et al.* 2018). Previous studies from Malta have also suggested an increase in fault rock heterogeneity with increasing fault displacements (Michie & Haines 2016; Michie *et al.* 2017), which is in agreement with the increased variability in cataclasite permeability at higher displacements (Figure 4-11). Additionally, the continuity of low permeability fault rock products (i.e. cataclasite), has been

shown to be greater with increasing fault displacement (Cooke *et al.* 2018). This means that the bulk fault core permeability is a product of displacement, even if the permeability of the fault rocks within that fault core is not.

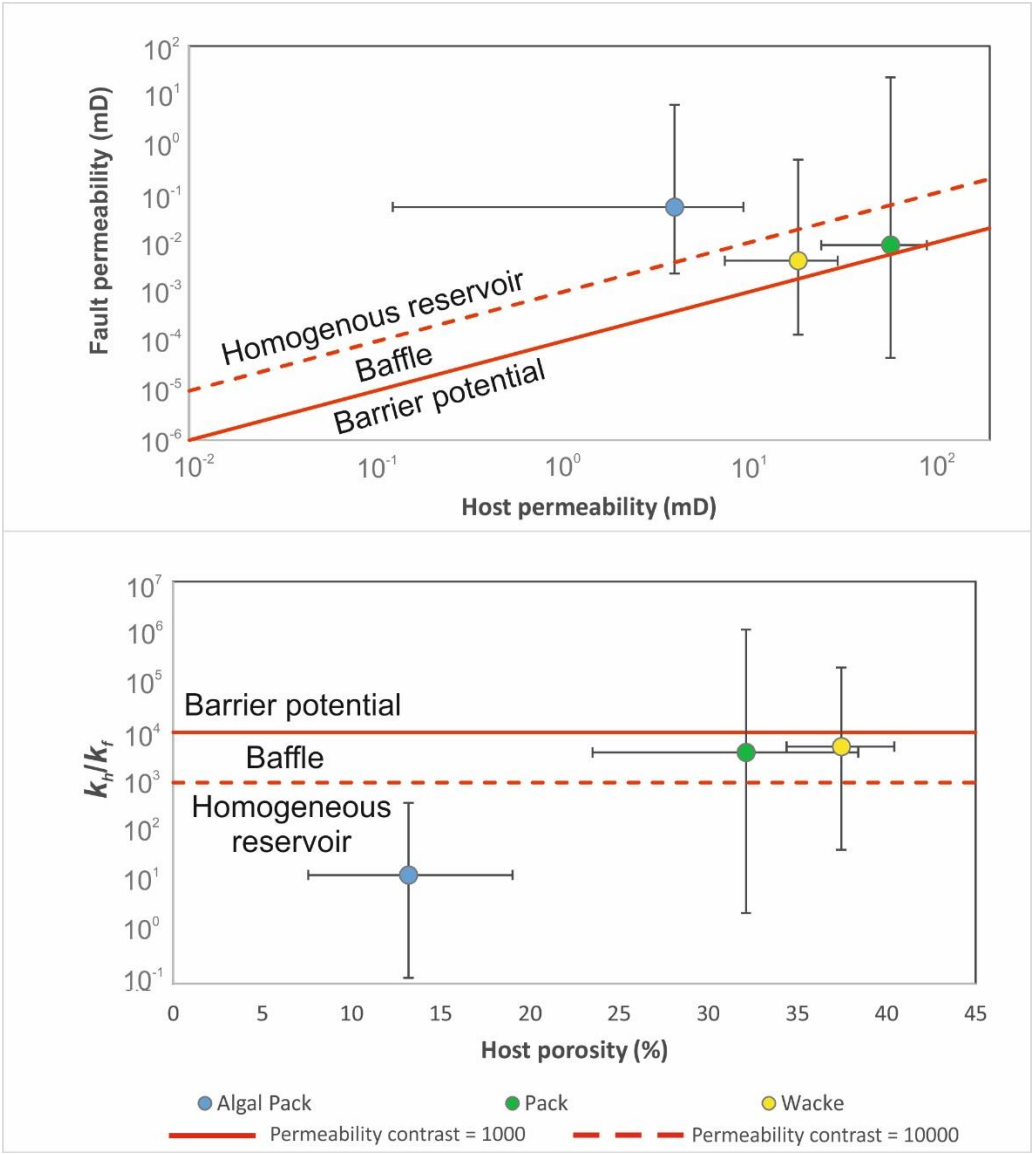

Figure 4-12: Top) Geometric mean of fault rock permeability plotted against the geometric mean of host permeability for each studied lithofacies. Bottom) Geometric mean of the contrast between fault rock sample permeability and corresponding average host rock permeability values plotted against the arithmetic mean of the host porosity. In both plots, the error bars indicate the 90th percentile range and the red lines represent the permeability contrast required for fault rock to impact fluid flow over production scales, either as a baffle to fluid flow (dashed line, >10^3), as a barrier to fluids (solid line, >10^4).

4.7.3. Implications for across fault fluid flow

Previous field observations of Maltese fault zones suggest that the sampled fault rocks are often either very thin (several centimetres in thickness), or are present only in discrete, discontinuous lenses (Michie *et al.* 2014; Cooke *et al.* 2018). In other words, although the fault zones may contain fault rocks with permeabilities that are sufficiently low to act as barriers to flow, they also have regions where fault rock permeability is high or patches where fault rock is absent (Michie & Haines 2016). Fault rock permeability data must be combined with information on the distribution of fault rock when estimating the overall across-fault fluid flow potential of any of these fault zones. Nevertheless, it is important to be able to predict the properties of fault rock that are present within a fault zone.

There is likely to be a large degree of heterogeneity in fault core permeability (Table 4-2; Figure 4-10 & Figure 4-12), assuming a continuous fault core composed of a mixture of fault rock products, as is typical of fault zones in Malta (Michie 2015) and other carbonate lithologies (e.g. Bastesen & Braathen 2010). An estimate of the bulk fault zone permeability is provided by the area-weighted arithmetic average permeability (Manzocchi *et al.* 1999). This is only possible with a joint understanding of fault zone architecture (i.e. the area of each fault zone element within a given fault zone) and the permeability of each of the fault zone elements, which is best calculated using the geometric mean permeability of all samples from that element. Therefore, the geometric mean is utilized for averaging fault rock permeability below.

Based upon pressure drawdown curves for a well near a partially communicating fault, Yaxley (1987) shows that for a sealing fault, a specific transmissibility ratio,α, of 0 is required:

$$\alpha = \left(\frac{k_f}{k_h}\right) \Big/ \left(\frac{l_f}{b}\right)$$

where, k_h and k_f correspond to the host and fault permeability, respectively, l_f is the thickness of the fault, and b is the distance between the well and the fault. For a fault to have a detectable impact on fluid flow over production timescales (i.e. fault behaves as a baffle to fluids, whereby the rate of across-fault fluid flow is reduced), a specific transmissibility ratio of <1.0 is required, and for a fault to be close to sealing (i.e. capable of supporting a hydrocarbon column over geological time), a ratio of 0.01 to 0.001 is required.

Threshold permeability contrast values, corresponding to the ratio of fault permeability to host permeability at which faults behave as a barrier or baffle to fluid flow, can be selected by plotting the permeability contrast for different specific transmissibility ratios, as a function of distance between an active well and assuming a fault core of 1 m thickness (Figure 4-13A). Using these relationships, it can be argued that a permeability contrast of >*c.* 10^3 is required for a fault to have a detectable impact on fluid flow ($\alpha < 1$) at distances >500 m from the well. At this distance, permeability contrasts must be greater than *c.* 10^5 for a fault to be close to sealing ($\alpha = 0.01$). These threshold values will vary depending on the distance to the fault and the thickness of the fault core. The control of fault thickness on this threshold permeability contrast can also be highlighted, assuming a distance between the well and fault of 1000 m (Figure 4-13B). The threshold permeability contrast required for a sealing fault reduces as fault thickness increases. For fault core thickness >1 m, a permeability contrast >10^4 is sufficient for a fault to have a significant impact on fluid flow (i.e. across fault fluid flow is prevented over production timescales). For fault core thickness of 0.1 to 1 m, this value tends towards 10^5. Faults with thicknesses below this range require greater permeability contrasts for the fault to significantly impact fluid flow. These relationships can be used to determine whether a fault rock can be classed as a baffle to fluid flow or as a barrier over production timescales; for a fault core that is 1 m thick, at a distance of 1000 m from a well, a fault core permeability reduction relative to the host rock of >10^3 is considered a baffle to fluid flow, and a permeability contrast of >10^4 is considered as having the potential to act as a significant barrier to fluid flow on production timescales. Permeability reductions of <10^3 are considered to have little to no impact on fluid flow within the drainage radius of the well. This range of permeabilities is thus termed the *homogeneous reservoir* for this study (comparable to a homogeneous reservoir with no fault).

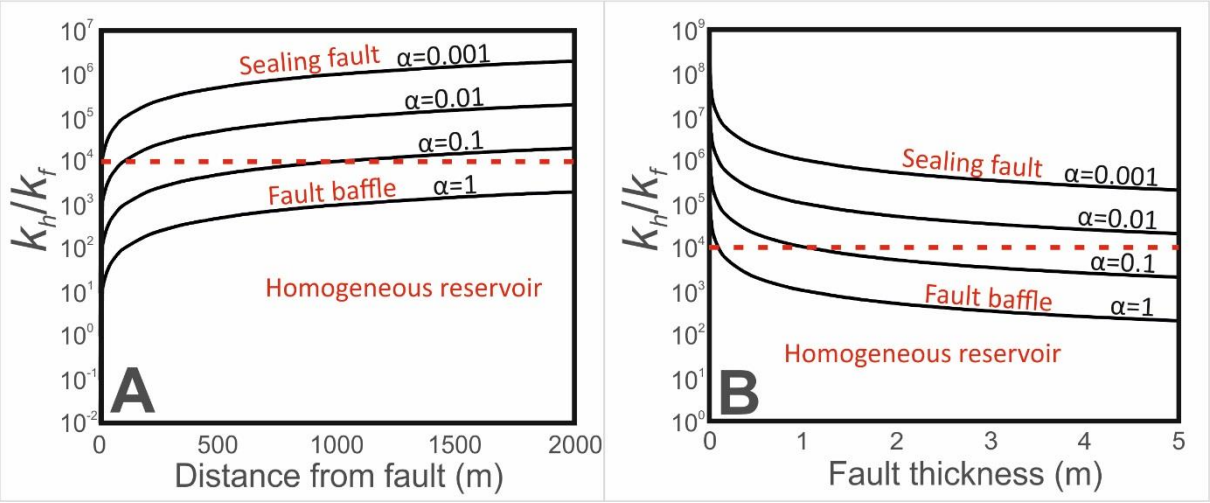

Figure 4-13: Permeability contrast (host permeability/fault permeability) as a function of the distance of an active well to a fault of 1 m thickness (A) and as a function of the fault thickness for a fault 1000 m away (B), calculated for faults of different transmissibilities, as defined by different specific transmissibility ratios, α. The red dashed line represents a permeability contrast of 10^4, which is utilised in this study as a general rule to determine whether a fault has potential to act as a barrier to fluids over production timescales.

Fault rocks within the presented dataset that exhibit a permeability contrast large enough to act as a baffle to fluid flow are derived from host rocks with a high initial porosity (>20%; i.e. packstones and wackestones; Figure 4-12). However, whilst the geometric mean permeability from these fault rocks are low enough to fall within this zone, there is still a range of fault rock values that have negligible impact on fluid flow. Around 30% of fault rocks from wackestones have permeability reductions of four orders of magnitude compared to their hosts; 60% of wackestone fault rocks have a permeability reduction of over three orders of magnitude (geometric mean permeability contrast for all wackestone fault rocks = $5x10^3$ mD). Around 30% of faults in packstones have permeability reductions of four orders of magnitude compared to their hosts and around 41% of these faults have a permeability reduction of over three orders of magnitude (Figure 4-14). This suggests that fault cores from both high porosity lithotypes (packstones and wackestones) have the potential to behave as a baffle to fluid flow on a production time-scale. Permeability reductions in high porosity carbonate rocks are commonly reported in studies of deformation bands (e.g. Tondi 2007; Rath *et al*. 2011; Rotevatn *et al*. 2016; Kaminskaite *et al*. 2019) and in fault cores (e.g. Micarelli *et al*. 2006). However, these fault core permeability

reductions are not as severe due to the pervasive cementation in the lowest permeability fault rocks reported here.

Permeability reductions in the lowest porosity (<20%) and permeability (<10 mD) host samples (algal packstones) do not exceed 10^3, with a geometric mean corresponding to only one order of magnitude permeability reduction. Some fault rocks have permeabilities that are higher than their hosts. This is common in carbonate fault rocks formed from low permeability host rocks, due to the brittle nature of deformation (e.g. Géraud *et al.* 2006; Ran *et al.* 2014); such fault rocks are likely to be transmissive.

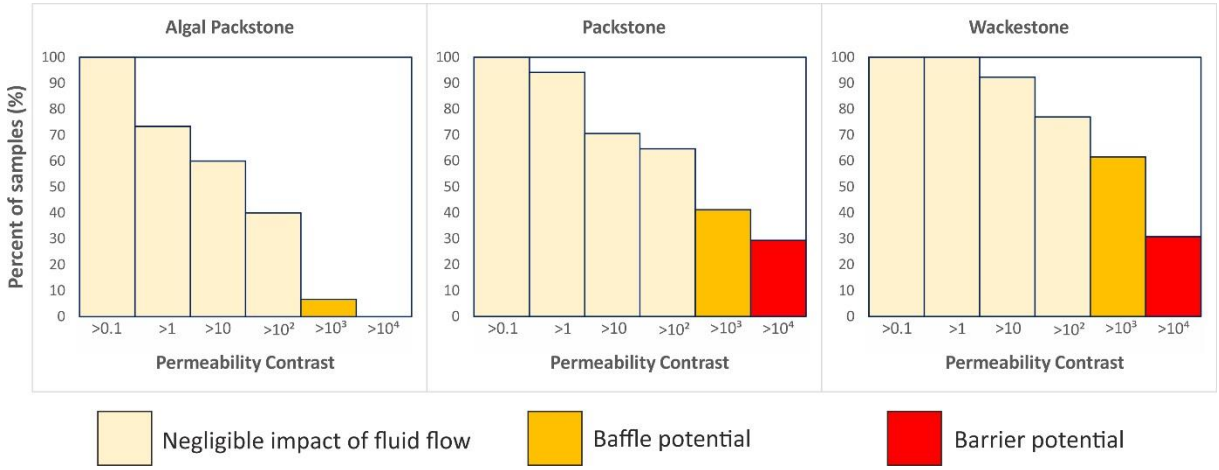

Figure 4-14: Proportion of fault rock samples from each lithotype that exhibit a given host to fault rock permeability contrast, shown by normalised frequency histograms.

Overall, it appears that significant barriers to fluid flow resulting from the presence of carbonate fault rocks are only present in formations that have host rock with a permeability of >10 mD and a porosity of >20% (Figure 4-12). However, under these conditions, 40 to 60% of fault rocks will have negligible impact on across fault fluid flow. Additionally, fractures cross cutting a low permeability fault core will also reduce the impact that the faults will have on fluid flow, but are difficult to predict. These results may be useful when considering carbonate-hosted fault rocks from similar lithologies and settings, by highlighting the potential ranges in fault rock permeability and the heterogeneities exhibited within these fault zones. However, additional work is required to achieve more global relationships between host and fault rock properties, which can aid the prediction of fault behaviour in carbonates.

4.8. Conclusions

Samples from three faulted lithotypes in Malta were analysed to determine the porosity and permeability heterogeneity within host, damage zone, and fault core. The lithotypes consisted of bioclastic packstones, algal packstones, and pelagic wackestones. Core plug X-ray tomography and permeability variability indicates that heterogeneity is retained within the fault zone; packstones are the most heterogeneous host rock, which exhibit the most heterogeneous fault cores, and vice versa for wackestones. Gas permeability measurements show that permeabilities as low as 10^{-6} mD are possible in the studied formations (shallowly buried, high porosity packstones and wackestones); the lowest permeability fault rocks being either cataclasite or cemented fault rocks, which exhibit the greatest degree of textural homogenisation relative to the host rock. Fault rock permeability does not appear to be controlled by the amount of throw, however the heterogeneity between cataclastic fault rock permeabilities on the outcrop scale increases with increasing fault throw.

Host rock to fault rock permeability contrasts of 10^3 are considered to act as a baffle to fluid flow over production timescales. Permeability contrasts of 10^4 are considered to have production timescale sealing potential in hydrocarbon reservoirs. Of the three studied lithotypes, only fault rocks derived from high porosity host rocks (bioclastic packstones and pelagic wackestones) show permeability contrasts high enough for them to act as effective barriers to fluid flow on a production time-scale. Of these samples, 40 - 60% are shown to have some recognizable control of fluid flow over production timescales.

The permeability of fault rocks measured during the current study suggest that they have the potential to act as significant barriers to fluid flow. However, the distribution of these low permeability fault rocks must also be taken into account when assessing how faults will impact fluid flow in the subsurface. Further work needs to be undertaken to understand the control of host rock porosity and texture on fault rock permeability and heterogeneity in other porous carbonate lithologies.

4.9. Acknowledgements and funding

This paper contains work conducted during a PhD undertaken as part of a Natural Environmental Research Council (NERC) studentship [studentship number 1652295]. We also thank Wintershall, ENI, Petrobras, OMV and ADNOC for project funding and support. Additional thanks goes to Dr

Sam Allshorn and Dr Carlos Grattoni for technical support, and two anonymous reviewers for their thorough reviews.

CHAPTER 5.

Implementing fault rock permeability and continuity into geocellular modelling of porous carbonate-hosted fault zones

Prepared for journal submission.

5.1. Abstract

Current fault seal analysis workflows are unable to predict the impact of faults in carbonate rocks because there is insufficient data on key parameters such as fault permeability and fault thickness. To fill this knowledge gap we present predictive relationships between fault throw, host porosity and host permeability, and fault rock continuity, thickness and permeability, in shallowly buried limestones from Malta. These relationships are used to populate geocellular models with fault properties. Fault rock continuity measurements, which show increasing fault rock continuity with increasing throw until a continuous fault core is achieved at 30 m throw, are implemented along with fault thickness estimates to simulate discontinuous fault cores at low throws. Host to fault rock permeability contrasts are used to predict the permeability of different fault rock types based upon the porosity of the protolith. Fault rock continuity and thickness measurements are used to predict fault rock distributions within a fault core at a given throw. Together, these relationships are used to predict bulk fault core permeability for a fault of known throw cutting a lithofacies of known porosity and permeability. These algorithms are utilised for fault transmissibility analysis in a geocellular model of Gozo, Malta. The algorithms predict that faults in these formations would have negligible impact on fluid flow at reservoir conditions unless each fault rock fabric is continuous within the fault core. In porous type III carbonate reservoirs, it is shown how faults would have a greater impact on fluid flow, assuming fractures do not cut the fault core. A database that includes a variety of carbonate lithofacies from a variety of settings is required to predict fault permeability in a more generalised manner. However, the methods used in this study outline relationships that could be further developed to aid carbonate fault seal analysis.

5.2. Introduction

Carbonate-hosted fault zones are commonly assumed to be either transmissive or behave as conduits to fluid flow in the subsurface, due to their typically brittle behaviour. This is despite a number of studies reporting low permeability carbonate-hosted fault rocks (e.g. Agosta *et al.* 2007; Michie & Haines 2016; Tondi *et al.* 2016; Kaminskaite *et al.* 2019) and several studies reporting production-scale sealing behaviour of faults in porous carbonate reservoirs (e.g. Acevedo 1980; Kosters *et al.* 1989; Hussain 1993; Jakobsen *et al.* 2005; Barkved *et al.* 2016). However, outcrop studies generally show that it is common for porous carbonate-hosted fault zones to exhibit a variety of fault rock microstructures (Bastesen & Braathen 2010; Michie 2015; Cooke *et al.* 2018), which can lead to a wide range in permeability along a single fault core (Michie & Haines 2016). This means that it is difficult to predict the impact of fault cores in porous carbonates on subsurface fluid flow.

In porous carbonates, strain is commonly localised along a fault core, forming cataclasite or fault gouge (e.g. Micarelli *et al.* 2006; Cooke *et al.* 2018; Ferraro *et al.* 2018). The processes by which these are formed include granular disaggregation (i.e. grain translation), intragranular extensional fracturing (IEF), grain chipping, and pressure solution. These mechanisms lead to a reduction in grain size and an increase in intergranular cements, thereby reducing porosity and permeability relative to the host rock (Micarelli *et al.* 2006; Agosta *et al.* 2007; Matonti *et al.* 2012; Michie & Haines 2016; Cooke *et al.* 2018). Additionally, fault breccia and recrystallised or cemented fault rocks are observed in porous carbonate fault zones (Michie 2015; Cooke *et al.* 2018). Fault breccia is described as a fault rock composed of clasts of host or deformed rock supported by a matrix of either cement, fine grained material, or a fracture mesh. The degree of clast rotation and fragmentation typically increases with increasing deformation (Woodcock & Mort 2008), and has been shown to have some bearing on the resultant permeability (Michie & Haines 2016). Cemented and recrystallised fault rocks typically exhibit permeability reductions relative to the host rock, due to the occlusion of the intergranular pore space (Cooke *et al.* 2019). Additionally, it is common for strain to be accommodated by the formation of deformation bands, either within the damage zone of a fault (e.g. Antonellini *et al.* 2014; Rotevatn *et al.* 2016; Cooke *et al.* 2018), or as part of a wide shear zone that lacks a localised fault core (e.g. Tondi *et al.* 2016; Kaminskaite *et al.* 2019). Deformation bands form via the same mechanisms as cataclasite, but to a lesser degree of deformation.

In siliciclastic rocks, the effect of faulting on fluid flow is well documented (e.g. Knipe 1997, 1992; Fulljames *et al.* 1997; Hesthammer & Fossen 2000; Fisher & Knipe 2001; Fisher *et al.* 2001; Yielding 2002; Bretan *et al.* 2003; Brown 2003; Flodin *et al.* 2005; Færseth 2006; Jolley *et al.* 2007). This has led to the advent of predictive tools that can be implemented within routine fault seal analysis, predicting the clay content of the fault core from clay-rich sequences (Yielding *et al.* 1997). These tools can then be used to derive fault permeability and hence hydrocarbon column height, from empirical relationships obtained from laboratory analysis of fault rocks (e.g. Sperrevik *et al.* 2002) or calibration with exploration data (e.g. Yielding 2002; Bretan *et al.* 2003). The predicted fault permeability can be used to calculate transmissibility multipliers when combined with scaling-relationships between fault thickness and throw. Transmissibility multipliers are applied to faulted cell connections in a reservoir model to take into account the effect that faults have on across-fault fluid flow (Manzocchi *et al.* 1999). Whilst the current methods of fault permeability prediction may be of use in carbonate-shale sequences to predict clay smearing, they are not applicable to fault zones in pure carbonate sequences.

The distribution of fault rocks is also a key parameter when predicting bulk fault permeability. Fault rock distributions can be quantified by fault rock thickness (FRT) measurements and fault rock continuity (FRC) estimates. FRT is typically accounted for through scaling relationships with fault throw, derived from empirical databases (e.g. Hull 1988). However, as with permeability, there is a great deal of heterogeneity in fault core thickness (Shipton *et al.* 2006; Cooke *et al.* 2018; Sosio De Rosa *et al.* 2018). The amount of fault rock coverage along the fault zone represents an estimate of FRC, and is expressed as a ratio of total exposure length to the total length of exposed fault rock (Cooke *et al.* 2018). Previous studies of FRC have provided different values of fault throw at which fault cores become continuous (Micarelli *et al.* 2006; Michie *et al.* 2014; Bauer *et al.* 2016; Cooke *et al.* 2018), suggesting there are additional controls on continuity to throw.

Efforts towards a method of predicting fault permeability in carbonate rocks are limited. A number of case studies from outcrops present petrophysical data on carbonate fault rocks (e.g. Billi *et al.* 2003; Micarelli *et al.* 2006; Agosta *et al.* 2007; Jeanne *et al.* 2012; Bauer *et al.* 2016; Delle Piane *et al.* 2016; Tondi *et al.* 2016), but few of these studies attempt to upscale this data to an overall fault permeability (e.g. Matonti *et al.* 2012; Michie *et al.* 2017). To date, only one study attempts to derive predictive relationships for fault permeability based upon input parameters that would be available from seismic and core (Michie *et al.* 2017). These relationships are based

upon the observed heterogeneity in fault core permeability in two formations of the Maltese stratigraphic sequence. The relationships suggest that when a grain-dominated or micrite-dominated lithofacies is self-juxtaposed by a fault, a homogenous fault core can be expected, each with distinctive deformation mechanisms. The permeability of this fault core decreases with increasing throw. A heterogeneous, permeable, fault core can be expected when the two lithofacies are juxtaposed against each other, which becomes increasingly heterogeneous and permeable with increasing throw. However, these predictions are based upon relationships from a limited number of fault zones and formations, thereby requiring additional data to calibrate the model.

This work aims to establish new generalised predictive algorithms for fault core thickness and fault permeability of the Maltese stratigraphy. Fault permeability predictions are based upon upscaling fault rock distribution and permeability data from a series of normal faults in Malta (Cooke *et al.* 2018, 2019). Upscaled fault permeability presented by Michie *et al.* (2017) is used to test the fault permeability algorithm. Traditional fault core thickness relationships are updated with FRC corrections to simulate the effect of discontinuous fault cores. The two algorithms are applied to a reservoir simulation model based on the island of Gozo, Malta, showing the effect of these algorithms on production. Additionally, a simple reservoir model is used to show how this might differ in a fractured porous reservoir. This work provides a basis for future work towards accurately predicting the across-fault flow potential of faults in porous carbonates.

5.3. Study area

Data were obtained from four carbonate formations exposed at eight different fault zones across the islands of Malta, located in the central Mediterranean (Figure 5-1). Malta is composed of a 300-1000 m thick sequence of Oligo-Miocene age carbonates, which are well exposed and have undergone limited post-burial diagenetic alterations (Haines *et al.* 2015). Maximum burial depths have been estimated to range from 300 – 1000 m (Dart *et al.* 1993; Kim *et al.* 2003). The sampled formations consist of algal packstones, packstones, and wackestones, which are described in the following section and highlighted in Figure 5-1.

5.4. Stratigraphic framework

The oldest exposed formation is the Chattian aged Lower Coralline Limestone (LCL), which is a shallow water bioclastic limestone that is subdivided into the Maghlaq member (not sampled),

comprising inner ramp wackestones and mudstones, the Attard member, comprising inner-middle ramp facies rhodolitic algal packstones, the Xlendi member, comprising shoal facies bioclastic packstones and biosparites, and the Il-Mara member (not sampled), comprising outer ramp facies wackestones (Pedley 1978; Brandano *et al.* 2009b, a). The LCL is capped by a hardground, which is overlain by the Aquitanian to Serravallian age Globigerina Limestone (GL). The GL is subdivided in to the Lower, Middle and Upper GL members, each of which are separated by a phosphoric conglomerate layer. The GL comprises fine-grained, pale yellow-cream biomicritic wackestones, rich in *Globigerina* foraminifera, representing a pelagic outer shelf environment (Pedley 1978; Pedley & Bennett 1985; Dart *et al.* 1993). Overlying the GL is the Blue Clay formation, comprising light to dark grey marls with up to 30% carbonate and 75% phyllosilicate content (John *et al.* 2003). The top of the Blue Clay is marked by a transitional boundary with the Greensand formation, which is often absent or thin (<10 m) and consists of glauconitic marly limestone (Pedley *et al.* 1976). The youngest formations in Malta are the Tortonian to Messinian age Upper Coralline Limestone (UCL), which has numerous lateral facies variations and is subdivided in to the Ghajn Melel member, comprising shallow water biomicrites, biosparites and biosparrudites, the Mtarfa member, comprising coralline algal biostrome facies wacke-packstones, the Tal-Piktal member, comprising coral and algal patch reef facies packstones, and the Gebel Imbark member, comprising shallow water, intertidal facies wackestones and packstones with white terrigenous clay beds representing subaerial events (Pedley 1978; Bosence & Pedley 1982; Dart *et al.* 1993).

5.5. Fault zones

Malta is characterised by a series of normal fault zones, striking either ENE-WSW or WNW-ESE. These faults formed from the late Miocene onwards as a response to N-S extension during crustal extension in the foreland of the Maghrebian-Apennine fold and thrust belt (Illies 1981; Dart *et al.* 1993). The fault zones in this study range in throw from 10-200 m and are predominantly normal, with a minor dextral oblique component to slip in Gozo. The higher throw faults juxtapose the youngest (UCL) and oldest members (LCL and GL) of the Maltese stratigraphic sequence, generating a wide fault zone containing a thick clay smear derived from the Blue Clay formation. The style of deformation within Maltese fault zones has been shown to be partially a product of the juxtaposed lithofacies; lower porosity formations, such as the algal packstone Attard member, and the mechanically weak wackestones, such as the GL, commonly host a distributed style of deformation, resulting in multiple anastomosing slip surfaces. Deformation in these rocks occurs

through extensional fracturing and fault breccia formation (Michie *et al.* 2014; Cooke *et al.* 2018). Contrastingly, more localised slip surfaces are observed in the higher porosity, grain-dominated formations (Cooke *et al.* 2018). Strain localisation in these higher porosity formations occurs through cataclasis, the formation of polished slip surfaces, and deformation band arrays in the damage zone. Diagenesis is a common feature of all fault zones, which leads to reduced porosity and permeability of fault rocks and the immediate vicinity of the fault zone.

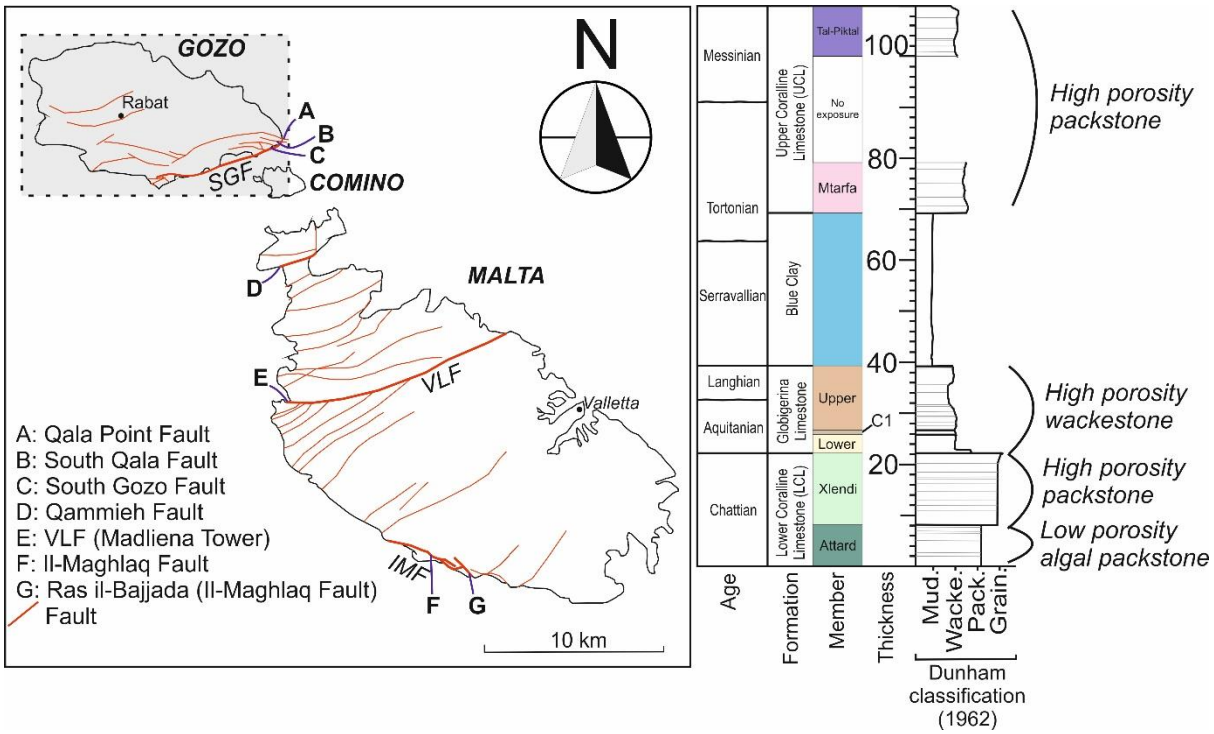

Figure 5-1: Map of the Maltese archipelago, highlighting all major faults. The greyed area represents the area used for the geocellular model. The stratigraphic sequence in the region of study sites A-C is shown on the right. After Cooke et al. (2018).

5.6. Methodology

5.6.1. Data sources

Fault rock continuity data

Fault rock continuity (FRC) data was obtained from 8 fault zones in Malta, representing the continuity of the fault core as a whole, rather than specific fault rock types. FRC measurements were undertaken according to the methodology outlined for fault rock continuity estimates in

Cooke *et al.* (2018). The data show that fault cores in Malta are discontinuous below 30 m, and are near continuous above this. A clear relationship between increasing fault throw and increasing fault core continuity up to around 30 m exists, after which FRC is *c.*1 (Figure 5-2).

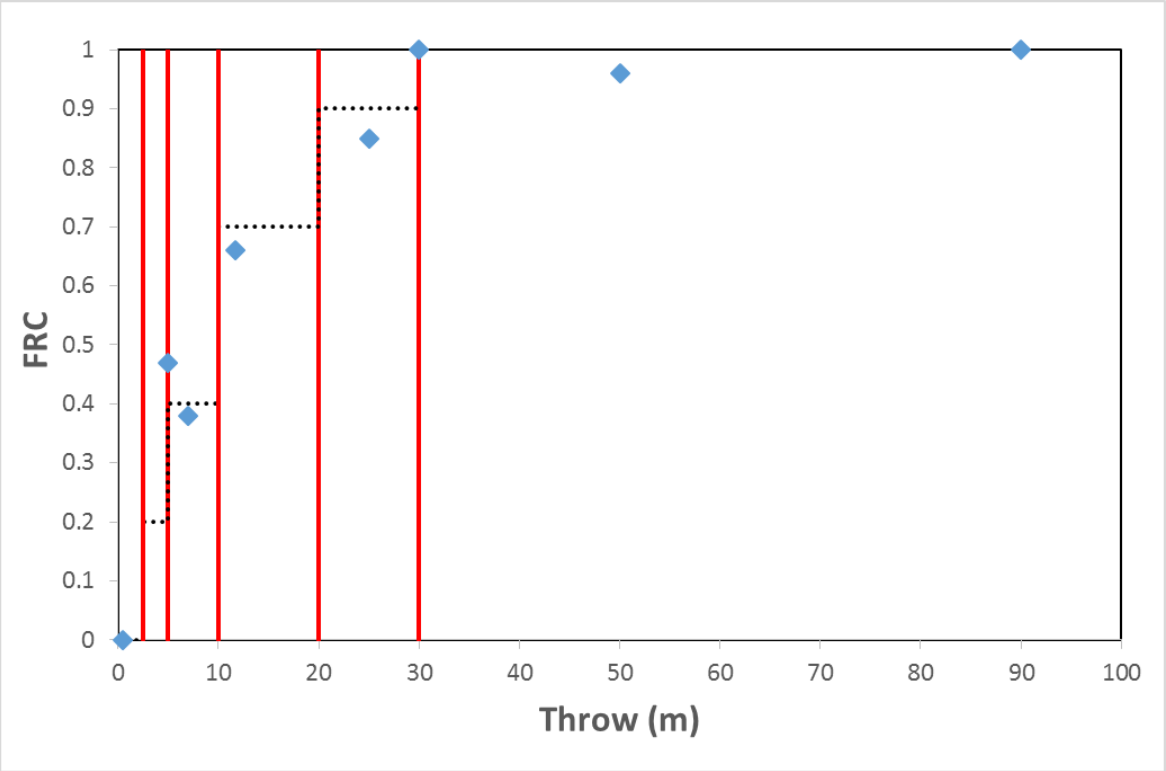

Figure 5-2: Fault rock continuity as a function of throw for 8 fault zones in Malta. The red lines represent arbitrary boundaries for discretised regions of fault rock continuity, represented by the percentages of fault rock coverage in each region.

Fault rock permeability data

The petrophysical data reported by Cooke *et al.* (2019) provides a rich dataset for both host and fault rock permeability (Figure 5-3). The fault rock data represent a mixture of fault rock types from within the fault zone, aiming to capture a representative portion of the fault rocks present. Permeability data were grouped according to numerous attributes, such as the host lithofacies, the architectural unit of the fault zone, the fault rock type, fault throw etc., in an effort to determine key relationships between host and fault rock properties.

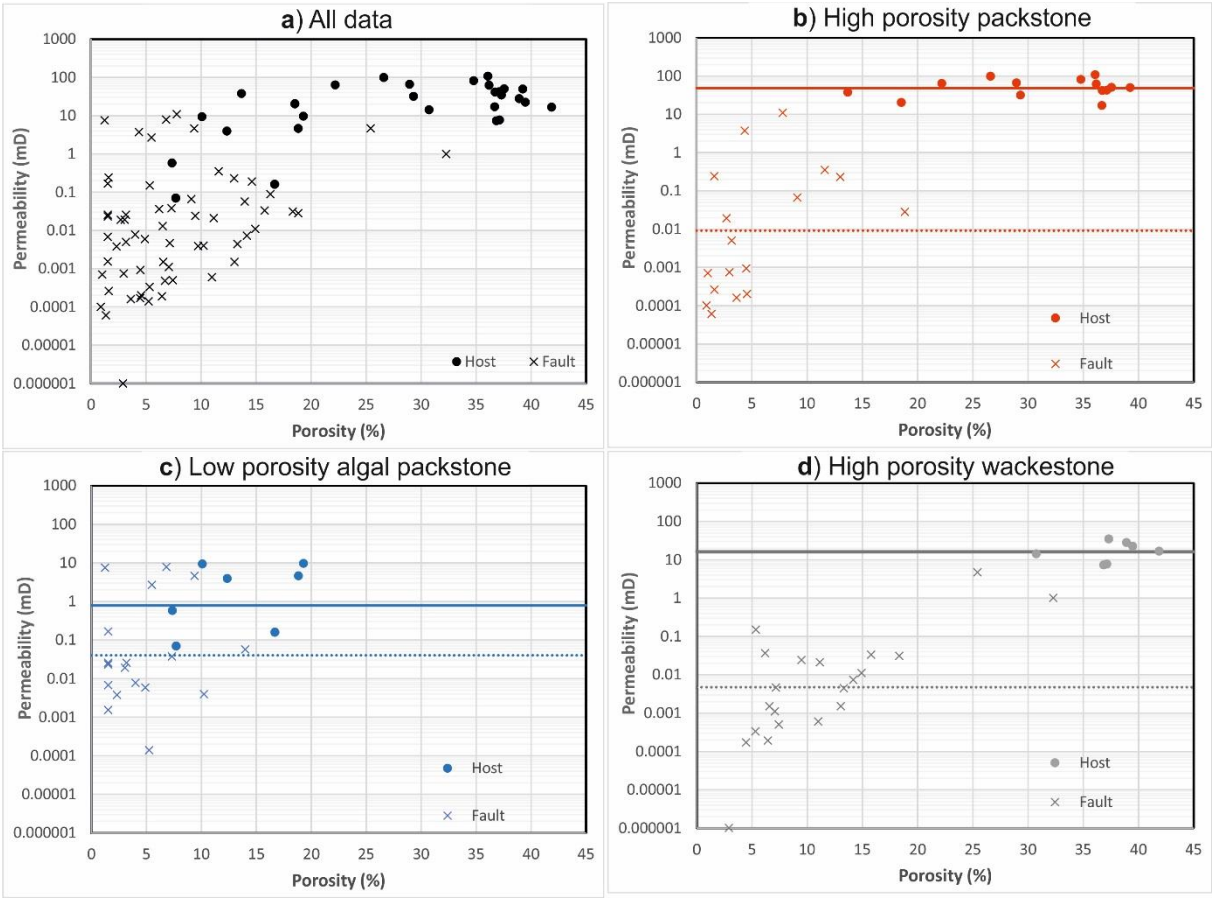

Figure 5-3: Poroperm distributions for three different lithotypes, presented in Cooke et al. (2019). Solid and dashed lines represent the geometric average host and fault rock permeability, respectively.

5.6.2. Upscaling continuity and permeability

The key properties used to calculate transmissibility multipliers in geocellular models are fault permeability and fault zone thickness (Manzocchi *et al.* 1999). The following subsections describe how the above data were upscaled to predict these properties in a structural framework model.

Permeability

Cells within a geocellular model are typically on the order of 100 m wide, such that a single cell is representative of the scale of most fault zone outcrops used for this study. A connection between a pair of cells juxtaposed at a fault will require a single bulk permeability value to represent a highly heterogeneous fault zone composed of numerous fault zone elements. Therefore, a form of upscaling or averaging of the sub-cellular properties that retains geological accuracy must be

used. Prior to this averaging, the permeability of the sub-cellular elements must be predicted (Manzocchi *et al.* 1999; Sperrevik *et al.* 2002; Michie *et al.* 2017).

The method of averaging subcellular fault zone elements must be selected to best represent realistic fault rock distributions. The arithmetic average permeability is representative of the bulk permeability of several flow-parallel layers; in a fault zone this represents a continuous fault core with variable permeability up/along the fault (Figure 5-4a). The harmonic average permeability is representative of the bulk permeability of several flow-perpendicular layers; in a fault zone this represents a fault core composed of continuous tabular layers of fault rock parallel to the fault surface (Figure 5-4b). The geometric mean represents the bulk permeability of a heterogeneous medium; in a fault zone this represents a fault core with variable permeability up/along the fault, in addition to throughout the thickness of the fault core (Figure 5-4c). The proportion of each type of fault rock in a fault zone can be used as a weighting which, together with the permeability of that fault rock, can be used to calculate a weighted average permeability. For the arithmetic average, weights correspond to the cross-sectional area of each fault rock type (Figure 5-4a). For the harmonic average, weights correspond to the thickness of each fault rock layer (Figure 5-4b). For the geometric average, weights correspond to a combination of cross sectional area and thickness of each fault rock type, corresponding to a volume-weighted average permeability. It follows that the fault zone architecture and distribution of fault zone elements determines the most suitable method of averaging (Manzocchi *et al.* 1999).

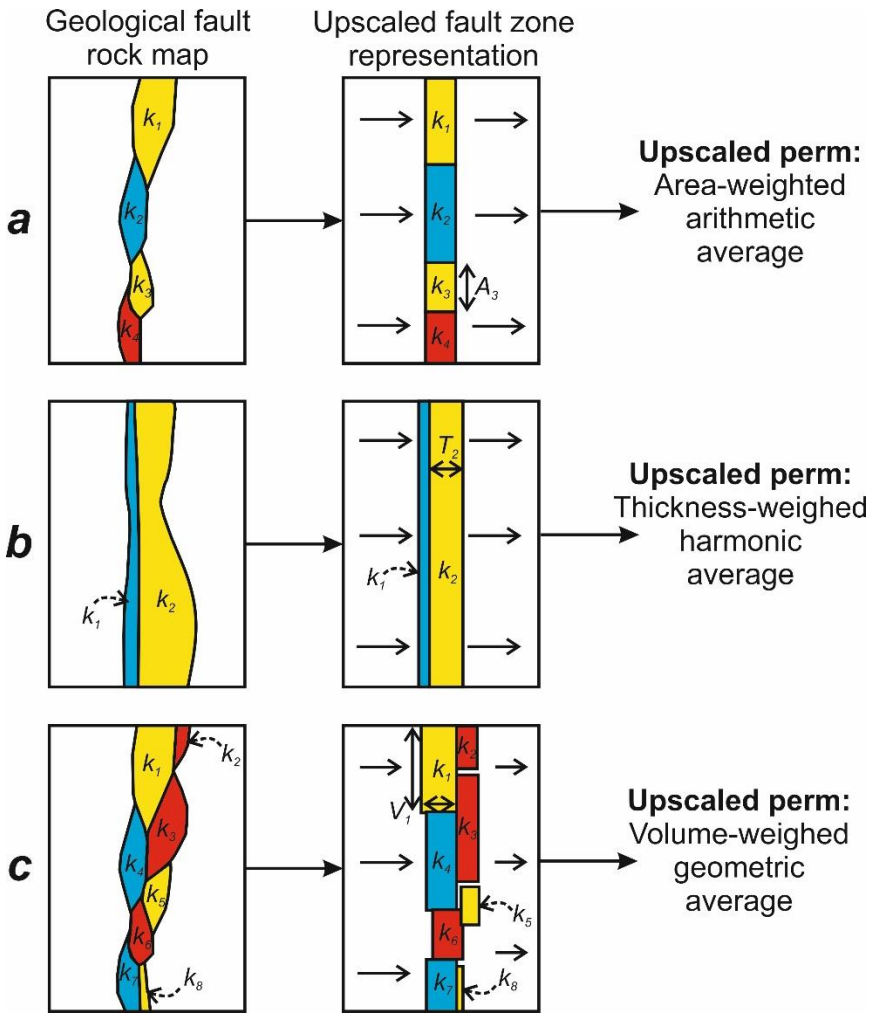

Figure 5-4: Schematic highlighting the best-suited method of upscaling fault core permeability from the permeability, k_i, and dimensions of different fault core elements. A_i represents the weighting applied for each method, corresponding to the cross sectional area (a), thickness (b), or volume (c) of each fault zone element.

Fault rocks in Malta are commonly arranged in lenticular overlapping geometries, which together form continuous fault cores at sufficient throws (>30 m, Figure 5-2). It is rare for a single fault rock type to be continuous across an entire fault zone, with the exception of Blue Clay smears and cataclasite veneers in high throw fault zones (>200 m), which are near continuous (Bonson *et al.* 2007; Cooke *et al.* 2018). Assuming no single fault core element is continuous, the bulk fault permeability will tend towards the higher permeability elements, through which flow will be concentrated, reflecting the area-weighted arithmetic average permeability of fault rock elements (Figure 5-4a). However, this assumes that permeability does not vary from one side of the fault to

the other (Sperrevik *et al.* 2002), as in Figure 5-4c, which is not always observed in Malta (Michie & Haines 2016; Cooke *et al.* 2019). Ultimately, fault rock distributions vary across fault zones, such that different averaging methods may be more appropriate to different regions of the fault zone. Therefore, a comparison between the area-weighted arithmetic average, $\overline{k_A}$, the thickness-weighted harmonic average, $\overline{k_H}$, and the volume-weighted geometric average, $\overline{k_G}$, is useful to see the range of potential bulk fault permeability values.

The area-weighted arithmetic permeability of a fault core of known area, A, composed of a number of fault rock elements, each with known area, A_i, and permeability, k_i, is:

Equation 5-1

$$\overline{k_A} = \frac{1}{A}\sum_{i=1}^{n} k_i A_i$$

The thickness-weighted geometric average permeability of a fault core of known thickness, T, composed of layers of fault rock of known thickness, T_i, is:

Equation 5-2

$$\overline{k_H} = \frac{\sum_{i=1}^{n} T_i}{\sum_{i=1}^{n} (T_i / K_i)}$$

The volume-weighted geometric average permeability of a fault core is:

Equation 5-3

$$\overline{k_G} = exp\left(\frac{\sum_{i=1}^{n} A_i T_i \, ln \, k_i}{\sum_{i=1}^{n} A_i \, T_i}\right)$$

To find a correlation that describes the observed evolution in fault zone architecture with increasing fault throw, FRT and FRC were used as quantifiable architectural parameters. The cross-sectional area of each fault rock element, A_i, is equal to FRC multiplied by the fault segment length, assuming 1D FRC measurements recorded along strike are representative of the 2D FRC across the entire fault surface. The thickness of each fault zone element, T_i, is equal to the arithmetic average thickness of that element. Calculating these parameters for different fault zone outcrops enables relationships to be established with parameters, namely fault throw and host rock porosity. Three primary fault rock types are present in Malta: cataclasites, cemented faults

and fault breccias. It is possible to predict the thickness and continuity of cataclasites and fault breccias by determining relationships with fault throw. It is more difficult to predict the thickness and continuity of cemented faults because cementation is a product of fluid and thermal history.

Cataclasite occurs principally in higher porosity formations in Malta, becoming thicker and more continuous with increasing fault throw (Cooke *et al.* 2018). These relationships can be represented by linear functions, which suggest cataclasite is continuous (FRC = 1) at *c*. 200 m throw. Reasonable linear relationships exists between FRT and throw in all fault rock types (R^2 = 0.77, 0.67, and 0.61 for cataclasite, fault breccia, and cemented faults, respectively). There is also a weak relationship between cataclasite continuity and throw (R^2 = 0.25). However, there is no clear FRC relationship for fault breccia or cemented faults (Figure 5-5). In cemented faults this is due to the lack of FRC data; there are three data points. An average value of 0.5 is selected for cemented faults. In fault breccia, there are a number of data points, such that the spread may relate to the different lithofacies within the dataset. Splitting fault breccia into either micrite or grain-dominated indicates that micritic fault breccia has a greater increase in FRT with throw, whereas grain-dominated fault breccia is more constant (Figure 5-6). There is no obvious difference between hanging wall and footwall fault breccia thickness, however, there are only 3 data points for hanging wall fault breccia which are from different lithofacies. In addition, at the observed throws (>30 m), fault breccia FRC appears to be relatively constant with throw, averaging a continuity of *c.*0.4 for grain-dominated fault breccia and 0.7 for micritic fault breccia (Figure 5-6). Therefore, a global average FRC of 0.55 is selected for fault breccia.

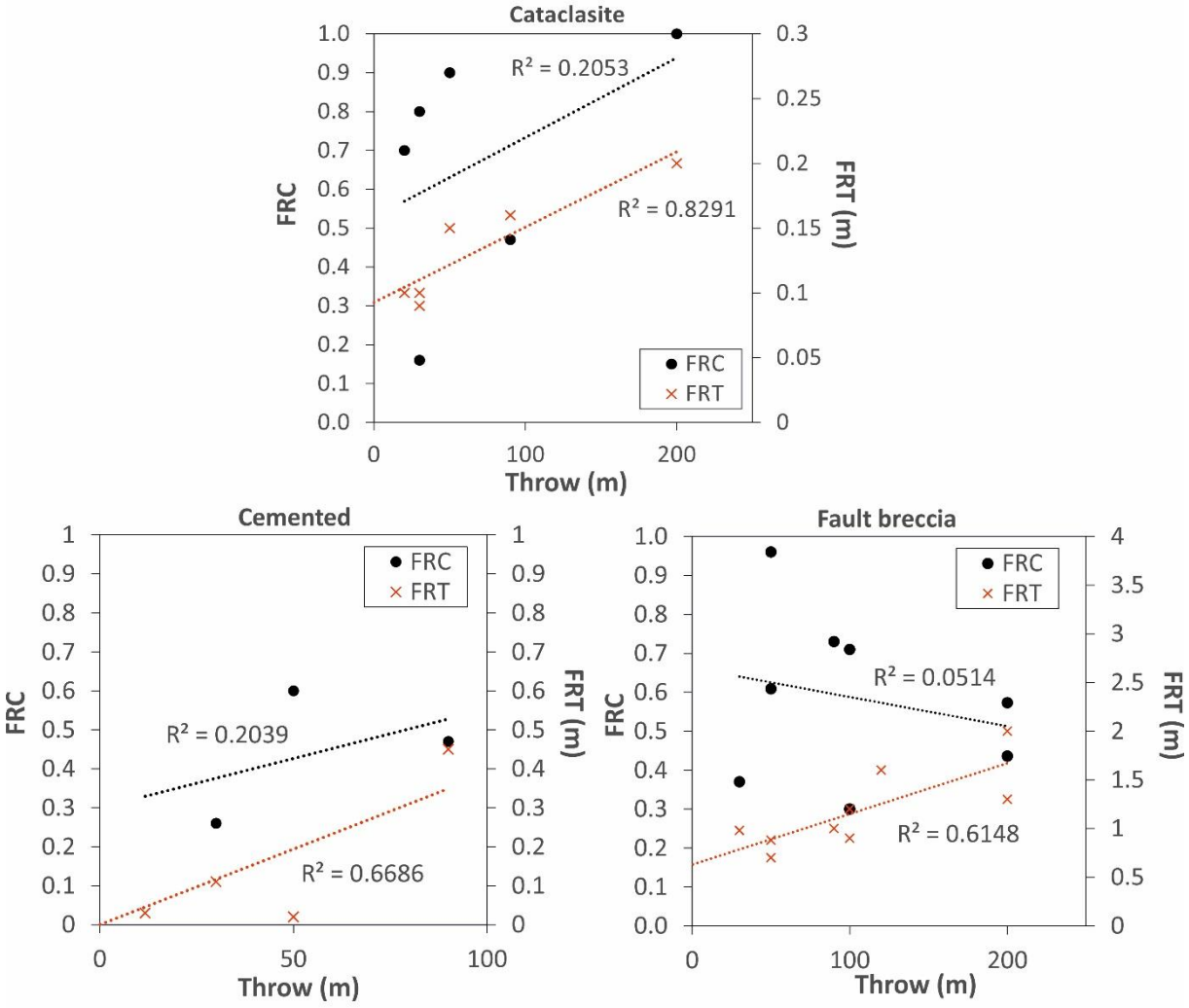

Figure 5-5: FRC and FRT as a function of throw for cataclasite, cemented faults, and fault breccia.

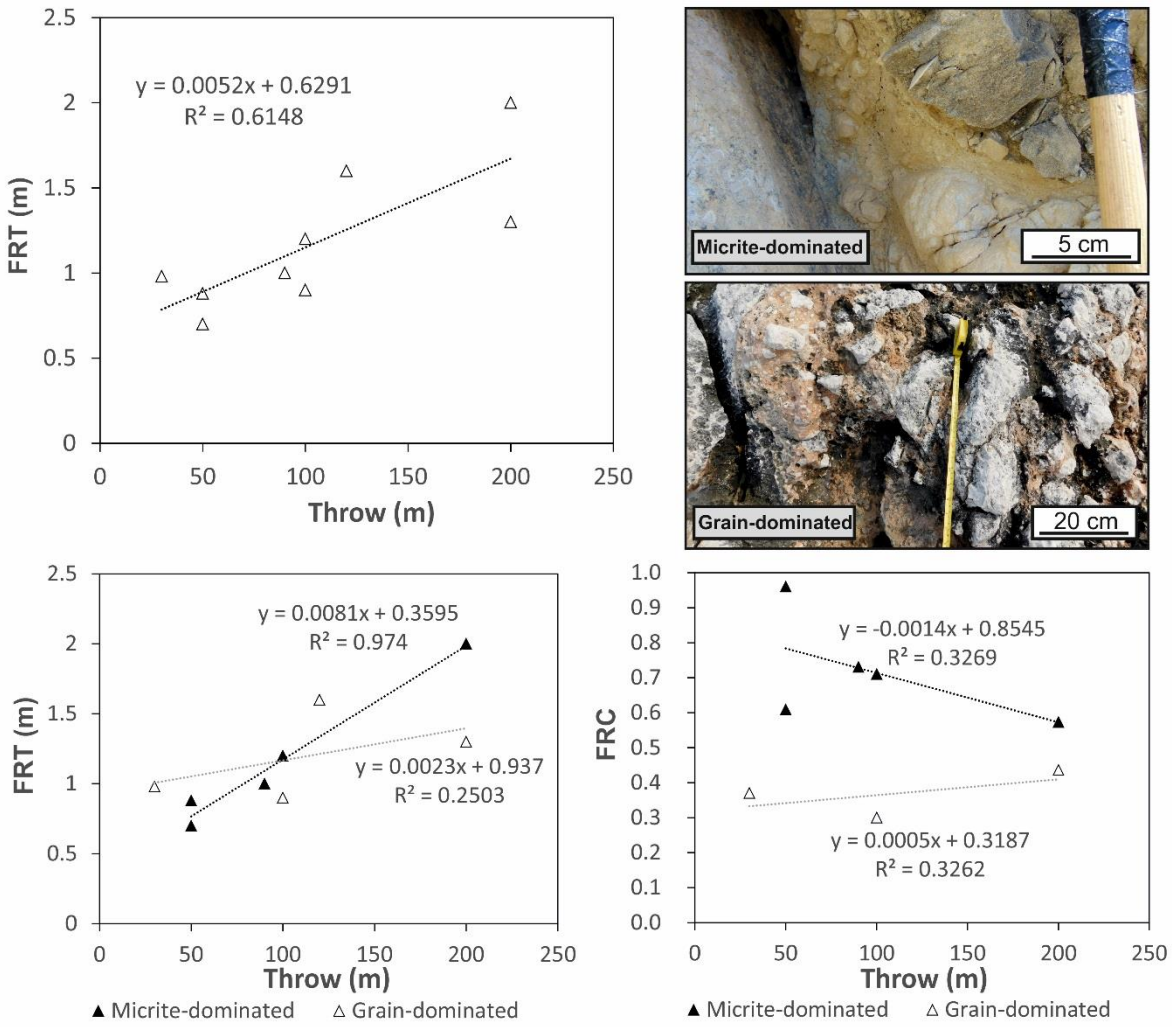

Figure 5-6: Plots of FRT and FRC as functions of throw for fault breccia in Malta. Images show outcrop examples of micrite and grain-dominated fault breccia.

In the studied lithofacies, good exponential relationships exist between host rock porosity and the corresponding host to fault rock permeability contrast for cataclasite ($R^2 = 0.66$) and fault breccia ($R^2 = 0.85$). For cemented fault rocks, an exponential relationship is a much poorer fit ($R^2 = 0.25$), (Figure 5-7A). Permeability contrast was calculated using the geometric average host rock permeability divided by the geometric average permeability of fault rock derived from that lithofacies. The permeability contrast increases with increasing host rock porosity, up to $>10^4$, $>10^3$, and 10^1 in a 30% porosity host rock for cataclasite, cemented faults, and fault breccia, respectively (Figure 5-7A). The weighted host to fault rock permeability contrast can be calculated for each side of a fault (hanging wall and footwall) of known throw cutting a rock of known porosity using the permeability contrast vs host rock porosity (Figure 5-7A) and FRT/FRC vs

throw relationships (Figure 5-5). The calculated permeability contrast assumes that the fault core is continuous and composed only of the three primary fault rocks. Fault cores in low porosity (<10%) host rocks are composed only of fault breccia and cemented faults, whereas fault cores in moderate to high porosity rocks (>10%) are composed of a mixture of all three fault rock types. Therefore, the weighting value for cataclasite is set to zero below 10% host porosity. The proportional volume of all fault rock types in the fault core varies with throw, based upon the FRC and FRT of each fault rock type. Cataclasite comprises 10-15% of the fault core, whereas fault breccia reduces from 90% of the fault core at very low throws, down to *c.*60% at 200 m throw. Cemented faults increase from absence up to *c.*25% at 200 m throw (Figure 5-7B).

Estimated host to fault permeability contrasts were calculated for faults cutting host rocks of 10% and 30% using the above relationships, highlighting the impact of throw on permeability contrast when using the area-weighted arithmetic average (Equation 5-1), the thickness-weighted harmonic average (Equation 5-2), and the volume-weighted geometric average (Equation 5-3), (Figure 5-7C). The data show that for a 10% porosity host rock, the area-weighted arithmetic average permeability predicts a permeability contrast from host to fault of around one order of magnitude (20). Using the volume-weighted geometric average reduces the permeability contrast by up to an order of magnitude relative to the arithmetic average; this reduction is lowest at low throws and the permeability contrast increases with increasing throw, towards a maximum of 10. Using the thickness-weighted harmonic average permeability predicts a fault core permeability contrast below the arithmetic average at low throws (<30 m), after which it increases to a maximum of *c.*40. For a 30% porosity host rock, the arithmetic area-weighted average permeability predicts a permeability contrast of two orders of magnitude (200). Using the volume-weighted geometric average predicts an initial permeability contrast of two orders of magnitude (150) at the lowest throws, increasing with increasing throw to a maximum towards three orders of magnitude (500). Using the thickness-weighted harmonic average permeability predicts relatively constant fault core permeability contrast of three orders of magnitude (*c.*4 x 10^3) (Figure 5-7C).

The core of all faults is composed of a mixture of fault rocks derived from the hanging wall and footwall. The method described above allows the prediction of permeability on either side of the fault, which can then be combined to predict a bulk fault core permeability. The harmonic average is the most suitable method of averaging if fault rock is continuous on either side of the fault. However, fault rock is often discontinuous on one or both sides of the fault, such that the

continuous fault core is a composite of hanging wall and footwall derived fault rocks. This suggests the arithmetic or geometric average of footwall and hanging wall fault rock permeability is more geologically accurate, with the exception of when the thickness-weighted harmonic average is used to calculate permeability on either side of the fault; by definition, all fault rock is continuous (Figure 5-4b), such that the harmonic average is most suitable for averaging footwall and hanging wall permeability. Therefore, the arithmetic average fault core permeability is used for the area-weighted arithmetic average footwall and hanging wall permeability and the geometric average fault core permeability is used for the area-weighted geometric average footwall and hanging wall permeability.

Michie *et al.* (2017) upscaled fault rock permeability data to bulk fault permeability for six fault outcrops in Malta using detailed fault zone maps. The upscaled permeability values were calculated by geometrically averaging fault rock permeability values on the sub-meter scale, then using the area-weighted arithmetic average of these values to estimate bulk fault core permeability. The predicted bulk fault permeability for the same faults using the methods outlined previously show how this more generalised approach compares with the case-by-case approach of upscaling permeability using detailed fault core maps (Figure 5-7D). In general, there is a good fit to the data from Michie *et al.* (2017), irrespective of which averaging method is used; with the exception of one fault, all predictions from this study are within an order of magnitude of those predicted by Michie *et al*. (2017). The harmonic average permeability generally predicts a lower permeability than the results from Michie *et al*. (2017), whereas the area-weighted arithmetic and volume-weighted harmonic average permeability predict higher values. All averaging methods predict a fault permeability that is between two and three orders of magnitude lower than the highest permeability fault from Michie *et al*. (2017); this fault has the largest throw (90 m), and juxtaposes the grain-dominated LCL against the micrite-dominated GL. The high permeability in this instance is interpreted to be a result of a highly heterogeneous fault core, comprising fault rocks from both of the juxtaposed lithofacies and a wide variety of lithofacies developed over a large throw. The effect of increasing throw on the range in permeability for each fault rock type is a factor that is not reflected in the algorithms presented above, such that these algorithms predict a much lower permeability for this fault.

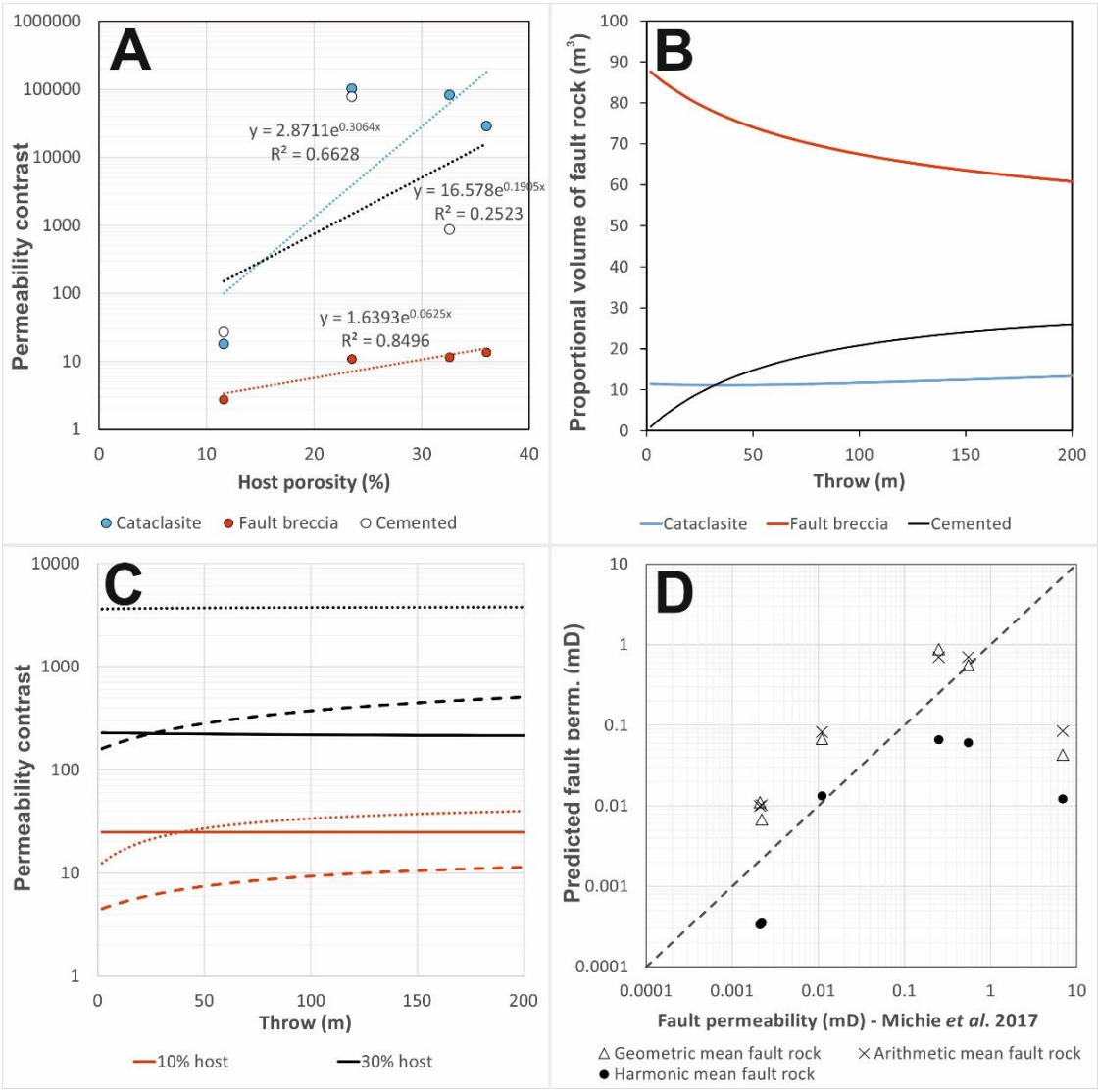

Figure 5-7: A) Permeability contrast (host to fault rock) for cataclasite, fault breccia cemented faults as a function of host rock porosity. B) Proportional volume of fault rock for each fault rock type as a function of throw. C) Permeability contrast as a function of throw for 10% and 30% porosity host rock, calculated using the area-weighted arithmetic average (solid lines), the volume-weighted geometric average (dashed lines), and the thickness-weighted harmonic average (dotted line). D) Predicted bulk fault permeability for different points along two Maltese fault zones plotted against upscaled fault rock permeability calculated using detailed fault zone maps (Michie et al. 2017). The dashed line represents a 1:1 correlation.

Continuity

Predicting fault core continuity is important in predicting the impact of the fault zone on fluid flow. A fault core composed of discontinuous low permeability fault rock will be unlikely to impact flow during production, due to the presence of leakage points along the fault. In contrast, a fault zone with a fault core composed of continuous low permeability fault rock is much more likely to have some effect on fluid flow during production. For a fault with a discontinuous fault core, the fault core thickness is greater than zero at some point along the fault surface and is equal to zero at all other points. Therefore, fault rock continuity relationships can be included within fault rock thickness calculations by assigning 0 m thickness to a given proportion of fault cells, depending on the FRC at that throw. The proportion of cells that are assigned 0 m thickness is dependent upon the estimated FRC at that point. This can be implemented as a discretized relationship between fault throw and FRC, whereby ranges of fault throw are assigned FRC values (Figure 5-2). The ranges containing discrete FRC values were arbitrarily chosen as 0-5 m, 5-10 m, 10-20 m, and 20-30 m (Figure 5-2). The discrete FRC value for each throw range was determined by calculating the average FRC within that range, with a continuous fault core assumed >30 m throw (Table 5-1).

To implement this relationship into fault rock property modelling, a random value between zero and one was generated for each fault cell. If this value was less than the discrete FRC value at that throw,D, then the FRT was calculated according to:

Equation 5-4 $$\boldsymbol{FRT = 0.005\, D}$$

If the value is greater than the FRC value, then fault thickness was set to zero. For example, for a FRC value of 0.2, there is an 80% chance that the random value will be greater than this value, such that only 20% of cells will be assigned a fault thickness greater than zero. This probabilistic method of fault thickness calculation enables the generation of a fault surface with properties that simulate patchy fault rock coverage, distributed randomly across the fault surface, with more fault rock coverage in regions of larger throw.

Throw (m)	Percent fault rock coverage
0 – 2.5	0%
2.5 – 5	20%
5 – 10	40%
10 – 20	70%
20 – 30	90%
> 30	100%

Table 5-1: Fault rock continuity values selected for throw ranges, based upon empirical field data (Figure 5-2).

5.6.3. Gozo model construction

A geocellular model of the island of Gozo was constructed and fault properties were calculated according to the above relationships to test the effect of fault rock permeability and continuity predictions on fluid flow within the Maltese stratigraphy. This model aimed to accurately represent the complex fault geometries observed in Gozo using data from field measurements and geological maps (e.g. Pedley *et al.* 1976). This model can then be used as an analogue to a faulted porous limestone reservoir so that the effect of different fault property modelling methodologies on production can be estimated.

A framework structural model was first produced as a basis on which to construct the geocellular model. To do so, a digital elevation model (DEM) of the island of Gozo (https://www2.jpl.nasa.gov/srtm/dataprod.htm) was imported to the TrapTester (T7) modelling software. The geological map of Gozo (Pedley *et al.* 1976) was imported as a surface and draped upon the DEM, producing a 3-dimensional geological map of the island (Figure 5-8A). The tops of all geological formations (LCL, GL, Blue Clay, and UCL) were traced and faults were picked onto the surface. The Greensand formation was excluded due to the poor lateral continuity. The horizon data was then interpolated using inbuilt gridding algorithms to produce gridded stratigraphic horizons. Fault surfaces were generated by projecting fault segments upwards and downwards by greater than the total stratigraphic thickness (500 m), ensuring faults cut the entire sequence. Where possible, fault dip measurements obtained from the field were used to project fault surfaces, and an angle of 65° was used for all other faults. Fault-separation polygons were created

on the fault surfaces, for all intersecting horizons, which were then manually adjusted to ensure geological accuracy, and horizon surfaces were regridded to account for faulting.

An irregular cellular grid was generated from the framework model with dimensions of 348 x 154 x 18 cells, spanning 15 x 9.3 x 0.6 km, and an average cell size of 43 x 60 x 10 m (Figure 5-8D). Faults were modelled using pillar gridding and 0% cell equancy, preserving fault geometries. Cells were populated with porosity and permeability data from laboratory measurements of host rocks. This data was input via 2 synthetic well logs to simulate lateral property variation within each formation, which were then used within a deterministic method to populate cells with the arithmetic and geometric average of porosity and permeability, respectively (Figure 5-8).

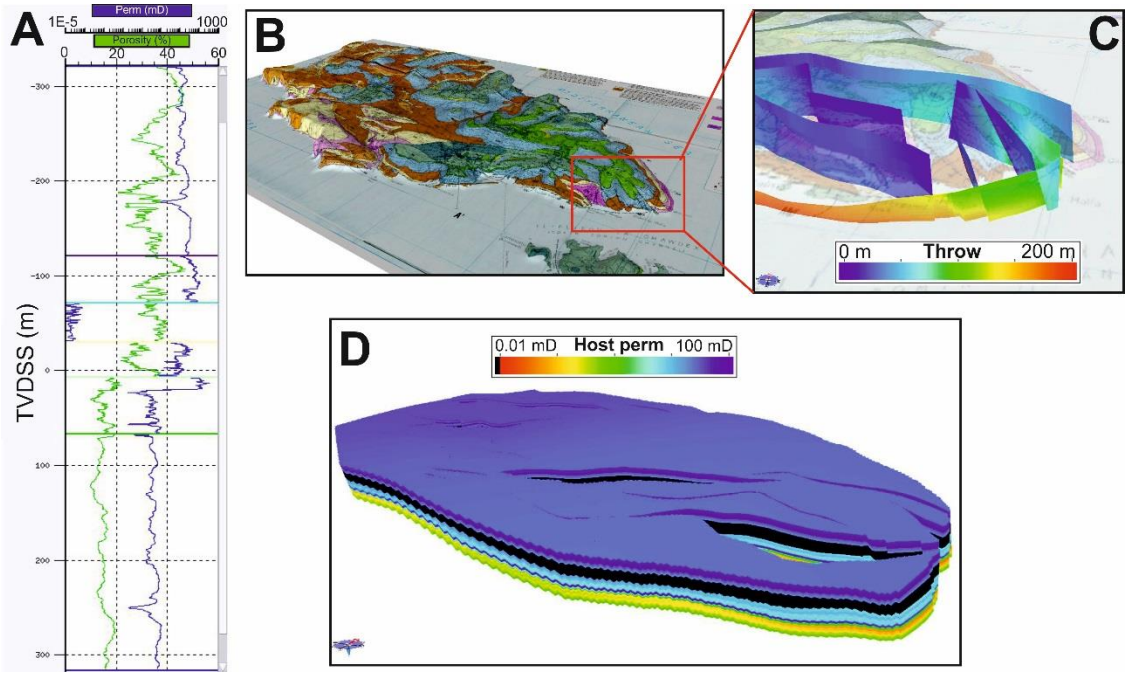

Figure 5-8: A) Example synthetic porosity and permeability log. Horizontal lines represent stratigraphic horizons. The green line is porosity (0% to 60%), and the blue line is permeability (10^{-5} mD to 10^{3} mD). B) Geological map draped over the DEM of Gozo. C) Example fault surfaces in eastern Gozo showing fault throw. D) Cellular grid populated with permeability data from synthetic logs.

Fault property modelling was then undertaken using the cellular grid. This consisted of modelling fault thickness and permeability for each fault cell connection, according to the methods outlined above, which are used to calculate transmissibility multipliers. The throw is

used to calculate fault rock thickness for each cell connection; the probabilistic fault rock continuity correction was applied to fault connections with throws less than 30 m. Throw, host porosity, and host permeability are used to calculate hanging wall and footwall permeability according to the above methods, which were then either arithmetically or geometrically averaged to calculate a combined fault core permeability (Figure 5-9). The Blue Clay was assigned a V_{shale} of 0.8, allowing fault property modelling to include clay smear potential (CSP) calculations (Yielding *et al.* 1997).

The cellular model constructed in TrapTester, with its cell properties and fault transmissibility multipliers, was exported to ECLIPSE for flow modelling.

5.6.4. Eclipse flow simulation

ECLIPSE 100 was used to model oil production from a two phase petroleum system (water and oil) within the cellular model. The depth of the reservoir ranges from -230 m to 350 m, due to the DEM being imported at sea level during model construction. To simulate the reservoir being at depth, reservoir equilibration pressure was set to 520 bar, with an oil-water contact at 200 m depth. This corresponds to a depth of *c.*2.5 km. A total of four vertical production wells and five vertical injection wells were positioned around the reservoir. Production wells were placed in the central unfaulted region and injection wells were positioned radially outwards, towards the edge of the reservoir (Figure 5-10). Production wells targeted the GL formation, below the sealing Blue Clay formation. Injection wells targeted the LCL, below the GL formation. The model simulated a total of 30 years at constant production and injection rates: production wells were set to a liquid production rate of 500 sm^3/day and injection wells were set to a water injection rate of 500 sm^3/day.

Four different model scenarios were simulated, each with different fault properties. Scenario A consisted of open faults, whereby all faults are completely transmissive (TM = 1). Scenario B consisted of closed faults, whereby all faults are completely sealing (TM = 0). Scenarios C, D and E consisted of faults with permeability calculated according to the area-weighted arithmetic average fault permeability, the volume-weighted geometric average permeability, and the thickness-weighted harmonic average fault rock permeability algorithms, respectively. Scenario F used the thickness-weighted harmonic average fault rock permeability in addition to the FRC correction algorithm.

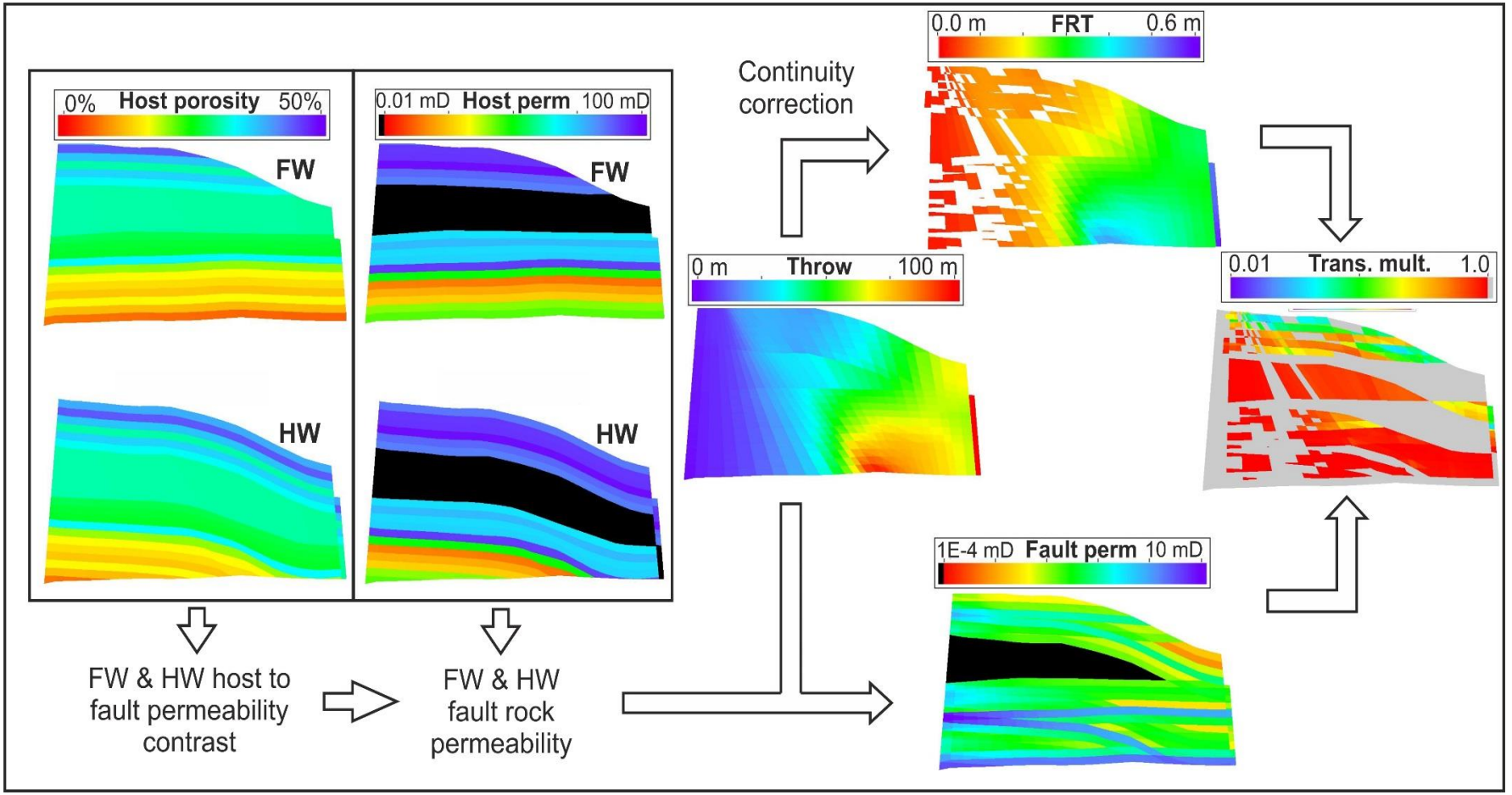

Figure 5-9: Example cellular fault (South Qala Fault) highlighting the process used to calculate transmissibility multipliers from host rock porosity, permeability and fault throw. Note that the Blue Clay formation is not accounted for within fault rock permeability estimates and CSP is not included within this example.

Property	Rock	Oil	Water	units
Compressibility	$4x10^{-5}$		$4.54x10^{-4}$	1/bars
Density		700	1050	kg/m^3
Viscosity		2.0	0.31	cP
Formation factor		1.15	1.029	rm^3/sm^3
Relative permeability		0.9	0	$@S_{wc} = 0.25$
		0.1	0.4	$@S_{or} = 0.3$

Table 5-2: Reservoir and fluid properties for flow simulation.

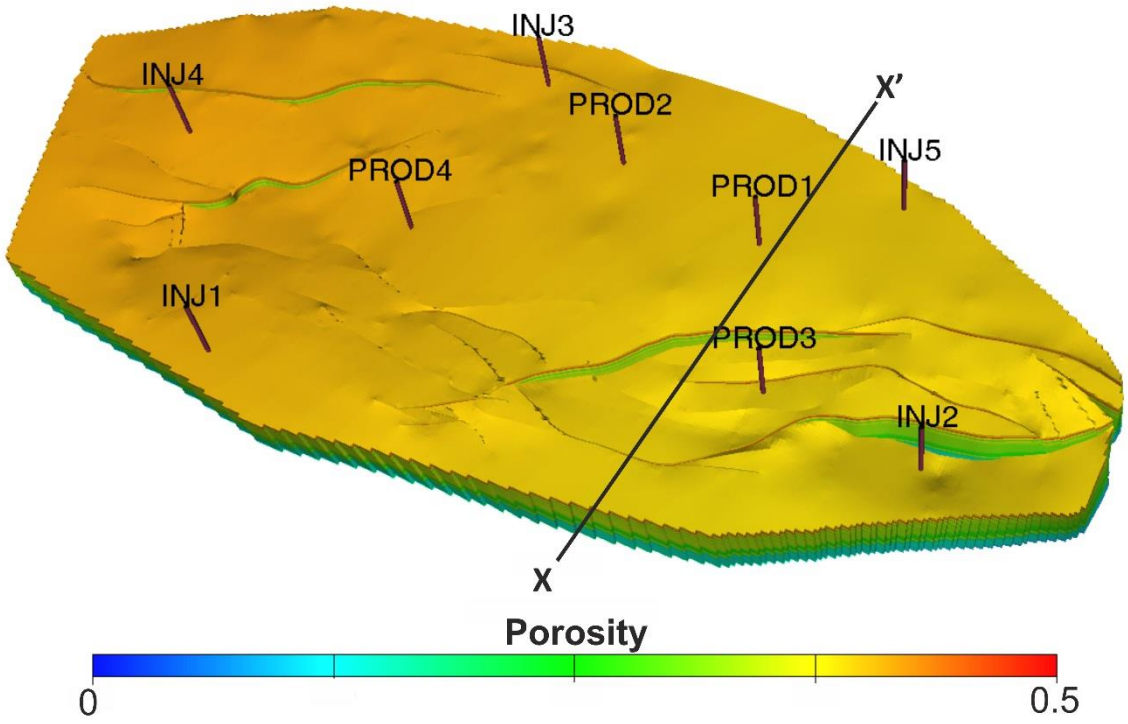

Figure 5-10: Cellular grid with production and injection well locations and location of X-X' cross section (Figure 5-14).

5.6.5. Faulted type III fractured reservoir model construction

An additional model was constructed to test the effect of a low permeability fault baffle (partial barrier to fluid flow on production timescales) on a porous fractured reservoir, compared with a non-fractured reservoir, assuming fractures do not crosscut the fault. A simple 101 x 142 x 5 cellular grid containing a central low permeability fault was generated in ECLIPSE 100. The total grid represents a 1000 x 1736 x 25 m volume. The grid consists of two fault blocks, each 100 x 43 x 5 in size, separated by a fault zone of 100 x 15 x 5. The rows that comprise the fault zone have gradually refined dimensions and permeability towards the central row, representing the fault core. The matrix was assigned a porosity of 25 % and a permeability of 1 mD, with dual permeability in some simulations. Fracture permeability is set to 1000 mD, porosity is 0.1 %, and a shape factor of 12 is selected. Permeability decreases within the fault zone block, down to a minimum of 10^{-3} mD. The grid boundaries have no-flow conditions. The reservoir was saturated with oil, at a depth of 2 km. A producer well and an injector well were placed at the boundaries of the reservoir, on either side of the fault. The reservoir properties are outlined in Table 5-2 and the grid geometry is shown in Figure 5-11. Four simulations were run, which represent: i) A reservoir with no fracturing and a low permeability fault; ii) a type III reservoir with a low permeability fault; iii) A type III reservoir with no fault; iv) A reservoir with no fracturing and no fault.

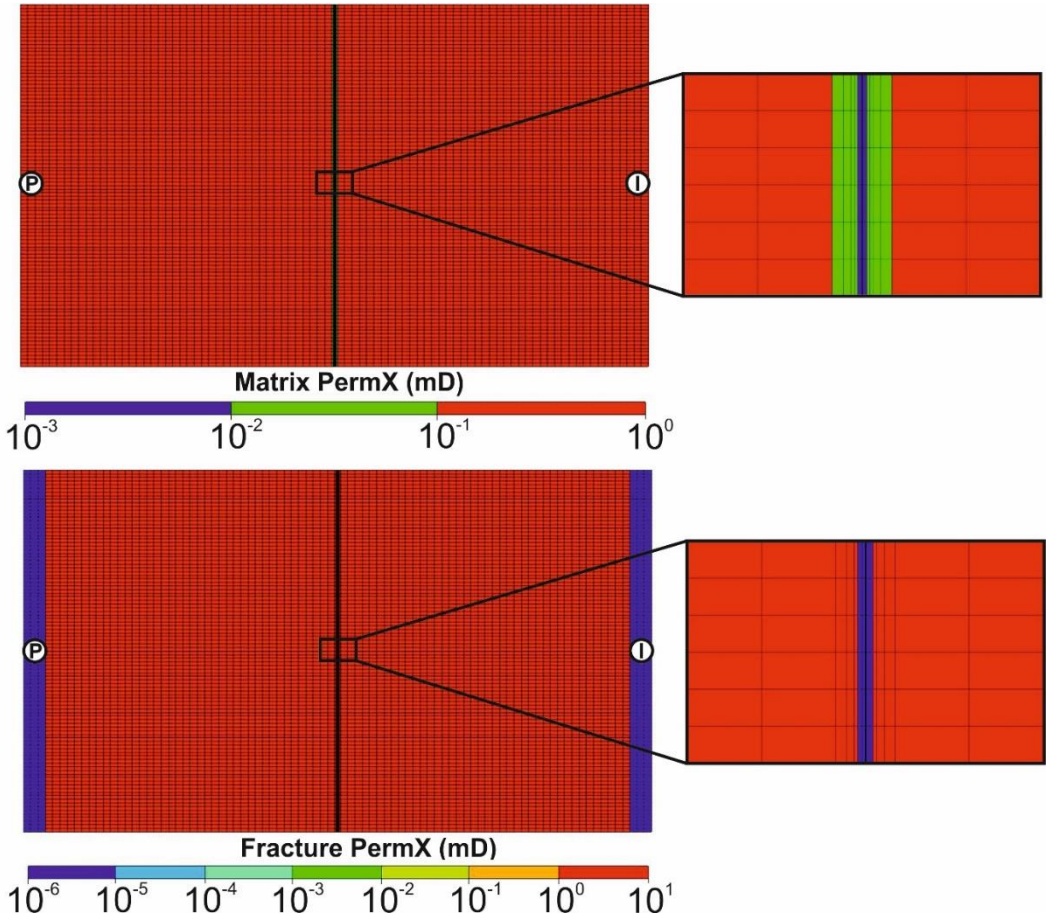

Figure 5-11: Cellular grid geometry for model of a low permeability fault in a type III fractured reservoir, showing the matrix permeability and the effective fracture permeability (fracture permeability x fracture porosity). I and P represent locations of the injector and producer wells.

5.7. Results

5.7.1. Gozo production simulation results

Total oil production over the 30 years of the simulation is lowest in scenario B, when all faults are closed to flow (17393 sm^3). This is 16% less than scenario A, when all faults are open to flow, which has the best production total (20689 sm^3). The difference between scenarios A, C & D is negligible, with a maximum difference of 0.2% between scenarios A and D (volume-weighted geometric average permeability), (Figure 5-12). Scenario E (thickness-weighted harmonic average permeability) and F (thickness-weighted harmonic average permeability with the FRC correction) reduced the total production relative to scenario A by 4% and 1.1%, respectively.

Total production rates remain around 1900 sm^3/day in these scenarios, but falls to <1600 sm^3/day within the first five years for scenario B (Figure 5-12). The reduced production that occurs when faults are closed (scenario B) is principally due to production well 3, which is targeting a fault block surrounded by a network of connected faults. This fault block is compartmentalised, limiting the potential oil volume accessible to the well (Figure 5-13 & Figure 5-14). Pressures surrounding injector wells is also raised relative to the other scenarios, due to the numerous pressure barriers present. In contrast, reservoir pressures for the other scenarios are generally much more homogeneous, as faults only have large impact on fluid flow where throw is sufficient to generate a juxtaposition seal (Figure 5-13). Lower throw faults have little to no impact on fluid flow in scenarios C and D, as the predicted fault rock permeability is not sufficiently low enough to generate baffles to fluid. Thus, pressure equilibration is possible across the faults (Figure 5-13 & Figure 5-14).

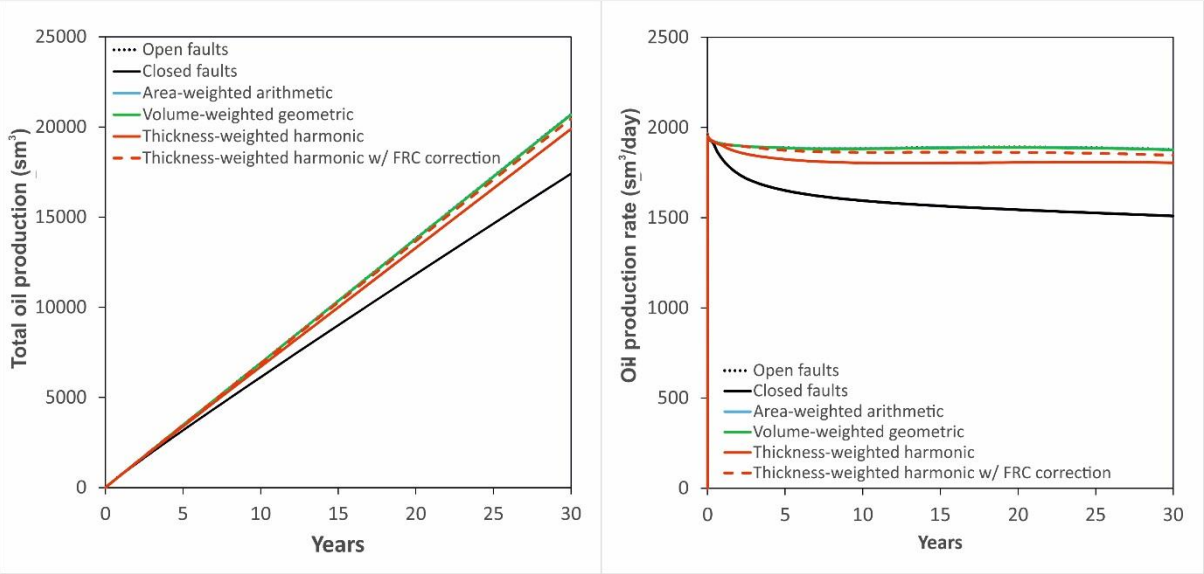

Figure 5-12: Total oil production and oil production rates for different simulations. See Appendix 2 for raw data.

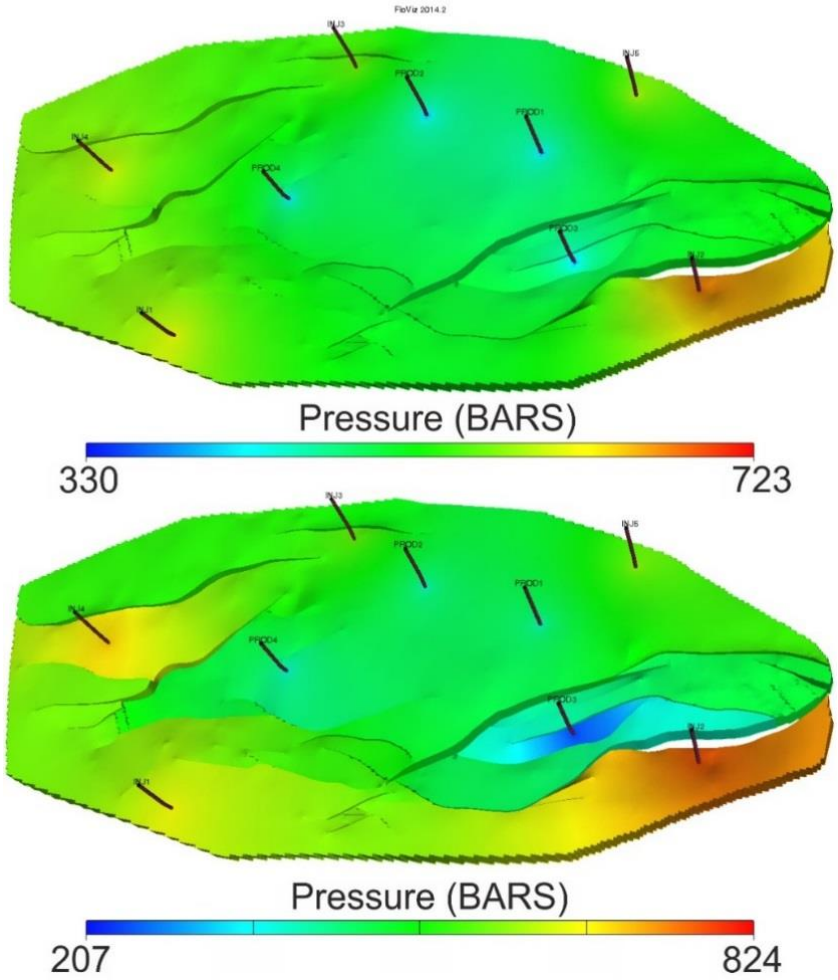

Figure 5-13: Reservoir pressures after 30 years of production. Top) scenario D: transmissibility multipliers calculated using area-weighted arithmetic fault permeability. Bottom) scenario B: all faults are closed (transmissibility multipliers of zero). Only layers 8-18 are shown as these are the targeted layers for production and injection.

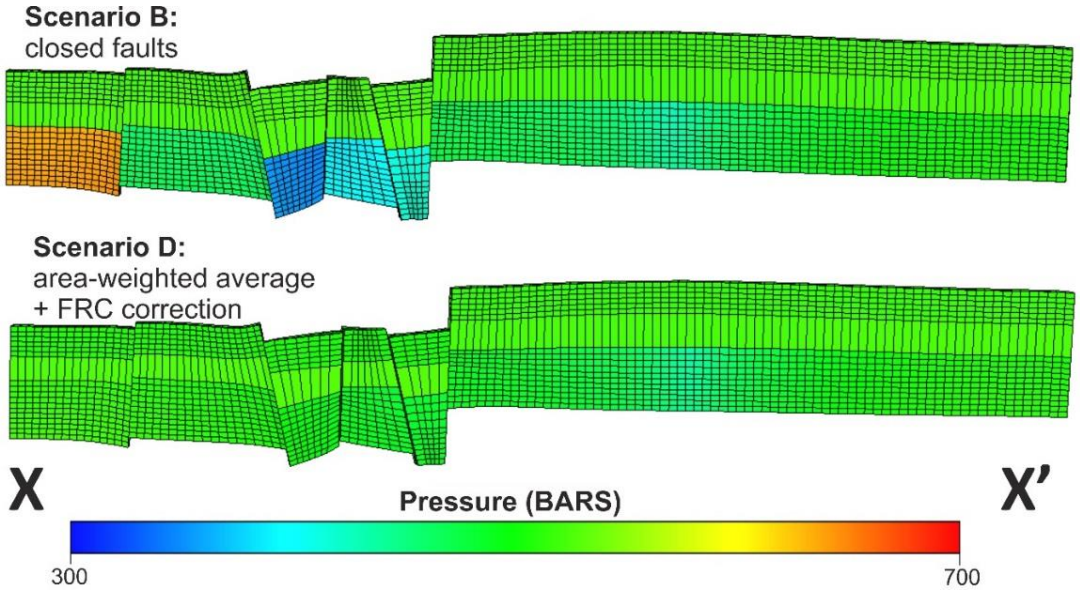

Figure 5-14: Cross section X-X' for scenario B and D. Central fault blocks become compartmentalised in scenario B, thereby reducing the potential production capacities in these fault blocks. Faults are transmissive in scenario D.

5.8. Faulted type III fractured reservoir model results

For a given fault permeability prediction, the effect on reservoir production depends on the host rock permeability. The host rock permeability measurements presented in this study are based upon core plug measurements, which characterises only the matrix permeability. Any contribution of fractures to the bulk host rock permeability are not accounted for in the above reservoir simulation. Therefore, if the host were to be a type III porous reservoir, whereby storage is dominated by the matrix and both fractures and matrix contribute to permeability, then the permeability reductions experienced between the host and fault would be larger than indicated in this study (Figure 5-7A).

By comparing production between two scenarios, one with a low permeability fault and the other with no fault, the impact of the fault on production can be observed (Figure 5-15). Production shows how a permeability reduction from 10^{-1} mD in the host rock (no fractures) to 10^{-4} mD in the fault core has very little impact on production. However, the permeability reduction experienced is larger with the addition of fracture permeability, meaning the presence of a low permeability fault zone has a greater effect on production; total production is reduced by *c.*11 % over 50 years of the simulation by introducing the low permeability fault.

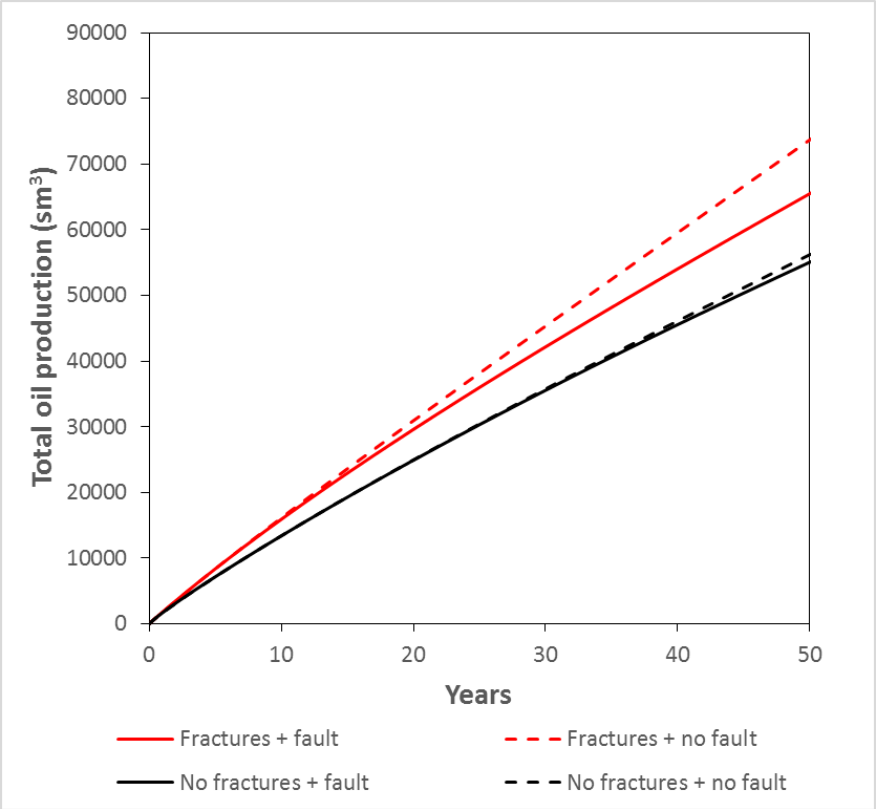

Figure 5-15: Oil production for a simple cellular grid, containing different combinations of matrix fractures (type III reservoir) and low permeability fault core. No fault represents scenarios in which fault properties are equal to the reservoir properties. See Appendix 2 for raw data.

5.9. Discussion

The cellular model of Gozo indicates that the fault zones studied at outcrop, and all other faults across the island, are likely to have no impact on fluid flow; faults only impact production when all fault rocks are considered continuous across the fault zone, such that the harmonic average of fault rock permeability (Equation 5-2) is used to calculate bulk fault permeability (Figure 5-12). However, fault rocks are generally discontinuous, even within continuous fault cores (Figure 5-5). Faults only impact fluid flow due to the juxtaposition of lithologies with contrasting petrophysical properties. However, it is worth noting that the majority of these faults are of low throw (<50 m), such that the effect of clay smearing is negligible.

5.9.1. Fault permeability and continuity

The composition of juxtaposing formations has been suggested to be a factor in fault core permeability in siliciclastic rocks, whereby the clay content either side of the fault controls the permeability of the fault core (e.g. Yielding *et al.* 1997; Fisher & Knipe 2001; Sperrevik *et al.* 2002), and in carbonates, whereby lithofacies with contrasting mechanical properties lead to heterogeneous fault cores that are likely to have across-fault fluid pathways (Michie & Haines 2016; Michie *et al.* 2017). The approach used within this study incorporates this in permeability calculations by separately predicting the permeability of the footwall and hanging wall derived fault rocks, then combining; the fault core is assumed to be composed of discontinuous footwall and hanging wall fault rock, which together form a continuous fault core, when using the area-weighted arithmetic average permeability or the volume-weighted geometric average permeability. Therefore, in cases where lithofacies of contrasting porosity are juxtaposed such that a heterogeneous fault core is expected, fault rocks of contrasting permeability are predicted for each side of the fault. The arithmetic average of both fault core components will predict a bulk fault permeability that tends towards the higher permeability, whilst the geometric average permeability will fall between the hanging wall and footwall permeability values on the logarithmic scale. This reflects the across-fault fluid pathways generated by the high permeability fault core elements (Figure 5-16). Hence, bulk fault permeability predictions will only result in a low permeability fault core in cases where the fault juxtaposes two high porosity formations. In contrast, the thickness-weighted harmonic average permeability predicts a permeability that is dominated by the lowest permeability fault rocks; these fault cores will have the largest impact on fluid flow (Figure 5-12). For a 50 m fault cutting a host rock of 30% porosity and 10 mD permeability, the area-weighted arithmetic average predicts a fault core permeability of *c*.0.3 mD, which is reduced to 0.003 mD if the thickness-weighted harmonic average permeability is used. However, using harmonic averaging for the fault zones in Malta is not representative of any fault zone with a throw of less than 200 m; cataclasite is potentially continuous at >200 m throw (Cooke *et al.* 2018) and continuous clay smears are accounted for separately using CSP algorithms. In large throw fault zones (hundreds of meters to kilometres of throw), thick fault cores that are likely laterally continuous over the scale of several grid cells are observed (e.g. Agosta *et al.* 2007; Smith *et al.* 2011; Bauer *et al.* 2016), such that this method of averaging may be suitable.

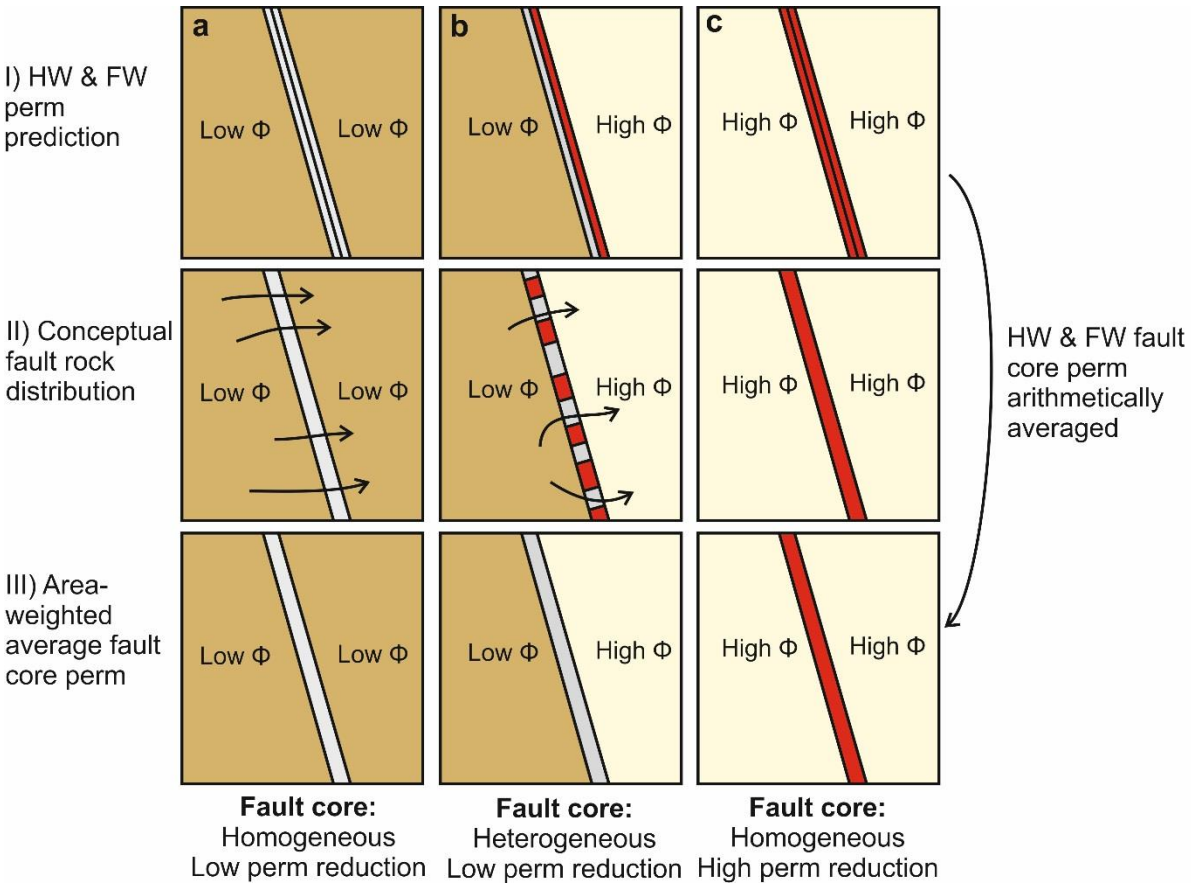

Figure 5-16: Schematic diagram showing how the area-weighted arithmetic averaging process works for two juxtaposed cells, depending on their porosity. Red fault rock is low permeability, grey is high permeability. The top row shows how the model predicts permeability on either side of the fault, depending on porosity. The central row shows the conceptual distribution of fault rock and pathways for fluids. The bottom row shows the permeability for that cell juxtaposition after arithmetic averaging.

A permeability reduction of 10^3 indicates that a fault may have a noticeable impact on production on reservoir scales (Fossen & Bale *et al*. 2007; Cooke *et al.* 2019). The only fault rocks that can exhibit such permeability reductions are cataclasite and cemented faults, which require a high host porosity of *c.*30% to achieve such permeability reductions (Figure 5-7). For the entire fault core to exhibit such permeability reductions, low permeability fault cells need to be distributed across the entire fault surface. Therefore, the juxtaposed reservoir units must have a high porosity at all faulted reservoir cells. A single reservoir heterogeneity that introduces a lower porosity to a faulted cell will introduce a potential pathway for fluid flow across the fault; this would apply to formations with heterogeneous facies distributions, such as reef complexes, which

are known to have lateral facies variations (e.g. Lucia 1995; Pomar & Ward 1999). The impact of lateral heterogeneity on fault permeability is highlighted by the fault properties for the Gozo cellular model, in which stratigraphic variability in porosity introduced through the synthetic sedimentary log generates up dip porosity heterogeneity, which is propagated through to up fault permeability heterogeneity. At the shallowest depths, the fault shown in Figure 5-9 juxtaposes two rows of high porosity cells, therefore leading to fault zone permeabilities of $<10^{-2}$ mD, whereas deeper levels of the fault juxtapose lower porosity formations which lead to fault zone permeabilities of $>10^{-1}$ mD, thus creating the potential for across-fault fluid flow. Such heterogeneities are reported along carbonate-hosted faults of similar throw, resulting from mechanical or stratigraphic variations (Matonti *et al.* 2012). At low throws, the lowest permeability fault rocks only make up a small portions of the fault zone (Figure 5-7B), reducing their contribution to the fault core permeability. Therefore, greater host porosities are required for the bulk fault core to experience a 10^3 permeability reduction relative to the host, unless the thickness-weighted harmonic average is used.

The reasonable correlation between each predictive algorithm and the data presented by Michie *et al.* (2017) provides some validation for this more generalised approach to predicting fault permeability, assuming these previous predictions are accurate due to the detailed nature in which they were calculated (Figure 5-7D). Variations from the previously predicted permeabilities may relate to there being different fault rock distributions at different lithofacies juxtapositions, whereby different data points may be best represented by different algorithms, based on the fault rock distribution along that juxtaposition. Additionally, the relationships presented in this study require further calibration and contain large degrees of uncertainty surrounding permeability contrasts and the fault rock distribution weightings used for averaging fault rock permeability. Michie *et al.* (2017) found that at juxtapositions of similar lithofacies, fault cores are relatively homogenous, containing limited deformation mechanisms and, therefore, little variability in permeability (note that these faults host low throws); this generally results in a low upscaled permeability. At juxtapositions of different lithofacies, the fault core is composed of a wider variety of fault rock fabrics, such that the fault core is characterised by a more heterogeneous permeability; this generally results in a higher upscaled permeability. The majority of data used in this study was obtained from fault rocks at juxtapositions of different lithofacies, thereby leading to a potentially wider range in permeability than expected for fault zones juxtaposing the same lithofacies; this means the relationships used to predict fault

permeability may not be representative of these low throw faults. Further to this, this study uses limited data to determine predictive relationships (3-4 data points), which has implications to trends. For example, the use of exponential functions to represent the relationship between permeability contrast and host rock porosity causes the function to underestimate permeability contrasts for host porosities of 20-30% (Figure 5-7). This is due to the lower permeability contrast experienced in the Attard member (10% host rock). Additional data points may help to constrain the fitting of trendlines to the data for all relationships used in the predictive algorithms, which would help to calibrate the relationships and aid more accurate fault permeability predictions. However, these relationships may be self-similar w.r.t. the Maltese formations, such that there may be a large data spread with the addition of carbonates from other settings. Diagenetic alteration of the fault core is a factor of the fluid and temperature histories of fault zone has experienced, and therefore may not be able to be predicted in the same manner as mechanically deformed fault rocks (i.e. cataclasite and fault breccia). This means that predictions of cemented faults, which are more a function of the fault zone fluid history, could also inhibit accurate fault permeability calculations.

Previous FRC data from Malta suggested fault cores are continuous at >60 m (Michie *et al.* 2014) and >30 m (Cooke *et al.* 2018), but none have explicitly stated a continuity threshold. All fault zones studied by Cooke *et al.* (2018) have continuous fault cores, of which the lowest throw is 30 m. Michie *et al.* (2014) states that the threshold for a continuous fault core is somewhere between 25 m and 60 m, with no fault zones studied between these throws. Therefore, the continuity relationship suggested in this study (Figure 5-6), with a FRC threshold of 30 m, agrees with these prior observations.

For a more generalised predictive algorithm, additional permeability and continuity data would be required for other faulted carbonates. In particular, additional data from lower-moderate porosity carbonates (<5-15%), lower fault throws (<30 m), and from deeper burial, in which crystal-plastic deformation mechanisms may be more prevalent to those observed in Malta. The role of increasing throw on permeability heterogeneity along the fault core, as indicated by Michie *et al*. (2017) will also be useful in calibrating these relationships.

5.9.2. Fault core fracturing

Whilst fault damage zones in carbonates are typically associated with brittle fracturing (e.g. Billi *et al.* 2003, 2007), moderate-high porosity rocks more commonly exhibit compactional features

in the damage zone, such as deformation bands (Rath *et al.* 2011; Cilona *et al.* 2012; Antonellini *et al.* 2014; Kaminskaite *et al.* 2019). Despite this, fractures are commonly observed in the damage zones of the most porous carbonate formations in Malta (Figure 5-17), particularly in the weaker GL formation and the lower porosity Attard member, which favour extensional fracturing (Michie 2015). This would typically indicate that these fault zones would be conduits for up-dip fluid flow. How these fractures impact across-fault fluid flow depends on whether the fractures crosscut the fault core. Fracturing in the fault core in Malta occurs in all brittle fault rocks (e.g. cataclasite), which commonly host slightly lower fracture intensities than the surrounding damage zone (Figure 5-17B). Fault breccia can often be highly fractured in isolated lenses (Figure 5-17A & C), or can be highly cemented with no open fractures. Fractures generally terminate at intersections with ductile fault core material, such as Blue Clay smears (Figure 5-17D). Overall, this indicates that fault core fracturing is isolated to uncemented lenses of fault breccia, or postdates the formation of fault rock and fault core cementation. Fault core cementation increases brittleness of the fault rock and, consequently, increases the susceptibility to later fracturing. In the case of the Maltese fault zones, late stage fracturing may have occurred during fault reactivation, or during uplift and exhumation. Therefore, these fractures may not be representative of the fault zone at reservoir conditions. Assuming fault core fractures postdate faulting and are not representative of these faults at subsurface conditions, fracturing is unlikely to contribute to the bulk fault core permeability. Additionally, fracture healing is often a common feature of fault zones, reducing the potential for fracture dominated permeability in the fault zone.

If fault core fractures are indeed absent in the subsurface, the lower production resulting from a low permeability fault in a fractured reservoir compared with a low permeability fault in a non-fractured reservoir (Figure 5-15) could have implications to certain porous reservoirs that have experienced faulting after a phase of fracturing. In Malta, this may have an impact on the effect of faulting, whereby permeability reductions are increased by at least an order of magnitude, depending on fracture intensities and permeability. To establish more robust predictions of the effect of faulting in a fractured reservoir on fluid flow, sensitivity analysis could be undertaken to determine the sensitivity of production results on a range of key parameters. Key parameters may include host rock porosities, absolute and relative permeability, pressures, fracture geometries etc., thus enabling a better understanding of the ranges of conditions in which faults may impact fluid flow in porous carbonates. Additionally, further work is required to locate

field examples of faults in porous type III reservoir analogues, allowing investigations in to fault core fracturing and bulk fault permeability reductions in these scenarios.

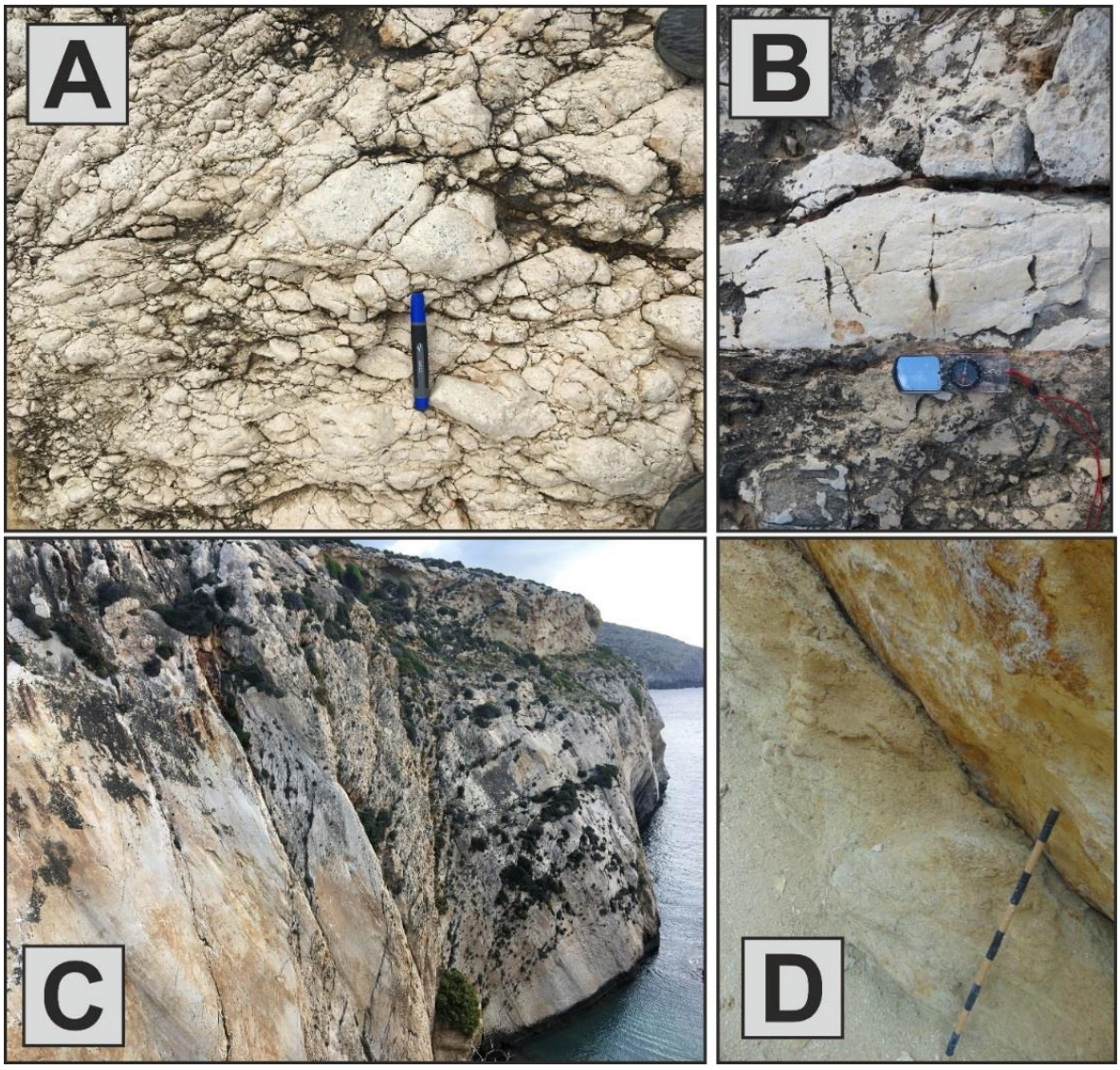

Figure 5-17: A) Example of highly fractured lens of fault breccia. B) Example of small aperture fractures crosscutting the fault core cataclasite. C) Example of a slip surface cut by several large aperture fractures, spaced by several meters (foreground), and highly fractured breccia lens (background). D) Example of ductile clay smear containing no fractures, juxtaposed against fractured hanging wall (hanging wall fractures not pictured).

5.10. Conclusions

Structural and petrophysical data from eight fault zones in Malta has been used to determine predictive relationships between host and fault properties. Fault rock continuity data indicates that fault cores become continuous after 30 m throw in the studied carbonates. Below this threshold, there is a clear relationship between increasing fault throw and increasing fault rock continuity. Fault rocks are divided in to three primary categories: cataclasite, fault breccia and cemented faults. Permeability contrasts between host rock and fault rock for each of these formations are calculated, showing reasonable relationships between increasing host rock porosity and increasing permeability contrast for each type of fault rock. These relationships are integrated in to fault core thickness calculations during fault zone modelling in TrapTester, whereby a proportion of fault cells (representing the estimated fault rock coverage) are assigned 0 m thickness.

Relationships are also derived between fault throw and the thickness and continuity of each fault rock type, allowing for predictions of the proportional area of the fault core that corresponds to each of the fault rocks. Together, this enables predictions of either area-weighted arithmetic or geometric average permeability for both sides of the fault separately, depending on the assumed fault rock distribution. Fault cores in Malta are characterised by a mixture of hanging wall and footwall derived fault rocks, therefore, combining predictions of hanging wall and footwall fault permeability provides a geologically realistic estimate of the overall fault core continuity for any two juxtaposed lithofacies.

A production simulation representing the island of Gozo was generated to test the impact of faults on fluid flow when using the outlined predictive relationships. Fault connectivity is poor in this model, however, fault bound compartments are still generated when faults are completely sealing, such that production is impacted by low permeability faults. The model shows faults to have negligible impact on fluid flow when using these relationships, due to the low fault throws and the high proportional area of high permeability fault breccia predicted in the fault zones. However, if individual fault rock types, such as cataclasite are continuous, the harmonic average of fault rock permeability is the most geologically realistic method of averaging, which would likely lead to much lower predicted fault permeabilities and, therefore, lower transmissibility multipliers. Additionally, production may be impacted more in a type III fractured reservoir, assuming fractures do not cut the fault core, as argued for Malta. In this scenario, the bulk host

rock permeability is increased due to the contribution of fracture permeability, thereby increasing the permeability contrast between host and fault.

Overall, additional fault rocks, such as recrystallised fault rocks, need to be included within the predictions for a more accurate model of faults in Malta. Following the same process with data from a series of other carbonate lithologies in different settings may enable more general predictive relationships which can be utilised in fault seal analysis workflows.

CHAPTER 6.

Discussion

The following sections address the research questions stated in Chapter 1, by outlining the key findings from Chapters 3-5 (Section 6.1) and comparing these findings to several additional examples of carbonate-hosted fault zones (Section 0). These discussions are drawn together in Section 6.3 to discuss the overarching controls on fault-related deformation in porous carbonate rocks, and the likely impact on fluid flow.

6.1. Summary of key findings

6.1.1. Research question 1

What are the key factors governing fault rock texture and permeability in shallowly buried porous carbonates?

Low-moderate porosity (5 - 15%) limestones (Attard member, LCL) experience limited cataclasis under low stresses (i.e. shallow burial). Instead, deformation is dilatant and relatively distributed, manifesting through extensional fracturing and brecciation (Figure 3-6). Dilatant deformation is common in fault zones from low porosity carbonates, leading to fracture-derived cataclasis over high throw accumulations (e.g. Billi *et al*. 2003; Agosta *et al*. 2007; Schröckenfuchs *et al*. 2015; Demurtas *et al*. 2016). Therefore, it is interpreted that cataclasite in these rocks would form as a result of continual pervasive fracturing over large displacements, but such fault rocks are rarely observed in the studied fault zones. The micritic GL behaves in a similar manner, experiencing extensional fracturing and no pervasive cataclasis, despite the porous granular texture (Figure 3-9). The lack of cataclasis of *Globigerina* foraminifera grains has been reported by several authors; Rotevatn *et al.* (2016) showed how echinoderm fossils are preferentially subject to cataclasis, which is suggested to be a result of the coarser and more angular echinoderm fragments relative to the solid shell framework and spherical shape of globigerina foraminifera. Thus, preventing grain rolling of echinoderm fragments and allows for high stress concentrations at sharp grain contacts. Additionally, syntaxial overgrowth cements, which commonly surround echinoderm fragments, may strengthen grain contacts and promote preferential cataclasis of echinoderms (Cilona *et al*. 2014). Alternatively, the minor clay content within the micritic host rock may help accommodate some of the strain during faulting, by enhancing processes such as

pressure solution (Viti *et al*. 2014), so that stresses are not high enough to enable intragranular extensional fracturing (IEV) of the *Globigerina* foraminifera (Michie *et al.* 2014). However, well developed pressure solution seams are not observed, only minor sutured grain contacts (Rotevatn *et al.* 2016).

The porous granular members of the LCL and UCL experience more localised deformation through grain-scale cataclasis, even at relatively low throws (<30 m) (Figure 3-7, Figure 3-10 & Figure 4-11). This occurs principally through the rolling of individual grains, leading to intragranular extensional fracturing (IEF), grain chipping, and comminution. Survivor bioclasts (i.e. individual grains with little to no deformation) are common in all cataclasite samples and are commonly observed in cataclasites elsewhere (e.g. Billi *et al*. 2003; Agosta *et al*. 2007; Demurtas *et al*. 2016; Ferraro *et al*. 2018). The formation of these grains may be a result of preferential deformation of weaker material that has already been generated through cataclasis. Survivor grains are generally subrounded, either through grain-chipping or due to their initial morphology; this allows them to move freely within the weaker matrix during cataclasis, without generating high stress concentrations at grain contacts (Cladouhos 1999). In high porosity syn-tectonic sediments (UCL), formations that have undergone deformation prior to complete lithification exhibit deformation bands in the fault damage zone, whereby the lack of intergranular cements allow reorganisation and the alignment of bioclasts along compaction or shear bands (Figure 3-8). These mechanisms of deformation band formation have been outlined previously in similar granular porous carbonates (Rath *et al*. 2011). Increased intergranular cements occur in these bands relative to the surrounding rock, resulting from preferential dissolution of bioclasts with poor metastability (e.g. Cilona *et al.* 2012; Kaminskaite *et al.* 2019), or minor pressure solution at grain contacts. Together with the tighter packing of bioclasts, increased cements lead to porosity reductions from >30% to 5 -10%. Deformation bands occur in arrays, distributed non-uniformly along strike, thereby providing evidence for the geometric model of deformation band formation, outlined by Nicol *et al.* (2013); deformation bands develop incrementally within clusters at fault irregularities (e.g. bends, relays, splays) as part of slip localisation, asperity removal, and strain weakening. This is in agreement with the observed location of deformation band arrays; deformation band arrays are located in the region of intersection between the SGF and the SQF (Figure 3-8), within the highly complex interactions of multiple subsidiary slip surfaces along the VLF (Michie *et al.* 2014), and within lenses of rotated host rock or at fault intersections along the IMF (Bonson *et al*. 2007; Rotevatn *et al*. 2016).

Pore space occlusion (cement precipitation) and destruction (cataclasis) results in microscale textural homogenisation from host rock to fault rock, as evidenced by core plug CT imaging. On larger scales, heterogeneity is increased from the host rock to the fault core, as evidenced by the variability in fault rock petrophysical properties (Table 4-1 & Table 4-2). Textural homogenisation within the fault core provides the potential for low permeability fault rocks (Figure 4-10); cataclasis in packstone rocks can result in permeabilities reaching as low as 10^{-6} mD. The lack of cataclasis in the GL wackestone formation does not prevent low permeability fault rocks from forming; cemented faults can exhibit similarly low permeabilities as cataclasites (Figure 4-10). However, the lower initial porosity and more complex pore network of the algal packstones means that cement precipitation is not as pervasive and, therefore, the potential for low permeability fault rocks in this lithofacies is more limited (Figure 4-12).

Results show how the permeability of the principal fault rock types (i.e. cataclasite, fault breccia, and cemented faults) are a product of the host rock porosity from which the fault rock is derived; host to fault rock permeability contrasts are greater for high porosity host rocks (Figure 4-12). Ultimately, the greater the porosity of the host rock, the greater the potential for pore occlusion and reduction in permeability. The exception to this relationship is within high porosity but low permeability rocks, such as clays and chalks, in which the potential permeability reduction is limited by the low initial permeability; in chalks, the high initial porosity is dominated by poorly connected intergranular porosity, such that grain crushing has negligible impact on the amount of connected porosity (Kaminskaite *et al.* 2019). Additionally, these relationships are based upon geometric averages of fault rock permeability, and do not account for the permeability heterogeneity of each fault rock type. No clear relationships between fault rock permeability and throw were established. However, throw is shown to control a number of factors influencing the bulk fault core permeability, such as fault rock distributions, thickness and continuity. Permeability contrasts of several orders of magnitude are achieved along faults with very minor displacements (e.g. Fisher & Knipe 2001), in addition to along deformation bands with negligible displacements (e.g. Kaminskaite *et al.* 2019). Thus, indicating that fault related deformation can drastically reduce permeability at any displacement.

Calcite cement precipitation is common in all faults and lithofacies observed in Malta. These cements act to occlude pore spaces in fault rocks or cement tabular regions between parallel slip surfaces. Structurally complex areas along small displacement normal faults in Malta have been shown to coincide with increased fluid rock interactions, attributed to higher fracture

connectivity than surrounding areas, which allows for localised flow of mineralised fluids (Dimmen *et al.* 2017). This can be observed in the studied fault zones, with porosity reducing along strike of the SQF, Gozo, towards the structurally complex relay zone (Figure 6-1); this indicates that calcite precipitation may be more prominent in lithofacies that are prone to distributed brittle deformation (i.e. algal packstones or wackestones). Without detailed analysis of cements, revealing the diagenetic evolution of these fault zones (e.g. Laubach *et al.* 2014; Aubert *et al.* 2019; Ferraro *et al*. 2019), the role of post-exhumation surficial cementation on fault properties cannot be fully deciphered.

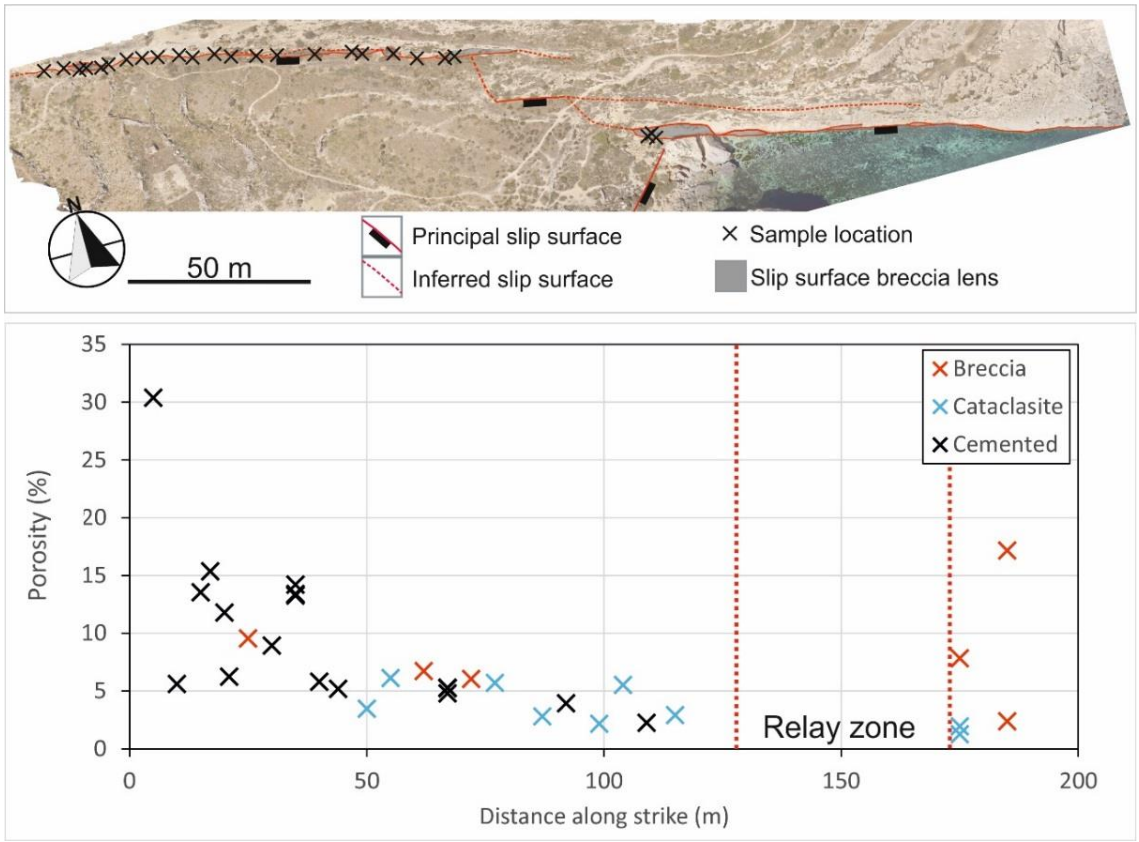

Figure 6-1: Along strike variation in porosity for the South Qala Fault, Gozo. Sample locations along the fault are shown in the map above. 0 m distance along strike represents the westernmost fault exposure.

6.1.2. Research question 2

What are the key controls on the thickness and continuity of fault rock in shallowly buried porous carbonate rocks?

The findings of research question 1 highlight how host rock composition and texture have an effect on the style of deformation and resulting fault rock textures, principally relating to whether deformation is more localised or distributed. The style of deformation is a major control on the thickness and continuity of fault rocks in the studied formations, whereby narrower fault cores are formed during localisation, and wider fault zones with several slip surfaces are expected under a distributed style of deformation. Therefore, the distribution of fault rock is also partially related to host rock composition and texture.

During distributed deformation, strain is accommodated through the formation of multiple slip surfaces and extensional fracturing (e.g. Faulkner *et al.* 2003; Ferrill *et al.* 2011; Michie *et al.* 2014). Thus, leading to a wide fault zone with high damage zone fracture intensities and a lack of continuous cataclastic fault rock along individual slip surfaces at the throws studied (<200 m). Fault breccia is a common product of distributed deformation, relating to the entrainment of lenses of host rock during fault segment interactions (e.g. Childs *et al*. 2009). Fault zones with these characteristics are termed distributed damage zones (DDZ), characterised by low fault rock continuities spread over multiple slip surfaces. Over increased fault displacements, it is likely that the fault bound lenses within these zones will become entrained within the fault zone, forming lenses of fault rock, such as fault breccia or fracture derived cataclasite. In contrast, the localised deformation observed in packstones leads to a narrow fault core with strain predominantly accommodated through the formation of cataclasite veneers. Fault linkage processes and asperity shearing still occur along these localised fault zones, such that fault breccia is still common, but to a lesser extent than in a DDZ due to fewer fault segment interactions. This is in agreement with the geometric fault core evolution model outlined by Childs *et al.* (2009). Fault zone outcrops in Malta that are characterised by a DDZ are generally on the order of tens to hundreds of meters long, whereas the entire fault length could be kilometres. This means that although fault zones may exhibit a DDZ at outcrop, the fault segment may be more localised along strike or down dip. This is evidenced along the IMF, which is exposed over several kilometres and contains structural irregularities along strike, leading to regions of more localised deformation and regions or highly complex fault segment interactions (Bonson *et al.* 2007). Therefore, fault zone statistics that help

to determine the occurrence of structural complexities would be extremely useful in predicting the true three-dimensional hydraulic behaviour of fault zones (e.g. Manzocchi *et al.* 2019).

Fault core continuity increases up to 30 m throw, after which fault cores are continuous in the studied fault zones (Figure 5-2). This differs from previous published thresholds for continuous fault cores (Micarelli *et al*. 2006; Michie *et al.* 2014; Bauer *et al*. 2016). However, a discontinuous fault core with high continuity is observed at 60 m throw, indicating that no single thresholds defines fault rock continuity. Additionally, this highlights the uncertainty surrounding fault rock continuity measurements. Fault cores are composites of discontinuous fault rocks derived from both the footwall and the hanging wall. Cataclasite and fault breccia distributions are also functions of fault throw. Cataclasite increases in thickness and continuity with throw, becoming continuous at around 200 m in high porosity packstones (Figure 3-15). Fault breccia thickness also increases with throw, but the continuity of fault breccia is not clearly influenced by throw (Figure 5-5). It is important to note the difficulty in estimating the full continuity of fault rock, due to inaccessible areas of the fault zone, erosion, sediment cover on the fault surface and only being able to observsse fault rock continuity over relatively small windows of entire fault lengths. Additionally, structural complexities will likely occur along all fault zones, such that regions of poor fault rock continuity will be distributed along the fault zone. Therefore, the throw threshold values suggested here are likely underestimates of the true fault rock continuity. In general, fault rock thickness is highly variable, which reflects the scatter in global fault core thickness for a given displacement (Solum & Huisman 2017). The average thickness may increase with displacement, but thinner areas of fault rock will act as potential leakage points. The difference between hanging wall and footwall fault zone thickness is not investigated within this study, predominantly due to a lack of fault zones with both a well exposed/preserved footwall and hanging wall. However, at a number of fault zones, the damage zones are wider in the hanging wall, such as the large throw exposures of the VLF, SGF, and IMF (>100 m). The lithology of the juxtaposed formations appears to have a greater deal of impact on the fault zones thickness in the studied fault zones; structural complexities such as fracture splay zones originating from mechanical contrasts between different formations have been shown to lead to wider hanging wall fault zones in the micrite-dominated GL formation (Michie *et al*. 2014). In addition, the footwall of the QPFZ has a much wider and more complex damage zone compared to the hanging wall, due to the low porosity of footwall host rock leading to distributed brittle deformation (Figure 3-6).

6.1.3. Research question 3

Can the bulk fault core permeability be predicted from lithological parameters in shallowly buried porous carbonates?

Relationships between host rock properties and fault rock permeability have been established, showing how increasing host rock porosity leads to reducing average fault rock permeability. This is also true for the three principal fault rock types (cataclasite, fault breccia, and cemented faults) (Figure 5-7). The average permeability was used to determine permeability reductions from host to fault rock for each fault rock type, which provides a simple predictor of fault rock permeability for carbonate lithofacies of known porosity and permeability. These relationships are weakly correlated for the formations in Malta, which is likely due to a number of reasons: the wide range in permeability recorded from different fault rock types is not reflected in the geometric average permeability values; as previously stated, the potential permeability reduction is also partly a function of other factors, such as the host rock permeability and grain size; only four data points are not sufficient to capture the heterogeneity that is inherent to carbonate-hosted fault zones and deformation. Moreover, these relationships are not necessarily broadly applicable to fault cores in other carbonate rocks, as additional controls on fault permeability, such as burial history, are not accounted for in this study; all formations in Malta have experienced similar burial and tectonic histories. The principle difference between the burial histories in the Maltese stratigraphic sequence is that the younger formations are syn-rift lithofacies (Dart *et al.* 1993), which has influences on the style of deformation (see discussion on deformation band formation in the UCL; Section 3.4.2). It is not clear whether this also influences fault rock distributions from the studied formations; the majority of faulted UCL in Malta is located in hanging wall blocks adjacent to clay smears that have no clear slip surfaces.

To predict overall fault core permeability, the different fault rock permeabilities predicted for a given lithofacies must be combined and upscaled based upon the distribution of fault rock in the fault core (Manzocchi *et al.* 1999) by using either the area-weighted arithmetic average, the thickness-weighted harmonic average, or the volume-weighted geometric average of fault rock permeability (Figure 5-4). Area-weighting arithmetic averaging accounts for the cross-sectional area of each fault rock, whilst assuming fault rocks are distributed in a sequence of flow-parallel layers. Thickness-weighting harmonic averaging accounts for the thickness of each fault rock, whilst assuming fault rocks are distributed in a sequence of flow-perpendicular layers. Volume-

weighting geometric averaging accounts for the volume of each fault rock within the fault core, whilst assuming fault rocks are distributed in a heterogeneous overlapping sequence. Arithmetic and geometric averaging best represent the majority of fault zones in Malta; upscaled bulk fault permeability calculated using these methods tends towards the higher permeability fault rocks, representing how flow is focussed through these units (Figure 5-16). Harmonic averaging best represents the high throw fault zones, in which fault cores are composed over more continuous layers of fault rock; upscaled bulk fault permeability calculated using this method tends towards the lower permeability fault rocks, representing how fluids have to flow through each layer of fault rock. Relationships between fault throw and fault rock distributions, outlined in Section 0, are used to predict the cross-sectional area and thickness of each fault rock type within a given fault core, thereby providing weightings for permeability averaging. As with permeability, these weightings are not likely to be broadly applicable to fault zones in different carbonate rocks; fault rock distribution relationships may be self-similar in the Maltese stratigraphic sequence, but there is additional controls on fault rock distributions which require a broader database of faulted carbonate lithologies to determine. Further limitations reside with these estimations of fault core permeability due to the relationships being based on just four lithofacies, of which only one has a low porosity (<15%). Therefore, any relationships would be better constrained by including a wider database of faulted carbonate lithofacies.

Upscaled bulk fault core permeabilities are not sufficiently low to have a noticeable impact on production of oil when fault rocks are discontinuous within the fault core (Figure 5-12). Production is marginally reduced when fault rocks are considered continuous within the fault core (thickness-weighted harmonic average permeability). This indicates that fault zones in Malta would be unlikely to be significant barriers to fluid flow at subsurface conditions. Whilst there is no subsurface data to support this, gas migration from fault lineations in the Malta Plateau, Central Mediterranean Sea, indicates that faults may behave as conduits to up fault fluid flow (Micallef *et al.* 2011). However, this may relate to damage zone fracturing and may not directly relate to the hydraulic behaviour of the fault core.

6.2. Comparisons to other fault zones

The following subsections describe fault zones outcrops from different carbonate lithologies, either from the authors own field observations or from published studies, in order to compare and contrast the controls on fault rock formation, distribution, and petrophysical properties with those of Malta.

6.2.1. Porous carbonates

Blackhall fault, Durham, UK (unpublished)

Blackhall colliery is a 40 m normal fault cutting porous, dolomitic, oolitic limestones from the Zechstein Roker Formation (Z2), located on the Durham coast, northeast UK (Figure 6-2a). The Roker formation is a shallow-water platform carbonate, up to 60 m thick and dominated by oolitic grainstone (Tucker 1991, Smith 1995). The hanging wall is an oolitic shoal facies, with porosity of 10-30%, and the footwall is an intertidal/supratidal facies, with a porosity of <10% (Clark 1986). Faulting occurred during the Mesozoic, which was succeeded by a period of inversion in the late Cenezoic (Arthur 1993). However, evidence of reverse fault movement was observed at outcrop. High porosity in the oolitic facies related to leaching of the central ooid cores during aerial exposure prior to burial (Clark 1980). Therefore, porosity would likely have been high at the time of faulting. The overlying intertidal facies has a lower porosity due to vadose compaction (Clark 1980). Generally, the intertidal facies is reported as having a poor reservoir quality, due to anhydrite cement precipitation occluding remaining porosity (Clark 1986). Whilst this is not observed at outcrop, anhydrite cements may have been leached post-exhumation.

Deformation is focused in the hanging wall rocks, whereby extension is accommodated by the formation of box jointing, which has subsequently been cemented by calcite (Figure 6-2e-f). Moving towards the principal slip surface, the fractures become increasingly pervasive, generating cement supported fault breccia which becomes more chaotic towards the slip surface (Figure 6-2b). Along the slip surface exists a narrow uncemented fault gouge that is around 2 cm in thickness, overlying a footwall derived cemented dolomitic fault gouge of similar thickness, with flow banding showing evidence of gouge fluidisation (Figure 6-2b-d). The footwall hosts regions of uncemented fault breccia, about 2 m thick. The hanging wall fault breccia is >10 m thick, however only a cross-section of the fault zone is present, so the continuity is unknown. Relative to the studied fault zones in Malta, this breccia is exceptionally thick, however the mechanisms

through which it has been generated are different. The Zechstein formation here is estimated to have been buried to a depth of 1.5 km (Clark 1986), and the pervasive calcite cement, together with fluidised calcite fault gouge, as evidenced by an irregular boundary of fault gouge exhibiting flame-like structures and cuspate-lobate margins (Figure 6-2d), may be suggestive of high fluid pressures or overpressures at the time of faulting, also leading to hydrofracturing in the hanging wall. Fluidisation structures along slip zones are also indicative of high strain rates during seismic slip (e.g. Demurtas *et al.* 2016; Smeraglia *et al.* 2017).

Under the mechanisms controlling fault rock formation in Malta, the high porosity oolitic dolomite would have formed a localised fault core and the tight footwall would have formed a distributed damage zone of fault breccia. This is in contrast to the deformation observed, whereby fault gouge is fracture derived, as evidenced by sheared clasts of host rock (Figure 6-2c). The relatively high stresses involved, together with the effect of pervasive mineralisation, are perhaps the cause of this. Additionally, the footwall here is much weaker than the Attard member of the LCL, which further allows pervasive fracturing adjacent to the fault. Under the higher stresses and the interpreted high fluid pressures at the time of faulting, much thicker zones of deformation are able to form, which can be highly altered through mineralisation. The lack of mineralisation of the fault breccia zone in the footwall indicates that either the gouge material may have provided a seal to mineralising fluids, or the tight porosity of the footwall intertidal facies at the time of faulting prevented the accumulation of high fluid pressures.

No permeability data is available from this fault zone due to difficulties collecting samples; fault breccia clasts are extremely soft and do not survive coring. However, porosity obtained from image analysis shows that fault gouge has a porosity of *c.*10%, whilst the calcite cemented matrix of the hanging wall fault breccia have porosities reduced to <1%. This may impact fluid flow in regions close to the slips surface where breccia is more chaotic and cement content is highest.

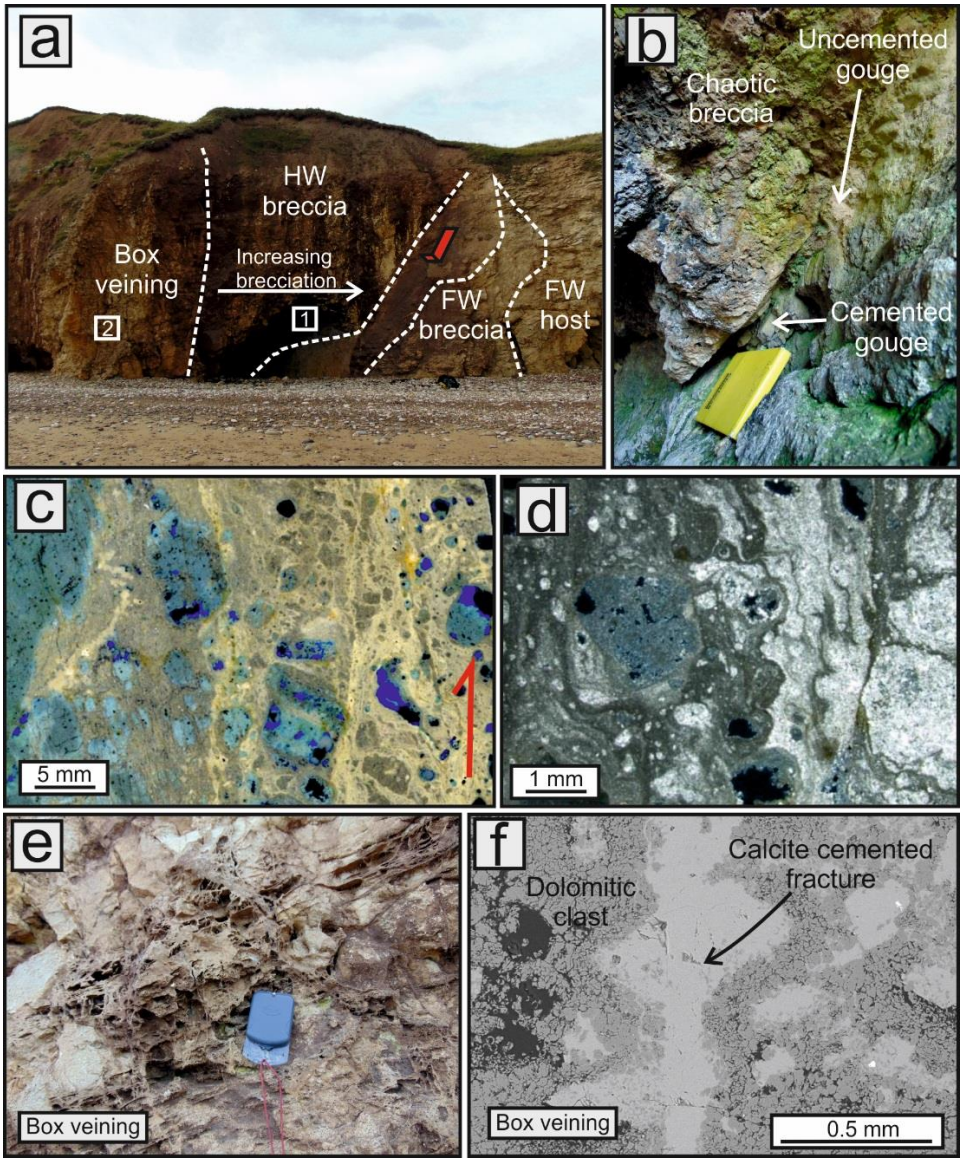

Figure 6-2: a) Photograph of the Blackhall Fault, Durham, UK. b) Fault rock at the PSS (location 1 on photo a). Fault breccia becomes increasingly chaotic towards the PSS, comprising an uncemented fault gouge overlying a cemented fault gouge. c) Cemented fault gouge. Porosity is blue, dolomite is dark grey, and calcite is light grey/yellow. From left to right the sample changes from fractured wall rock to sheared breccia and to fluidised gouge. d) Photomicrograph of the cemented gouge, showing evidence of fluidisation. e) Box veining in the hanging wall, consisting of clasts of host rock surrounded by a calcite cement (location 2 on photo a). f) SEM image of calcite cement between two clasts of host rock from an area of box veining.

Strike-slip faults, Southeastern France Basin (Jeanne *et al.* 2012)

Jeanne *et al.* (2012) describe the structural and petrophysical properties of a low displacement strike-slip fault in a layered sequence of porous (15-20%) and low porosity (<5%) carbonates. They show how the porous layers have progressively reduced porosity towards the fault core due to micromechanisms such as pressure solution. In the low porosity layers, fracture intensities and fracture porosity progressively increase towards the fault core. The fault core is variable in composition, with fault gouge occurring along slip surfaces and between parallel indurated slip surfaces. The gouge is 10 times thicker when formed between parallel slip surfaces, compared to that of single slip surface (30 cm vs 3 cm), and is associated with wing crack development between the overlapping faults. Along single slip planes, the gouge formation is associated with the gradual incorporation of thin (20 cm) fault breccia to the fault core. Gouge is discontinuous, as a result of the fault being composed of multiple slip surfaces along which strain is localised in specific areas (between relays and along portions of single slip surfaces). The fault rock formation in this fault zone is consistent with the geometric model of fault zone evolution, whereby fault irregularities such as overlapping fault zones lead to the incorporation of host rock to the fault core (Bonson *et al.* 2007; Childs *et al.* 2009). The contrasting deformation mechanisms observed between the low porosity and porous members of the damage zone are also consistent with the deformation observed in Maltese fault zones. However, the incorporation of breccia within the fault gouge (i.e. fracture derived cataclasis) is something rarely observed in Malta. This is potentially due to a combination of factors, such as the lack of fault gouge preservation in Malta due to preferential weathering, or the more complex mechanical stratigraphy in the Southeastern France Basin, which typically leads to more structurally complex fault zones (Ferrill & Morris *et al.* 2008), or the presence of pre-existing fracture planes that may promote fracture-derived cataclasis.

Castellas fault, SE France (Matonti *et al.* 2012)

The Castellas fault in SE France is 40-80° dipping fault with 1.5 to greater than 5 m throw, cutting a succession of low to moderate porosity (5-16%), fine grained calcarenite packstones to grainstones. The fault has been subject to two episodes of slip, the first due to extension and the second due to a sinistral strike slip event. The initial stage of normal fault movement occurred when bedding was horizontal, producing a fault breccia core and fault parallel tension gashes. The fault breccia is characterised by angular clasts with a laminated micritic matrix, suggesting sedimentary filling of void space occurred after extensional deformation. This fault breccia is cut

by a secondary fault breccia unit, which is characterised by more rounded clasts with a fine grained or calcite cement matrix and stylolitisation. The second breccia unit is interpreted to be a result of the sinistral reactivation following bed rotation. The fault zone is highly complex, with fault cores varying from areas of absence, to thin (several cm) fault gouge, and various types of fault breccia. Structural variations may be a result of changes in mechanical properties of the faulted succession. Additionally, the host facies are reported as having highly variable porosity within a single facies, ranging from 5-16%, which is likely to lead to complexities in deformation. This agrees with CT data from Maltese fault zones, which indicate that host rock textural heterogeneity is retained through deformation, generating heterogeneous fault cores.

The structural complexity is interpreted to result in variable hydraulic properties of the fault zone. On the microscale, structural units that have experienced large amounts of deformation and cementation are considered to be impermeable barriers to flow, whereas regions of uncemented fault rocks or where fault core does not exist are considered to be conduits or have no impact on flow. At the meter scale, fractures cut through some of the low permeability units. These areas are likely to be conduits to flow where fractures cut these units and have sufficient connectivity. Additional regions of the fault zone were identified as having mixed conduit/barrier conditions, such as regions of thick and continuous cemented fault breccia forming a fault core that behaves as a barrier to across-fault fluid flow, surrounded by fractured wall rocks that behave as conduits for along-fault fluid flow. Variability in the hydraulic behaviour of fault zones is also exhibited in Malta, whereby variable fault rock distributions, fault geometries, and fault rock petrophysical properties result in areas of low fault core permeability adjacent to areas of high permeability fault core. Whilst this generates a mixture of hydraulic behaviours that may influence fluid flow at the local scale, they are likely to have negligible impact on fluid flow at the reservoir scale.

6.2.2. Low porosity carbonates

Elbingerode fault, Harz Mts., Germany (Unpublished)

The Elbingerode fault is a large scale fault of unknown displacement, cutting a tight (<2% porosity) Devonian crystalline limestone reef complex. The polished PSS and footwall damage zone are well exposed for approximately 800 m along strike in an open limestone quarry near Elbingerode, Germany (Figure 6-3a). The Devonian limestone has been buried to a depth of 6 km and subject to a high geothermal gradient, relating to local Devonian volcanism (Weller, 1991). Deformation is dominated by extensional fracturing and by plastic mechanisms, such as calcite

twinning, diffusive mass transfer, and grain boundary migration. Brittle deformation is highly distributed in the footwall, leading to fault parallel fracturing, fault breccia formation, and fracture derived cataclasite formation. Along planar segments of the polished fault surface, there is commonly a thin layer of fault breccia, from <1 cm to 8 cm. The fault breccia is composed of sheared clasts of host rock supported by a calcite matrix. Clast size varies from several cm to <1 mm, becoming smaller towards the PSS, forming a fracture-derived cataclasite in some areas (Figure 6-3b, e & f). Along more irregular regions of the fault surface, relating to fault bends or changes in dip angle, there are often discontinuous, large (several meters thick), highly fractured lenses of fault breccia. The architectural controls on fault rock distribution are similar to that of Malta despite the considerably different host rock texture and burial history.

The low host rock porosity promotes extensional fracturing and subsequent fault breccia formation, leading to fracture-derived cataclasite (Figure 6-3b). This cataclasite differs from the grain-scale cataclasite occurring in Malta, as it forms due to pervasive fracturing and cementing of the matrix rather than deformation of individual bioclasts. These processes lead to thin <2 cm veneers of cataclasite immediately adjacent to the PSS, which have diffuse boundaries with chaotic breccia in to the footwall. This is more reminiscent of the damage zone-fault core transition described in low porosity rocks studied by Billi *et al.* (2003). The high stress and temperature experienced by the rocks at the time of faulting lead to crystal-plastic deformation mechanisms accompanying brittle deformation. Plastic deformation mechanisms are also observed in Malta; minor diffusive mass transfer occurs due to pressure solution at grain contacts, principally in cataclasite and deformation bands, and grain boundary migration is reported, leading to recrystallised fault rock fabrics (Michie *et al.* 2014). However, these processes are much less prominent than along the Elbingerode fault, due to the elevated pressures and temperatures at the time of faulting.

The permeability of the undeformed Devonian limestones are on the order of 10^{-4} mD to 10^{-5} mD. Fault rocks range in permeability from 10 mD to 10^{-4} mD, with porosities from 2% to 10%. The fault rock fabric has no clear impact permeability. Combining this permeability data with structural observations, which show high fault parallel fracture intensities, indicates that faults in these tight limestones are likely to behave as conduits to fluid flow. A cross-section exposure of a separate parallel fault, Fault 2 (Figure 6-3c), approximately 100 m south, shows there to pervasive fracturing in the fault core, with clast size reducing down to a fine grained fault gouge along the

footwall PSS (Figure 6-3d-e). This fractured region of the fault core is likely not preserved along the main quarry wall, and provides further evidence of the fault behaving as a conduit to fluids.

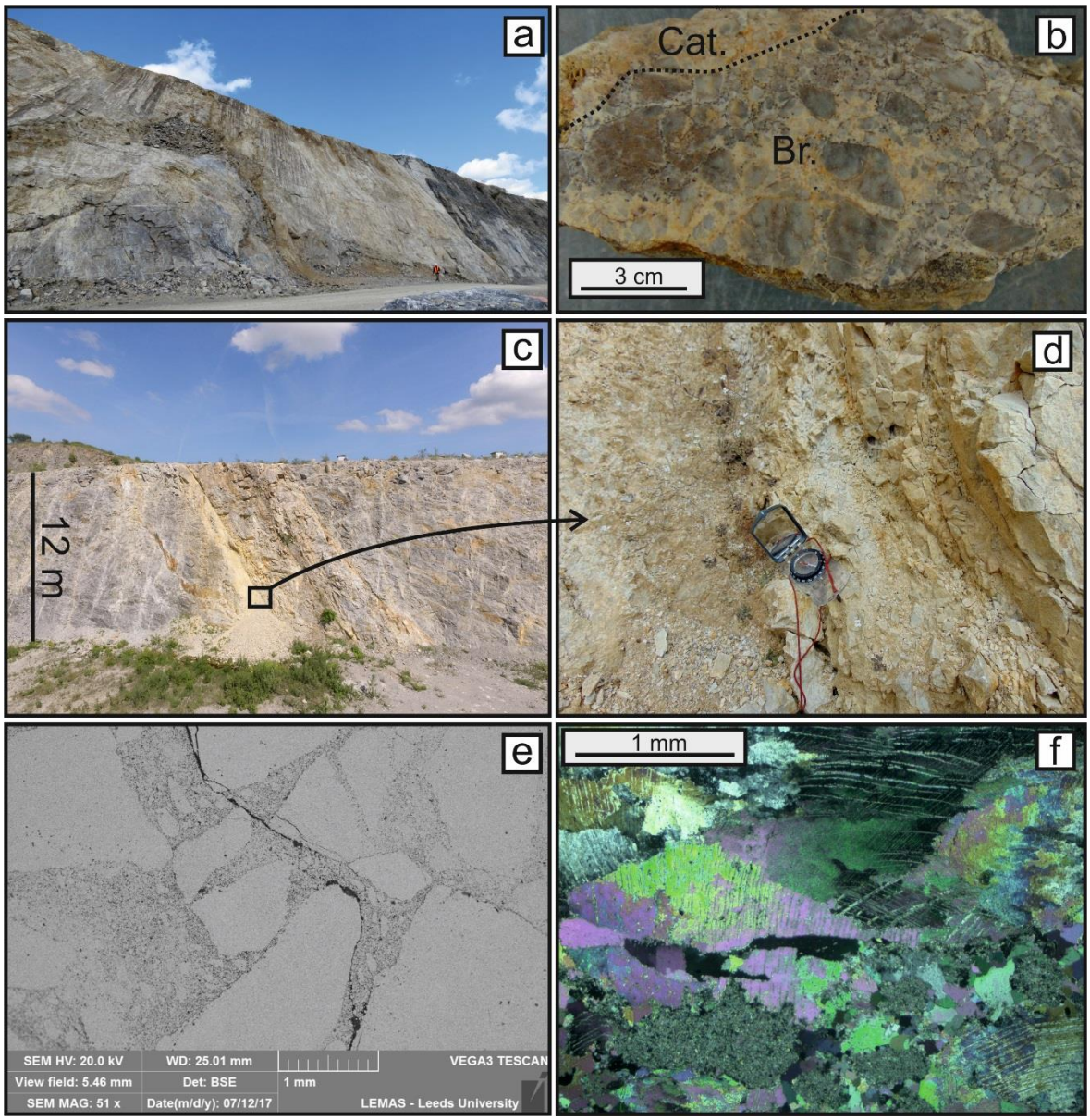

Figure 6-3: a) Photograph of the Elbingerode fault exposure along the quarry wall. b) Hand specimen of fault breccia (Br.) with veneer of fracture-derived cataclasite (Cat.). c) Photograph of secondary normal fault in the quarry wall (fault 2), showing multiple parallel slip surfaces that hosts a fine grained fault gouge. d) Image of fault 2 core with reducing grain size towards a fault gouge. e) SEM image of cataclasite from the fault 2 core. f) Photomicrograph (XPL) of breccia from the Elbingerode fault, comprising a micritic clast surrounded by pressure solution seams and recrystallised veining that exhibits tapered twinning.

Pisia and Doumena faults, Corinth Rift, Greece (Bastesen *et al.* 2009)

Bastesen *et al.* (2009) studied the Pisia and Doumena faults of the Corinth Rift, Greece, cutting micritic carbonate rocks with a throw of *c.*500 m. Faults have been progressively uplifted and exhumed. Fault surfaces vary between undulating and planar, with dip changes that are interpreted to be a result of faulting during progressive rotation of the footwall block, or segment growth and linkage. The first of these interpretations includes initial faulting at depth, generating lenses of indurated fault rocks affected by pressure solution processes. The second phase of faulting occurred at shallower depths, leading to the generation of thick porous breccia and a planar PSS. Thus, highlighting how the confining pressure at the time of faulting is a key parameter determining the deformation mechanisms, thickness, and texture of fault rocks. The latter interpretation of fault geometries formed via vertical segment linkage, leading to releasing and restraining fault overlaps. Releasing overlaps lead to lenses of fault breccia, whereas restraining overlaps lead to high fracture densities. Lenses of fault breccia are ascribed to formation of R and P-shears and fault geometries such as bends or jogs. These findings are consistent with this study; faulting in Malta is most similar to the planar faults with parallel slip surfaces and similarly formed under low stresses due to the shallow burial of the Maltese sediments. Fault breccia is also commonly attributed to fault surface irregularities and fault linkage, in addition to examples of parallel planar slip surfaces bounding thick lenses of porous breccia.

Vado di Carno Fault, Central Apennines, Italy (Demurtas *et al.* 2016)

The Vado di Carno Fault zone, near Campo Imperatore, Central Apennines, is an array of normal faults with *c*.2 km of cumulative throw. The fault zone was exhumed from 2 km burial depth, juxtaposing quaternary colluvial deposits in the hanging wall against dolostones in the footwall. The footwall damage zone is 300 m thick, with extensive cataclasis; cataclasite layers of up to 30 cm thick are observed along individual slip surfaces for hundreds of meters in to the footwall, bounding various structural units. The PSS which represents the contact with the quaternary deposits comprises a polished slip surface with a 20 cm thick unit of cataclasite composed of mixed hanging wall and footwall material, containing fluidised injections of ultracataclasite. In to the footwall, the dolostone hosts a 40 m thick cataclastic unit, representing in-situ shattering and containing localised calcite veins and fluidized cataclasites. The cataclasite unit is generally calcite cemented. Outside of the cataclastic unit is the high strain damage zone, with a large zone of low strain damage zone embedded within. The high strain damage zone contains pervasive fracturing.

The low strain damage zone contains much lower fracture intensities. A breccia unit is located along low angle oblique faults, which is classed as a mosaic-crackle breccia and is characterised by pervasive dolomite veining with a gradational change to the high strain damage zone. The formation of the cataclasite through in-situ pulverisation is interpreted to be a result of high strain rate dynamic loading over multiple episodes of earthquake rupture. Fault breccia results from extensional reactivation of a pre-existing thrust. This fault zone is much more mature, exhumed from over 1 km greater depths, and is hosted by a different mineralogy than those observed in Malta. The combination of these factors means that the fault zone is much wider and much more complex than the fault zones in Malta. Additionally, the interpreted high strain-rate origins of the cataclasite are not comparable with the grain-scale cataclasites found in Malta. However, the initial shattering of the low porosity host rock leads to a highly fractured zone, in which the rhombs can be subject to similar forms of cataclasis as granular sediments.

SEPM fault system, Northern Calcareous Alps, Austria (Schröckenfuchs *et al*. 2015)

The Salzach – Ennstal – Mariazell – Puchberg (SEMP) fault system is a strike slip fault zone in the Northern Calcareous Alps, Austria. The total sinistral displacement along the SEMP is estimated to be 60-70 km. The SEMP forms a 12 km wide zone of abundant E to NE striking sinistral strike slip faults in the studied area, from which the Middle Triassic Wetterstein Formation was studied along minor branch faults. Faults accommodate relatively minor displacements of tens to hundreds of meters and formed at shallow crustal depths and temperatures. The faults cut tight dolomites (maximum burial of several kilometres).

Deformation manifests through distributed tensile microfracturing and pulverisation of the rock mass, producing fragments down to <25 μm. Grain fragments show little to no evidence of shearing, indicating that in-situ pulverisation is the dominant deformation mechanism. Slip localisation forming cataclasites are restricted to narrow (up to tens of centimetres) cataclastic zones. Mosaic breccia with calcite cement supported clasts occur containing evidence of shear. Additionally, geopeatal fragments are observed in the matrix, providing evidence that the fault breccia passed through a porous stage in which filling of void space could occur, prior to cementation. Schröckenfuchs *et al*. (2015) interpreted pulverisation along these faults to be a result of slip on rough faults with high amplitude to wavelength ratios, leading to the juxtaposition of fault irregularities and consequent heterogeneous stress conditions. These fault zones bear little resemblance to those in Malta, due to the dominant mechanisms of pulverisation along the

SEPM fault system. As with the Vado di Carno fault, the SEPM fault system is also much more complex with varying deformation mechanisms to those observed in Malta. However, these faults are of similar displacements to the faults in Malta. Despite this, similar mechanisms to the Vado di Carno fault are described here, indicating that both mineralogy and the stress conditions during faulting can lead to such different styles of fault-related deformation.

6.2.3. Mixed carbonate-siliciclastic sequences

Balcones fault system, Texas, USA (Ferrill & Morris 2008)

Ferrill & Morris (2008) describe how mechanical layering has an effect on fault zone architecture in the Balcones fault system, Texas. They note that faults that develop in massive, competent, clay poor, limestones and dolomites are characterised by planar faults, low displacement gradients, and steep dips (>70°). Faults that develop in less competent, clay-rich strata are impeded by shale beds, which results in folding and locally shallow dipping beds (<60°). This leads to narrow, localised fault zones in competent formations, and wider fault zones in incompetent formations.

Comparing the studied sequences in Malta, the competent formations of the Xlendi member (LCL) typically have narrower fault zones with more localised deformation when compared with the overlying GL formation, which is mechanically weaker (Kaminskaite & Fisher, in review), has a wider fault zone consisting of distributed deformation, and often contains fault-related folding of beds with higher concentrations of phosphoric nodules. Faults in the Attard member of the LCL also have characteristics of faults in competent formations, with the exception of the narrow fault zone. This is particularly evident at the QPFZ, in which a distributed damage zone is present in the Attard member footwall. However, complex larger scale structures relating to the dextral wrenching of the SGF are interpreted to be a possible cause of this distributed zone of deformation. The lack of localised deformation along these slip surfaces, as discussed in Section 6.1.1, is likely a result of the low effective stresses at the time of faulting. This indicates that in addition to the criteria outlined by Ferrill & Morris (2008), depth of burial, structural context, and host rock porosity are all additional factors in determining the fault zone architecture, and consequent fault rock thickness.

6.2.4. Laboratory deformation of carbonate rocks

(Kaminskaite & Fisher in review)

Through mechanical testing, Kaminskaite & Fisher (in review) show how carbonates with >10% porosity deform in the ductile failure regime at confining pressures of 20 MPa, via cataclasis, compaction, and shear enhanced compaction, and in the brittle regime, via shear failure, at lower confining pressures. Carbonates with <10% porosity deform in the brittle regime. At >25% porosity, finer grained samples, such as the GL, are more prone to grain packing, thereby forming compaction bands. At higher grain sizes, such as in the LCL and UCL, grain crushing is more prominent. These findings are represented in the Maltese fault zones; the GL wackestone is fine grained and appears resistant to cataclasis, but forms compaction bands in some damage zones (Rotevatn *et al.* 2016). In general, cataclasis is observed in the GL formations hosting higher concentrations of macro fossils, but rarely observed in those containing just fine-grained *Globigerina* foraminifera and micritic matrix. The porous members of the LCL and UCL have larger grain sizes and are prone to grain crushing and microfracturing, which results in the formation of cataclasite. Additionally, mechanical testing of the LCL reported brittle deformation of samples containing red algae, forming transitional shear planes as opposed to cataclasis, which is in agreement with the lack of granular cataclasis observed in algal packstones, rich in red algae. The authors report one sample of the Attard member, which exhibits cataclastic flow. However, this has an anomalously high porosity of 22% and is not likely to be representative of the Attard member as a whole; the Attard member exhibits porosity in the range of 5-15%. Grain crushing of algal rhodolith grains are observed under mechanical deformation, however, it is possible the stresses required for this were not achieved during faulting Malta, such that limited grain crushing is observed at outcrop.

6.3. What are the key controls on deformation and fault permeability in carbonates?

Porosity is one of the principal controls on the mode of deformation in carbonates, whereby low porosity carbonates are prone to dilation and porous carbonates are prone to compaction (e.g. Baud *et al.* 2000; Kaminskaite & Fisher in review; Section 4.7.2). Burial depth, grainsize, fault displacement, mineralogy, diagenesis and fluid histories all exhibit additional controls on deformation in carbonates. The influence of these factors on carbonate-hosted fault zones can be

observed in the fault zones of Malta and throughout the literature. Dilatant, fracture derived fault rocks occur in low porosity (<10%) carbonates (e.g. Bastesen *et al.* 2009; Demurtas *et al.* 2016), overpressured porous carbonates (e.g. Woodcock & Mort 2008; Peacock *et al.* 2019), or during high strain rate dynamic loading (e.g. Demurtas *et al.* 2016). These deformation mechanisms lead to the generation of cataclasite through pervasive fracturing and mechanical attrition, or in-situ shattering of wall rocks. In contrast, porous granular carbonates are subject to grain scale cataclasis, which occurs through the deformation of individual grains (Cooke *et al*. 2018; Figure 3-7 & Figure 3-10). This leads to porosity reduction via compaction and IEF, reducing grainsize and providing loci for cement precipitation. Note that a granular texture may be achieved in low porosity carbonates through fracture-derived cataclasis, thereby enabling subsequent deformation to occur via grain-scale cataclasis (Billi *et al.* 2003). Fine-grained porous carbonates, such as the GL formation in Malta, resist cataclastic deformation at low stresses (shallow burial), whilst allowing compaction related deformation in addition to areas of dilatancy, as evidenced by the lack of cataclasis observed in the GL, the propensity for GL damage zones to host high fracture intensities and dilatational fault breccia, and the formation of compaction bands in fault damage zones and mechanical deformation experiments (Michie *et al.* 2014; Rotevatn *et al.* 2016; Cooke *et al.* 2018; Kaminskaite & Fisher in review). In porous carbonates, arrays of deformation bands are widely reported in literature and observed in several damage zones in Malta. Faulting prior to early diagenesis in granular sediments can aid deformation band formation by readily enabling grain translation (Rath *et al*. 2011; Cooke *et al.* 2018), which is also observed in sandstones (Fossen *et al.* 2007). The location of arrays of deformation bands in Malta agrees with prior models of the geometric origin of deformation bands; deformation band arrays form due to incremental strain accommodation during slip surface propagation or asperity shearing at fault irregularities (Nicol *et al.* 2013).

Mineralogy has been shown to play some part in the style of deformation observed in carbonate-hosted fault zones. The reactivity of limestones means that fault cores are commonly cemented, either through the circulation of mineralising fluids or through local pressure solution and diffusive mass transfer. Regions of fault zones lacking brittle fault rock often host tabular layers of cemented fault, resulting in porosity reductions (e.g. Cooke *et al.* 2018, 2019). Pressure solution and crystal plastic deformation can occur at very shallow burial depths in limestones (e.g. Matonti *et al.* 2012; Cooke *et al.* 2018), but become more prevalent with increasing stress and temperatures (e.g. Elbingerode fault, Section 6.2.2). In general, faults cutting limestone formations

form narrow, localised fault cores (e.g. Agosta *et al*. 2007; Matonti et al. 2012; Ferraro *et al*. 2018), as is commonly observed in Malta. In contrast, dolomites are less soluble and more brittle than limestones (Liu *et al.* 2005), such that fault related deformation favours brittle deformation rather than plastic deformation. As a potential result of this, faults in dolomites have been shown to form much more distributed fault zones, whereby damage zones are highly fractured, with fracture densities much higher than observed in limestones. These zones contain networks of anastomosing cataclasite bands that could be potential barriers to fluid flow over large strain accumulations (Mollema & Antonellini 1999; Frost *et al*. 2009; Fondriest *et al*. 2015; Schröckenfuchs *et al*. 2015; Bauer *et al.* 2016; Demurtas *et al.* 2016; Kaminskaite *et al*. in prep).

The structure of fault zones in carbonates is fundamental in determining their hydraulic behaviour. Fault displacement is the key control on both fault rock thickness and continuity, whereby displacement is proportional to thickness and continuity of the fault core, and of individual fault rock types (Cooke *et al.* 2018). However, threshold values of continuous fault cores vary between different faulted sequences (e.g. Micarelli *et al.* 2006; Bauer *et al.* 2016; Cooke *et al.* 2018), demonstrating that additional factors control fault rock distributions. The same processes that govern the style of microscale deformation also have implications on the overall fault zone architecture; fault rock derived from either low porosity formations or porous carbonates from greater burial depths at the time of faulting may lead to the formation of thicker fault rock.

In all fault zones, complexities in fault geometry commonly reduce the potential for continuous fault rock, due to differential and distributed strain localisation along the fault (Matonti *et al.* 2012; Cooke *et al.* 2018). This damage may manifest through either increased fracture intensities or fault rock production, thereby having potential consequences for the hydraulic behaviour of the fault. The occurrence and distribution of complexities can be influenced by the host rock mechanical properties, or by heterogeneity in host rock texture. Faulting in formations that are prone to fracturing can lead to a distributed strain distribution, thereby reducing the amount of localised fault rock formed along fault cores. In contrast, strain softening that occurs during fracture-derived cataclasis may help to localise further strain along the fault core, assuming fault core embrittlement due to cementation does not occur prior to further episodes of deformation. Faults cutting a sequence with contrasting mechanically properties can exhibit a change in fault dip, changes from brittle to ductile behaviour, or variation in fracture intensities (e.g. Ferrill & Morris 2008; Michie *et al.* 2014; Agosta *et al.* 2015).

Additionally, heterogeneities in host rock texture can be incorporated within the fault zone, whereby lateral variations in porosity, relating to sedimentological structures or diagenesis, can lead to differential deformation mechanisms along fault strike (Cooke *et al.* 2019), or may impact fault propagation, subsequently leading to a complex fault geometry that hosts various structural irregularities.

The permeability of carbonate fault rocks is highly variable, and can change by several orders of magnitude over a small area along strike (e.g. Michie & Haines 2016; Cooke *et al.* 2019). Cemented cataclasite derived from porous carbonates can achieve very low permeabilities, as low as 10^{-6} mD (Cooke *et al.* 2019). However, cataclasis is not necessary to form a low permeability fault core; structural diagenesis or crystal-plastic deformation leading to pore occlusion along the fault zone can produce similarly low permeability values (e.g. Cooke *et al.* 2019). Similarly, cataclasites that lack cement or have only been subject to minor brittle deformation can exhibit high permeability (Agosta *et al.* 2007; Cooke *et al.* 2019). The influence of diagenesis on permeability implies a temporal evolution in carbonate fault rock permeability; initial deformation results in a permeability increase when fracture derived cataclasite is formed, and a subsequent permeability decrease when the fault core becomes cemented. Post-diagenesis deformation will result in a further permeability increase, whereas further deformation prior to cementation will likely lead to a permeability decrease. In contrast, grain-scale cataclasis in porous carbonates will likely result in a permeability decrease. Subsequent deformation may either be localised along a fault gouge, incorporate further increasing amounts of wall rock in to the fault core, thereby retaining a low permeability, or convert to fracture derived cataclasis if the fault core has been cemented, resulting in an increased permeability.

Bulk fault permeability is a function of structural complexity; faults in heterogeneous carbonate facies are likely to more variable deformation along strike, which can lead to both structural and petrophysical complexity, thereby reducing the potential for a low permeability fault to form. However, in some instances where continuous parallel layers of tabular fault rocks are formed ('in series'), the bulk fault permeability is much lower than if discontinuous lenses of fault rock are formed, which together comprise a continuous fault core (Cooke *et al.* in prep). In shallowly buried carbonates, it is unlikely that faults will have reservoir-scale impacts on fluid flow, due to the large amount of complexity observed within fault zone outcrops (Matonti *et al.* 2012; Cooke *et al.* 2018, 2019, in prep). However, in all settings, extensive aseismic diagenesis may enable the formation of a continuous low permeability fault core.

CHAPTER 7.

Conclusions

7.1. Aims and objectives

The research presented in this thesis aims to provide a better understanding on the lithological controls on both fault rock permeability and fault rock distributions in porous carbonate-hosted fault zones. Moreover, this work aims to characterise the potential across-fault fluid flow potential in such fault zones. In order to achieve these aims, the objectives of the thesis were threefold:

1. Provide detailed investigations in to fault-related deformation in four low-high porosity carbonate lithofacies from Malta (Chapter 3), whilst characterising the petrophysical properties of the fault rocks (Chapter 4).

2. Investigate the distributions of fault rock within the fault zones in Malta, with a focus on the along-strike fault rock continuity (Chapter 3).

3. Determine the key lithological controls on the permeability and distribution of fault rocks in Malta (Chapters 3-5), towards the generation of predictive relationships of bulk fault permeability (Chapter 5).

Finally, the results from the novel research undertaken within this study were compared with various carbonate-hosted fault zones, from the literature and the author's own observations, to attempt to determine the key controls on deformation in porous carbonate-hosted fault zones (Chapter 6).

7.2. Key findings

This work shows that, under low stresses, lower porosity (<15%) carbonate lithofacies are more prone to distributed brittle deformation, whereas moderate to high porosity (>15%) grain-dominated lithofacies are prone to localised grain-scale cataclasis. This means lower porosity formations form extensional fractures and fault breccia, but do not form cataclasite at the studied displacements. From the studied exposures, fault throws of 30 m are required for a continuous fault core, but 100-200 m throw is required for a continuous cataclasite veneer along wall rocks that are prone to cataclastic deformation (high porosity, coarse grained). Fault rocks have reduced

micro-scale heterogeneity compared to host rocks, whilst the outcrop scale heterogeneity is increased.

Fault rock permeability values range from 10^{-6}-100 mD. The lowest permeability fault rocks (cataclasites) are derived from the high porosity host rocks (wackestones, packstones), and the highest permeability fault rocks (fault breccia) are derived from the low porosity host rocks (algal packstones). The geometric average permeability cataclasite fault rock samples is 10^{-3} mD, but range from 10^{-6}-10^{-1} mD. For fault breccia, the geometric average is 0.1 mD, but range from 10^{-3}-100 mD. For cemented fault rock, the geometric average permeability is 10^{-2} mD, but ranges from 10^{-4}-10 mD. The large range in cataclasite permeability values is related to the degree of deformation and cementation.

Fault rock samples expressed as permeability contrast relative to the geometric average of host rock permeability are used to estimate the impact of fault rocks on fluid flow over production timescales. Assuming a 1 m thick fault that is 1000 m from a producing well, a permeability reduction from host rock to fault rock of $<10^3$ would have no noticeable impact on fluid flow, a reduction of $>10^3$ is required for a fault to have a detectable impact on fluid flow over production timescales (baffle), and a reduction of $>10^4$ is required for a fault to act as a significant barrier to fluid flow. Samples which exhibit permeability contrasts sufficient to be classed as a significant barrier are only derived from high porosity packstone and wackestone host rocks; 30% of these samples fit this criteria and 60% are classed as a baffle. For the lower porosity, algal packstone samples, there are no samples classed as a barrier and <10% of samples are classed as a baffle.

The permeability and fault rock distribution data are used to calculate relationships between host rock porosity and fault rock permeability for different fault rock fabrics, and between throw and fault rock distributions (fault rock thickness/continuity). These relationships are used to create predictive algorithms for bulk fault permeability. Fault permeability estimates are generated using modified algorithms in the T7 TransGen (Badley Geoscience Ltd.) plugin. The models incorporate a discretized throw-continuity relationship at low throws (<30 m), by assigning 0 m fault rock thickness to a percentage of cell juxtapositions within each throw range. Predictions of fault permeability indicate that faults in Malta are unlikely to impact fluid flow over production timescales, unless low permeability fault rocks are continuous within the fault core.

Results suggest that shallowly-buried porous carbonates are only likely to impact fluid flow if the host rock has high porosity and has a relatively homogeneous texture. Further work is

required to determine the effects of increased depth at the time of faulting on deformation. However, comparisons with literature indicate that deformation through in-situ shattering or pulverisation may occur at greater burial depths or during high pore pressures.

7.3. Future work

The magnitude and character of deformation observed at faulted outcrops from different carbonate lithologies indicates that deformation has a number of controls. A large database of host and fault rock behaviour is required for any attempt at establishing a predictive relationship for fault permeability. Therefore, further studies at a range of porous fault zone outcrops will be useful for determining these relationships or provide a database of fault rock properties from a variety of reservoir analogues. Comparisons of the findings in this thesis with fault rocks derived from similar porous lithofacies (e.g. algal packstones) would be useful to confirm controls on deformation. Porous carbonates from deeper burial would help to constrain the effect of stress conditions on deformation. Bulk fault permeability estimates from other carbonate-hosted fault zone outcrops, or from subsurface data, would enable the relationships presented in this thesis to be compared with real data. Furthermore, applications of the fault permeability algorithms to subsurface data from carbonate reservoirs in which faults are interpreted to impact fluid flow would be useful to test the relationships presented.

Fault core permeability in Malta and other carbonate-hosted fault zones is highly dependent upon whether fault rocks are cemented. The reactivity of carbonate rocks means that fault zone calcite cementation is difficult to predict, unlike in siliciclastic rocks, whereby quartz cementation is largely temperature controlled. Diagenesis in carbonate-host fault zones can occur through a combination of compaction and pressure solution, multiple fracturing and cementation episodes, and dissolution. Detailed analysis of the fault core cements in Malta would enable an understanding of fluid and diagenetic histories, including microthermometric (fluid inclusion) and geochemical (stable isotope) analysis. Thereby enabling an understanding of the temporal evolution of fault core permeability in Malta.

The findings that lithofacies heterogeneity can impact the heterogeneity of fault cores may have impacts to predictive relationships of fault core permeability; more heterogeneous fault cores are less likely to have continuous low permeability fault rock. Additional CT measurements and permeability variability analysis from other carbonate-hosted fault zones would be useful to

confirm these findings. Additional databases of fault rock textural heterogeneity may also allow quantifiable relationships between host rock heterogeneity and fault core heterogeneity.

In addition to fault rock permeability, fault rock and fault core continuity are both crucial to the bulk fault permeability. Further fault core and fault rock continuity measurements would enable comparisons of those recorded in Malta to establish the controls on displacement-continuity thresholds. Predictions of continuity thresholds can be applied to fault property modelling in order to better predict fault permeability and improve fault core continuity corrections to fault rock thickness algorithms.

This thesis predominantly deals with the matrix properties of the fault core, which have been shown to be highly variable and only partly contribute to bulk fault permeability; fractures are often considered to be the primary feature that impacts fluid flow. Further modelling of the impact of fractures on fluid flow, either cutting or terminating at the fault core, would be beneficial in considering the importance of low permeability fault rocks relative to fractures. Additionally, sensitivity analysis on these models is critical to fully understand any controls on fluid flow. This is achieved by stochastically varying input parameters to account for variety in fault rock properties and the uncertainty within any predictions of fault core properties.

References

Acevedo, J.S. 1980. Giant fields of the southern zone - Mexico. *AAPG Memoir*, **30**, 339–385.

Agosta, F. 2008. Fluid flow properties of basin-bounding normal faults in platform carbonates, Fucino Basin, central Italy. *Geological Society, London, Special Publications*, **299**, 277–291, https://doi.org/10.1144/SP299.17.

Agosta, F. & Aydin, A. 2006. Architecture and deformation mechanism of a basin-bounding normal fault in Mesozoic platform carbonates, central Italy. *Journal of Structural Geology*, **28**, 1445–1467, https://doi.org/10.1016/j.jsg.2006.04.006.

Agosta, F. & Kirschner, D.L. 2003. Fluid conduits in carbonate-hosted seismogenic normal faults of central Italy. *Journal of Geophysical Research*, **108**, 2221, https://doi.org/10.1029/2002JB002013.

Agosta, F., Prasad, M. & Aydin, A. 2007. Physical properties of carbonate fault rocks, fucino basin (Central Italy): implications for fault seal in platform carbonates. *Geofluids*, **7**, 19–32.

Agosta, F., Alessandroni, M., Antonellini, M., Tondi, E. & Giorgioni, M. 2010. From fractures to flow: A field-based quantitative analysis of an outcropping carbonate reservoir. *Tectonophysics*, **490**, 197–213.

Agosta, F., Wilson, C. & Aydin, A. 2015. The role of mechanical stratigraphy on normal fault growth across a Cretaceous carbonate multi-layer, central Texas (USA). *Italian Journal of Geosciences*, **134**, 423–441, https://doi.org/10.3301/IJG.2014.20.

Allan, U.S. 1989. Model for Hydrocarbon Migration and Entrapment Within Faulted Structures. *AAPG Bulletin*, **73**, 803–811.

Antonellini, M. & Aydin, A. 1994. Effect of faulting on fluid flow in porous sandstones: petrophysical properties. *AAPG bulletin*, **78**, 355–377, https://doi.org/10.1306/bdff90aa-1718-11d7-8645000102c1865d.

Antonellini, M., Petracchini, L., Billi, A. & Scrocca, D. 2014. First reported occurrence of deformation bands in a platform limestone, the Jurassic Calcare Massiccio Fm., northern Apennines, Italy. *Tectonophysics*, **628**, 85–104, https://doi.org/10.1016/j.tecto.2014.04.034.

API. 1998. *Recommended Practices for Core Analysis, Second Edition*.

Arthur, T.J., 1993. Mesozoic structural evolution of the UK Southern North Sea: insights from analysis of fault systems. In: J.R. Parker (Editor), Petroleum Geology of Northwest Europe: Proceedings of the 4th Conference. Geological Society London, 1269-1280.

Aubert, I., Lamarche, J. & Leonide, P. 2019. Deciphering background fractures from damage fractures in fault zones and their effect on reservoir properties in microporous carbonates (Urgonian limestones, SE France). *Petroleum Geoscience*, petgeo2019-010, https://doi.org/10.1144/petgeo2019-010.

Aydin, A. 2000. Fractures, faults, and hydrocarbon entrapment, migration and flow. *Marine and Petroleum Geology*, **17**, 797–814.

Aydin, A. & Johnson, A. 1978. Development of faults as zones of deformation bands and as slip surfaces in sandstones. *Pure and Applied Geophysics*, **116**, 931–942.

Ballas, G., Fossen, H. & Soliva, R. 2015. Factors controlling permeability of cataclastic deformation bands and faults in porous sandstone reservoirs. *Journal of Structural Geology*, **76**, 1–21,

https://doi.org/10.1016/j.jsg.2015.03.013.

Barkved, O.I., Kjelstadli, R.M., Kristiansen, T.G., Buer, K. & Kommedal, J.H. 2016. Permanent seismic monitoring of the Valhall field, Norway. *In*: *International Petroleum Technology Conference*. 10902., https://doi.org/10.2523/iptc-10902-ms.

Bastesen, E. & Braathen, A. 2010. Extensional faults in fine grained carbonates – analysis of fault core lithology and thickness-displacement relationships. *Journal of Structural Geology*, **32**, 1609–1628, https://doi.org/10.1016/j.jsg.2010.09.008.

Bastesen, E., Braathen, A., Nøttveit, H., Gabrielsen, R.H. & Skar, T. 2009. Extensional fault cores in micritic carbonate – Case studies from the Gulf of Corinth, Greece. *Journal of Structural Geology*, **31**, 403–420.

Baud, P., Schubnel, A. & Wong, T. 2000. Dilatancy, compaction, and failure mode in Solnhofen limestone. *Journal of Geophysical Research*, **105**, 19289–19303, https://dx.doi.org/10.1029/2000JB900133.

Bauer, H. & Decker, K. 2010. Fault architecture, fault rocks and fault rock properties in carbonate rocks. *In*: *EGU General Assembly Conference Abstracts*. 5112.

Bauer, H., Schröckenfuchs, T.C. & Decker, K. 2016. Hydrogeological properties of fault zones in a karstified carbonate aquifer (Northern Calcareous Alps, Austria). *Hydrogeology Journal*, **24**, 1147–1170, https://doi.org/10.1007/s10040-016-1388-9.

Berg, S.S. & Skar, T. 2005. Controls on damage zone asymmetry of a normal fault zone: outcrop analyses of a segment of the Moab fault, SE Utah. *Journal of Structural Geology*, **27**, 1803–1822.

Billi, A. 2005. Grain size distribution and thickness of breccia and gouge zones from thin (<1 m) strike-slip fault cores in limestone. *Journal of Structural Geology*, **27**, 1823–1837, https://doi.org/10.1016/j.jsg.2005.05.013.

Billi, A. 2010. Microtectonics of low-P low-T carbonate fault rocks. *Journal of Structural Geology*, **32**, 1392–1402, https://doi.org/10.1016/j.jsg.2009.05.007.

Billi, A., Salvini, F. & Storti, F. 2003. The damage zone-fault core transition in carbonate rocks: implications for fault growth, structure and permeability. *Journal of Structural Geology*, **25**, 1779–1794, https://doi.org/10.1016/S0191-8141(03)00037-3.

Billi, A., Valle, A., Brilli, M., Faccenna, C. & Funiciello, R. 2007. Fracture-controlled fluid circulation and dissolutional weathering in sinkhole-prone carbonate rocks from central Italy. *Journal of Structural Geology*, **29**, 385–395.

Birkle, P. & Angulo, M. 2005. Conceptual hydrochemical model of late Pleistocene aquifers at the Samario – Sitio Grande petroleum reservoir, Gulf of Mexico, Mexico. *Applied Geochemistry*, **20**, 1077–1098, https://doi.org/10.1016/j.apgeochem.2005.01.013.

Boccaletti, M., Cello, G. & Tortorici, L. 1987. Transtensional tectonics in the Sicily Channel. *Journal of Structural Geology*, **7**, 869–876.

Bockel-Rebelle, M.-O., Hassall, J.K., et al. 2004. Faults, fracture corridors and diffuse fracturing: ranking the main structural heterogeneities within onshore Abu Dhabi fields. *In*: *11th Abu Dhabi International Petroleum Exhibition and Conference*. SPE 88676.

Bonson, C.G., Childs, C., Walsh, J.J., M.P.J., S. & & Carboni, V. 2007. Geometric and kinematic controls on the internal structure of a large normal fault in massive limestones: The Maghlaq Fault, Malta. *Journal of Structural Geology*, **29**, 336–354, https://doi.org/10.1016/j.jsg.2006.06.016.

Bosence, D.W.J. & Pedley, H.M. 1982. Sedimentology and palaeoecology of a Miocene coralline algal biostrome from the Maltese Islands. *Palaeogeography, Palaeoclimatology, Palaeoecology*, **38**, 9–43, https://doi.org/10.1016/0031-0182(82)90062-1.

Brandano, M., Frezza, V., Tomassetti, L., Pedley, M. & Matteucci, R. 2009a. Facies analysis and palaeoenvironmental interpretation of the Late Oligocene Attard Member (Lower Coralline Limestone Formation), Malta. *Sedimentology*, **56**, 1138–1158.

Brandano, M., Frezza, V., Tomassetti, L. & Cuffaro, M. 2009b. Heterozoan carbonates in oligotrophic tropical waters: The Attard member of the lower coralline limestone formation (Upper Oligocene, Malta). *Palaeogeography, Palaeoclimatology, Palaeoecology*, **274**, 54–63.

Bretan, P., Yielding, G. & Jones, H. 2003. Using calibrated shale gouge ratio to estimate hydrocarbon column heights. *AAPG Bulletin*, **87**, 397–413, https://doi.org/10.1306/08010201128.

Brown, A. 2003. Capillary effects on fault-fill sealing. *AAPG Bulletin*, **87**, 381–395, https://doi.org/10.1306/08010201127.

Burkhard, M. 1993. Calcite twins, their geometry, appearance and significance as stress-strain markers and indicators of tectonic regime: a review. *Journal of Structural Geology*, **15**, 351–368.

Caine, J.S. & Forster, C.B. 1999. Fault zone architecture and fluid flow: Insight from field data and numerical modeling. *In*: Haneberg, W. C., Mozley, P. S., Moore, J. C. & Goodwin, L. B. (eds) *Faults and Subsurface Fluid Flow in the Shallow Crust*. AGU, 101–127., https://doi.org/10.1029/GM113p0101.

Caine, J.S., Evans, J.P. & Forster, C.B. 1996. Fault zone architecture and permeability structure. *Geology*, **24**, 1025–1028, https://doi.org/10.1130/0091-7613(1996)024<1025:FZAAPS>2.3.CO;2.

Chester, F., Evans, J. & Biegel, R. 1993. Internal structure and weakening mechanisms of the San Andreas Fault. *Journal of Geophysical Research*, **98**, 771–786, https://doi.org/10.1016/0148-9062(93)92238-l.

Chester, F.M. & Logan, J.M. 1986. Implications for mechanical properties of brittle faults from observations of the Punchbowl Fault Zone, California. *Pure and Applied Geophysics*, **124**, 79–106, https://doi.org/10.1007/bf00875720.

Chester, F.M., Chester, J.S., Kirschner, D.L., Schulz, S.E. & Evans, J.P. 2004. Structure of large-displacement, strike-slip fault zones in the brittle continental crust. *In*: Karner, G. D., Taylor, B., Driscoll, N. W. & Kohlstedt, D. L. (eds) *Rheology and Deformation of the Lithosphere at Continental Margins*. Columbia University Press, 223–260., https://doi.org/10.7312/karn12738-009.

Childs, C., Watterson, J. & Walsh, J.J. 1996. A model for the structure and development of fault zones. *Journal of the Geological Society*, **153**, 337–340.

Childs, C., Manzocchi, T., Walsh, J.J., Bonson, C.G., Nicol, A. & Schöpfer, M.P.J. 2009. A geometric model of fault zone and fault rock thickness variations. *Journal of Structural Geology*, **31**, 117–127, https://doi.org/10.1016/j.jsg.2008.08.009.

Chilingar, G. V & Yen, T.F. 1983. Some notes on wettability and relative permeabilities of carbonate reservoir rocks , II. *Energy Sources*, **7**, 67–75, https://doi.org/10.1080/00908318308908076.

Cilona, A., Baud, P., Tondi, E., Agosta, F., Vinciguerra, S., Rustichelli, A. & Spiers, C.J. 2012. Deformation bands in porous carbonate grainstones: Field and laboratory observations. *Journal of Structural Geology*, **45**, 137–157, https://doi.org/10.1016/j.jsg.2012.04.012.

Cilona, A., Faulkner, D.R., et al. 2014. The effects of rock heterogeneity on compaction localization in porous

carbonates. *Journal of Structural Geology*, **67**, 75–93, https://doi.org/10.1016/J.JSG.2014.07.008.

Clark, D.N. 1980. The diagenesis of Zechstein carbonate sediments. *Contributions to sedimentology*, **9**, 167–203.

Clark, D.N. 1986. The Distribution of Porosity in Zechstein Carbonates. *Geological Society, London, Special Publications*, **23**, 121 LP – 149, https://doi.org/10.1144/GSL.SP.1986.023.01.09.

Cooke, A.P., Fisher, Q.J., Michie, E.A.H. & Yielding, G. 2018. Investigating the controls on fault rock distribution in normal faulted shallow burial limestones, Malta, and the implications for fluid flow. *Journal of Structural Geology*, **114**, 22–42, https://doi.org/10.1016/j.jsg.2018.05.024.

Cooke, A.P., Fisher, Q.J., Michie, E.A.H. & Yielding, G. 2019. Permeability of carbonate fault rocks: a case study from Malta. *Petroleum Geoscience*. http://dx.doi.org/10.1144/petgeo2019-055.

Cooke, A.P., Michie, E.A.H., Yielding, G. & Fisher, Q.J. In prep. *Implementing Fault Rock Permeability and Continuity into Geocellular Modelling of Porous Carbonate-Hosted Fault Zones*.

Corona, F. V, Brauckmann, F., Beckmann, H., Gobi, A., Grassmann, S., Neble, J. & Roettgen, K. 2012. Cross-fault pressure depletion, Zechstein carbonate reservoir, Weser-Ems area, Northern German Gas Basin. *In*: *3rd EAGE International Conference on Fault and Top Seals*. Abstract A06.

Cowie, P.A. & Scholz, C.H. 1992. Physical explanation for the displacement-length relationship of faults using a post-yield fracture mechanics model. *Journal of Structural Geology*, **14**, 1133–1148.

Crawford, B.R., Myers, R.., Woronow, A., Faulkner, D.R. & Rutter, E.H. 2002. Porosity-permeability relationships in clay-bearing fault gouge: Presented at the Society of Petroleum Engineers/International Society of Rock Mechanics, Rock Mechanics Conference, Irving, Texas, October 20-23,. *SPE/ISRM 78214*, 13p.

Dart, C.J., Bosence, D.W.J. & McClay, K.R. 1993. Stratigraphy and structure of the Maltese graben system. *Journal of the Geological Society, London*, **150**, 1153–1166, https://doi.org/10.1144/gsjgs.150.6.1153.

Dawers, N.H. & Anders, M.H. 1995. Displacement-length scaling and fault linkage. *Journal of Structural Geology*, **17**.

de Medeiros, W.E., do Nascimento, A.F., Antunes, A.F., Jardim de Sá, E.F. & Lima Neto, F.F. 2007. Spatial pressure compartmentalization in faulted reservoirs as a consequence of fault connectivity: a fluid flow modelling perspective, Xaréu oil field, NE Brazil. *Petroleum Geoscience*, **13**, 341–352, https://doi.org/10.1144/1354-079306-709.

De Paola, N., Collettini, C., Faulkner, D.R. & Trippetta, F. 2008. Fault zone architecture and deformation processes within evaporitic rocks in the upper crust. *Tectonics*, **27**, 1–21, https://doi.org/10.1029/2007TC002230.

Delle Piane, C., Giwelli, A., et al. 2016. Frictional and hydraulic behaviour of carbonate fault gouge during fault reactivation — An experimental study. *Tectonophysics*, **690**, 21–34, https://doi.org/10.1016/j.tecto.2016.07.011.

Demurtas, M., Fondriest, M., Balsamo, F., Clemenzi, L., Storti, F., Bistacchi, A. & Di, G. 2016. Structure of a normal seismogenic fault zone in carbonates: The Vado di Corno Fault, Campo Imperatore, Central Apennines (Italy). *Journal of Structural Geology*, **90**, 185–206, https://doi.org/10.1016/j.jsg.2016.08.004.

Dimmen, V., Rotevatn, A., Peacock, D.C.P., Nixon, C.W. & Nærland, K. 2017. Quantifying structural controls on fluid flow: Insights from carbonate-hosted fault damage zones on the Maltese Islands. *Journal of Structural Geology*, **101**, 43–57, https://doi.org/10.1016/j.jsg.2017.05.012.

Du Bernard, X., Eichhubl, P. & Aydin, A. 2002. Dilation bands: A new form of localized failure in granular media. *Geophysical Research Letters*, **29**, 2176, https://doi.org/10.1029/2002GL015966.

Engelder, J.T. 1974. Cataclasis and the generation of fault gouge. *Geological Society of America Bulletin*, **85**, 1515–1522.

Erslev, E.A. 1991. Trishear fault-propagation folding. *Geology*, **19**, 617–620.

Evans, J.P. 1990. Thickness-displacement relationships for fault zones. *Journal of Structural Geology*, **12**, 1061–1065.

Evans, J.P., Forster, C.B. & Goddard, J. V. 1997. Permeability of fault-related rocks, and implications for hydraulic structure of fault zones. *Journal of Structural Geology*, **19**, 1393–1404.

Færseth, R.B. 2006. Shale smear along large faults: continuity of smear and the fault seal capacity. *Journal of the Geological Society, London*, **163**, 741–751.

Færseth, R.B., Johnsen, E. & Sperrevik, S. 2007. Methodology for risking fault seal capacity: Implications of fault zone architecture. *AAPG Bulletin*, **91**, 1231–1246.

Faulkner, D.R., Lewis, A.C. & Rutter, E.H. 2003. On the internal structure and mechanics of large strike-slip fault zones: field observations of the Carboneras fault in southeastern Spain. *Tectonophysics*, **367**, 235–251, https://doi.org/10.1016/S0040-1951(03)00134-3.

Faulkner, D.R., Jackson, C.A.L., Lunn, R.J., Schlische, R.W., Shipton, Z.K., Wibberley, C.A.J. & Withjack, M.O. 2010. A review of recent developments concerning the structure, mechanics and fluid flow properties of fault zones. *Journal of Structural Geology*, **32**, 1557–1575.

Faulkner, D.R., Mitchell, T.M., Jensen, E. & Cembrano, J. 2011. Scaling of fault damage zones with displacement and the implications for fault growth processes. *Journal of Geophysical Research*, **116**, https://doi.org/10.1029/2010JB007788.

Ferraro, F., Grieco, D.S., Agosta, F. & Prosser, G. 2018. Space-time evolution of cataclasis in carbonate fault zones. *Journal of Structural Geology*, **110**, 45–64, https://doi.org/10.1016/j.jsg.2018.02.007.

Ferraro, F., Agosta, F., Ukar, E., Grieco, D.S., Cavalcante, F., Belviso, C. & Prosser, G. 2019. Structural diagenesis of carbonate fault rocks exhumed from shallow crustal depths: An example from the central-southern Apennines, Italy. *Journal of Structural Geology*, https://doi.org/10.1016/j.jsg.2019.02.008.

Ferrill, D.A. & Morris, A.P. 2003. Dilational normal faults. *Journal of Structural Geology*, **25**, 183–196.

Ferrill, D.A. & Morris, A.P. 2008. Fault zone deformation controlled by carbonate mechanical stratigraphy, Balcones fault system, Texas. *AAPG Bulletin*, **92**, 359–380, https://doi.org/10.1306/10290707066.

Ferrill, D.A., Morris, A.P., Evans, M.A., Burkhard, M., Groshong, R.H. & Onasch, C.M. 2004. Calcite twin morphology: a low-temperature deformation geothermometer. *Journal of Structural Geology*, **26**, 1521–1529, https://doi.org/10.1016/j.jsg.2003.11.028.

Fisher, Q.J., T.J., Haneef, J., Grattoni, C.A., Allshorn, S. & Lorinczi, P. 2018. Permeability of fault rocks in siliciclastic reservoirs: Recent advances. *Marine and Petroleum Geology*, **91**, 29-42, https://doi.org/10.1016/j.marpetgeo.2017.12.019.

Fisher, Q. & Knipe, R. 2001. The permeability of faults within siliciclastic petroleum reservoirs of the North Sea and Norwegian Continental Shelf. *Marine and Petroleum Geology*, **18**, 1063–1081, https://doi.org/10.1016/S0264-8172(01)00042-3.

Fisher, Q.J. & Knipe, R.J. 1998. Fault sealing processes in siliciclastic sediments. *In*: Jones, G., Fisher, Q. J. & Knipe, R. J. (eds) *Faulting, Fault Sealing and Fluid Flow in Hydrocarbon Reservoirs*. Geological Society, London, Special Publications, 117–134., https://doi.org/10.1144/GSL.SP.1998.147.01.08.

Fisher, Q.J., Harris, S.D., McAllister, E., Knipe, R.J. & Bolton, A.J. 2001. Hydrocarbon flow across faults by capillary leakage revisited. *Marine and Petroleum Geology*, **18**, 251–257.

Fitz-Diaz, E., Hudleston, P., Siebenaller, L., Kirschner, D., Camprubí, A., Tolson, G. & Pi Puig, T. 2011. Insights into fluid flow and water-rock interaction during deformation of carbonate sequences in the Mexican fold-thrust belt. *Journal of Structural Geology*, **33**, 1237–1253, https://doi.org/10.1016/j.jsg.2011.05.009.

Flodin, E., Gerdes, M., Aydin, A. & Wiggins, W. 2005. Petrophysical properties and sealing capacity of fault rock, Aztec Sandstone, Nevada. *In*: Tsuji, Y. & Sorkhabi, R. (eds) *Faults, Fluid Flow, and Petroleum Traps*. AAPG Memoir, 197–218., https://doi.org/10.1306/M851033.

Fondriest, M., Smith, S. a. F., Candela, T., Nielsen, S.B., Mair, K. & Di Toro, G. 2013. Mirror-like faults and power dissipation during earthquakes. *Geology*, **41**, 1175–1178.

Fondriest, M., Aretusini, S., Toro, G. Di & Smith, S.A.F. 2015. Fracturing and rock pulverization along an exhumed seismogenic fault zone in dolostones: The Foiana Fault Zone (Southern Alps, Italy). *Tectonophysics*, **654**, 56–74, https://doi.org/10.1016/j.tecto.2015.04.015.

Fossen, H. & Bale, A. Deformation bands and their influence on fluid flow. *AAPG Bulletin*, **91**, 1685-1700.

Fossen, H., Johansen, T.E.S., Hesthammer, J. & Rotevatn, A. 2005. Fault interaction in porous sandstone and implications for reservoir management; examples from southern Utah. *AAPG Bulletin*, **89**, 1593–1606, https://doi.org/10.1306/07290505041.

Fossen, H., Schultz, R.A., Shipton, Z.K. & Mair, K. 2007. Deformation bands in sandstone: a review. *Journal of the Geological Society*, **164**, 755–769.

Frost, E., Dolan, J., Sammis, C., Hacker, B., Cole, J. & Ratschbacher, L. 2009. Progressive strain localization in a major strike-slip fault exhumed from midseismogenic depths: Structural observations from the Salzach-Ennstal-Mariazell-Puchberg fault system, Austria. *Journal of Geophysical Research: Solid Earth*, **114**, https://doi.org/10.1029/2008JB005763.

Fulljames, J., Zijerveld, L. & Franssen, R. 1997. Fault seal processes: systematic analysis of fault seals over geological and production time scales. *In*: Møller-Pedersen, P. & Koestler, A. G. (eds) *Hydrocarbon Seals: Importance for Exploration and Production.* Special publication of the Norwegian Petroleum Society, 51–59., https://doi.org/10.1016/S0928-8937(97)80006-9.

Gabrielsen, R.H., Braathen, A., Kjemperud, M. & Valdresbra, M.L.R. 2016. The geometry and dimensions of fault-core lenses. *Geological Society, London, Special Publications*, **439**.

Gatt, P. 2007. Controls on Plio-Quaternary foreland sedimentation in the region of the Maltese Islands. *Bollettino-Societa Geologica Italiana (Italian Journal of Geoscience)*, **126**, 119–129.

Groshong, R. 1988. Low-temperature deformation mechanisms and their interpretation. *Geological Society of America Bulletin*, **100**, 1329–1360.

Géraud, Y., Diraison, M. & Orellana, N. 2006. Fault zone geometry of a mature active normal fault: A potential high permeability channel (Pirgaki fault, Corinth rift, Greece). *Tectonophysics*, **426**, 61–76, https://doi.org/10.1016/j.tecto.2006.02.023.

Hadizadeh, J. 1994. Interaction of cataclasis and pressure solution in a low-temperature carbonate shear zone.

Pure and Applied Geophysics, **143**, 255–280, https://doi.org/10.1007/bf00874331.

Haines, T.J., Neilson, J.E., Healy, D., Michie, E.A.H. & Aplin, A.C. 2015. The impact of carbonate texture on the quantification of total porosity by image analysis. *Computers & Geosciences*, **85**, 112–125.

Haines, T.J., Michie, E.A.H., Neilson, J.E. & Healy, D. 2016. Permeability evolution across carbonate hosted normal fault zones. *Marine and Petroleum Geology*, **72**, 62–82, https://doi.org/10.1016/j.marpetgeo.2016.01.008.

Harris, S.D., Vaszi, a. Z. & Knipe, R.J. 2007. Three-dimensional upscaling of fault damage zones for reservoir simulation. *Geological Society, London, Special Publications*, **292**, 353–374, https://doi.org/10.1144/SP292.20.

Hausegger, S., Kurz, W., Rabitsch, R., Kiechl, E. & Brosch, F.-J. 2010. Analysis of the internal structure of a carbonate damage zone: Implications for the mechanisms of fault breccia formation and fluid flow. *Journal of Structural Geology*, **32**, 1349–1362, https://doi.org/10.1016/j.jsg.2009.04.014.

Hesthammer, J. & Fossen, H. 2000. Uncertainties associated with fault sealing analysis. *Petroleum Geoscience*, **6**, 37–45, https://doi.org/10.1144/petgeo.6.1.37.

Heum, O.R. 1996. A fluid dynamic classification of hydrocarbon entrapment. *Petroleum Geoscience*, **2**, 145–158.

Heynekamp, M.R., Goodwin, L.B., Mozley, P.S. & Haneberg, W.C. 1999. Controls on fault-zone architecture in poorly lithified sediments, Rio Grande Rift, New Mexico: Implications for fault-zone permeability and fluid flow. *In*: Haneberg, W. C., Mozley, P. S., Moore, J. C. & Goodwin, L. B. (eds) *In: , Faults and Subsurface Fluid Flow in the Shallow Crust. American Geophysics Union. Geophysical Monograph Series.* 27–49., https://doi.org/10.1029/gm113p0101.

Higgins, M.W. 1971. Cataclastic rocks. *Geological Survey Professional Paper*, **687**, 97.

Hugman III, R. & Friedman, M. 1979. Effects of texture and composition on mechanical behavior of experimentally deformed carbonate rocks. *AAPG Bulletin*, **63**, 1478–1489.

Hull, J. 1988. Thickness-displacement relationships for deformation zones. *Journal of Structural Geology*, **10**, 431–435.

Hussain, A. 1993. Dukhan field (onshore Qatar) Uwainat reservoir optimum development scheme. *Society of Petroleum Engineers*, 169–199, https://doi.org/10.2523/25530-ms.

Illies, J.H. 1981. Graben formation - the Maltese Islands - a case history. *Tectonophysics*, **73**, 151–168.

Ingram, G.M., Urai, J.L. & Naylor, M.A. 1997. Sealing processes and top seal assessment. *In: Møller-Pedersen, P Koestler (Editors), Hydrocarbon Seals: Importance for Exploration and Production, NPF Special Publication 7*, 165–174.

Jackson, J. & Mckenzie, D. 1999. A hectare of fresh striations on the Arkitsa Fault, central Greece. *Journal of Structural Geology*, **21**, 1–6.

Jakobsen, F., Ineson, J.R., Kristensen, L., Nytoft, H.P. & Stemmerik, L. 2005. The Valdemar Field, Danish Central Graben: field compartmentalization and regional prospectivity of the Lower Cretaceous chalk play. *In*: Doré, A. G. & Vining, B. A. (eds) *Petroleum Geology: North-West Europe and Global Perspectives — Proceedingsofthe 6th Petroleum Geology Conference*. Geological Society, London, 1–10.

Jeanne, P., Guglielmi, Y., Lamarche, J., Cappa, F. & Marié, L. 2012. Architectural characteristics and petrophysical properties evolution of a strike-slip fault zone in a fractured porous carbonate reservoir.

Journal of Structural Geology, **44**, 93–109, https://doi.org/10.1016/j.jsg.2012.08.016.

John, C.M., Mutti, M. & Adatte, T. 2003. Mixed carbonate-siliciclastic record on the North African margin (Malta) - coupling of weathering processes and mid Miocene climate. *Geological Society of America Bulletin*, **115**, 217–229, https://doi.org/10.1130/0016-7606(2003)115<0217:MCSROT>2.0.CO;2.

Jolley, S.J., Dijk, H., Lamens, J.H., Fisher, Q.J., Manzocchi, T., Eikmans, H. & Huang, Y. 2007. Faulting and fault sealing in production simulation models: Brent Province, northern North Sea. *Petroleum Geoscience*, **13**, 321–340.

Jongsma, D., Woodside, J.M., King, G.C.P. & van Hinte, J.E. 1987. The Medina Wrench : a key to the kinematics of the central and eastern Mediterranean over the past 5 Ma. *Earth and Planetary Science Letters*, **82**, 87–106.

Joussineau, G. De & Aydin, A. 2007. The evolution of the damage zone with fault growth in sandstone and its multiscale characteristics. *Journal of Geophysical Research*, **112**, B12401, https://doi.org/10.1029/2006JB004711.

Kaminskaite, I. & Fisher, Q.J. In review. Laboratory Deformation of Carbonate Rocks: Deformation Mechanisms at Yield and Their Controlling Parameters.

Kaminskaite, I., Fisher, Q.J. & Michie, E.A.H. In prep. Faults in tight limestones and dolomites in San Vito lo Capo, Sicily, Italy: Internal architecture and petrophysical properties.

Kaminskaite, I., Fisher, Q.J. & Michie, E.A.H. 2019. Microstructure and petrophysical properties of deformation bands in high porosity carbonates. *Journal of Structural Geology*, **119**, 61–80, https://doi.org/10.1016/j.jsg.2018.12.001.

Kennedy, L.A. & Logan, J.M. 1998. Microstructures of cataclasites in a limestone-on-shale thrust fault: implications for low-temperature recrystallization of calcite. *Tectonophysics*, **295**, 167–186.

Kennedy, L.A. & White, J.C. 2001. Low-temperature recrystallization in calcite: Mechanisms and consequences. *Geology*, **29**, 1027–1030.

Kerans, C. 1993. Description and interpretation of karst - related breccia fabrics, Ellenburger Group, West Texas. 181–200.

Khalil, S.M. & Mcclay, K.R. 2002. Extensional fault-related folding, northwestern Red Sea, Egypt. *Journal of Structural Geology*, **24**, 743–762.

Kim, Y.S., Peacock, D.C.P. & Sanderson, D.J. 2003. Mesoscale strike-slip faults and damage zones at Marsalforn, Gozo Island, Malta. *Journal of Structural Geology*, **25**, 793–812, https://doi.org/10.1016/S0191-8141(02)00200-6.

Kim, Y.S., Peacock, D.C.P. & Sanderson, D.J. 2004. Fault damage zones. *Journal of Structural Geology*, **26**, 503–517.

Kim, Y.S. & Sanderson, D.J. 2005. The relationship between displacement and length of faults: A review. *Earth-Science Reviews*, **68**, 317–334, https://doi.org/10.1016/j.earscirev.2004.06.003.

Klinkenberg, L.J. 1941. The permeability of porous media to liquids and gases. *Drilling and production practice*, 200–213.

Knai, T.A. & Knipe, R.J. 1998. The impact of faults on fluid flow in the Heidrun Field. In: Jones, G., Fisher, Q. J. & Knipe, R. J. (eds) Faulting, Fault Sealing and Fluid Flow in Hydrocarbon Reservoirs. *Geological Society,*

London, Special Publications, **147**, 269–282.

Knipe, R.J. 1992. Faulting processes and fault seal. *In: Structural and tectonic modelling and its application to petroleum geology, R. M Larsen, H. Brekke, B. T. Larsen, E. Talleras (Eds.) Amsterdam, Elsevier*, **1**, 325–342.

Knipe, R.J. 1997. Juxtaposition and seal diagrams to help analyze fault seals in hydrocarbon reservoirs. *AAPG Bulletin*, **81**, 187–195, https://doi.org/10.1306/522b42df-1727-11d7-8645000102c1865d.

Kosters, E.C., Bebout, D.G., et al. 1989. *Atlas of Major Texas Gas Reservoirs*.

Lee, Y.J., Wiltschko, D. V, Grossman, E.L., Morse, J.W. & Lamb, W.M. 1997. Sequential vein growth with fault displacement: An example from the Austin Chalk Formation, Texas. *Journal of Geophysical Research*, **102**, 22611–22628.

Lander, R.H. & Laubach, S.E. 2015. Insights into rates of fracture growth and sealing from a model for quartz cementation in fractured sandstones. *Bulletin of the Geological Society of America*, **127**, 516–538, https://doi.org/10.1130/B31092.1.

Laubach, S.E., Eichhubl, P., Hargrove, P., Ellis, M.A. & Hooker, J.N. 2014. Fault core and damage zone fracture attributes vary along strike owing to interaction of fracture growth, quartz accumulation, and differing sandstone composition. *Journal of Structural Geology*, **68**, 207-226, https://doi.org/10.1016/j.jsg.2014.08.007.

Lindsay, N.G., Murphy, F.C., Walsh, J.J. & Watterson, J. 1992. Outcrop Studies of Shale Smears on Fault Surface. *The Geological Modelling of Hydrocarbon Reservoirs and Outcrop Analogues*, 113–123, https://doi.org/doi:10.1002/9781444303957.ch6.

Liu, Z., Yuan, D. and Dreybrodt, W., 2005. Comparative study of dissolution rate-determining mechanisms of limestone and dolomite. *Environmental Geology*, **49**, 274-279.

Loveless, S., Bense, V. & Turner, J. 2011. Fault architecture and deformation processes within poorly lithified rift sediments, Central Greece. *Journal of Structural Geology*, **33**, 1554–1568, https://doi.org/https://doi.org/10.1016/j.jsg.2011.09.008.

Lucia, F.J. 1995. Rock-fabric/petrophysical classification of carbonate pore space for reservoir characterization. *AAPG Bulletin*, **79**, 1275–1300, https://doi.org/10.1306/7834d4a4-1721-11d7-8645000102c1865d.

Maas, J.G. & Hebing, A. 2013. Quantitative X-ray CT for SCAL plug homogeneity assessment. *SCA*, **4**.

Manzocchi, T., Childs, C., et al. 2019. Parameterising and modelling sub-seismic fault structure for assessing compartmentalisation and juxtaposition risk. In: Fifth International Conference on Fault and Top Seals, https://doi.org/10.3997/2214-4609.201902339.

Manzocchi, T., Walsh, J.J., Nell, P. & Yielding, G. 1999. Fault transmissibility multipliers for flow simulation models. *Petroleum Geoscience*, **5**, 53–63, https://doi.org/10.1144/petgeo.5.1.53.

Matonti, C., Lamarche, J., Guglielmi, Y. & Marié, L. 2012. Structural and petrophysical characterization of mixed conduit/seal fault zones in carbonates: Example from the Castellas fault (SE France). *Journal of Structural Geology*, **39**, 103–121.

Mauldon, M. & Dershowitz, W. 2000. A multi-dimensional system of fracture abundance measures. *Geological Society of America Abstracts with Programs*, **32**.

Mauldon, M., Dunne, W.M. & Rohrbaugh, M.B. 2001. Circular scanlines and circular windows: new tools for

characterizing the geometry of fracture traces. *Journal of Structural Geology*, **23**, 247–258.

Mcclay, K., Bonora, M. & Mcclay, K. 2001. fault systems. *AAPG Bulletin*, **85**, 233–260.

Mcgrath, G. & Davison, I. 1995. Damage zone geometry around fault tips. *Journal of Structural Geology*, **17**, 1011–1024.

Micallef, A., Berndt, C. & Debono, G. 2011. Fluid flow systems of the Malta Plateau, Central Mediterranean Sea. *Marine Geology*, **284**, 74–85.

Micarelli, L., Benedicto, A. & Wibberley, C.A.J. 2006. Structural evolution and permeability of normal fault zones in highly porous carbonate rocks. *Journal of Structural Geology*, **28**, 1214–1227, https://doi.org/10.1016/j.jsg.2006.03.036.

Michie, E.A.H. 2015. Influence of host lithofacies on fault rock variation in carbonate fault zones: A case study from the Island of Malta. *Journal of Structural Geology*, **76**, 61–79, https://doi.org/10.1016/j.jsg.2015.04.005.

Michie, E.A.H. & Haines, T.J. 2016. Variability and heterogeneity of the petrophysical properties of extensional carbonate fault rocks, Malta. *Petroleum Geoscience*, **23**, https://doi.org/10.1144/petgeo2015-027.

Michie, E.A.H., Haines, T.J., Healy, D., Neilson, J.E., Timms, N.E. & Wibberley, C.A.J. 2014. Influence of carbonate facies on fault zone architecture. *Journal of Structural Geology*, **65**, 82–99, https://doi.org/10.1016/j.jsg.2014.04.007.

Michie, E.A.H., Yielding, G. & Fisher, Q.J. 2017. Predicting transmissibilities of carbonate-hosted fault zones. *Geological Society, London, Special Publications*, **459**, 121–137, https://doi.org/10.1144/sp459.9.

Mitchell, T.M. & Faulkner, D.R. 2009. The nature and origin of off-fault damage surrounding strike-slip fault zones with a wide range of displacements: A field study from the Atacama fault system, northern Chile. *Journal of Structural Geology*, **31**, 802–816.

Mollema, P.N. & Antonellini, M. 1999. Development of strike-slip faults in the dolomites of the Sella. *Journal of Structural Geology*, **21**, 273–292.

Molli, G., White, J.C., Kennedy, L. & Taini, V. 2011. Low-temperature deformation of limestone, Isola Palmaria, northern Apennine, Italy – The role of primary textures, precursory veins and intracrystalline deformation in localization. *Journal of Structural Geology*, **33**, 255–270.

Morrow, N.R. 1990. Wettability and its effect on oil recovery. *Journal of Petroleum Technology*, **42**, 1476–1484.

Morrow, N.R., Lim, H.T. & Ward, J.S. 1986. Effect of crude-oil-induced wettability changes on oil recovery. *SPE Formation Evaluation*, 89–103.

Mort, K. & Woodcock, N.H. 2008. Quantifying fault breccia geometry: Dent Fault, NW England. *Journal of Structural Geology*, **30**, 701–709, https://doi.org/10.1016/j.jsg.2008.02.005.

Nicol, A., Childs, C., Walsh, J.J. & Schafer, K.W. 2013. A geometric model for the formation of deformation band clusters. *Journal of Structural Geology*, **55**, 21-33. https://doi.org/10.1016/j.jsg.2013.07.004.

Peacock, D.C.P., Rotevatn, A. & Sanderson, D.J. 2019. Brecciation driven by changes in fluid column heights. *Terra Nova*, **31**, 76–81, https://doi.org/10.1111/ter.12371.

Pedley, H.M. 1978. A new lithostratigraphical and palaeoenvironmental interpretation for the coralline limestone formations (Miocene) of the Maltese Islands. *Overseas geology and mineral resources*, **54**, 1–

17.

Pedley, H.M. & Bennett, S.M. 1985. Phosphorites, hardgrounds and syndepositional solution subsidence: a palaeoenvironmental model from the Miocene of the Maltese Islands. *Sedimentary Geology*, **45**, 1–34, https://doi.org/10.1016/0037-0738(85)90022-3.

Pedley, H.M., House, M.R. & Waugh, B. 1976. The geology of Malta and Gozo. *Proceedings of the Geologists' Association*, **87**, 325–341.

Pomar, L. & Ward, W.C. 1999. Reservoir-scale heterogeneity in depositional packages and diagenetic patterns on a reef-rimmed platform, Upper Miocene, Mallorca, Spain. *AAPG Bulletin*, **83**, 1759–1773, https://doi.org/10.1306/e4fd425b-1732-11d7-8645000102c1865d.

Přikryl, R. 2001. Some microstructural aspects of strength variation in rocks. *International Journal of Rock Mechanics & Mining Sciences*, **38**, 671–682.

Ran, G., Shalev, E., Yechieli, Y., Sagy, A. & Weisbrod, N. 2014. The permeability of fault zones: a case study of the Dead Sea rift (Middle East). *Hydrogeology Journal*, **22**, 425–440, https://doi.org/10.1007/s10040-013-1055-3.

Rath, A., Exner, U., Tschegg, C., Grasemann, B., Laner, R. & Draganits, E. 2011. Diagenetic control of deformation mechanisms in deformation bands in a carbonate grainstone. *AAPG Bulletin*, **95**, 1369–1381, https://doi.org/10.1306/01031110118.

Rawling, G.C. & Goodwin, L.B. 2006. Structural record of the mechanical evolution of mixed zones in faulted poorly lithified sediments, Rio Grande rift, New Mexico, USA. *Journal of Structural Geology*, **28**, 1623–1639, https://doi.org/10.1016/j.jsg.2006.06.008.

Rawling, G.C., Goodwin, L.B. & Wilson, J.L. 2001. Internal architecture, permeability structure, and hydrologic significance of contrasting fault-zone types. *Geology*, **29**, 43–46, https://doi.org/10.1130/0091-7613(2001)029<0043:IAPSAH>2.0.CO;2.

Reuther, C.-D. & Eisbacher, G.H. 1985. Pantelleria Rift - crustal extension in a convergent intraplate setting. *Geologische Rundschau*, **74**, 585–597.

Richter, D.H. 1967. Person field, Karnes Co, TX. *In*: *Typical Oil and Gas Fields of South Texas*. Corpus Christi Geological Society, 156–160.

Riley, P.R., Goodwin, L.B. & Lewis, C.J. 2010. Controls on fault damage zone width, structure, and symmetry in the Bandelier Tuff, New Mexico. *Journal of Structural Geology*, **32**, 766–780.

Rohrbaugh, M.B., Dunne, W.M. & Mauldon, M. 2002. Estimating fracture trace intensity, density, and mean length using circular scan lines and windows. *AAPG Bulletin*, **86**, 2089–2104.

Rotevatn, A., Torabi, A., Fossen, H. & Braathen, A. 2008. Slipped deformation bands: A new type of cataclastic deformation bands in Western Sinai, Suez rift, Egypt. *Journal of Structural Geology*, **30**, 1317–1331.

Rotevatn, A., Thorsheim, E., Bastesen, E., Fossmark, H.S.S., Torabi, A. & Sælen, G. 2016. Sequential growth of deformation bands in carbonate grainstones in the hangingwall of an active growth fault: Implications for deformation mechanisms in different tectonic regimes. *Journal of Structural Geology*, **90**, 27–47, https://doi.org/10.1016/j.jsg.2016.07.003.

Rutter, E.H. 1986. On the nomenclature of mode of failure transitions in rocks. *Tectonophysics*, **122**, 381–387.

Rutter, E.H. & Hadizadeh, J. 1991. On the influence of porosity on the low-temperature brittle-ductile transition

in siliciclastic rocks. *Journal of Structural Geology*, **13**, 609–614, https://doi.org/10.1016/0191-8141(91)90047-m.

Savage, H.M. & Brodsky, E.E. 2011. Collateral damage: Evolution with displacement of fracture distribution and secondary fault strands in fault damage zones. *Journal of Geophysical Research: Solid Earth (1978-2012)*, **116**.

Schlische, R.W. 1995. Geometry and origin of fault-related folds in extensional settings. *AAPG Bulletin*, **79**, 1661–1678.

Schlumberger. 2007. *Schlumberger Market Analysis*.

Schröckenfuchs, T., Bauer, H., Grasemann, B. & Decker, K. 2015. Rock pulverization and localization of a strike-slip fault zone in dolomite rocks (Salzach-Ennstal-Mariazell-Puchberg fault, Austria). *Journal of Structural Geology*, https://doi.org/10.1016/j.jsg.2015.06.009.

Scholz, C.H. 1987. Wear and gouge formation in brittle faulting. *Geology*, **15**, 493–495, https://doi.org/10.1130/0091-7613(1987)15<493:WAGFIB>2.0.CO;2.

Schowalter, T.T. 1979. Mechanics of secondary hydrocarbon migration and entrapment. *AAPG Bulletin*, **63**, 723–760.

Schultz, R.A. & Siddharthan, R. 2005. A general framework for the occurrence and faulting of deformation bands in porous granular rocks. *Tectonophysics*, **411**, 1–18, https://doi.org/10.1016/j.tecto.2005.07.008.

Shipton, Z. & Cowie, P. 2001. Damage zone and slip-surface evolution over um to km scales in high-porosity Navajo sandstone, Utah. *Journal of Structural Geology*, **23**, 1825–1844.

Shipton, Z.K., Soden, A.M., Kirkpatrick, J.D., Bright, A.M. & Lunn, R.J. 2006. How thick is a fault? Fault displacement-thickness scaling revisited. *In*: Abercrombie, R. (ed.) *Earthquakes: Radiated Energy and Physics of Faulting*. AGU, 193–198., https://doi.org/10.1029/170GM19.

Sibson, R.H. 1977. Fault rocks and fault mechanisms. *Journal of the Geological Society*, **133**, 191–213, https://doi.org/10.1144/gsjgs.133.3.0191.

Sibson, R.H. 1986. Brecciation processes in fault zones: inferences from earthquake rupturing. *Pure and Applied Geophysics*, **124**, 159–175.

Siman-Tov, S., Aharonov, E., Sagy, A. & Emmanuel, S. 2013. Nanograins form carbonate fault mirrors. *Geology*, **41**, 703–706, https://doi.org/10.1130/G34087.1.

Smeraglia, L., Aldega, L., Billi, A., Carminati, E. & Doglioni, C. 2016. Phyllosilicate injection along extensional carbonate-hosted faults and implications for co-seismic slip propagation: Case studies from the central Apennines, Italy. *Journal of Structural Geology*, **93**, 29–50, https://doi.org/10.1016/j.jsg.2016.10.003.

Smeraglia, L., Bettucci, A., Billi, A., Carminati, E., Cavallo, A., Di Toro, G., Natali, M., Passeri, D., Rossi, M., & Spagnuolo, E. 2017. Microstructural evidence for seismic and aseismic slips along clay-bearing, carbonate faults, *Journal of Geophysysical Research: Solid Earth*, **122**, 3895– 3915, doi:10.1002/2017JB014042.

Smith, D.A. 1980. Sealing and Nonsealing Faults In Louisiana Gulf Coast Salt Basin. *AAPG Bulletin*, **64**, 145–172.

Smith, D. B. 1995. Marine of Permian England. *Geological Conservation Review Series*, **8**, 205.

Smith, S.A.F., Billi, A., Toro, G. Di & Spiess, R. 2011. Principal Slip Zones in Limestone: Microstructural Characterization and Implications for the Seismic Cycle (Tre Monti Fault, Central Apennines, Italy). *Pure*

and Applied Geophysics, **168**, 2365–2393, https://doi.org/10.1007/s00024-011-0267-5.

Solum, J.G. & Huisman, B.A.H. 2017. Toward the creation of models to predict static and dynamic fault-seal potential in carbonates. *Petroleum Geoscience*, **23**, https://doi.org/10.1144/petgeo2016-044.

Sosio De Rosa, S., Shipton, Z.K., Lunn, R.J., Kremer, Y. & Murray, T. 2018. Along-strike fault core thickness variations of a fault in poorly lithified sediments, Miri (Malaysia). *Journal of Structural Geology*, **116**, 189–206, https://doi.org/10.1016/j.jsg.2018.08.012.

Sperrevik, S., Gillespie, P.A., Fisher, Q., Halvorsen, T. & Knipe, R.J. 2002. Empirical estimation of fault rock properties. *Norwegian Petroleum Society Special Publications*, **11**, 109–125, https://doi.org/10.1016/S0928-8937(02)80010-8.

Storti, F., Billi, A. & Salvini, F. 2003. Particle size distributions in natural carbonate fault rocks: insights for non-self-similar cataclasis. *Earth and Planetary Science Letters*, **206**, 173–186.

Suppe, J. 1983. Geometry and kinematics of fault-bend folding. *American Journal of Science*, **283**, 684–721, https://doi.org/10.2475/ajs.283.7.684.

Tarasewicz, J.P.T., Woodcock, N.H. & Dickson, J.A.D. 2005. Carbonate dilation breccias: Examples from the damage zone to the Dent Fault, northwest England. *Bulletin of the Geological Society of America*, https://doi.org/10.1130/B25568.1.

Taylor, D.J. & Dietvorst, J.P.A. 1991. The Cormorant Field, Blocks 211/21a, 211/26a, UK North Sea. *In*: *Abbotts, I. L. (Ed.), 1991, United Kingdom Oil and Gas Fields, 25 Years Commemorative Volume, Geological Society Memoir No. 14*. 73–81.

Tondi, E. 2007. Nucleation, development and petrophysical properties of faults in carbonate grainstones: Evidence from the San Vito Lo Capo peninsula (Sicily, Italy). *Journal of Structural Geology*, **29**, 614–628, https://doi.org/10.1016/j.jsg.2006.11.006.

Tondi, E., Antonellini, M., Aydin, A., Marchegiani, L. & Cello, G. 2006. The role of deformation bands, stylolites and sheared stylolites in fault development in carbonate grainstones of Majella Mountain, Italy. *Journal of Structural Geology*, **28**, 376–391.

Tondi, E., Rustichelli, A., et al. 2016. Hydraulic properties of fault zones in porous carbonates, examples from central and southern Italy. *Italian Journal of Geosciences*, **135**, 68–79, https://doi.org/10.3301/IJG.2015.08.

Treiber, L.E., Archer, D.L. & Owens, W.W. 1972. Laboratory evaluation of the wettability of 50 oil producing reservoirs. *SPE Journal*, **December**, 531–540.

Trocchio, J.T. 1990. Investigation of Fateh Mishrif fluid-conductive faults. *Society of Petroleum Engineers*, 1038–1045.

Tucker, M. E. 1991, Sequence stratigraphy of carbonate-evaporite basins: Models and application to the Upper Permian (Zechstein) of northeast England and adjoining North Sea. *Journal of the Geological Society*, **148**, 1019–1036, doi:10.1144/gsjgs.148.6.1019.

Ukar, E. & Laubach, S.E. 2016. Syn- and postkinematic cement textures in fractured carbonate rocks: Insights from advanced cathodoluminescence imaging. *Tectonophysics*, **690**, 190-205, https://doi.org/10.1016/j.tecto.2016.05.001.

Vajdova, V., Baud, P. & Wong, T. 2004. Compaction, dilatancy, and failure in porous carbonate rocks. *Journal of Geophysical Research*, **109**, 1–16, https://doi.org/10.1029/2003JB002508.

van der Zee, W. & Urai, J.L. 2005. Processes of normal fault evolution in a siliciclastic sequence: a case study from Miri, Sarawak, Malaysia. *Journal of Structural Geology*, **27**, 2281–2300, https://doi.org/10.1016/j.jsg.2005.07.006.

van der Zee, W., Urai, J.L. & Richard, P.D. 2003. Lateral clay injection into normal faults. *GeoArabia*, **8**, 501–522.

Vega Riveros, G., Saputelli, L., Patino, J., Chacon, A. & Solis, R. 2011. Reserves estimation uncertainty in a mature naturally-fractured carbonate field located in Latin America. *In*: *Offshore Technology Conference Brasil*. OTC 22517.

Viti, C., Collettini, C. & Tesei, T. 2014. Pressure solution seams in carbonatic fault rocks: mineralogy, micro/nanostructures and deformation mechanism. *Contributions to Mineralogy and Petrology*, 167–970, https://doi.org/10.1007/s00410-014-0970-1.

Walsh, J.J., Nicol, A. & Childs, C. 2002. An alternative model for the growth of faults. *Journal of Structural Geology*, **24**, 1669–1675, https://doi.org/10.1016/S0191-8141(01)00165-1.

Watterson, J., Childs, C. & Walsh, J.J. 1998. Widening of fault zones by erosion of asperities formed by bed-parallel slip. *Geology*, **26**, 71–74, https://doi.org/10.1130/0091-7613(1998)026<0071.

Watts, N.L. 1987. Theoretical aspects of cap-rock and fault seals for single- and two-phase hydrocarbon columns. *Marine and Petroleum Geology*, **4**, 274–307.

Weber, K.J., Mandl, G.J., Pilaar, W.F., Lehner, B.V.F. & Precious, R.G. 1978. The Role Of Faults In Hydrocarbon Migration And Trapping In Nigerian Growth Fault Structures. *Offshore Technology Conference*, 11, https://doi.org/10.4043/3356-MS.

Wibberley, C.A.J. & Shimamoto, T. 2003. Internal structure and permeability of major strike-slip fault zones: the Median Tectonic Line in Mie Prefecture, Southwest Japan. *Journal of Structural Geology*, **25**, 59–78, https://doi.org/10.1016/s0191-8141(02)00014-7.

Wibberley, C.A.J., Petit, J.-P. & Rives, T. 2007. The mechanics of fault distribution and localization in high-porosity sands, Provence, France. *Geological Society, London, Special Publications*, **289**, 19–46, https://doi.org/https://doi.org/10.1144/sp289.3.

Wibberley, C.A.J., Yielding, G. & Di Toro, G. 2008. Recent advances in the understanding of fault zone internal structure: a review. *In: Wibberley, C. A. J., Kurz, W., Imber, J., Holdsworth, R. E. & Collettini, C. (eds). The internal structure of fault zones: Implications for mechanical and fluid-flow properties. Geological Society, London, Special Publications*, **299**, 5–33.

Williams, R.T., Goodwin, L.B. & Mozley, P.S. 2017. Diagenetic controls on the evolution of fault-zone architecture and permeability structure: Implications for episodicity of fault-zone fluid transport in extensional basins. *Bulletin of the Geological Society of America*, **129**, 464–478, https://doi.org/10.1130/B31443.1.

Wilson, J.E., Chester, J.S. & Chester, F.M. 2003. Microfracture analysis of fault growth and wear processes, Punchbowl Fault, San Andreas system, California. *Journal of Structural Geology*, **25**, 1855–1873, https://doi.org/10.1016/s0191-8141(03)00036-1.

Wiprut, D. & Zoback, M.D. 2000. Fault reactivation and fluid flow along a previously dormant normal fault in the northern North Sea. *Geology*, **28**, 595–598.

Wong, T., David, C. & Zhu, W. 1997. The transition from brittle faulting to cataclastic flow in porous sandstones: Mechanical deformation. *Journal of Geophysical Research*, **102**, 3009–3025, https://doi.org/10.1029/96jb03281.

Woodcock, N.H. & Mort, K.M. 2008. Classification of fault breccias and related fault rocks. *Geological Magazine*, **145**, 435–440, https://doi.org/10.1017/S0016756808004883.

Woodcock, N.H. & Underhill, J.R. 1987. Emplacement-related fault patterns around the Northern Granite, Arran, Scotland. *Geological Society of America Bulletin*, **98**, 515–527.

Woodcock, N.H., Omma, J.E. & Dickson, J.A.D. 2006. Chaotic breccia along the Dent Fault, NW England: implosion or collapse of a fault void? *Journal of the Geological Society, London*, **163**, 431–446.

Woodcock, N.H., Dickson, J. a. D. & Tarasewicz, J.P.T. 2007. Transient permeability and reseal hardening in fault zones: evidence from dilation breccia textures. *Geological Society, London, Special Publications*, **270**, 43–53.

Wright, V., Woodcock, N.H. & Dickson, J.A.D. 2009. Fissure fills along faults: Variscan examples from Gower, South Wales. *Geological Magazine*, **146**, 890–902, https://doi.org/10.1017/S001675680999001X.

Yaxley, L.M. 1987. Effect of a partially communicating fault on transient pressure behavior. *Society of Petroleum Engineers*, https://doi.org/10.2118/14311-PA.

Yielding, G., Freeman, B. & Needham, D. 1997. Quantitative fault seal prediction. *AAPG bulletin*, **6**, 897–917.

Yielding, G., Bretan, P. & Freeman, B. 2010. Fault seal calibration: a brief review. *Geological Society, London, Special Publications*, **347**, 243–255, https://doi.org/10.1144/sp347.1

Zhang, J., Wong, T.-F. & Davis, D.M. 1990. Micromechanics of pressure-induced grain crushing in porous rocks. *Journal of Geophysical Research*, **95**, 341–352, https://dx.doi.org/10.1029/JB095iB01p00341.

Appendices

Appendix 1: Core plug info

The following table provides the sample details for each core plug used within this study, including the location and porosity, permeability and Hounsfield unit standard deviation (σ_{HU}) for each plug.

Core plug no.	Sample description	Sample orientation	Fault zone	Host lithology	Lithology	Fault kinematics	Throw (m)	Bulk volume (cc)	He-Por. (%)	Perm. (mD)	σHU (HU)
ma174	Host	z	Qala Point Fault Zone	LCL (Attard member)	Algal Packstone	Oblique normal	30		16.7	0.16	
ma175	Host	z	Qala Point Fault Zone	LCL (Attard member)	Algal Packstone	Oblique normal	30		7.7	0.07	
ma15_038cz1	Cemented	x	Qala Point Fault Zone	LCL (Attard member)	Algal Packstone	Oblique normal	30	52.44	4.9	0.0059	269.59
ma15_038cz2	Cemented	x	Qala Point Fault Zone	LCL (Attard member)	Algal Packstone	Oblique normal	30	51.27	6.62	2.68	
ma15_038cz3	Cemented	x	Qala Point Fault Zone	LCL (Attard member)	Algal Packstone	Oblique normal	30	20.09	5.49	0.019	
ma15_038cy	Cemented	x	Qala Point Fault Zone	LCL (Attard member)	Algal Packstone	Oblique normal	30	20.78	5.51	0.026	
ma15_038cx	Cemented	x	Qala Point Fault Zone	LCL (Attard member)	Algal Packstone	Oblique normal	30	21.13	5.29	0.038	
ma15_039z1	Mosaic Breccia	z	Qala Point Fault Zone	LCL (Attard member)	Algal Packstone	Oblique normal	30	15.18	7.32	4.6	
ma15_039z2	Mosaic Breccia	z	Qala Point Fault Zone	LCL (Attard member)	Algal Packstone	Oblique normal	30	17.49	9.37	7.52	
ma15_041z1	Mosaic Breccia	z	Qala Point Fault Zone	LCL (Attard member)	Algal Packstone	Oblique normal	30	36.68	4.01	0.0078	421.53
ma15_041z2	Mosaic Breccia	z	Qala Point Fault Zone	LCL (Attard member)	Algal Packstone	Oblique normal	30	55.09	1.23	0.004	199.34

ma15_043z	Cemented	z	Qala Point Fault Zone	LCL (Attard member)	Algal Packstone	Oblique normal	30	10.33	1.52	0.168	
ma15_045z1	Host	z	Qala Point Fault Zone	LCL (Attard member)	Algal Packstone	Oblique normal	30	54.86	18.84	4.61	285.21
ma15_045z2	Host	z	Qala Point Fault Zone	LCL (Attard member)	Algal Packstone	Oblique normal	30	50.1	7.36	0.58	265.01
ma15_045y	Host	y	Qala Point Fault Zone	LCL (Attard member)	Algal Packstone	Oblique normal	30	53.82	19.3	9.7	284.92
ma15_049z	Chaotic Breccia	z	Qala Point Fault Zone	LCL (Attard member)	Algal Packstone	Strike-slip	30	13.14	2.33	0.0038	
ma15_050z	Chaotic Breccia	z	Qala Point Fault Zone	LCL (Attard member)	Algal Packstone	Strike-slip	30	25.25	1.52	0.023	
ma15_050x	Chaotic Breccia	x	Qala Point Fault Zone	LCL (Attard member)	Algal Packstone	Strike-slip	30	19.41	1.52	0.0068	
ma15_050y	Chaotic Breccia	y	Qala Point Fault Zone	LCL (Attard member)	Algal Packstone	Strike-slip	30	22.95	1.52	0.026	
ma15_050z2	Chaotic Breccia	z	Qala Point Fault Zone	LCL (Attard member)	Algal Packstone	Strike-slip	30	22.98	1.52	0.0015	
ma005z	Crackle Breccia	z	Qala Point Fault Zone	LCL (Attard member)	Algal Packstone	Oblique normal	30	42.39	6.75	2.3	
ma007z	Crackle Breccia	z	Qala Point Fault Zone	LCL (Attard member)	Algal Packstone	Oblique normal	30	50.64	6.82	7.84	294.93
ma010z1	Cemented	z	Qala Point Fault Zone	LCL (Attard member)	Algal Packstone	Oblique normal	30	54.8	5.24	0.00014	301.06

ma010z2	Crackle Breccia	z	Qala Point Fault Zone	LCL (Attard member)	Algal Packstone	Oblique normal	30	42.16	16.93	14	441.58
ma012z	Cemented	z	Qala Point Fault Zone	LCL (Attard member)	Algal Packstone	Oblique normal	30	48.11	13.87	0.16	225.27
ma104z1	Host	z	Qala Point Fault Zone	LCL (Attard member)	Algal Packstone	Normal	30	50.68	10.1	9.36	368.86
ma104z2	Host	z	Qala Point Fault Zone	LCL (Attard member)	Algal Packstone	Normal	30	51.62	12.35	3.93	422.23
ma080z	Cataclasite	z	Qammieh Fault	LCL (Attard member)	Algal Packstone	Normal	90	53.7	13.98	0.057	287.91
ma089az	Fractured cataclasite	z	Victoria Lines Fault	LCL (Attard member)	Algal Packstone	Normal	195	34.88	9.73	0.0039	220.4
ma089bz	Fractured cataclasite	z	Victoria Lines Fault	LCL (Attard member)	Algal Packstone	Normal	195	47.38	14.63	0.19	493.18
ma15_038by	Calcrete infill	x	Qala Point Fault Zone	n/a	Calcrete	Oblique normal	30	20.07	4.49	0.022	
ma15_038bx	Calcrete infill	x	Qala Point Fault Zone	n/a	Calcrete	Oblique normal	30	11.28	3.18	0.0002	
ma15_057x	Cataclasite	x	Fault D'	LCL (Xlendi member)	Packstone	Normal	11.7	10.78	1.63	0.000062	35.23
ma15_057y	Cataclasite	y	Fault D'	LCL (Xlendi member)	Packstone	Normal	11.7	19.78	7.04	0.000012	221.33
ma15_057z	Cataclasite	z	Fault D'	LCL (Xlendi member)	Packstone	Normal	11.7	12.54	1.62	0.000046	62.09

ma083z1	Cataclasite	z	Il-Maghlaq Fault	LCL (Xlendi member)	Packstone	Normal	210	6.23	2.95	4.3E-06	1.58
ma083z2	Damage	z	Il-Maghlaq Fault	LCL (Xlendi member)	Packstone	Normal	210	38.01	6.52	0.013	196.43
ma084z	Cataclasite	z	Il-Maghlaq Fault	LCL (Xlendi member)	Packstone	Normal	210	8.52	3.2	0.000048	7.15
ma086	Damage	z	Il-Maghlaq Fault	LCL (Xlendi member)	Packstone	Normal	210	11.58	18.43	17.71	236.49
ma087z	Fractured	z	Il-Maghlaq Fault	LCL (Xlendi member)	Packstone	Normal	210	46.51	33.79	16.2	248.36
ma068z	Single Deformation Band	z	Il-Maghlaq Fault	LCL (Xlendi member)	Packstone	Normal	20	52.98	12.92	78.07	385.77
ma070	Cataclasite	z	Il-Maghlaq Fault	LCL (Xlendi member)	Packstone	Normal	20	41.44	1.02	0.0007	128.26
ma077z	Clustered Deformation Band	z	Il-Maghlaq Fault	LCL (Xlendi member)	Packstone	Normal	20	45.91	16.23	26.62	505.1
ma096y	Cataclasite	y	Il-Maghlaq Fault	LCL (Xlendi member)	Packstone	Normal	210	16.27	0.73		115.32
ma096z	Cataclasite	z	Il-Maghlaq Fault	LCL (Xlendi member)	Packstone	Normal	210	16.36	6.72	0.00048	148.42
ma171x	Host	x	Qala Point Fault Zone	LCL (Xlendi member)	Packstone	Oblique normal	30		26.6	98.8	

ma171y	Host	y	Qala Point Fault Zone	LCL (Xlendi member)	Packstone	Oblique normal	30		18.54	20.3	
ma15_038az	Cataclasite	x	Qala Point Fault Zone	LCL (Xlendi member)	Packstone	Oblique normal	30	35.04	4.55	0.005	171.89
ma15_038ay	Cataclasite	x	Qala Point Fault Zone	LCL (Xlendi member)	Packstone	Oblique normal	30	22.14	3.05	0.00093	
ma15_042z	Microbreccia	z	Qala Point Fault Zone	LCL (Xlendi member)	Packstone	Oblique normal	30	55.29	10.12	144	423.44
ma15_044z	Mosaic Breccia	z	Qala Point Fault Zone	LCL (Xlendi member)	Packstone	Oblique normal	30	19.75	4.35	3.71	
ma15_046z	Host	z	Qala Point Fault Zone	LCL (Xlendi member)	Packstone	Oblique normal	30	43.07	6.75		257.16
ma15_046y	Host	y	Qala Point Fault Zone	LCL (Xlendi member)	Packstone	Oblique normal	30	38.76	13.69		350
ma002z	Cataclasite	z	Qala Point Fault Zone	LCL (Xlendi member)	Packstone	Oblique normal	30	40.1	13.01	0.0034	459.39
ma003z	Mosaic Breccia	z	Qala Point Fault Zone	LCL (Xlendi member)	Packstone	Oblique normal	30	29.88	7.78	10.9	228.9
ma103x	Host	x	Qala Point Fault Zone	LCL (Xlendi member)	Packstone	Normal	30	49.79	24.81	71.9	382.86
ma103y	Host	y	Qala Point Fault Zone	LCL (Xlendi member)	Packstone	Normal	30	70.94	25.38	77	405.35
ma103z	Host	z	Qala Point Fault Zone	LCL (Xlendi member)	Packstone	Normal	30	67.26	22.21	64	210.2

ma081y	Cataclasite	y	Qammieh Fault	UCL	Packstone	Normal	90	33.05	9.11	0.066	255.96
ma081z	Fractured	z	Qammieh Fault	UCL	Packstone	Normal	90	40.3	10.4	35.71	310.74
ma098x	Host	z	Qammieh Fault	UCL	Packstone	Normal	90	61.4	28.97	66.13	552.14
ma098y	Host	z	Qammieh Fault	UCL	Packstone	Normal	90	31.51	29.32	31.75	
ma098z	Host	z	Qammieh Fault	UCL	Packstone	Normal	90	58.2	34.78	81.72	
ma099x	Host	z	Qammieh Fault	UCL	Packstone	Normal	90	54.85	39.25	49.79	429.23
ma099y	Host	z	Qammieh Fault	UCL	Packstone	Normal	90	39.39	36.72	41.49	456.95
ma099z	Host	z	Qammieh Fault	UCL	Packstone	Normal	90	35.46	37.56	50.26	391.12
ma100x	Host	z	Qammieh Fault	UCL	Packstone	Normal	90	38.01	36.69		751.18
ma019x	Host	z	South Gozo Fault	UCL	Packstone	Normal	40	67.52	43.68	14.6	492.85
ma022y1	Fractured	y	South Gozo Fault	UCL	Packstone	Normal	40	52.31	2.09	31	153.67
ma022y31	Damage	y	South Gozo Fault	UCL	Packstone	Normal	40	49.71	23.85	40.9	302.38

ma022z3	Clustered Deformation Band	z	South Gozo Fault	UCL	Packstone	Normal	40	66.2	20.97	0.52	300.26
ma023y	Fractured	y	South Gozo Fault	UCL	Packstone	Normal	40	74.7	39.95	102.5	258.49
ma023z1	Fractured	z	South Gozo Fault	UCL	Packstone	Normal	40	50	40.51	87.6	241.75
ma024z	Fractured	z	South Gozo Fault	UCL	Packstone	Normal	40	60.09	23.57	24.4	212.46
ma026x	Damage	z	South Gozo Fault	UCL	Packstone	Normal	40	33.74	27.86	54.8	301.23
ma026z	Single Deformation Band	z	South Gozo Fault	UCL	Packstone	Normal	40	70.93	22.17	0.86	290.4
ma028z1	Clustered Deformation Band	z	South Gozo Fault	UCL	Packstone	Normal	40	75.03	23.91	0.15	
ma029y1	Cataclasite	y	South Gozo Fault	UCL	Packstone	Normal	40	21.12	2.97	0.00074	130.36
ma029y3	Clustered Deformation Band	y	South Gozo Fault	UCL	Packstone	Normal	40	37.63	28.47	83.9	201.73
ma029z11	Cataclasite	z	South Gozo Fault	UCL	Packstone	Normal	40	32.5	11.61	0.35	254.85

ma029z12	Clustered Deformation Band	z	South Gozo Fault	UCL	Packstone	Normal	40	42.74	32.84	93.7	296.69
ma030z	Clustered Deformation Band	z	South Gozo Fault	UCL	Packstone	Normal	40	11.51	26.73	1.25	
ma031z	Cataclasite	z	South Gozo Fault	UCL	Packstone	Normal	40	54.8	0.9	0.0001	184.39
ma065x	Host	z	South Gozo Fault	UCL	Packstone	Normal	40	76.1	37.13	42.4	241.46
ma065y	Host	y	South Gozo Fault	UCL	Packstone	Normal	40	75.16	36.07	107.8	301.23
ma065z	Host	z	South Gozo Fault	UCL	Packstone	Normal	40	57.08	36.18	62.16	197.91
ma033a	Microbreccia	z	South Qala Fault	Xlendi	Packstone	Normal	60	14.12	18.84	0.028	394.4
ma057a	Cataclasite	z	South Qala Fault	Xlendi	Packstone	Normal	60	14.14	1.36	0.00006	
ma057b	Cataclasite	z	South Qala Fault	Xlendi	Packstone	Normal	60	6.37	2.7	0.019	43.35
ma066x	Cemented	x	South Qala Fault	Xlendi	Packstone	Normal	60	23.29	3.69	0.003	346.32
ma066y	Cemented	y	South Qala Fault	Xlendi	Packstone	Normal	60	21.33	1.62	0.00026	318.97

ma066z	Cemented	z	South Qala Fault	Xlendi	Packstone	Normal	60	13.38	3.62	0.00016	378.35
ma079z	Single Deformation Band	z	Victoria Lines Fault	Xlendi	Packstone	Normal	90	37.86	20.03	0.11	335.92
ma090	Cataclasite	z	Victoria Lines Fault	Xlendi	Packstone	Normal	195	43.75	16.31	0.089	
ma15_055h	Host	z	Fault D'	MGL	Wackestone	Normal	11.7	49.52	36.84	7.32	
ma15_055z1	Fractured	z	Fault D'	MGL	Wackestone	Normal	11.7	52.6	36.38	7.61	124.29
ma15_055z2	Cemented/re crystallised	z	Fault D'	MGL	Wackestone	Normal	11.7	42.39	28.68	0.12	195.51
ma069z	Breccia	z	Il-Maghlaq Fault	MGL	Wackestone	Normal	20	58.13	25.41	4.66	546.54
ma073z	Clustered Deformation Band	z	Il-Maghlaq Fault	MGL	Wackestone	Normal	20	33.49	26.07	0.78	190.13
ma074z1	Clustered Deformation Band	z	Il-Maghlaq Fault	MGL	Wackestone	Normal	20	60.61	28.88	4.32	219.74
ma074z2	Clustered Deformation Band	z	Il-Maghlaq Fault	MGL	Wackestone	Normal	20	41.27	28.53	1.91	198.87
ma075y	Clustered Deformation Band	y	Il-Maghlaq Fault	MGL	Wackestone	Normal	20	39.64	26	6.1	170.85

ma075z	Clustered Deformation Band	z	Il-Maghlaq Fault	MGL	Wackestone	Normal	20	45.68	24.42	6.4	178.19
ma076z	Clustered Deformation Band	z	Il-Maghlaq Fault	MGL	Wackestone	Normal	20	53.18	28.77	0.5	213.15
ma097x	Host	x	Il-Maghlaq Fault	LCL (Maghlaq member)	Wackestone	Normal	210	51.1	18.13	0.04	306.04
ma097y	Host	y	Il-Maghlaq Fault	LCL (Maghlaq member)	Wackestone	Normal	210	46.65	18.53	0.17	295.14
ma097z	Host	z	Il-Maghlaq Fault	LCL (Maghlaq member)	Wackestone	Normal	210	43.93	17.67	0.12	283.61
ma082z	Cataclasite	z	Qammieh Fault	LGL	Wackestone	Normal	90	6.36	9.47	0.024	158.18
ma094z	Host	z	Qammieh Fault	LGL	Wackestone	Normal	90	5.82	37.31	34.61	215.93
ma095x	Host	z	Qammieh Fault	LGL	Wackestone	Normal	90	24.19	39.48	22.44	148.69
ma095y	Host	z	Qammieh Fault	LGL	Wackestone	Normal	90	31.96	41.87	16.66	177.61
ma095z	Host	z	Qammieh Fault	LGL	Wackestone	Normal	90	41.39	38.92	27.95	180.49

ma105z	Cemented	z	South Gozo Fault	GL	Wackestone	Normal	80	54.29	4.47	0.00017	
ma106z	Breccia	z	South Gozo Fault	GL	Wackestone	Normal	80	52.18	32.28	1	213.83
ma108a	Smeared host		South Gozo Fault	Greensand Fm.	Wackestone	Normal	80				
ma034y	Cemented	z	South Qala Fault	LGL	Wackestone	Normal	60	5.23	32.78		346.8
ma035	Cemented	z	South Qala Fault	LGL	Wackestone	Normal	60	13.19	7.43	0.0005	90.37
ma036	Cemented	z	South Qala Fault	LGL	Wackestone	Normal	60	10.76	14.16	0.0073	127.02
ma037	Cemented	z	South Qala Fault	LGL	Wackestone	Normal	60	10.79	15.78	0.033	138.21
ma038	Cemented	z	South Qala Fault	LGL	Wackestone	Normal	60	16.37	10.1	0.0006	162.25
ma040	Microbreccia	z	South Qala Fault	LGL	Wackestone	Normal	60	12.55	11.15	0.021	155.54
ma042x	Cemented	x	South Qala Fault	LGL	Wackestone	Normal	60	13.13	13.04	0.0015	130.62
ma042y	Cemented	y	South Qala Fault	LGL	Wackestone	Normal	60	13.37	14.92	0.011	130.87
ma042z	Cemented	z	South Qala Fault	LGL	Wackestone	Normal	60	18.9	13.32	0.0044	147.88

ma044	Cemented	z	South Qala Fault	LGL	Wackestone	Normal	60	17.05	6.57	0.0015	99.19
ma045	Cataclasite	z	South Qala Fault	LGL	Wackestone	Normal	60	9.91	5.31	0.00033	69.9
ma046	Cataclasite	z	South Qala Fault	LGL	Wackestone	Normal	60	9.69	6.44	0.00019	71.81
ma048x	Microbreccia	x	South Qala Fault	LGL	Wackestone	Normal	60	9.4	6.18	0.036	189.29
ma048y	Microbreccia	y	South Qala Fault	LGL	Wackestone	Normal	60	17.25	7.08	0.0011	342.15
ma048z	Microbreccia	z	South Qala Fault	LGL	Wackestone	Normal	60	13.84	7.16	0.0046	527.32
ma049	Microbreccia	z	South Qala Fault	LGL	Wackestone	Normal	60	9.89	5.34	0.15	88.01
ma053	Cataclasite	z	South Qala Fault	LGL	Wackestone	Normal	60	9.1	2.18	0.00009	28.89
ma055	Cemented	z	South Qala Fault	LGL	Wackestone	Normal	60				
ma056	Cataclasite	z	South Qala Fault	LGL	Wackestone	Normal	60	10.62	2.9	0.000001	116.84
ma15_029z	Host	z	Fault D'	MGL	Wackestone	Normal	11.7	61.58	37.13	7.72	158.11
ma15_031z	Host	z	Fault D'	MGL	Wackestone	Normal	11.7	60.33	30.73	14.2	184.93
ma092	Cemented	z	Victoria Lines Fault	LGL	Wackestone	Normal	195	29.85	18.33	0.031	

ma18_001	Host	x	n/a	MGL	Wackestone	Normal	n/a	19.58	33.17	4.42	
ma18_003x	Host	x	South Qala Fault	LGL	Wackestone	Normal	60	20.13	36.26	4.28	
ma18_003y	Host	y	South Qala Fault	LGL	Wackestone	Normal	60	26.67	37.15	16.21	
ma18_004	Host	x	Victoria Lines Fault	LGL	Wackestone	Normal	60	12.43	23.59	4.85	

Appendix 2: Production model data

The following tables provides the raw data output from the ECLIPSE flow simulation models, from both the Gozo production simulations (Tables 1-6; Section 5.7.1) and the faulted type III fractured reservoir model (Tables 7-9; Section 5.8). The table headings are as follows:

Heading	Description
FPR	Average field pressure
FOPR	Field oil production rate
FOPT	Field oil production total
WBHP	Well bottom hole pressure
FWPR	Field water production rate
FWPT	Field water production total
WWCT	Well water cut

Table 1: Open faults

TIME	FPR	FOPR	FOPT	WBHP	WBHP	WBHP	WBHP	WBHP	WBHP	WBHP	WBHP	WBHP	FWPR	FWPT
DAYS	BARSA	SM3/ DAY	SM3 (^10^3)	BARSA	BARSA	BARSA	BARSA	BARSA	BARSA	BARSA	BARSA	BARSA	SM3/ DAY	SM3
				PROD1	PROD2	PROD3	PROD4	INJ1	INJ2	INJ3	INJ4	INJ5		
0	526.08	0	0	527.62	528.45	532.24	526.89	525.03	542.33	533.42	527.53	530.04	0.00	0
1	526.08	1963.374	2	317.68	320.51	231.42	162.33	712.80	649.75	726.11	745.18	700.67	36.63	37
2	526.08	1951.654	4	299.48	302.90	209.47	138.51	727.13	650.33	738.10	762.52	709.96	48.35	83
4	526.08	1947.292	7	287.01	290.68	195.44	122.96	721.52	649.13	730.21	758.27	704.84	52.71	171
6	526.08	1947.714	12	279.00	282.58	186.63	112.67	714.58	645.80	720.82	749.50	697.39	52.29	294
8	526.08	1949.282	16	274.80	278.23	181.91	107.09	710.20	643.42	715.32	741.97	694.10	50.72	396
10	526.08	1951.071	20	271.82	275.09	178.44	103.02	706.79	641.90	711.91	736.96	690.96	48.93	494
15	526.08	1950.575	29	267.23	270.16	172.70	100.00	700.15	640.52	704.01	727.60	686.82	45.17	720
20	526.08	1947.825	39	263.99	266.66	168.47	100.00	696.29	640.32	699.66	721.40	685.46	42.39	932
30	526.08	1943.834	58	259.78	262.07	162.74	100.00	693.32	641.19	696.38	715.72	686.03	39.54	1327
40	526.08	1940.485	78	256.72	258.75	158.50	100.00	692.32	642.30	695.15	712.78	687.43	38.11	1709
50	526.08	1937.608	97	254.34	256.16	155.17	100.00	692.04	643.45	694.82	711.50	688.90	37.40	2083
80	526.08	1931.583	155	249.69	251.16	148.70	100.00	692.51	646.41	695.06	711.23	692.62	36.91	3190
115	526.08	1926.57	223	245.86	247.10	143.42	100.00	693.68	649.18	695.53	712.29	696.03	36.88	4480
150	526.08	1922.726	290	242.94	244.02	139.38	100.00	695.11	651.50	696.34	713.43	698.69	36.98	5775
200	526.08	1918.534	386	239.78	240.70	134.99	100.00	697.10	654.39	697.44	715.00	701.91	37.22	7636
250	526.08	1915.14	482	237.26	238.06	131.46	100.00	698.97	656.95	698.50	716.37	704.58	37.47	9509
350	526.09	1910.11	673	233.64	234.25	126.20	100.00	702.24	661.27	700.43	718.46	708.62	37.94	13303
450	526.10	1906.192	863	230.86	231.31	122.04	100.00	704.95	664.98	701.86	720.06	711.79	38.36	17139
550	526.11	1903.039	1054	228.64	228.93	118.63	100.00	707.29	668.28	703.04	721.36	714.31	38.74	21013
650	526.12	1900.44	1244	226.81	226.94	115.75	100.00	709.35	671.26	704.03	722.44	716.31	39.07	24920
750	526.13	1898.263	1433	225.26	225.22	113.30	100.00	711.17	673.96	704.81	723.33	717.92	39.37	28856

850	526.14	1896.416	1623	223.92	223.70	111.18	100.00	712.79	676.44	705.41	724.10	719.23	39.63	32820
950	526.15	1894.836	1813	222.73	222.34	109.33	100.00	714.25	678.73	705.89	724.79	720.30	39.87	36806
1200	526.19	1892.034	2286	220.38	219.56	105.89	100.00	717.25	683.71	706.65	726.18	721.96	40.27	46874
1450	526.23	1890.063	2758	218.42	217.21	103.29	100.00	719.75	688.01	707.01	727.34	722.90	40.51	57002
1700	526.26	1888.722	3230	216.72	215.17	101.30	100.00	721.87	691.82	707.13	728.36	723.34	40.59	67149
1950	526.30	1887.616	3702	215.22	213.36	100.00	100.00	723.71	695.25	707.05	729.31	723.44	40.49	77272
2200	526.35	1885.777	4174	213.85	211.75	100.00	100.00	725.32	698.37	706.84	730.19	723.29	40.20	87322
2450	526.39	1884.639	4645	212.60	210.29	100.00	100.00	726.76	701.24	706.55	731.03	722.96	39.78	97268
2700	526.44	1884.031	5116	211.44	208.97	100.00	100.00	728.06	703.89	706.19	731.85	722.51	39.26	107082
2950	526.48	1883.829	5587	210.36	207.76	100.00	100.00	729.23	706.37	705.79	732.65	721.97	38.64	116743
3200	526.53	1883.944	6058	209.34	206.64	100.00	100.00	730.30	708.68	705.36	733.43	721.36	37.96	126231
3450	526.58	1884.3	6529	208.38	205.61	100.00	100.00	731.28	710.86	704.93	734.19	720.71	37.21	135535
3700	526.63	1884.832	7000	207.47	204.66	100.00	100.00	732.18	712.91	704.49	734.93	720.03	36.44	144646
3950	526.68	1885.486	7471	206.60	203.77	100.00	100.00	733.02	714.85	704.06	735.66	719.32	35.66	153561
4200	526.73	1886.219	7943	205.77	202.95	100.00	100.00	733.79	716.69	703.63	736.38	718.61	34.88	162282
4450	526.78	1886.994	8415	204.98	202.17	100.00	100.00	734.52	718.44	703.21	737.08	717.89	34.13	170814
4700	526.83	1887.776	8887	204.22	201.45	100.00	100.00	735.20	720.09	702.81	737.76	717.18	33.41	179168
4950	526.88	1888.535	9359	203.48	200.77	100.00	100.00	735.84	721.67	702.42	738.43	716.47	32.75	187356
5200	526.93	1889.249	9831	202.77	200.13	100.00	100.00	736.44	723.18	702.05	739.08	715.76	32.16	195396
5450	526.99	1889.897	10303	202.08	199.54	100.00	100.00	737.01	724.61	701.69	739.71	715.07	31.65	203308
5700	527.04	1890.465	10776	201.41	198.97	100.00	100.00	737.56	725.99	701.34	740.33	714.39	31.22	211112
5950	527.09	1890.943	11249	200.76	198.44	100.00	100.00	738.07	727.30	701.02	740.94	713.72	30.88	218831
6200	527.15	1891.325	11722	200.13	197.94	100.00	100.00	738.56	728.55	700.71	741.52	713.06	30.63	226489
6450	527.20	1891.605	12195	199.52	197.46	100.00	100.00	739.03	729.75	700.41	742.10	712.42	30.48	234109
6700	527.26	1891.783	12668	198.92	197.01	100.00	100.00	739.48	730.90	700.13	742.65	711.79	30.42	241714
6950	527.31	1891.863	13140	198.34	196.59	100.00	100.00	739.91	732.01	699.87	743.19	711.18	30.45	249327
7200	527.37	1891.841	13613	197.78	196.18	100.00	100.00	740.32	733.07	699.62	743.72	710.59	30.58	256971
7450	527.43	1891.716	14086	197.23	195.79	100.00	100.00	740.72	734.08	699.39	744.23	710.01	30.79	264669
7700	527.48	1891.487	14559	196.69	195.42	100.00	100.00	741.10	735.06	699.17	744.73	709.45	31.10	272443

7950	527.54	1891.157	15032	196.17	195.07	100.00	100.00	741.47	736.00	698.96	745.21	708.90	31.49	280314
8200	527.60	1890.729	15505	195.67	194.73	100.00	100.00	741.83	736.90	698.76	745.69	708.37	31.96	288305
8450	527.66	1890.207	15977	195.19	194.40	100.00	100.00	742.17	737.76	698.58	746.14	707.85	32.52	296434
8700	527.71	1889.588	16450	194.72	194.09	100.00	100.00	742.50	738.60	698.41	746.59	707.35	33.15	304723
8950	527.77	1888.862	16922	194.27	193.78	100.00	100.00	742.82	739.40	698.24	747.02	706.87	33.88	313193
9200	527.83	1888.016	17394	193.83	193.48	100.00	100.00	743.14	740.17	698.09	747.45	706.40	34.71	321869
9450	527.89	1887.037	17866	193.39	193.20	100.00	100.00	743.44	740.92	697.95	747.86	705.95	35.65	330781
9700	527.95	1885.915	18337	192.97	192.92	100.00	100.00	743.73	741.64	697.82	748.26	705.51	36.71	339958
9950	528.01	1884.645	18808	192.54	192.65	100.00	100.00	744.02	742.33	697.70	748.65	705.08	37.89	349431
10200	528.07	1883.225	19279	192.13	192.39	100.00	100.00	744.30	742.99	697.59	749.03	704.67	39.20	359232
10450	528.13	1881.658	19750	191.71	192.14	100.00	100.00	744.57	743.63	697.49	749.40	704.27	40.64	369392
10700	528.20	1879.955	20219	191.30	191.90	100.00	100.00	744.83	744.25	697.39	749.76	703.89	42.19	379940
10950	528.26	1878.125	20689	190.89	191.67	100.00	100.00	745.08	744.85	697.31	750.11	703.52	43.85	390903

Table 2: Closed faults

TIME	FPR	FOPR	FOPT	WBHP	WBHP	WBHP	WBHP	WBHP	WBHP	WBHP	WBHP	WBHP	FWPR	FWPT
DAYS	BARSA	SM3/ DAY	SM4 (^10^3)	BARSA	BARSA	BARSA	BARSA	BARSA	BARSA	BARSA	BARSA	BARSA	SM3/ DAY	SM4
				PROD1	PROD2	PROD3	PROD4	INJ1	INJ2	INJ3	INJ4	INJ5		
0	526.08	0	0	527.62	528.45	532.24	526.89	525.03	542.33	533.42	527.53	530.04	0.00	0
1	526.08	1963.373	2	317.68	320.51	231.42	162.33	712.80	649.75	726.11	745.18	700.67	36.63	37
2	526.08	1951.647	4	299.48	302.90	209.44	138.51	727.13	650.33	738.10	762.52	709.96	48.35	83
4	526.08	1947.261	7	287.01	290.68	195.27	122.96	721.52	649.13	730.21	758.27	704.84	52.74	171
6	526.08	1947.613	12	279.00	282.58	186.09	112.67	714.58	645.80	720.82	749.50	697.39	52.39	295
8	526.08	1949.102	16	274.80	278.23	180.96	107.09	710.20	643.42	715.33	741.97	694.10	50.90	397
10	526.08	1950.797	20	271.82	275.09	176.98	103.01	706.79	641.90	711.93	736.96	690.96	49.20	495
15	526.08	1949.972	29	267.23	270.16	169.72	100.00	700.15	640.52	704.07	727.60	686.82	45.72	724
20	526.08	1946.877	39	263.99	266.66	163.82	100.00	696.29	640.32	699.80	721.40	685.46	43.25	940

30	526.08	1942.158	58	259.78	262.07	154.61	100.00	693.32	641.19	696.79	715.72	686.03	41.04	1351
40	526.08	1938.083	78	256.72	258.75	146.91	100.00	692.32	642.30	695.89	712.79	687.43	40.23	1753
50	526.08	1934.497	97	254.34	256.16	140.19	100.00	692.04	643.45	695.92	711.52	688.90	40.13	2154
80	526.08	1926.508	155	249.69	251.16	124.28	100.00	692.52	646.41	697.35	711.34	692.62	41.33	3394
115	526.08	1919.363	222	245.86	247.11	108.79	100.00	693.70	649.18	699.10	712.61	696.03	43.12	4903
150	526.08	1907.557	289	242.94	244.02	100.00	100.00	695.16	651.51	701.05	714.05	698.69	44.56	6463
200	526.09	1880.824	383	239.77	240.72	100.00	100.00	697.22	654.40	703.55	716.17	701.91	45.67	8747
250	526.09	1858.639	476	237.24	238.11	100.00	100.00	699.17	656.98	705.78	718.19	704.58	46.69	11081
350	526.11	1824.403	658	233.58	234.38	100.00	100.00	702.69	661.40	709.48	721.79	708.63	48.34	15915
450	526.13	1796.951	838	230.74	231.54	100.00	100.00	705.70	665.26	712.23	725.00	711.81	49.60	20876
550	526.16	1774.357	1015	228.44	229.27	100.00	100.00	708.38	668.76	714.41	727.96	714.34	50.58	25934
650	526.19	1755.404	1191	226.51	227.38	100.00	100.00	710.80	671.98	716.16	730.72	716.36	51.36	31069
750	526.22	1739.265	1365	224.86	225.75	100.00	100.00	713.00	674.98	717.51	733.31	718.00	51.98	36268
850	526.26	1725.349	1537	223.40	224.30	100.00	100.00	715.02	677.81	718.55	735.77	719.35	52.51	41519
950	526.29	1713.218	1709	222.10	222.99	100.00	100.00	716.90	680.51	719.36	738.12	720.46	52.96	46814
1200	526.39	1690.116	2131	219.44	220.21	100.00	100.00	721.02	686.73	720.50	743.55	722.30	53.81	60267
1450	526.50	1671.927	2549	217.18	217.72	100.00	100.00	724.68	692.45	721.00	748.55	723.43	54.46	73883
1700	526.61	1657.171	2964	215.19	215.44	100.00	100.00	728.01	697.86	721.07	753.22	724.11	54.96	87624
1950	526.73	1644.889	3375	213.39	213.32	100.00	100.00	731.07	703.02	720.85	757.60	724.45	55.35	101461
2200	526.85	1634.45	3783	211.74	211.32	100.00	100.00	733.93	708.01	720.45	761.76	724.55	55.62	115367
2450	526.97	1625.428	4190	210.20	209.42	100.00	100.00	736.63	712.84	719.91	765.69	724.47	55.80	129317
2700	527.10	1617.51	4594	208.74	207.62	100.00	100.00	739.20	717.54	719.29	769.44	724.26	55.89	143290
2950	527.22	1610.47	4997	207.36	205.90	100.00	100.00	741.66	722.14	718.61	773.02	723.95	55.91	157268
3200	527.35	1604.144	5398	206.03	204.25	100.00	100.00	744.01	726.65	717.90	776.45	723.56	55.88	171237
3450	527.49	1598.409	5797	204.75	202.68	100.00	100.00	746.27	731.08	717.17	779.73	723.10	55.80	185187
3700	527.62	1593.167	6196	203.51	201.17	100.00	100.00	748.46	735.43	716.43	782.87	722.59	55.69	199109
3950	527.76	1588.341	6593	202.30	199.73	100.00	100.00	750.58	739.73	715.69	785.90	722.04	55.56	212998
4200	527.89	1583.87	6989	201.13	198.35	100.00	100.00	752.64	743.96	714.96	788.80	721.46	55.41	226851
4450	528.03	1579.701	7384	199.97	197.02	100.00	100.00	754.64	748.13	714.25	791.60	720.85	55.27	240669

4700	528.17	1575.792	7778	198.84	195.74	100.00	100.00	756.59	752.26	713.54	794.29	720.21	55.14	254456
4950	528.31	1572.105	8171	197.73	194.51	100.00	100.00	758.50	756.33	712.85	796.88	719.55	55.04	268215
5200	528.45	1568.609	8563	196.63	193.33	100.00	100.00	760.36	760.35	712.18	799.38	718.88	54.96	281955
5450	528.60	1565.278	8954	195.54	192.20	100.00	100.00	762.18	764.33	711.52	801.79	718.19	54.92	295684
5700	528.74	1562.088	9345	194.47	191.10	100.00	100.00	763.97	768.27	710.88	804.12	717.49	54.92	309413
5950	528.89	1559.02	9734	193.41	190.04	100.00	100.00	765.72	772.17	710.27	806.37	716.78	54.96	323154
6200	529.03	1556.057	10123	192.36	189.01	100.00	100.00	767.44	776.02	709.67	808.55	716.06	55.06	336919
6450	529.18	1553.188	10512	191.31	188.02	100.00	100.00	769.13	779.83	709.08	810.65	715.34	55.21	350723
6700	529.33	1550.399	10899	190.29	187.06	100.00	100.00	770.79	783.61	708.52	812.69	714.61	55.42	364577
6950	529.47	1547.679	11286	189.27	186.12	100.00	100.00	772.43	787.35	707.97	814.66	713.88	55.68	378497
7200	529.62	1545.023	11672	188.26	185.21	100.00	100.00	774.04	791.05	707.44	816.57	713.15	56.00	392497
7450	529.77	1542.426	12058	187.27	184.32	100.00	100.00	775.63	794.71	706.93	818.42	712.42	56.37	406588
7700	529.92	1539.886	12443	186.29	183.45	100.00	100.00	777.20	798.34	706.43	820.22	711.69	56.78	420784
7950	530.07	1537.408	12827	185.32	182.60	100.00	100.00	778.75	801.94	705.95	821.96	710.96	57.24	435093
8200	530.22	1534.986	13211	184.38	181.77	100.00	100.00	780.29	805.50	705.48	823.65	710.23	57.73	449525
8450	530.38	1532.606	13594	183.44	180.97	100.00	100.00	781.80	809.03	705.03	825.29	709.51	58.26	464090
8700	530.53	1530.254	13977	182.51	180.18	100.00	100.00	783.30	812.53	704.60	826.89	708.79	58.85	478804
8950	530.68	1527.923	14359	181.59	179.41	100.00	100.00	784.78	815.99	704.17	828.44	708.07	59.50	493680
9200	530.83	1525.604	14740	180.67	178.66	100.00	100.00	786.25	819.42	703.77	829.95	707.36	60.22	508735
9450	530.99	1523.292	15121	179.76	177.92	100.00	100.00	787.70	822.83	703.37	831.42	706.65	61.00	523984
9700	531.14	1520.987	15501	178.84	177.21	100.00	100.00	789.13	826.20	702.99	832.85	705.95	61.84	539443
9950	531.29	1518.683	15881	177.93	176.52	100.00	100.00	790.56	829.54	702.63	834.24	705.26	62.74	555127
10200	531.45	1516.373	16260	177.02	175.83	100.00	100.00	791.97	832.85	702.27	835.59	704.57	63.71	571055
10450	531.60	1514.048	16639	176.11	175.17	100.00	100.00	793.37	836.13	701.93	836.92	703.89	64.76	587244
10700	531.76	1511.706	17017	175.21	174.51	100.00	100.00	794.75	839.39	701.60	838.21	703.21	65.88	603713
10950	531.91	1509.328	17394	174.32	173.85	100.00	100.00	796.13	842.62	701.28	839.46	702.55	67.09	620485

Table 3: Area-weighted arithmetic average fault permeability

TIME	FPR	FOPR	FOPT	WBHP	WBHP	WBHP	WBHP	WBHP	WBHP	WBHP	WBHP	WBHP	FWPR	FWPT
DAYS	BARSA	SM3/ DAY	SM5 ($^{10^3}$)	BARSA	BARSA	BARSA	BARSA	BARSA	BARSA	BARSA	BARSA	BARSA	SM3/ DAY	SM5
				PROD1	PROD2	PROD3	PROD4	INJ1	INJ2	INJ3	INJ4	INJ5		
0	526.08	0	0	527.62	528.45	532.24	526.89	525.03	542.33	533.42	527.53	530.04	0.00	0
1	526.08	1963.374	2	317.68	320.51	231.42	162.33	712.80	649.75	726.11	745.18	700.67	36.63	37
2	526.08	1951.653	4	299.48	302.90	209.47	138.51	727.13	650.33	738.10	762.52	709.96	48.35	83
4	526.08	1947.291	7	287.01	290.68	195.43	122.96	721.52	649.13	730.21	758.27	704.84	52.71	171
6	526.08	1947.711	12	279.00	282.58	186.61	112.67	714.58	645.80	720.82	749.50	697.39	52.29	294
8	526.08	1949.278	16	274.80	278.23	181.89	107.09	710.20	643.42	715.32	741.97	694.10	50.72	396
10	526.08	1951.065	20	271.82	275.09	178.41	103.02	706.79	641.90	711.92	736.96	690.96	48.93	494
15	526.08	1950.564	29	267.23	270.16	172.65	100.00	700.15	640.52	704.01	727.60	686.82	45.18	720
20	526.08	1947.809	39	263.99	266.66	168.39	100.00	696.29	640.32	699.66	721.40	685.46	42.40	932
30	526.08	1943.808	58	259.78	262.07	162.61	100.00	693.32	641.19	696.39	715.72	686.03	39.57	1328
40	526.08	1940.451	78	256.72	258.75	158.33	100.00	692.32	642.30	695.17	712.78	687.43	38.14	1709
50	526.08	1937.568	97	254.34	256.16	154.97	100.00	692.04	643.45	694.84	711.50	688.90	37.44	2084
80	526.08	1931.529	155	249.69	251.16	148.43	100.00	692.51	646.41	695.10	711.23	692.62	36.96	3192
115	526.08	1926.503	223	245.86	247.10	143.09	100.00	693.68	649.18	695.57	712.29	696.03	36.93	4485
150	526.08	1922.65	290	242.94	244.02	139.01	100.00	695.11	651.50	696.39	713.44	698.69	37.05	5782
200	526.08	1918.448	386	239.78	240.70	134.58	100.00	697.10	654.39	697.50	715.02	701.91	37.29	7646
250	526.08	1915.047	482	237.26	238.06	131.02	100.00	698.97	656.95	698.56	716.39	704.58	37.54	9523
350	526.09	1910.006	673	233.63	234.25	125.72	100.00	702.24	661.27	700.50	718.50	708.62	38.02	13325
450	526.10	1906.078	863	230.85	231.31	121.52	100.00	704.95	664.99	701.93	720.11	711.79	38.45	17170
550	526.11	1902.915	1053	228.63	228.93	118.07	100.00	707.30	668.29	703.11	721.43	714.31	38.83	21053
650	526.12	1900.306	1243	226.79	226.94	115.17	100.00	709.36	671.27	704.09	722.51	716.31	39.16	24969
750	526.13	1898.119	1433	225.23	225.22	112.68	100.00	711.18	673.97	704.87	723.42	717.92	39.47	28916

850	526.14	1896.262	1623	223.88	223.70	110.53	100.00	712.80	676.45	705.47	724.20	719.23	39.73	32889
950	526.15	1894.671	1812	222.69	222.34	108.66	100.00	714.26	678.76	705.95	724.90	720.29	39.98	36887
1200	526.19	1891.842	2285	220.31	219.56	105.16	100.00	717.27	683.75	706.71	726.31	721.95	40.40	46986
1450	526.23	1889.845	2758	218.33	217.20	102.51	100.00	719.78	688.05	707.07	727.49	722.88	40.65	57148
1700	526.26	1888.477	3230	216.62	215.15	100.48	100.00	721.91	691.87	707.18	728.53	723.32	40.74	67333
1950	526.30	1886.31	3702	215.09	213.34	100.00	100.00	723.75	695.31	707.10	729.48	723.41	40.61	77487
2200	526.35	1884.451	4173	213.71	211.72	100.00	100.00	725.37	698.44	706.89	730.38	723.25	40.33	87570
2450	526.39	1883.282	4643	212.45	210.26	100.00	100.00	726.82	701.32	706.60	731.23	722.91	39.93	97553
2700	526.44	1882.643	5114	211.27	208.93	100.00	100.00	728.12	703.99	706.24	732.06	722.45	39.42	107407
2950	526.48	1882.414	5585	210.18	207.71	100.00	100.00	729.30	706.47	705.83	732.87	721.90	38.81	117111
3200	526.53	1882.505	6055	209.14	206.59	100.00	100.00	730.38	708.80	705.41	733.66	721.28	38.14	126645
3450	526.58	1882.841	6526	208.17	205.55	100.00	100.00	731.37	710.99	704.98	734.43	720.62	37.41	135997
3700	526.63	1883.355	6997	207.25	204.59	100.00	100.00	732.28	713.05	704.54	735.18	719.93	36.64	145157
3950	526.68	1883.996	7468	206.37	203.70	100.00	100.00	733.12	715.00	704.10	735.92	719.22	35.87	154124
4200	526.73	1884.72	7939	205.53	202.86	100.00	100.00	733.90	716.85	703.67	736.65	718.50	35.09	162897
4450	526.78	1885.487	8410	204.73	202.08	100.00	100.00	734.64	718.61	703.25	737.36	717.78	34.34	171483
4700	526.83	1886.266	8882	203.95	201.35	100.00	100.00	735.32	720.28	702.84	738.05	717.06	33.63	179890
4950	526.89	1887.025	9354	203.21	200.67	100.00	100.00	735.97	721.87	702.45	738.73	716.34	32.97	188133
5200	526.94	1887.74	9826	202.49	200.02	100.00	100.00	736.58	723.39	702.07	739.39	715.63	32.38	196227
5450	526.99	1888.392	10298	201.79	199.42	100.00	100.00	737.16	724.83	701.71	740.03	714.93	31.86	204192
5700	527.05	1888.966	10770	201.11	198.85	100.00	100.00	737.71	726.22	701.37	740.66	714.24	31.43	212049
5950	527.10	1889.452	11242	200.46	198.31	100.00	100.00	738.23	727.54	701.04	741.27	713.56	31.08	219819
6200	527.16	1889.841	11715	199.82	197.80	100.00	100.00	738.73	728.81	700.72	741.87	712.90	30.83	227527
6450	527.21	1890.13	12187	199.19	197.32	100.00	100.00	739.20	730.02	700.43	742.45	712.25	30.68	235197
6700	527.27	1890.319	12660	198.59	196.87	100.00	100.00	739.66	731.18	700.15	743.02	711.62	30.61	242850
6950	527.32	1890.409	13133	198.00	196.44	100.00	100.00	740.09	732.29	699.88	743.57	711.01	30.64	250511
7200	527.38	1890.398	13605	197.43	196.02	100.00	100.00	740.51	733.36	699.63	744.10	710.41	30.76	258200
7450	527.44	1890.285	14078	196.87	195.63	100.00	100.00	740.92	734.39	699.39	744.62	709.82	30.97	265942
7700	527.49	1890.069	14550	196.33	195.26	100.00	100.00	741.31	735.37	699.17	745.13	709.25	31.27	273759

7950	527.55	1889.755	15023	195.80	194.90	100.00	100.00	741.68	736.32	698.96	745.62	708.70	31.65	281671
8200	527.61	1889.343	15495	195.29	194.55	100.00	100.00	742.04	737.23	698.76	746.10	708.17	32.12	289700
8450	527.67	1888.839	15967	194.80	194.22	100.00	100.00	742.39	738.11	698.58	746.56	707.65	32.66	297865
8700	527.73	1888.238	16439	194.33	193.90	100.00	100.00	742.73	738.96	698.40	747.02	707.14	33.29	306187
8950	527.78	1887.529	16911	193.87	193.59	100.00	100.00	743.06	739.77	698.24	747.46	706.65	34.00	314688
9200	527.84	1886.703	17383	193.43	193.29	100.00	100.00	743.38	740.55	698.09	747.89	706.18	34.82	323393
9450	527.90	1885.747	17854	192.99	193.00	100.00	100.00	743.69	741.31	697.95	748.30	705.72	35.75	332330
9700	527.96	1884.649	18325	192.55	192.72	100.00	100.00	743.99	742.03	697.82	748.71	705.28	36.79	341528
9950	528.02	1883.404	18796	192.13	192.45	100.00	100.00	744.28	742.74	697.70	749.11	704.85	37.97	351020
10200	528.09	1882.012	19267	191.70	192.19	100.00	100.00	744.56	743.41	697.59	749.49	704.43	39.26	360836
10450	528.15	1880.472	19737	191.28	191.94	100.00	100.00	744.83	744.06	697.48	749.87	704.03	40.68	371006
10700	528.21	1878.795	20207	190.87	191.69	100.00	100.00	745.10	744.69	697.39	750.24	703.64	42.22	381561
10950	528.27	1876.991	20676	190.46	191.46	100.00	100.00	745.36	745.30	697.30	750.59	703.27	43.87	392528

Table 4: Volume-weighted geometric average fault permeability

TIME	FPR	FOPR	FOPT	WBHP	WBHP	WBHP	WBHP	WBHP	WBHP	WBHP	WBHP	WBHP	FWPR	FWPT
DAYS	BARSA	SM3/ DAY	SM6 (^10^3)	BARSA	BARSA	BARSA	BARSA	BARSA	BARSA	BARSA	BARSA	BARSA	SM3/ DAY	SM6
				PROD1	PROD2	PROD3	PROD4	INJ1	INJ2	INJ3	INJ4	INJ5		
0	526.08	0	0	527.62	528.45	532.24	526.89	525.03	542.33	533.42	527.53	530.04	0.00	0
1	526.08	1963.374	2	317.68	320.51	231.42	162.33	712.80	649.75	726.11	745.18	700.67	36.63	37
2	526.08	1951.653	4	299.48	302.90	209.47	138.51	727.13	650.33	738.10	762.52	709.96	48.35	83
4	526.08	1947.291	7	287.01	290.68	195.43	122.96	721.52	649.13	730.21	758.27	704.84	52.71	171
6	526.08	1947.709	12	279.00	282.58	186.60	112.67	714.58	645.80	720.82	749.50	697.39	52.29	294
8	526.08	1949.274	16	274.80	278.23	181.87	107.09	710.20	643.42	715.32	741.97	694.10	50.73	396
10	526.08	1951.06	20	271.82	275.09	178.38	103.02	706.79	641.90	711.92	736.96	690.96	48.94	494
15	526.08	1950.552	29	267.23	270.16	172.59	100.00	700.15	640.52	704.01	727.60	686.82	45.19	720
20	526.08	1947.791	39	263.99	266.66	168.30	100.00	696.29	640.32	699.66	721.40	685.46	42.42	932

30	526.08	1943.779	58	259.78	262.07	162.47	100.00	693.32	641.19	696.40	715.72	686.03	39.59	1328
40	526.08	1940.412	78	256.72	258.75	158.15	100.00	692.32	642.30	695.18	712.78	687.43	38.18	1710
50	526.08	1937.52	97	254.34	256.16	154.75	100.00	692.04	643.45	694.85	711.50	688.90	37.48	2085
80	526.08	1931.464	155	249.69	251.16	148.14	100.00	692.51	646.41	695.12	711.24	692.62	37.01	3195
115	526.08	1926.425	223	245.86	247.10	142.73	100.00	693.68	649.18	695.61	712.30	696.03	37.00	4490
150	526.08	1922.561	290	242.94	244.02	138.60	100.00	695.11	651.50	696.43	713.45	698.69	37.12	5790
200	526.08	1918.347	386	239.78	240.70	134.13	100.00	697.10	654.39	697.55	715.03	701.91	37.37	7658
250	526.08	1914.937	482	237.26	238.06	130.52	100.00	698.97	656.95	698.61	716.41	704.58	37.63	9540
350	526.09	1909.88	673	233.62	234.25	125.15	100.00	702.24	661.27	700.55	718.54	708.62	38.12	13351
450	526.10	1905.938	863	230.83	231.31	120.90	100.00	704.96	664.99	701.98	720.17	711.79	38.55	17207
550	526.11	1902.759	1053	228.60	228.93	117.39	100.00	707.31	668.30	703.16	721.50	714.31	38.94	21101
650	526.12	1900.136	1243	226.75	226.94	114.43	100.00	709.37	671.28	704.15	722.60	716.30	39.29	25030
750	526.13	1897.932	1433	225.18	225.22	111.89	100.00	711.19	673.99	704.93	723.52	717.91	39.60	28990
850	526.14	1896.058	1623	223.81	223.70	109.69	100.00	712.81	676.48	705.52	724.32	719.22	39.88	32979
950	526.15	1894.45	1812	222.60	222.34	107.76	100.00	714.28	678.79	706.01	725.03	720.28	40.14	36992
1200	526.19	1891.576	2285	220.20	219.55	104.14	100.00	717.29	683.79	706.77	726.47	721.93	40.59	47139
1450	526.23	1889.535	2758	218.18	217.19	101.38	100.00	719.81	688.11	707.12	727.68	722.85	40.87	57358
1700	526.26	1887.235	3229	216.43	215.13	100.00	100.00	721.95	691.94	707.23	728.75	723.27	40.96	67597
1950	526.31	1884.399	3700	214.88	213.31	100.00	100.00	723.80	695.40	707.15	729.72	723.34	40.83	77805
2200	526.35	1882.467	4171	213.47	211.68	100.00	100.00	725.43	698.54	706.94	730.64	723.16	40.58	87950
2450	526.39	1881.225	4641	212.17	210.20	100.00	100.00	726.89	701.43	706.64	731.51	722.81	40.20	98000
2700	526.44	1880.52	5111	210.97	208.86	100.00	100.00	728.20	704.11	706.28	732.36	722.33	39.71	107928
2950	526.49	1880.232	5582	209.85	207.63	100.00	100.00	729.39	706.61	705.87	733.19	721.76	39.13	117711
3200	526.54	1880.273	6052	208.80	206.49	100.00	100.00	730.48	708.95	705.45	734.00	721.13	38.47	127329
3450	526.58	1880.567	6522	207.80	205.44	100.00	100.00	731.47	711.15	705.01	734.78	720.45	37.76	136769
3700	526.63	1881.047	6992	206.86	204.47	100.00	100.00	732.39	713.22	704.57	735.56	719.75	37.01	146022
3950	526.69	1881.659	7462	205.96	203.56	100.00	100.00	733.24	715.18	704.12	736.32	719.02	36.25	155084
4200	526.74	1882.361	7933	205.10	202.71	100.00	100.00	734.04	717.04	703.69	737.06	718.29	35.49	163955
4450	526.79	1883.113	8404	204.28	201.92	100.00	100.00	734.78	718.81	703.27	737.78	717.55	34.74	172641

4700	526.84	1883.881	8875	203.49	201.18	100.00	100.00	735.48	720.50	702.86	738.50	716.82	34.03	181150
4950	526.90	1884.636	9346	202.72	200.48	100.00	100.00	736.13	722.10	702.46	739.19	716.09	33.38	189494
5200	526.95	1885.351	9817	201.99	199.83	100.00	100.00	736.75	723.62	702.08	739.87	715.37	32.78	197690
5450	527.00	1886.005	10289	201.27	199.21	100.00	100.00	737.34	725.08	701.71	740.53	714.66	32.26	205756
5700	527.06	1886.586	10760	200.58	198.63	100.00	100.00	737.90	726.48	701.37	741.17	713.96	31.83	213713
5950	527.11	1887.082	11232	199.91	198.08	100.00	100.00	738.43	727.81	701.03	741.80	713.27	31.48	221584
6200	527.17	1887.484	11704	199.25	197.56	100.00	100.00	738.94	729.09	700.72	742.42	712.60	31.22	229390
6450	527.22	1887.787	12176	198.62	197.07	100.00	100.00	739.42	730.31	700.42	743.01	711.94	31.06	237155
6700	527.28	1887.991	12648	198.00	196.61	100.00	100.00	739.89	731.49	700.14	743.60	711.30	30.99	244903
6950	527.34	1888.097	13120	197.40	196.17	100.00	100.00	740.33	732.61	699.87	744.16	710.68	31.01	252655
7200	527.39	1888.104	13592	196.81	195.75	100.00	100.00	740.76	733.69	699.61	744.71	710.07	31.12	260435
7450	527.45	1888.011	14064	196.24	195.35	100.00	100.00	741.17	734.73	699.37	745.25	709.48	31.32	268265
7700	527.51	1887.818	14536	195.69	194.97	100.00	100.00	741.57	735.73	699.15	745.77	708.90	31.60	276166
7950	527.57	1887.528	15008	195.15	194.60	100.00	100.00	741.95	736.69	698.94	746.28	708.34	31.97	284159
8200	527.63	1887.143	15480	194.63	194.25	100.00	100.00	742.32	737.61	698.74	746.77	707.80	32.43	292266
8450	527.68	1886.669	15951	194.13	193.91	100.00	100.00	742.68	738.50	698.55	747.25	707.27	32.96	300505
8700	527.74	1886.099	16423	193.65	193.58	100.00	100.00	743.03	739.36	698.38	747.72	706.76	33.56	308897
8950	527.80	1885.42	16894	193.18	193.26	100.00	100.00	743.37	740.18	698.21	748.17	706.26	34.27	317463
9200	527.86	1884.625	17365	192.72	192.96	100.00	100.00	743.69	740.98	698.06	748.61	705.78	35.07	326230
9450	527.92	1883.702	17836	192.27	192.66	100.00	100.00	744.01	741.75	697.92	749.04	705.32	35.98	335224
9700	527.98	1882.64	18307	191.83	192.38	100.00	100.00	744.32	742.48	697.79	749.46	704.87	37.01	344475
9950	528.04	1881.435	18777	191.39	192.10	100.00	100.00	744.62	743.20	697.67	749.87	704.43	38.16	354014
10200	528.11	1880.087	19247	190.96	191.83	100.00	100.00	744.91	743.88	697.55	750.27	704.01	39.43	363871
10450	528.17	1878.591	19717	190.53	191.57	100.00	100.00	745.19	744.55	697.45	750.66	703.60	40.82	374077
10700	528.23	1876.957	20186	190.11	191.32	100.00	100.00	745.47	745.19	697.35	751.04	703.21	42.34	384661
10950	528.29	1875.195	20655	189.69	191.09	100.00	100.00	745.74	745.81	697.26	751.40	702.83	43.96	395651

Table 5: thickness-weighted harmonic average fault permeability

TIME	FPR	FOPR	FOPT	WBHP	WBHP	WBHP	WBHP	WBHP	WBHP	WBHP	WBHP	WBHP	FWPR	FWPT
DAYS	BARSA	SM3/ DAY	SM7 (^10^3)	BARSA	BARSA	BARSA	BARSA	BARSA	BARSA	BARSA	BARSA	BARSA	SM3/ DAY	SM7
				PROD1	PROD2	PROD3	PROD4	INJ1	INJ2	INJ3	INJ4	INJ5		
0	526.08	0	0	527.62	528.45	532.24	526.89	525.03	542.33	533.42	527.53	530.04	0.00	0
1	526.08	1963.373	2	317.68	320.51	231.42	162.33	712.80	649.75	726.11	745.18	700.67	36.63	37
2	526.08	1951.649	4	299.48	302.90	209.45	138.51	727.13	650.33	738.10	762.52	709.96	48.35	83
4	526.08	1947.27	7	287.01	290.68	195.32	122.96	721.52	649.13	730.21	758.27	704.84	52.73	171
6	526.08	1947.644	12	279.00	282.58	186.25	112.67	714.58	645.80	720.82	749.50	697.39	52.36	295
8	526.08	1949.158	16	274.80	278.23	181.25	107.09	710.20	643.42	715.33	741.97	694.10	50.84	397
10	526.08	1950.884	20	271.82	275.09	177.44	103.01	706.79	641.90	711.93	736.96	690.96	49.12	495
15	526.08	1950.181	29	267.23	270.16	170.72	100.00	700.15	640.52	704.05	727.60	686.82	45.53	723
20	526.08	1947.221	39	263.99	266.66	165.45	100.00	696.29	640.32	699.76	721.40	685.46	42.95	937
30	526.08	1942.815	58	259.78	262.07	157.68	100.00	693.32	641.19	696.66	715.72	686.03	40.47	1342
40	526.08	1939.076	78	256.72	258.75	151.53	100.00	692.32	642.30	695.64	712.79	687.43	39.39	1736
50	526.08	1935.839	97	254.34	256.16	146.45	100.00	692.04	643.45	695.52	711.51	688.90	38.99	2126
80	526.08	1928.946	155	249.69	251.16	135.77	100.00	692.52	646.41	696.40	711.30	692.62	39.25	3304
115	526.08	1923.113	222	245.86	247.10	126.61	100.00	693.69	649.18	697.47	712.48	696.03	39.91	4700
150	526.08	1918.584	289	242.94	244.02	119.44	100.00	695.13	651.51	698.76	713.78	698.69	40.58	6121
200	526.08	1913.6	385	239.77	240.71	111.63	100.00	697.15	654.40	700.38	715.64	701.91	41.42	8192
250	526.08	1909.552	481	237.25	238.08	105.40	100.00	699.05	656.98	701.80	717.32	704.58	42.14	10299
350	526.09	1899.301	671	233.58	234.30	100.00	100.00	702.41	661.36	704.16	720.07	708.63	42.96	14594
450	526.10	1886.694	859	230.74	231.39	100.00	100.00	705.23	665.18	705.81	722.32	711.80	43.28	18923
550	526.11	1876.912	1047	228.44	229.05	100.00	100.00	707.70	668.61	707.10	724.25	714.32	43.53	23276
650	526.13	1868.921	1234	226.50	227.08	100.00	100.00	709.90	671.74	708.13	725.92	716.32	43.74	27650
750	526.14	1862.164	1420	224.83	225.37	100.00	100.00	711.85	674.62	708.90	727.38	717.94	43.92	32042

850	526.16	1856.308	1606	223.36	223.86	100.00	100.00	713.62	677.30	709.47	728.69	719.26	44.09	36451
950	526.18	1851.141	1791	222.04	222.50	100.00	100.00	715.23	679.82	709.91	729.89	720.33	44.26	40877
1200	526.23	1841.027	2251	219.30	219.65	100.00	100.00	718.62	685.44	710.55	732.35	721.99	44.65	52040
1450	526.28	1832.912	2709	216.92	217.18	100.00	100.00	721.53	690.42	710.81	734.44	722.89	45.02	63295
1700	526.34	1826.319	3166	214.80	214.98	100.00	100.00	724.06	694.95	710.82	736.25	723.28	45.33	74627
1950	526.40	1820.944	3621	212.86	212.99	100.00	100.00	726.29	699.12	710.66	737.88	723.29	45.57	86020
2200	526.46	1816.564	4075	211.06	211.16	100.00	100.00	728.30	702.99	710.37	739.36	723.03	45.72	97451
2450	526.52	1813.017	4528	209.36	209.47	100.00	100.00	730.13	706.61	710.00	740.73	722.56	45.79	108897
2700	526.59	1810.166	4981	207.75	207.90	100.00	100.00	731.80	710.01	709.57	742.03	721.95	45.76	120337
2950	526.66	1807.9	5433	206.22	206.42	100.00	100.00	733.34	713.21	709.10	743.27	721.22	45.65	131750
3200	526.72	1806.132	5885	204.75	205.04	100.00	100.00	734.77	716.26	708.60	744.46	720.41	45.46	143115
3450	526.80	1804.787	6336	203.34	203.73	100.00	100.00	736.10	719.15	708.08	745.60	719.54	45.21	154417
3700	526.87	1803.799	6787	201.99	202.50	100.00	100.00	737.34	721.90	707.55	746.72	718.62	44.89	165640
3950	526.94	1803.111	7237	200.67	201.33	100.00	100.00	738.51	724.54	707.03	747.81	717.68	44.53	176773
4200	527.01	1802.678	7688	199.41	200.21	100.00	100.00	739.61	727.06	706.51	748.88	716.72	44.13	187806
4450	527.09	1802.455	8139	198.18	199.16	100.00	100.00	740.66	729.47	705.99	749.93	715.74	43.71	198733
4700	527.16	1802.407	8589	196.98	198.15	100.00	100.00	741.65	731.79	705.49	750.96	714.76	43.27	209550
4950	527.24	1802.5	9040	195.82	197.20	100.00	100.00	742.59	734.01	705.00	751.97	713.78	42.82	220255
5200	527.31	1802.706	9491	194.69	196.29	100.00	100.00	743.49	736.16	704.53	752.97	712.81	42.38	230850
5450	527.39	1802.999	9941	193.59	195.42	100.00	100.00	744.36	738.22	704.07	753.95	711.84	41.95	241338
5700	527.47	1803.358	10392	192.51	194.59	100.00	100.00	745.18	740.21	703.63	754.91	710.89	41.54	251723
5950	527.54	1803.763	10843	191.46	193.79	100.00	100.00	745.98	742.13	703.20	755.86	709.94	41.16	262012
6200	527.62	1804.198	11294	190.44	193.03	100.00	100.00	746.75	743.98	702.80	756.80	709.02	40.81	272214
6450	527.70	1804.648	11745	189.44	192.31	100.00	100.00	747.49	745.77	702.41	757.72	708.10	40.49	282337
6700	527.78	1805.097	12197	188.47	191.61	100.00	100.00	748.21	747.50	702.03	758.63	707.21	40.23	292394
6950	527.86	1805.532	12648	187.52	190.94	100.00	100.00	748.91	749.17	701.68	759.52	706.33	40.01	302395
7200	527.94	1805.944	13100	186.59	190.30	100.00	100.00	749.59	750.79	701.34	760.40	705.47	39.84	312355
7450	528.01	1806.326	13551	185.69	189.67	100.00	100.00	750.25	752.36	701.02	761.26	704.63	39.73	322287
7700	528.09	1806.671	14003	184.81	189.08	100.00	100.00	750.89	753.88	700.71	762.11	703.81	39.67	332204

7950	528.17	1806.971	14455	183.96	188.50	100.00	100.00	751.52	755.36	700.42	762.95	703.01	39.67	342121
8200	528.25	1807.227	14906	183.14	187.94	100.00	100.00	752.13	756.79	700.15	763.77	702.23	39.72	352052
8450	528.33	1807.427	15358	182.34	187.40	100.00	100.00	752.72	758.18	699.89	764.58	701.47	39.84	362011
8700	528.41	1807.556	15810	181.56	186.87	100.00	100.00	753.31	759.53	699.64	765.37	700.73	40.02	372017
8950	528.49	1807.601	16262	180.80	186.37	100.00	100.00	753.88	760.85	699.42	766.15	700.01	40.30	382091
9200	528.57	1807.554	16714	180.05	185.87	100.00	100.00	754.44	762.13	699.20	766.91	699.31	40.66	392256
9450	528.65	1807.414	17166	179.32	185.40	100.00	100.00	754.99	763.37	699.00	767.66	698.62	41.12	402535
9700	528.73	1807.18	17618	178.60	184.94	100.00	100.00	755.53	764.58	698.81	768.39	697.96	41.66	412951
9950	528.81	1806.853	18069	177.89	184.49	100.00	100.00	756.05	765.76	698.63	769.12	697.31	42.30	423526
10200	528.89	1806.436	18521	177.19	184.06	100.00	100.00	756.57	766.91	698.47	769.83	696.69	43.02	434282
10450	528.97	1805.934	18972	176.50	183.65	100.00	100.00	757.08	768.03	698.32	770.52	696.08	43.83	445239
10700	529.05	1805.359	19424	175.82	183.26	100.00	100.00	757.58	769.12	698.18	771.20	695.49	44.70	456414
10950	529.13	1804.718	19875	175.16	182.88	100.00	100.00	758.07	770.18	698.05	771.87	694.91	45.64	467824

Table 6: thickness-weighted harmonic average fault permeability with fault rock continuity correction

TIME	FPR	FOPR	FOPT	WBHP	WBHP	WBHP	WBHP	WBHP	WBHP	WBHP	WBHP	WBHP	FWPR	FWPT
DAYS	BARSA	SM3/ DAY	SM8 ($^10^3$)	BARSA	BARSA	BARSA	BARSA	BARSA	BARSA	BARSA	BARSA	BARSA	SM3/ DAY	SM8
				PROD1	PROD2	PROD3	PROD4	INJ1	INJ2	INJ3	INJ4	INJ5		
0	526.08	0	0	527.62	528.45	532.24	526.89	525.03	542.33	533.42	527.53	530.04	0.00	0
1	526.08	1963.374	2	317.68	320.51	231.42	162.33	712.80	649.75	726.11	745.18	700.67	36.63	37
2	526.08	1951.652	4	299.48	302.90	209.47	138.51	727.13	650.33	738.10	762.52	709.96	48.35	83
4	526.08	1947.285	7	287.01	290.68	195.40	122.96	721.52	649.13	730.21	758.27	704.84	52.71	171
6	526.08	1947.693	12	279.00	282.58	186.52	112.67	714.58	645.80	720.82	749.50	697.39	52.31	294
8	526.08	1949.246	16	274.80	278.23	181.72	107.09	710.20	643.42	715.32	741.97	694.10	50.75	396
10	526.08	1951.017	20	271.82	275.09	178.15	103.02	706.79	641.90	711.92	736.96	690.96	48.98	494
15	526.08	1950.459	29	267.23	270.16	172.16	100.00	700.15	640.52	704.02	727.60	686.82	45.27	721
20	526.08	1947.652	39	263.99	266.66	167.68	100.00	696.29	640.32	699.67	721.40	685.46	42.54	933

30	526.08	1943.556	58	259.78	262.07	161.48	100.00	693.32	641.19	696.42	715.72	686.03	39.78	1331
40	526.08	1940.116	78	256.72	258.75	156.85	100.00	692.32	642.30	695.21	712.78	687.43	38.42	1715
50	526.08	1937.163	97	254.34	256.16	153.18	100.00	692.04	643.45	694.90	711.51	688.90	37.77	2093
80	526.08	1930.983	155	249.69	251.16	146.02	100.00	692.51	646.41	695.20	711.24	692.62	37.40	3215
115	526.08	1925.847	223	245.86	247.10	140.18	100.00	693.68	649.18	695.70	712.31	696.03	37.46	4526
150	526.08	1921.915	290	242.93	244.02	135.74	100.00	695.11	651.51	696.54	713.47	698.69	37.64	5844
200	526.08	1917.634	386	239.77	240.70	130.95	100.00	697.11	654.39	697.67	715.08	701.91	37.93	7740
250	526.08	1914.176	481	237.24	238.06	127.11	100.00	698.97	656.95	698.74	716.49	704.58	38.22	9652
350	526.09	1909.048	672	233.55	234.25	121.38	100.00	702.25	661.29	700.69	718.70	708.62	38.75	13527
450	526.10	1905.037	863	230.68	231.31	116.81	100.00	704.97	665.03	702.12	720.43	711.79	39.23	17450
550	526.11	1901.782	1053	228.34	228.93	113.00	100.00	707.33	668.35	703.30	721.88	714.30	39.67	21417
650	526.12	1899.07	1243	226.35	226.93	109.72	100.00	709.41	671.35	704.29	723.11	716.28	40.08	25424
750	526.13	1896.765	1433	224.63	225.20	106.85	100.00	711.23	674.09	705.07	724.16	717.87	40.47	29471
850	526.14	1894.779	1622	223.09	223.67	104.31	100.00	712.87	676.60	705.66	725.11	719.16	40.84	33555
950	526.16	1893.049	1811	221.70	222.29	102.04	100.00	714.35	678.93	706.15	725.96	720.18	41.19	37675
1200	526.19	1886.963	2283	218.77	219.44	100.00	100.00	717.40	683.99	706.91	727.76	721.71	41.80	48124
1450	526.23	1880.448	2753	216.20	216.98	100.00	100.00	719.97	688.37	707.26	729.33	722.46	42.20	58674
1700	526.27	1875.477	3222	213.88	214.79	100.00	100.00	722.17	692.25	707.36	730.75	722.68	42.50	69300
1950	526.32	1871.668	3690	211.75	212.82	100.00	100.00	724.09	695.75	707.27	732.08	722.52	42.69	79973
2200	526.37	1868.763	4157	209.76	211.02	100.00	100.00	725.79	698.94	707.05	733.34	722.08	42.76	90662
2450	526.42	1866.582	4624	207.89	209.35	100.00	100.00	727.32	701.87	706.73	734.55	721.45	42.71	101340
2700	526.47	1864.978	5090	206.12	207.80	100.00	100.00	728.71	704.59	706.34	735.74	720.67	42.55	111978
2950	526.52	1863.833	5556	204.44	206.35	100.00	100.00	729.99	707.12	705.91	736.91	719.79	42.30	122554
3200	526.57	1863.058	6022	202.84	204.98	100.00	100.00	731.17	709.49	705.45	738.06	718.84	41.98	133049
3450	526.63	1862.575	6487	201.30	203.68	100.00	100.00	732.25	711.72	704.97	739.19	717.84	41.60	143448
3700	526.68	1862.317	6953	199.82	202.46	100.00	100.00	733.27	713.83	704.48	740.31	716.81	41.17	153741
3950	526.74	1862.232	7419	198.40	201.30	100.00	100.00	734.22	715.82	703.99	741.42	715.76	40.72	163922
4200	526.80	1862.271	7884	197.03	200.20	100.00	100.00	735.11	717.70	703.51	742.51	714.70	40.27	173989
4450	526.86	1862.393	8350	195.71	199.15	100.00	100.00	735.95	719.50	703.03	743.59	713.64	39.82	183944

4700	526.92	1862.562	8815	194.44	198.15	100.00	100.00	736.75	721.20	702.57	744.65	712.59	39.40	193795
4950	526.98	1862.744	9281	193.20	197.20	100.00	100.00	737.52	722.83	702.11	745.70	711.54	39.02	203551
5200	527.04	1862.916	9747	192.00	196.29	100.00	100.00	738.24	724.38	701.67	746.73	710.50	38.70	213226
5450	527.10	1863.057	10213	190.83	195.42	100.00	100.00	738.94	725.86	701.25	747.75	709.48	38.44	222837
5700	527.16	1863.151	10678	189.70	194.59	100.00	100.00	739.61	727.28	700.84	748.75	708.48	38.25	232399
5950	527.22	1863.189	11144	188.59	193.79	100.00	100.00	740.25	728.63	700.45	749.73	707.49	38.14	241933
6200	527.29	1863.163	11610	187.52	193.03	100.00	100.00	740.87	729.93	700.08	750.70	706.52	38.10	251457
6450	527.35	1863.066	12076	186.47	192.31	100.00	100.00	741.47	731.17	699.72	751.65	705.57	38.14	260991
6700	527.41	1862.893	12541	185.46	191.61	100.00	100.00	742.06	732.36	699.38	752.59	704.65	38.26	270555
6950	527.48	1862.645	13007	184.47	190.94	100.00	100.00	742.62	733.50	699.05	753.51	703.74	38.45	280169
7200	527.54	1862.319	13473	183.50	190.29	100.00	100.00	743.17	734.60	698.74	754.41	702.85	38.73	289852
7450	527.61	1861.917	13938	182.57	189.67	100.00	100.00	743.70	735.65	698.45	755.29	701.98	39.09	299623
7700	527.67	1861.439	14404	181.66	189.08	100.00	100.00	744.22	736.66	698.17	756.16	701.14	39.51	309501
7950	527.74	1860.89	14869	180.78	188.50	100.00	100.00	744.73	737.64	697.91	757.01	700.32	40.01	319503
8200	527.81	1860.266	15334	179.93	187.94	100.00	100.00	745.23	738.57	697.67	757.85	699.51	40.57	329647
8450	527.87	1859.561	15799	179.10	187.40	100.00	100.00	745.71	739.47	697.43	758.67	698.73	41.21	339950
8700	527.94	1858.763	16263	178.29	186.88	100.00	100.00	746.19	740.34	697.22	759.47	697.96	41.94	350436
8950	528.01	1857.861	16728	177.50	186.38	100.00	100.00	746.65	741.18	697.01	760.26	697.22	42.77	361129
9200	528.08	1856.846	17192	176.73	185.89	100.00	100.00	747.11	741.98	696.82	761.03	696.50	43.70	372055
9450	528.14	1855.709	17656	175.97	185.41	100.00	100.00	747.56	742.76	696.65	761.79	695.79	44.75	383242
9700	528.21	1854.442	18120	175.22	184.95	100.00	100.00	748.00	743.50	696.48	762.54	695.11	45.91	394719
9950	528.28	1853.047	18583	174.49	184.51	100.00	100.00	748.43	744.22	696.33	763.27	694.44	47.19	406515
10200	528.35	1851.526	19046	173.76	184.08	100.00	100.00	748.86	744.92	696.19	763.98	693.80	48.57	418658
10450	528.42	1849.883	19508	173.05	183.67	100.00	100.00	749.28	745.59	696.06	764.69	693.17	50.07	431177
10700	528.49	1848.126	19970	172.35	183.27	100.00	100.00	749.69	746.24	695.94	765.38	692.56	51.67	444095
10950	528.56	1846.265	20432	171.67	182.89	100.00	100.00	750.09	746.86	695.83	766.05	691.96	53.36	457436

Table 7: Fractures & fault

TIME	FPR	FOPR	FOPT	FWPR	WWCT	WWCT	WBHP	WBHP
DAYS	BARSA	SM3/DAY	SM3	SM3/DAY			BARSA	BARSA
					PROD	INJ	PROD	INJ
0	220.7493	0	0.00	0.00	0.00	0.00	220.15	220.15
1	220.7492	8	8.24	0.46	0.05	0.00	140.00	300.00
2	220.7492	8	15.78	0.43	0.05	0.00	140.00	300.00
3	220.7491	7	22.91	0.40	0.05	0.00	140.00	300.00
4	220.749	7	29.75	0.39	0.05	0.00	140.00	300.00
5	220.7489	7	36.40	0.38	0.05	0.00	140.00	300.00
6	220.7488	7	42.90	0.37	0.05	0.00	140.00	300.00
7	220.7487	6	49.29	0.36	0.05	0.00	140.00	300.00
8	220.7486	6	55.59	0.35	0.05	0.00	140.00	300.00
9	220.7485	6	61.80	0.35	0.05	0.00	140.00	300.00
10	220.7483	6	67.95	0.35	0.05	0.00	140.00	300.00
13	220.7479	6	85.94	0.34	0.05	0.00	140.00	300.00
20	220.7468	6	126.36	0.33	0.05	0.00	140.00	300.00
30	220.745	6	182.04	0.31	0.05	0.00	140.00	300.00
40	220.7432	5	236.22	0.31	0.05	0.00	140.00	300.00
50	220.7417	5	289.29	0.30	0.05	0.00	140.00	300.00
60	220.7403	5	341.48	0.29	0.05	0.00	140.00	300.00
70	220.739	5	392.97	0.29	0.05	0.00	140.00	300.00
80	220.7379	5	443.90	0.29	0.05	0.00	140.00	300.00
90	220.7368	5	494.37	0.28	0.05	0.00	140.00	300.00
100	220.7359	5	544.45	0.28	0.05	0.00	140.00	300.00
110	220.7352	5	594.20	0.28	0.05	0.00	140.00	300.00
120	220.7345	5	643.67	0.28	0.05	0.00	140.00	300.00
130	220.734	5	692.90	0.28	0.05	0.00	140.00	300.00
140	220.7335	5	741.92	0.28	0.05	0.00	140.00	300.00
150	220.7331	5	790.76	0.28	0.05	0.00	140.00	300.00
160	220.7328	5	839.43	0.28	0.05	0.00	140.00	300.00
170	220.7325	5	887.97	0.27	0.05	0.00	140.00	300.00
180	220.7323	5	936.37	0.27	0.05	0.00	140.00	300.00
190	220.7321	5	984.65	0.27	0.05	0.00	140.00	300.00
200	220.732	5	1032.83	0.27	0.05	0.00	140.00	300.00
210	220.732	5	1080.92	0.27	0.05	0.00	140.00	300.00
240	220.7325	5	1224.48	0.27	0.05	0.00	140.00	300.00
310	220.7357	5	1556.74	0.27	0.05	0.00	140.00	300.00
410	220.7429	5	2027.32	0.27	0.05	0.00	140.00	300.00
460	220.747	5	2261.69	0.27	0.06	0.00	140.00	300.00
510	220.7515	5	2495.24	0.28	0.06	0.00	140.00	300.00
610	220.7617	5	2959.27	0.28	0.06	0.00	140.00	300.00
710	220.7727	5	3420.40	0.29	0.06	0.00	140.00	300.00

810	220.7844	5	3878.73	0.29	0.06	0.00	140.00	300.00
910	220.7965	5	4334.31	0.30	0.06	0.00	140.00	300.00
1010	220.8092	5	4787.21	0.30	0.06	0.00	140.00	300.00
1110	220.8223	5	5237.45	0.31	0.06	0.00	140.00	300.00
1210	220.8357	4	5685.08	0.32	0.07	0.00	140.00	300.00
1310	220.8495	4	6130.14	0.32	0.07	0.00	140.00	300.00
1410	220.8636	4	6572.65	0.33	0.07	0.00	140.00	300.00
1510	220.8779	4	7012.66	0.34	0.07	0.00	140.00	300.00
1610	220.8925	4	7450.21	0.34	0.07	0.00	140.00	300.00
1710	220.9073	4	7885.34	0.35	0.07	0.00	140.00	300.00
1810	220.9223	4	8318.10	0.36	0.08	0.00	140.00	300.00
1910	220.9376	4	8748.54	0.36	0.08	0.00	140.00	300.00
2010	220.9531	4	9176.71	0.37	0.08	0.00	140.00	300.00
2110	220.9689	4	9602.68	0.37	0.08	0.00	140.00	300.00
2210	220.9847	4	10026.51	0.38	0.08	0.00	140.00	300.00
2310	221.0008	4	10448.27	0.39	0.08	0.00	140.00	300.00
2410	221.017	4	10867.98	0.39	0.09	0.00	140.00	300.00
2510	221.0334	4	11285.69	0.40	0.09	0.00	140.00	300.00
2610	221.0499	4	11701.45	0.40	0.09	0.00	140.00	300.00
2710	221.0665	4	12115.30	0.41	0.09	0.00	140.00	300.00
2810	221.0832	4	12527.26	0.41	0.09	0.00	140.00	300.00
2910	221.1001	4	12937.40	0.42	0.09	0.00	140.00	300.00
3010	221.117	4	13345.74	0.42	0.09	0.00	140.00	300.00
3110	221.1341	4	13752.32	0.42	0.09	0.00	140.00	300.00
3210	221.1512	4	14157.19	0.43	0.10	0.00	140.00	300.00
3310	221.1685	4	14560.38	0.43	0.10	0.00	140.00	300.00
3410	221.1858	4	14961.92	0.44	0.10	0.00	140.00	300.00
3510	221.2032	4	15361.86	0.44	0.10	0.00	140.00	300.00
3610	221.2207	4	15760.22	0.44	0.10	0.00	140.00	300.00
3710	221.2382	4	16157.04	0.45	0.10	0.00	140.00	300.00
3810	221.2558	4	16552.34	0.45	0.10	0.00	140.00	300.00
3820	221.2575	4	16591.86	0.45	0.10	0.00	140.00	300.00
3832.5	221.2597	4	16641.23	0.45	0.10	0.00	140.00	300.00
3852.031	221.2632	4	16718.31	0.45	0.10	0.00	140.00	300.00
3881.016	221.2683	4	16832.58	0.45	0.10	0.00	140.00	300.00
3910	221.2734	4	16946.73	0.45	0.10	0.00	140.00	300.00
3960	221.2822	4	17143.27	0.46	0.10	0.00	140.00	300.00
4010	221.2911	4	17339.45	0.46	0.10	0.00	140.00	300.00
4110	221.3088	4	17730.39	0.46	0.11	0.00	140.00	300.00
4210	221.3266	4	18119.95	0.46	0.11	0.00	140.00	300.00
4310	221.3444	4	18508.14	0.47	0.11	0.00	140.00	300.00
4410	221.3623	4	18894.99	0.47	0.11	0.00	140.00	300.00
4510	221.3802	4	19280.53	0.47	0.11	0.00	140.00	300.00
4610	221.3981	4	19664.79	0.47	0.11	0.00	140.00	300.00

4710	221.416	4	20047.79	0.48	0.11	0.00	140.00	300.00
4810	221.4339	4	20429.58	0.48	0.11	0.00	140.00	300.00
4910	221.4518	4	20810.16	0.48	0.11	0.00	140.00	300.00
5010	221.4698	4	21189.56	0.48	0.11	0.00	140.00	300.00
5110	221.4877	4	21567.80	0.48	0.11	0.00	140.00	300.00
5210	221.5057	4	21944.91	0.49	0.11	0.00	140.00	300.00
5310	221.5236	4	22320.91	0.49	0.12	0.00	140.00	300.00
5410	221.5415	4	22695.80	0.49	0.12	0.00	140.00	300.00
5510	221.5595	4	23069.62	0.49	0.12	0.00	140.00	300.00
5610	221.5774	4	23442.38	0.49	0.12	0.00	140.00	300.00
5710	221.5952	4	23814.09	0.50	0.12	0.00	140.00	300.00
5810	221.6131	4	24184.77	0.50	0.12	0.00	140.00	300.00
5910	221.6309	4	24554.44	0.50	0.12	0.00	140.00	300.00
6010	221.6487	4	24923.12	0.50	0.12	0.00	140.00	300.00
6110	221.6664	4	25290.81	0.50	0.12	0.00	140.00	300.00
6210	221.6841	4	25657.54	0.50	0.12	0.00	140.00	300.00
6310	221.7018	4	26023.33	0.51	0.12	0.00	140.00	300.00
6410	221.7193	4	26388.18	0.51	0.12	0.00	140.00	300.00
6510	221.7368	4	26752.12	0.51	0.12	0.00	140.00	300.00
6610	221.7543	4	27115.15	0.51	0.12	0.00	140.00	300.00
6710	221.7715	4	27477.28	0.51	0.12	0.00	140.00	300.00
6810	221.7887	4	27838.54	0.51	0.12	0.00	140.00	300.00
6910	221.8058	4	28198.94	0.51	0.12	0.00	140.00	300.00
7010	221.8228	4	28558.47	0.51	0.13	0.00	140.00	300.00
7110	221.8396	4	28917.17	0.52	0.13	0.00	140.00	300.00
7210	221.8563	4	29275.03	0.52	0.13	0.00	140.00	300.00
7310	221.8729	4	29632.08	0.52	0.13	0.00	140.00	300.00
7410	221.8893	4	29988.31	0.52	0.13	0.00	140.00	300.00
7510	221.9057	4	30343.74	0.52	0.13	0.00	140.00	300.00
7610	221.9218	4	30698.39	0.52	0.13	0.00	140.00	300.00
7710	221.9379	4	31052.25	0.52	0.13	0.00	140.00	300.00
7810	221.9538	4	31405.35	0.52	0.13	0.00	140.00	300.00
7910	221.9696	4	31757.69	0.52	0.13	0.00	140.00	300.00
8010	221.9852	4	32109.28	0.52	0.13	0.00	140.00	300.00
8110	222.0008	4	32460.13	0.52	0.13	0.00	140.00	300.00
8210	222.0162	4	32810.25	0.53	0.13	0.00	140.00	300.00
8310	222.0316	3	33159.66	0.53	0.13	0.00	140.00	300.00
8410	222.0468	3	33508.35	0.53	0.13	0.00	140.00	300.00
8510	222.0619	3	33856.34	0.53	0.13	0.00	140.00	300.00
8610	222.0769	3	34203.64	0.53	0.13	0.00	140.00	300.00
8710	222.0918	3	34550.26	0.53	0.13	0.00	140.00	300.00
8810	222.1066	3	34896.20	0.53	0.13	0.00	140.00	300.00
8910	222.1214	3	35241.48	0.53	0.13	0.00	140.00	300.00
9010	222.1361	3	35586.10	0.53	0.13	0.00	140.00	300.00

9110	222.1507	3	35930.07	0.53	0.13	0.00	140.00	300.00
9210	222.1653	3	36273.40	0.53	0.13	0.00	140.00	300.00
9310	222.1798	3	36616.10	0.53	0.13	0.00	140.00	300.00
9410	222.1943	3	36958.17	0.53	0.13	0.00	140.00	300.00
9510	222.2088	3	37299.63	0.53	0.14	0.00	140.00	300.00
9610	222.2232	3	37640.48	0.53	0.14	0.00	140.00	300.00
9710	222.2376	3	37980.72	0.54	0.14	0.00	140.00	300.00
9810	222.252	3	38320.37	0.54	0.14	0.00	140.00	300.00
9910	222.2663	3	38659.44	0.54	0.14	0.00	140.00	300.00
10010	222.2807	3	38997.92	0.54	0.14	0.00	140.00	300.00
10110	222.295	3	39335.84	0.54	0.14	0.00	140.00	300.00
10210	222.3093	3	39673.18	0.54	0.14	0.00	140.00	300.00
10310	222.3237	3	40009.98	0.54	0.14	0.00	140.00	300.00
10410	222.338	3	40346.22	0.54	0.14	0.00	140.00	300.00
10510	222.3523	3	40681.91	0.54	0.14	0.00	140.00	300.00
10610	222.3666	3	41017.07	0.54	0.14	0.00	140.00	300.00
10710	222.3809	3	41351.71	0.54	0.14	0.00	140.00	300.00
10810	222.3952	3	41685.81	0.54	0.14	0.00	140.00	300.00
10910	222.4095	3	42019.41	0.54	0.14	0.00	140.00	300.00
11010	222.4239	3	42352.49	0.54	0.14	0.00	140.00	300.00
11110	222.4382	3	42685.07	0.54	0.14	0.00	140.00	300.00
11210	222.4525	3	43017.15	0.54	0.14	0.00	140.00	300.00
11310	222.4667	3	43348.74	0.54	0.14	0.00	140.00	300.00
11410	222.481	3	43679.84	0.54	0.14	0.00	140.00	300.00
11510	222.4953	3	44010.48	0.54	0.14	0.00	140.00	300.00
11610	222.5096	3	44340.63	0.54	0.14	0.00	140.00	300.00
11710	222.5238	3	44670.32	0.54	0.14	0.00	140.00	300.00
11810	222.5381	3	44999.55	0.54	0.14	0.00	140.00	300.00
11910	222.5523	3	45328.33	0.54	0.14	0.00	140.00	300.00
12010	222.5666	3	45656.65	0.55	0.14	0.00	140.00	300.00
12110	222.5808	3	45984.54	0.55	0.14	0.00	140.00	300.00
12210	222.595	3	46311.98	0.55	0.14	0.00	140.00	300.00
12310	222.6092	3	46639.00	0.55	0.14	0.00	140.00	300.00
12410	222.6234	3	46965.59	0.55	0.14	0.00	140.00	300.00
12510	222.6376	3	47291.75	0.55	0.14	0.00	140.00	300.00
12610	222.6517	3	47617.50	0.55	0.14	0.00	140.00	300.00
12710	222.6659	3	47942.84	0.55	0.14	0.00	140.00	300.00
12810	222.68	3	48267.78	0.55	0.14	0.00	140.00	300.00
12910	222.6942	3	48592.32	0.55	0.14	0.00	140.00	300.00
13010	222.7083	3	48916.47	0.55	0.14	0.00	140.00	300.00
13110	222.7224	3	49240.23	0.55	0.14	0.00	140.00	300.00
13210	222.7365	3	49563.61	0.55	0.15	0.00	140.00	300.00
13310	222.7505	3	49886.61	0.55	0.15	0.00	140.00	300.00
13410	222.7646	3	50209.23	0.55	0.15	0.00	140.00	300.00

13510	222.7786	3	50531.49	0.55	0.15	0.00	140.00	300.00
13610	222.7927	3	50853.38	0.55	0.15	0.00	140.00	300.00
13710	222.8067	3	51174.92	0.55	0.15	0.00	140.00	300.00
13810	222.8207	3	51496.10	0.55	0.15	0.00	140.00	300.00
13910	222.8346	3	51816.93	0.55	0.15	0.00	140.00	300.00
14010	222.8486	3	52137.41	0.55	0.15	0.00	140.00	300.00
14110	222.8625	3	52457.55	0.55	0.15	0.00	140.00	300.00
14210	222.8764	3	52777.35	0.55	0.15	0.00	140.00	300.00
14310	222.8904	3	53096.82	0.55	0.15	0.00	140.00	300.00
14410	222.9042	3	53415.95	0.55	0.15	0.00	140.00	300.00
14510	222.9181	3	53734.76	0.55	0.15	0.00	140.00	300.00
14610	222.932	3	54053.25	0.55	0.15	0.00	140.00	300.00
14710	222.9458	3	54371.42	0.55	0.15	0.00	140.00	300.00
14810	222.9596	3	54689.27	0.55	0.15	0.00	140.00	300.00
14910	222.9734	3	55006.81	0.55	0.15	0.00	140.00	300.00
15010	222.9872	3	55324.05	0.55	0.15	0.00	140.00	300.00
15110	223.0009	3	55640.98	0.55	0.15	0.00	140.00	300.00
15210	223.0146	3	55957.61	0.55	0.15	0.00	140.00	300.00
15310	223.0284	3	56273.94	0.55	0.15	0.00	140.00	300.00
15410	223.042	3	56589.98	0.55	0.15	0.00	140.00	300.00
15510	223.0557	3	56905.73	0.55	0.15	0.00	140.00	300.00
15610	223.0694	3	57221.19	0.55	0.15	0.00	140.00	300.00
15710	223.083	3	57536.37	0.56	0.15	0.00	140.00	300.00
15810	223.0966	3	57851.27	0.56	0.15	0.00	140.00	300.00
15910	223.1102	3	58165.89	0.56	0.15	0.00	140.00	300.00
16010	223.1237	3	58480.25	0.56	0.15	0.00	140.00	300.00
16110	223.1373	3	58794.32	0.56	0.15	0.00	140.00	300.00
16210	223.1508	3	59108.14	0.56	0.15	0.00	140.00	300.00
16310	223.1643	3	59421.69	0.56	0.15	0.00	140.00	300.00
16410	223.1778	3	59734.98	0.56	0.15	0.00	140.00	300.00
16510	223.1913	3	60048.01	0.56	0.15	0.00	140.00	300.00
16610	223.2047	3	60360.79	0.56	0.15	0.00	140.00	300.00
16710	223.2181	3	60673.32	0.56	0.15	0.00	140.00	300.00
16810	223.2315	3	60985.59	0.56	0.15	0.00	140.00	300.00
16910	223.2448	3	61297.63	0.56	0.15	0.00	140.00	300.00
17010	223.2582	3	61609.42	0.56	0.15	0.00	140.00	300.00
17110	223.2715	3	61920.97	0.56	0.15	0.00	140.00	300.00
17210	223.2848	3	62232.28	0.56	0.15	0.00	140.00	300.00
17310	223.2981	3	62543.36	0.56	0.15	0.00	140.00	300.00
17410	223.3113	3	62854.21	0.56	0.15	0.00	140.00	300.00
17510	223.3246	3	63164.82	0.56	0.15	0.00	140.00	300.00
17610	223.3378	3	63475.21	0.56	0.15	0.00	140.00	300.00
17710	223.3509	3	63785.38	0.56	0.15	0.00	140.00	300.00
17810	223.3641	3	64095.33	0.56	0.15	0.00	140.00	300.00

17910	223.3772	3	64405.06	0.56	0.15	0.00	140.00	300.00
18010	223.3903	3	64714.57	0.56	0.15	0.00	140.00	300.00
18110	223.4034	3	65023.88	0.56	0.15	0.00	140.00	300.00
18210	223.4165	3	65332.96	0.56	0.15	0.00	140.00	300.00
18310	223.4295	3	65641.84	0.56	0.15	0.00	140.00	300.00
18410	223.4425	3	65950.52	0.56	0.15	0.00	140.00	300.00
18510	223.4555	3	66258.99	0.56	0.15	0.00	140.00	300.00
18610	223.4685	3	66567.26	0.56	0.15	0.00	140.00	300.00
18710	223.4814	3	66875.34	0.56	0.15	0.00	140.00	300.00
18810	223.4943	3	67183.21	0.56	0.15	0.00	140.00	300.00
18910	223.5072	3	67490.89	0.56	0.15	0.00	140.00	300.00
19010	223.5201	3	67798.38	0.56	0.15	0.00	140.00	300.00
19110	223.5329	3	68105.69	0.56	0.15	0.00	140.00	300.00
19210	223.5457	3	68412.80	0.56	0.15	0.00	140.00	300.00
19310	223.5585	3	68719.73	0.56	0.15	0.00	140.00	300.00
19410	223.5712	3	69026.48	0.56	0.16	0.00	140.00	300.00
19510	223.584	3	69333.04	0.56	0.16	0.00	140.00	300.00
19610	223.5967	3	69639.43	0.56	0.16	0.00	140.00	300.00
19710	223.6094	3	69945.64	0.56	0.16	0.00	140.00	300.00
19810	223.622	3	70251.68	0.56	0.16	0.00	140.00	300.00
19910	223.6347	3	70557.54	0.56	0.16	0.00	140.00	300.00
20010	223.6473	3	70863.23	0.56	0.16	0.00	140.00	300.00
20110	223.6599	3	71168.76	0.56	0.16	0.00	140.00	300.00
20210	223.6724	3	71474.12	0.56	0.16	0.00	140.00	300.00

Table 8: fractures & no fault

TIME	FPR	FOPR	FOPT	FWPR	WWCT	WWCT	WBHP	WBHP
DAYS	BARSA	SM3/DAY	SM3	SM3/DAY			BARSA	BARSA
					PROD	INJ	PROD	INJ
0	220.75	0	0	0.00	0.00	0.00	220.15	220.15
1	220.75	8.239083	8	0.46	0.05	0.00	140.00	300.00
2	220.75	7.545854	16	0.43	0.05	0.00	140.00	300.00
3	220.75	7.121178	23	0.40	0.05	0.00	140.00	300.00
4	220.75	6.843968	30	0.39	0.05	0.00	140.00	300.00
5	220.75	6.649175	36	0.38	0.05	0.00	140.00	300.00
6	220.75	6.503618	43	0.37	0.05	0.00	140.00	300.00
7	220.75	6.38883	49	0.36	0.05	0.00	140.00	300.00
8	220.75	6.294261	56	0.35	0.05	0.00	140.00	300.00
9	220.75	6.214529	62	0.35	0.05	0.00	140.00	300.00
10	220.75	6.146113	68	0.35	0.05	0.00	140.00	300.00
13	220.75	5.996889	86	0.34	0.05	0.00	140.00	300.00
20	220.75	5.775103	126	0.33	0.05	0.00	140.00	300.00
30	220.75	5.567574	182	0.31	0.05	0.00	140.00	300.00

40	220.74	5.418539	236	0.31	0.05	0.00	140.00	300.00
50	220.74	5.306344	289	0.30	0.05	0.00	140.00	300.00
60	220.74	5.219111	341	0.29	0.05	0.00	140.00	300.00
70	220.74	5.149499	393	0.29	0.05	0.00	140.00	300.00
80	220.74	5.093015	444	0.29	0.05	0.00	140.00	300.00
90	220.74	5.046558	494	0.28	0.05	0.00	140.00	300.00
100	220.74	5.007818	544	0.28	0.05	0.00	140.00	300.00
110	220.74	4.975084	594	0.28	0.05	0.00	140.00	300.00
120	220.73	4.947131	644	0.28	0.05	0.00	140.00	300.00
130	220.73	4.923041	693	0.28	0.05	0.00	140.00	300.00
140	220.73	4.902099	742	0.28	0.05	0.00	140.00	300.00
150	220.73	4.883748	791	0.28	0.05	0.00	140.00	300.00
160	220.73	4.867545	839	0.28	0.05	0.00	140.00	300.00
170	220.73	4.853137	888	0.27	0.05	0.00	140.00	300.00
180	220.73	4.840234	936	0.27	0.05	0.00	140.00	300.00
190	220.73	4.828606	985	0.27	0.05	0.00	140.00	300.00
200	220.73	4.818057	1033	0.27	0.05	0.00	140.00	300.00
210	220.73	4.808429	1081	0.27	0.05	0.00	140.00	300.00
240	220.73	4.785208	1224	0.27	0.05	0.00	140.00	300.00
310	220.74	4.746661	1557	0.27	0.05	0.00	140.00	300.00
410	220.74	4.705935	2027	0.27	0.05	0.00	140.00	300.00
460	220.75	4.687862	2262	0.27	0.06	0.00	140.00	300.00
510	220.75	4.671329	2495	0.28	0.06	0.00	140.00	300.00
610	220.76	4.641518	2959	0.28	0.06	0.00	140.00	300.00
710	220.77	4.613648	3421	0.29	0.06	0.00	140.00	300.00
810	220.78	4.587163	3880	0.29	0.06	0.00	140.00	300.00
910	220.80	4.561835	4336	0.30	0.06	0.00	140.00	300.00
1010	220.81	4.537585	4789	0.30	0.06	0.00	140.00	300.00
1110	220.82	4.514273	5241	0.31	0.06	0.00	140.00	300.00
1210	220.84	4.491816	5690	0.32	0.07	0.00	140.00	300.00
1310	220.85	4.470199	6137	0.32	0.07	0.00	140.00	300.00
1410	220.86	4.449388	6582	0.33	0.07	0.00	140.00	300.00
1510	220.88	4.429364	7025	0.34	0.07	0.00	140.00	300.00
1610	220.89	4.41012	7466	0.35	0.07	0.00	140.00	300.00
1710	220.91	4.391633	7905	0.35	0.07	0.00	140.00	300.00
1810	220.92	4.373975	8343	0.36	0.08	0.00	140.00	300.00
1910	220.94	4.357053	8778	0.37	0.08	0.00	140.00	300.00
2010	220.95	4.340844	9212	0.37	0.08	0.00	140.00	300.00
2110	220.97	4.325693	9645	0.38	0.08	0.00	140.00	300.00
2210	220.99	4.311214	10076	0.39	0.08	0.00	140.00	300.00
2310	221.00	4.297405	10506	0.39	0.08	0.00	140.00	300.00
2410	221.02	4.284154	10934	0.40	0.09	0.00	140.00	300.00
2510	221.04	4.271412	11361	0.41	0.09	0.00	140.00	300.00
2610	221.05	4.259155	11787	0.41	0.09	0.00	140.00	300.00

2710	221.07	4.247358	12212	0.42	0.09	0.00	140.00	300.00
2810	221.09	4.236029	12636	0.43	0.09	0.00	140.00	300.00
2910	221.10	4.225137	13058	0.43	0.09	0.00	140.00	300.00
3010	221.12	4.214657	13480	0.44	0.09	0.00	140.00	300.00
3110	221.14	4.204566	13900	0.44	0.10	0.00	140.00	300.00
3210	221.16	4.194873	14320	0.45	0.10	0.00	140.00	300.00
3310	221.18	4.185554	14738	0.45	0.10	0.00	140.00	300.00
3410	221.19	4.176568	15156	0.46	0.10	0.00	140.00	300.00
3510	221.21	4.16789	15573	0.46	0.10	0.00	140.00	300.00
3610	221.23	4.159508	15988	0.47	0.10	0.00	140.00	300.00
3710	221.25	4.151433	16404	0.48	0.10	0.00	140.00	300.00
3810	221.27	4.143644	16818	0.48	0.10	0.00	140.00	300.00
3910	221.29	4.136126	17232	0.48	0.10	0.00	140.00	300.00
4010	221.30	4.128858	17644	0.49	0.11	0.00	140.00	300.00
4110	221.32	4.121824	18057	0.49	0.11	0.00	140.00	300.00
4210	221.34	4.115012	18468	0.50	0.11	0.00	140.00	300.00
4310	221.36	4.10841	18879	0.50	0.11	0.00	140.00	300.00
4410	221.38	4.102094	19289	0.51	0.11	0.00	140.00	300.00
4510	221.40	4.096135	19699	0.51	0.11	0.00	140.00	300.00
4610	221.42	4.090307	20108	0.52	0.11	0.00	140.00	300.00
4710	221.44	4.084685	20516	0.52	0.11	0.00	140.00	300.00
4810	221.46	4.079257	20924	0.52	0.11	0.00	140.00	300.00
4910	221.48	4.073984	21332	0.53	0.11	0.00	140.00	300.00
5010	221.50	4.068852	21739	0.53	0.12	0.00	140.00	300.00
5110	221.52	4.063857	22145	0.54	0.12	0.00	140.00	300.00
5210	221.54	4.058992	22551	0.54	0.12	0.00	140.00	300.00
5310	221.56	4.054255	22956	0.54	0.12	0.00	140.00	300.00
5410	221.57	4.049642	23361	0.55	0.12	0.00	140.00	300.00
5510	221.59	4.04515	23766	0.55	0.12	0.00	140.00	300.00
5610	221.61	4.040773	24170	0.55	0.12	0.00	140.00	300.00
5710	221.63	4.036514	24573	0.56	0.12	0.00	140.00	300.00
5810	221.65	4.03238	24977	0.56	0.12	0.00	140.00	300.00
5910	221.67	4.028358	25380	0.56	0.12	0.00	140.00	300.00
6010	221.69	4.024443	25782	0.57	0.12	0.00	140.00	300.00
6110	221.71	4.020627	26184	0.57	0.12	0.00	140.00	300.00
6210	221.73	4.016906	26586	0.57	0.12	0.00	140.00	300.00
6310	221.75	4.013276	26987	0.58	0.13	0.00	140.00	300.00
6410	221.77	4.009732	27388	0.58	0.13	0.00	140.00	300.00
6510	221.79	4.00628	27789	0.58	0.13	0.00	140.00	300.00
6610	221.81	4.002918	28189	0.58	0.13	0.00	140.00	300.00
6710	221.83	3.999632	28589	0.59	0.13	0.00	140.00	300.00
6810	221.85	3.996418	28989	0.59	0.13	0.00	140.00	300.00
6910	221.87	3.993272	29388	0.59	0.13	0.00	140.00	300.00
7010	221.89	3.990193	29787	0.60	0.13	0.00	140.00	300.00

7110	221.92	3.987181	30186	0.60	0.13	0.00	140.00	300.00
7210	221.94	3.984233	30584	0.60	0.13	0.00	140.00	300.00
7310	221.96	3.981348	30982	0.60	0.13	0.00	140.00	300.00
7410	221.98	3.978524	31380	0.61	0.13	0.00	140.00	300.00
7510	222.00	3.97576	31778	0.61	0.13	0.00	140.00	300.00
7610	222.02	3.973054	32175	0.61	0.13	0.00	140.00	300.00
7710	222.04	3.970409	32572	0.61	0.13	0.00	140.00	300.00
7810	222.06	3.967825	32969	0.62	0.13	0.00	140.00	300.00
7910	222.08	3.965306	33365	0.62	0.13	0.00	140.00	300.00
8010	222.10	3.962846	33762	0.62	0.14	0.00	140.00	300.00
8110	222.12	3.960442	34158	0.62	0.14	0.00	140.00	300.00
8210	222.14	3.95809	34553	0.63	0.14	0.00	140.00	300.00
8310	222.16	3.955787	34949	0.63	0.14	0.00	140.00	300.00
8410	222.18	3.953531	35344	0.63	0.14	0.00	140.00	300.00
8510	222.20	3.95132	35739	0.63	0.14	0.00	140.00	300.00
8610	222.22	3.949152	36134	0.63	0.14	0.00	140.00	300.00
8710	222.24	3.947026	36529	0.64	0.14	0.00	140.00	300.00
8810	222.26	3.94494	36924	0.64	0.14	0.00	140.00	300.00
8910	222.28	3.942894	37318	0.64	0.14	0.00	140.00	300.00
9010	222.30	3.940887	37712	0.64	0.14	0.00	140.00	300.00
9110	222.32	3.938917	38106	0.65	0.14	0.00	140.00	300.00
9210	222.34	3.936984	38500	0.65	0.14	0.00	140.00	300.00
9310	222.36	3.935088	38893	0.65	0.14	0.00	140.00	300.00
9410	222.38	3.933227	39286	0.65	0.14	0.00	140.00	300.00
9510	222.40	3.931401	39679	0.65	0.14	0.00	140.00	300.00
9610	222.42	3.92961	40072	0.66	0.14	0.00	140.00	300.00
9710	222.44	3.927907	40465	0.66	0.14	0.00	140.00	300.00
9810	222.46	3.926273	40858	0.66	0.14	0.00	140.00	300.00
9910	222.48	3.924653	41250	0.66	0.14	0.00	140.00	300.00
10010	222.51	3.923065	41643	0.66	0.14	0.00	140.00	300.00
10110	222.53	3.921531	42035	0.66	0.14	0.00	140.00	300.00
10210	222.55	3.920028	42427	0.67	0.15	0.00	140.00	300.00
10310	222.57	3.91855	42819	0.67	0.15	0.00	140.00	300.00
10410	222.59	3.917096	43210	0.67	0.15	0.00	140.00	300.00
10510	222.61	3.915666	43602	0.67	0.15	0.00	140.00	300.00
10610	222.63	3.91426	43993	0.67	0.15	0.00	140.00	300.00
10710	222.65	3.912881	44385	0.68	0.15	0.00	140.00	300.00
10810	222.67	3.911526	44776	0.68	0.15	0.00	140.00	300.00
10910	222.69	3.910197	45167	0.68	0.15	0.00	140.00	300.00
11010	222.71	3.908895	45558	0.68	0.15	0.00	140.00	300.00
11110	222.73	3.907629	45948	0.68	0.15	0.00	140.00	300.00
11210	222.75	3.906391	46339	0.68	0.15	0.00	140.00	300.00
11310	222.77	3.90518	46730	0.69	0.15	0.00	140.00	300.00
11410	222.79	3.903996	47120	0.69	0.15	0.00	140.00	300.00

11510	222.81	3.902836	47510	0.69	0.15	0.00	140.00	300.00
11610	222.83	3.9017	47900	0.69	0.15	0.00	140.00	300.00
11710	222.85	3.900589	48291	0.69	0.15	0.00	140.00	300.00
11810	222.87	3.899502	48680	0.69	0.15	0.00	140.00	300.00
11910	222.89	3.898438	49070	0.70	0.15	0.00	140.00	300.00
12010	222.91	3.897396	49460	0.70	0.15	0.00	140.00	300.00
12110	222.93	3.896376	49850	0.70	0.15	0.00	140.00	300.00
12210	222.95	3.895377	50239	0.70	0.15	0.00	140.00	300.00
12310	222.97	3.894399	50629	0.70	0.15	0.00	140.00	300.00
12410	222.99	3.893441	51018	0.70	0.15	0.00	140.00	300.00
12510	223.01	3.892503	51407	0.70	0.15	0.00	140.00	300.00
12610	223.03	3.891591	51796	0.71	0.15	0.00	140.00	300.00
12710	223.05	3.890699	52186	0.71	0.15	0.00	140.00	300.00
12810	223.07	3.889827	52575	0.71	0.15	0.00	140.00	300.00
12910	223.09	3.888973	52963	0.71	0.15	0.00	140.00	300.00
13010	223.11	3.888136	53352	0.71	0.15	0.00	140.00	300.00
13110	223.13	3.887315	53741	0.71	0.15	0.00	140.00	300.00
13210	223.15	3.886509	54130	0.71	0.16	0.00	140.00	300.00
13310	223.17	3.885718	54518	0.72	0.16	0.00	140.00	300.00
13410	223.19	3.884941	54907	0.72	0.16	0.00	140.00	300.00
13510	223.21	3.884179	55295	0.72	0.16	0.00	140.00	300.00
13610	223.23	3.883431	55683	0.72	0.16	0.00	140.00	300.00
13710	223.25	3.882698	56072	0.72	0.16	0.00	140.00	300.00
13810	223.27	3.881979	56460	0.72	0.16	0.00	140.00	300.00
13910	223.29	3.881274	56848	0.72	0.16	0.00	140.00	300.00
14010	223.30	3.880584	57236	0.73	0.16	0.00	140.00	300.00
14110	223.32	3.879907	57624	0.73	0.16	0.00	140.00	300.00
14210	223.34	3.879244	58012	0.73	0.16	0.00	140.00	300.00
14310	223.36	3.878594	58400	0.73	0.16	0.00	140.00	300.00
14320	223.37	3.878521	58439	0.73	0.16	0.00	140.00	300.00
14332.5	223.37	3.878441	58487	0.73	0.16	0.00	140.00	300.00
14352.03	223.37	3.878316	58563	0.73	0.16	0.00	140.00	300.00
14381.02	223.38	3.878132	58675	0.73	0.16	0.00	140.00	300.00
14410	223.38	3.877947	58788	0.73	0.16	0.00	140.00	300.00
14460	223.39	3.877633	58982	0.73	0.16	0.00	140.00	300.00
14510	223.40	3.877321	59175	0.73	0.16	0.00	140.00	300.00
14610	223.42	3.876713	59563	0.73	0.16	0.00	140.00	300.00
14710	223.44	3.876114	59951	0.73	0.16	0.00	140.00	300.00
14810	223.46	3.875528	60338	0.74	0.16	0.00	140.00	300.00
14910	223.48	3.874954	60726	0.74	0.16	0.00	140.00	300.00
15010	223.50	3.874393	61113	0.74	0.16	0.00	140.00	300.00
15110	223.52	3.873844	61501	0.74	0.16	0.00	140.00	300.00
15210	223.54	3.873307	61888	0.74	0.16	0.00	140.00	300.00
15310	223.56	3.872782	62275	0.74	0.16	0.00	140.00	300.00

15410	223.58	3.872269	62662	0.74	0.16	0.00	140.00	300.00
15510	223.60	3.871768	63050	0.74	0.16	0.00	140.00	300.00
15610	223.61	3.871278	63437	0.74	0.16	0.00	140.00	300.00
15710	223.63	3.870799	63824	0.75	0.16	0.00	140.00	300.00
15810	223.65	3.870332	64211	0.75	0.16	0.00	140.00	300.00
15910	223.67	3.869877	64598	0.75	0.16	0.00	140.00	300.00
16010	223.69	3.869432	64985	0.75	0.16	0.00	140.00	300.00
16110	223.71	3.868999	65372	0.75	0.16	0.00	140.00	300.00
16210	223.73	3.868577	65759	0.75	0.16	0.00	140.00	300.00
16310	223.75	3.868165	66145	0.75	0.16	0.00	140.00	300.00
16410	223.77	3.867764	66532	0.75	0.16	0.00	140.00	300.00
16510	223.79	3.867374	66919	0.75	0.16	0.00	140.00	300.00
16610	223.80	3.866993	67306	0.76	0.16	0.00	140.00	300.00
16710	223.82	3.866623	67692	0.76	0.16	0.00	140.00	300.00
16810	223.84	3.866262	68079	0.76	0.16	0.00	140.00	300.00
16910	223.86	3.865912	68465	0.76	0.16	0.00	140.00	300.00
17010	223.88	3.86557	68852	0.76	0.16	0.00	140.00	300.00
17110	223.90	3.865238	69239	0.76	0.16	0.00	140.00	300.00
17210	223.92	3.864916	69625	0.76	0.16	0.00	140.00	300.00
17310	223.94	3.864602	70011	0.76	0.16	0.00	140.00	300.00
17410	223.95	3.864297	70398	0.76	0.17	0.00	140.00	300.00
17510	223.97	3.864	70784	0.76	0.17	0.00	140.00	300.00
17610	223.99	3.863713	71171	0.77	0.17	0.00	140.00	300.00
17710	224.01	3.863433	71557	0.77	0.17	0.00	140.00	300.00
17810	224.03	3.863162	71943	0.77	0.17	0.00	140.00	300.00
17910	224.05	3.862899	72330	0.77	0.17	0.00	140.00	300.00
18010	224.07	3.862645	72716	0.77	0.17	0.00	140.00	300.00
18110	224.08	3.862398	73102	0.77	0.17	0.00	140.00	300.00
18210	224.10	3.862158	73488	0.77	0.17	0.00	140.00	300.00
18310	224.12	3.861927	73875	0.77	0.17	0.00	140.00	300.00
18410	224.14	3.861702	74261	0.77	0.17	0.00	140.00	300.00
18510	224.16	3.861486	74647	0.77	0.17	0.00	140.00	300.00
18610	224.18	3.861277	75033	0.78	0.17	0.00	140.00	300.00
18710	224.19	3.861074	75419	0.78	0.17	0.00	140.00	300.00
18810	224.21	3.860879	75805	0.78	0.17	0.00	140.00	300.00
18910	224.23	3.860691	76191	0.78	0.17	0.00	140.00	300.00
19010	224.25	3.860511	76577	0.78	0.17	0.00	140.00	300.00
19110	224.27	3.860337	76963	0.78	0.17	0.00	140.00	300.00
19210	224.28	3.860172	77349	0.78	0.17	0.00	140.00	300.00
19310	224.30	3.860013	77735	0.78	0.17	0.00	140.00	300.00
19410	224.32	3.859866	78121	0.78	0.17	0.00	140.00	300.00
19510	224.34	3.859726	78507	0.78	0.17	0.00	140.00	300.00
19520	224.34	3.859707	78546	0.78	0.17	0.00	140.00	300.00
19532.5	224.34	3.85969	78594	0.78	0.17	0.00	140.00	300.00

19552.03	224.35	3.859664	78670	0.78	0.17	0.00	140.00	300.00
19581.02	224.35	3.859626	78781	0.78	0.17	0.00	140.00	300.00
19610	224.36	3.859587	78893	0.78	0.17	0.00	140.00	300.00
19660	224.37	3.859523	79086	0.78	0.17	0.00	140.00	300.00
19710	224.37	3.859459	79279	0.78	0.17	0.00	140.00	300.00
19810	224.39	3.859339	79665	0.79	0.17	0.00	140.00	300.00
19910	224.41	3.859222	80051	0.79	0.17	0.00	140.00	300.00
20010	224.43	3.859111	80437	0.79	0.17	0.00	140.00	300.00
20020	224.43	3.859096	80476	0.79	0.17	0.00	140.00	300.00
20032.5	224.43	3.859083	80524	0.79	0.17	0.00	140.00	300.00
20052.03	224.44	3.859062	80599	0.79	0.17	0.00	140.00	300.00
20081.02	224.44	3.859031	80711	0.79	0.17	0.00	140.00	300.00
20110	224.45	3.859001	80823	0.79	0.17	0.00	140.00	300.00
20160	224.45	3.858951	81016	0.79	0.17	0.00	140.00	300.00
20210	224.46	3.858901	81209	0.79	0.17	0.00	140.00	300.00

Table 9: no fractures & fault

TIME	FPR	FOPR	FOPT	FWPR	WWCT	WWCT	WBHP	WBHP
DAYS	BARSA	SM3/DAY	SM3	SM3/DAY			BARSA	BARSA
					PROD	INJ	PROD	INJ
0	220.74	0	0	0.00	0.00	0.00	220.15	220.15
1	220.74	8.24337	8	0.46	0.05	0.00	140.00	300.00
2	220.74	7.572302	16	0.42	0.05	0.00	140.00	300.00
3	220.74	7.136856	23	0.40	0.05	0.00	140.00	300.00
4	220.74	6.854326	30	0.38	0.05	0.00	140.00	300.00
5	220.74	6.656702	36	0.37	0.05	0.00	140.00	300.00
6	220.74	6.509477	43	0.36	0.05	0.00	140.00	300.00
7	220.74	6.394149	49	0.36	0.05	0.00	140.00	300.00
8	220.74	6.299199	56	0.35	0.05	0.00	140.00	300.00
9	220.74	6.218726	62	0.35	0.05	0.00	140.00	300.00
10	220.74	6.149466	68	0.34	0.05	0.00	140.00	300.00
13	220.74	5.997339	86	0.34	0.05	0.00	140.00	300.00
20	220.74	5.765815	126	0.32	0.05	0.00	140.00	300.00
30	220.74	5.541698	182	0.31	0.05	0.00	140.00	300.00
40	220.74	5.372335	236	0.30	0.05	0.00	140.00	300.00
50	220.74	5.238416	288	0.29	0.05	0.00	140.00	300.00
60	220.73	5.127983	339	0.29	0.05	0.00	140.00	300.00
70	220.73	5.034954	390	0.28	0.05	0.00	140.00	300.00
80	220.73	4.955236	439	0.28	0.05	0.00	140.00	300.00
90	220.73	4.885925	488	0.27	0.05	0.00	140.00	300.00
100	220.73	4.824782	536	0.27	0.05	0.00	140.00	300.00
110	220.73	4.770274	584	0.27	0.05	0.00	140.00	300.00
120	220.73	4.721278	631	0.26	0.05	0.00	140.00	300.00

130	220.73	4.676834	678	0.26	0.05	0.00	140.00	300.00
140	220.73	4.636214	724	0.26	0.05	0.00	140.00	300.00
150	220.73	4.598868	770	0.26	0.05	0.00	140.00	300.00
160	220.73	4.564376	816	0.26	0.05	0.00	140.00	300.00
170	220.73	4.532375	861	0.25	0.05	0.00	140.00	300.00
180	220.73	4.502554	906	0.25	0.05	0.00	140.00	300.00
190	220.73	4.474662	951	0.25	0.05	0.00	140.00	300.00
200	220.73	4.448488	995	0.25	0.05	0.00	140.00	300.00
210	220.73	4.423854	1040	0.25	0.05	0.00	140.00	300.00
240	220.73	4.360154	1171	0.24	0.05	0.00	140.00	300.00
310	220.73	4.24808	1468	0.24	0.05	0.00	140.00	300.00
410	220.73	4.129465	1881	0.23	0.05	0.00	140.00	300.00
510	220.74	4.037553	2285	0.23	0.05	0.00	140.00	300.00
610	220.75	3.963531	2681	0.22	0.05	0.00	140.00	300.00
710	220.75	3.901526	3071	0.22	0.05	0.00	140.00	300.00
810	220.76	3.850243	3456	0.22	0.05	0.00	140.00	300.00
910	220.77	3.805219	3837	0.21	0.05	0.00	140.00	300.00
1010	220.78	3.765032	4213	0.21	0.05	0.00	140.00	300.00
1110	220.78	3.730312	4586	0.21	0.05	0.00	140.00	300.00
1210	220.79	3.698684	4956	0.21	0.05	0.00	140.00	300.00
1310	220.80	3.669923	5323	0.21	0.05	0.00	140.00	300.00
1410	220.80	3.643597	5687	0.20	0.05	0.00	140.00	300.00
1510	220.81	3.618974	6049	0.20	0.05	0.00	140.00	300.00
1610	220.82	3.596435	6409	0.20	0.05	0.00	140.00	300.00
1710	220.82	3.575467	6766	0.20	0.05	0.00	140.00	300.00
1810	220.83	3.555818	7122	0.20	0.05	0.00	140.00	300.00
1910	220.84	3.537305	7476	0.20	0.05	0.00	140.00	300.00
2010	220.84	3.519784	7828	0.20	0.05	0.00	140.00	300.00
2110	220.85	3.50314	8178	0.20	0.05	0.00	140.00	300.00
2210	220.86	3.487268	8527	0.20	0.05	0.00	140.00	300.00
2310	220.86	3.472087	8874	0.19	0.05	0.00	140.00	300.00
2410	220.87	3.457525	9220	0.19	0.05	0.00	140.00	300.00
2510	220.88	3.44352	9564	0.19	0.05	0.00	140.00	300.00
2610	220.88	3.430016	9907	0.19	0.05	0.00	140.00	300.00
2710	220.89	3.416967	10249	0.19	0.05	0.00	140.00	300.00
2810	220.90	3.404333	10589	0.19	0.05	0.00	140.00	300.00
2910	220.90	3.39208	10928	0.19	0.05	0.00	140.00	300.00
3010	220.91	3.380175	11266	0.19	0.05	0.00	140.00	300.00
3110	220.91	3.368592	11603	0.19	0.05	0.00	140.00	300.00
3210	220.92	3.357305	11939	0.19	0.05	0.00	140.00	300.00
3310	220.93	3.346293	12274	0.19	0.05	0.00	140.00	300.00
3410	220.93	3.335537	12607	0.19	0.05	0.00	140.00	300.00
3510	220.94	3.325019	12940	0.19	0.05	0.00	140.00	300.00
3610	220.94	3.314725	13271	0.19	0.05	0.00	140.00	300.00

3710	220.95	3.30464	13602	0.18	0.05	0.00	140.00	300.00
3810	220.96	3.294751	13931	0.18	0.05	0.00	140.00	300.00
3910	220.96	3.285047	14260	0.18	0.05	0.00	140.00	300.00
4010	220.97	3.275518	14587	0.18	0.05	0.00	140.00	300.00
4110	220.97	3.266156	14914	0.18	0.05	0.00	140.00	300.00
4210	220.98	3.25695	15240	0.18	0.05	0.00	140.00	300.00
4310	220.98	3.247894	15564	0.18	0.05	0.00	140.00	300.00
4410	220.99	3.238979	15888	0.18	0.05	0.00	140.00	300.00
4510	221.00	3.2302	16211	0.18	0.05	0.00	140.00	300.00
4610	221.00	3.22155	16533	0.18	0.05	0.00	140.00	300.00
4710	221.01	3.213025	16855	0.18	0.05	0.00	140.00	300.00
4810	221.01	3.204617	17175	0.18	0.05	0.00	140.00	300.00
4910	221.02	3.196323	17495	0.18	0.05	0.00	140.00	300.00
5010	221.02	3.188137	17814	0.18	0.05	0.00	140.00	300.00
5110	221.03	3.180057	18132	0.18	0.05	0.00	140.00	300.00
5210	221.03	3.172077	18449	0.18	0.05	0.00	140.00	300.00
5310	221.04	3.164194	18765	0.18	0.05	0.00	140.00	300.00
5410	221.04	3.156405	19081	0.18	0.05	0.00	140.00	300.00
5510	221.05	3.148706	19396	0.18	0.05	0.00	140.00	300.00
5610	221.05	3.141093	19710	0.18	0.05	0.00	140.00	300.00
5710	221.06	3.133565	20023	0.18	0.05	0.00	140.00	300.00
5810	221.06	3.126117	20336	0.17	0.05	0.00	140.00	300.00
5910	221.07	3.118748	20648	0.17	0.05	0.00	140.00	300.00
6010	221.07	3.111454	20959	0.17	0.05	0.00	140.00	300.00
6110	221.08	3.104235	21269	0.17	0.05	0.00	140.00	300.00
6210	221.08	3.097086	21579	0.17	0.05	0.00	140.00	300.00
6310	221.09	3.090008	21888	0.17	0.05	0.00	140.00	300.00
6410	221.09	3.082997	22196	0.17	0.05	0.00	140.00	300.00
6510	221.10	3.076052	22504	0.17	0.05	0.00	140.00	300.00
6610	221.10	3.069173	22811	0.17	0.05	0.00	140.00	300.00
6710	221.11	3.062357	23117	0.17	0.05	0.00	140.00	300.00
6810	221.11	3.055603	23423	0.17	0.05	0.00	140.00	300.00
6910	221.12	3.04891	23727	0.17	0.05	0.00	140.00	300.00
7010	221.12	3.042278	24032	0.17	0.05	0.00	140.00	300.00
7110	221.12	3.035704	24335	0.17	0.05	0.00	140.00	300.00
7210	221.13	3.029188	24638	0.17	0.05	0.00	140.00	300.00
7310	221.13	3.02273	24940	0.17	0.05	0.00	140.00	300.00
7410	221.14	3.016327	25242	0.17	0.05	0.00	140.00	300.00
7510	221.14	3.009979	25543	0.17	0.05	0.00	140.00	300.00
7610	221.15	3.003686	25843	0.17	0.05	0.00	140.00	300.00
7710	221.15	2.997446	26143	0.17	0.05	0.00	140.00	300.00
7810	221.15	2.991259	26442	0.17	0.05	0.00	140.00	300.00
7910	221.16	2.985124	26741	0.17	0.05	0.00	140.00	300.00
8010	221.16	2.979039	27039	0.17	0.05	0.00	140.00	300.00

8110	221.17	2.973005	27336	0.17	0.05	0.00	140.00	300.00
8210	221.17	2.96702	27633	0.17	0.05	0.00	140.00	300.00
8310	221.17	2.961085	27929	0.17	0.05	0.00	140.00	300.00
8410	221.18	2.955197	28224	0.17	0.05	0.00	140.00	300.00
8510	221.18	2.949357	28519	0.17	0.05	0.00	140.00	300.00
8610	221.19	2.943563	28814	0.16	0.05	0.00	140.00	300.00
8710	221.19	2.937816	29107	0.16	0.05	0.00	140.00	300.00
8810	221.19	2.932115	29401	0.16	0.05	0.00	140.00	300.00
8910	221.20	2.926458	29693	0.16	0.05	0.00	140.00	300.00
9010	221.20	2.920846	29985	0.16	0.05	0.00	140.00	300.00
9110	221.21	2.915277	30277	0.16	0.05	0.00	140.00	300.00
9210	221.21	2.909752	30568	0.16	0.05	0.00	140.00	300.00
9310	221.21	2.90427	30858	0.16	0.05	0.00	140.00	300.00
9410	221.22	2.89883	31148	0.16	0.05	0.00	140.00	300.00
9510	221.22	2.893431	31438	0.16	0.05	0.00	140.00	300.00
9610	221.22	2.888074	31726	0.16	0.05	0.00	140.00	300.00
9710	221.23	2.882758	32015	0.16	0.05	0.00	140.00	300.00
9810	221.23	2.877482	32302	0.16	0.05	0.00	140.00	300.00
9910	221.24	2.872246	32590	0.16	0.05	0.00	140.00	300.00
10010	221.24	2.867049	32876	0.16	0.05	0.00	140.00	300.00
10110	221.24	2.861891	33163	0.16	0.05	0.00	140.00	300.00
10210	221.25	2.856772	33448	0.16	0.05	0.00	140.00	300.00
10310	221.25	2.851691	33733	0.16	0.05	0.00	140.00	300.00
10410	221.25	2.846647	34018	0.16	0.05	0.00	140.00	300.00
10510	221.26	2.841641	34302	0.16	0.05	0.00	140.00	300.00
10610	221.26	2.836672	34586	0.16	0.05	0.00	140.00	300.00
10710	221.27	2.83174	34869	0.16	0.05	0.00	140.00	300.00
10810	221.27	2.826844	35152	0.16	0.05	0.00	140.00	300.00
10910	221.27	2.822482	35434	0.16	0.05	0.00	140.00	300.00
11010	221.28	2.817692	35716	0.16	0.05	0.00	140.00	300.00
11110	221.28	2.812933	35997	0.16	0.05	0.00	140.00	300.00
11210	221.28	2.808192	36278	0.16	0.05	0.00	140.00	300.00
11310	221.29	2.803479	36558	0.16	0.05	0.00	140.00	300.00
11410	221.29	2.798796	36838	0.16	0.05	0.00	140.00	300.00
11510	221.29	2.794145	37117	0.16	0.05	0.00	140.00	300.00
11610	221.30	2.789526	37396	0.16	0.05	0.00	140.00	300.00
11710	221.30	2.784939	37675	0.16	0.05	0.00	140.00	300.00
11810	221.30	2.780385	37953	0.16	0.05	0.00	140.00	300.00
11910	221.31	2.775862	38231	0.16	0.05	0.00	140.00	300.00
12010	221.31	2.771371	38508	0.16	0.05	0.00	140.00	300.00
12110	221.31	2.766912	38784	0.15	0.05	0.00	140.00	300.00
12210	221.32	2.762485	39061	0.15	0.05	0.00	140.00	300.00
12310	221.32	2.758089	39336	0.15	0.05	0.00	140.00	300.00
12410	221.32	2.753725	39612	0.15	0.05	0.00	140.00	300.00

12510	221.33	2.749391	39887	0.15	0.05	0.00	140.00	300.00
12610	221.33	2.745088	40161	0.15	0.05	0.00	140.00	300.00
12710	221.33	2.740816	40435	0.15	0.05	0.00	140.00	300.00
12810	221.34	2.736574	40709	0.15	0.05	0.00	140.00	300.00
12910	221.34	2.732362	40982	0.15	0.05	0.00	140.00	300.00
13010	221.34	2.72818	41255	0.15	0.05	0.00	140.00	300.00
13110	221.35	2.724028	41527	0.15	0.05	0.00	140.00	300.00
13210	221.35	2.719905	41799	0.15	0.05	0.00	140.00	300.00
13310	221.35	2.715811	42071	0.15	0.05	0.00	140.00	300.00
13410	221.36	2.711747	42342	0.15	0.05	0.00	140.00	300.00
13510	221.36	2.707711	42613	0.15	0.05	0.00	140.00	300.00
13610	221.36	2.703704	42883	0.15	0.05	0.00	140.00	300.00
13710	221.37	2.699725	43153	0.15	0.05	0.00	140.00	300.00
13810	221.37	2.695775	43423	0.15	0.05	0.00	140.00	300.00
13910	221.37	2.691852	43692	0.15	0.05	0.00	140.00	300.00
14010	221.38	2.687958	43961	0.15	0.05	0.00	140.00	300.00
14110	221.38	2.68409	44229	0.15	0.05	0.00	140.00	300.00
14210	221.38	2.68025	44497	0.15	0.05	0.00	140.00	300.00
14310	221.39	2.676438	44765	0.15	0.05	0.00	140.00	300.00
14410	221.39	2.672652	45032	0.15	0.05	0.00	140.00	300.00
14510	221.39	2.668893	45299	0.15	0.05	0.00	140.00	300.00
14610	221.40	2.66516	45566	0.15	0.05	0.00	140.00	300.00
14710	221.40	2.661454	45832	0.15	0.05	0.00	140.00	300.00
14810	221.40	2.657775	46098	0.15	0.05	0.00	140.00	300.00
14910	221.41	2.654121	46363	0.15	0.05	0.00	140.00	300.00
15010	221.41	2.650493	46628	0.15	0.05	0.00	140.00	300.00
15110	221.41	2.646891	46893	0.15	0.05	0.00	140.00	300.00
15210	221.42	2.643314	47157	0.15	0.05	0.00	140.00	300.00
15310	221.42	2.639762	47421	0.15	0.05	0.00	140.00	300.00
15410	221.42	2.636236	47685	0.15	0.05	0.00	140.00	300.00
15510	221.43	2.632735	47948	0.15	0.05	0.00	140.00	300.00
15610	221.43	2.629258	48211	0.15	0.05	0.00	140.00	300.00
15710	221.43	2.625806	48473	0.15	0.05	0.00	140.00	300.00
15810	221.44	2.622378	48736	0.15	0.05	0.00	140.00	300.00
15910	221.44	2.618975	48998	0.15	0.05	0.00	140.00	300.00
16010	221.44	2.615596	49259	0.15	0.05	0.00	140.00	300.00
16110	221.45	2.612241	49520	0.15	0.05	0.00	140.00	300.00
16210	221.45	2.608909	49781	0.15	0.05	0.00	140.00	300.00
16310	221.45	2.605601	50042	0.15	0.05	0.00	140.00	300.00
16410	221.46	2.602317	50302	0.15	0.05	0.00	140.00	300.00
16510	221.46	2.599056	50562	0.15	0.05	0.00	140.00	300.00
16610	221.46	2.595818	50821	0.15	0.05	0.00	140.00	300.00
16710	221.46	2.592602	51081	0.15	0.05	0.00	140.00	300.00
16810	221.47	2.58941	51340	0.14	0.05	0.00	140.00	300.00

16910	221.47	2.586241	51598	0.14	0.05	0.00	140.00	300.00
17010	221.47	2.583094	51857	0.14	0.05	0.00	140.00	300.00
17110	221.48	2.579969	52115	0.14	0.05	0.00	140.00	300.00
17210	221.48	2.576867	52372	0.14	0.05	0.00	140.00	300.00
17310	221.48	2.573786	52630	0.14	0.05	0.00	140.00	300.00
17410	221.49	2.570728	52887	0.14	0.05	0.00	140.00	300.00
17510	221.49	2.567692	53144	0.14	0.05	0.00	140.00	300.00
17610	221.49	2.564677	53400	0.14	0.05	0.00	140.00	300.00
17710	221.50	2.561683	53656	0.14	0.05	0.00	140.00	300.00
17810	221.50	2.558711	53912	0.14	0.05	0.00	140.00	300.00
17910	221.50	2.55576	54168	0.14	0.05	0.00	140.00	300.00
18010	221.51	2.55283	54423	0.14	0.05	0.00	140.00	300.00
18110	221.51	2.549921	54678	0.14	0.05	0.00	140.00	300.00
18210	221.51	2.547033	54933	0.14	0.05	0.00	140.00	300.00
18310	221.52	2.544166	55187	0.14	0.05	0.00	140.00	300.00
18410	221.52	2.541319	55441	0.14	0.05	0.00	140.00	300.00
18510	221.52	2.538492	55695	0.14	0.05	0.00	140.00	300.00
18610	221.53	2.535686	55949	0.14	0.05	0.00	140.00	300.00
18710	221.53	2.5329	56202	0.14	0.05	0.00	140.00	300.00
18810	221.53	2.530134	56455	0.14	0.05	0.00	140.00	300.00
18910	221.53	2.527388	56708	0.14	0.05	0.00	140.00	300.00
19010	221.54	2.524661	56960	0.14	0.05	0.00	140.00	300.00
19110	221.54	2.521954	57212	0.14	0.05	0.00	140.00	300.00
19210	221.54	2.519267	57464	0.14	0.05	0.00	140.00	300.00
19310	221.55	2.516599	57716	0.14	0.05	0.00	140.00	300.00
19410	221.55	2.51395	57967	0.14	0.05	0.00	140.00	300.00
19510	221.55	2.51132	58218	0.14	0.05	0.00	140.00	300.00
19610	221.56	2.50871	58469	0.14	0.05	0.00	140.00	300.00
19710	221.56	2.506118	58720	0.14	0.05	0.00	140.00	300.00
19810	221.56	2.503545	58970	0.14	0.05	0.00	140.00	300.00
19910	221.57	2.50099	59220	0.14	0.05	0.00	140.00	300.00
20010	221.57	2.498454	59470	0.14	0.05	0.00	140.00	300.00
20110	221.57	2.495936	59720	0.14	0.05	0.00	140.00	300.00
20210	221.58	2.493436	59969	0.14	0.05	0.00	140.00	300.00

Table 10: no fractures & no fault

TIME	FPR	FOPR	FOPT	FWPR	WWCT	WWCT	WBHP	WBHP
DAYS	BARSA	SM3/DAY	SM3	SM3/DAY			BARSA	BARSA
					PROD	INJ	PROD	INJ
0	220.74	0	0	0.00	0.00	0.00	220.15	220.15
1	220.74	8.241264	8	0.46	0.05	0.00	140.00	300.00
2	220.74	7.569792	16	0.42	0.05	0.00	140.00	300.00
3	220.74	7.134459	23	0.40	0.05	0.00	140.00	300.00

4	220.74	6.852245	30	0.38	0.05	0.00	140.00	300.00
5	220.74	6.654958	36	0.37	0.05	0.00	140.00	300.00
6	220.74	6.508041	43	0.36	0.05	0.00	140.00	300.00
7	220.74	6.392976	49	0.36	0.05	0.00	140.00	300.00
8	220.74	6.298241	56	0.35	0.05	0.00	140.00	300.00
9	220.74	6.217948	62	0.35	0.05	0.00	140.00	300.00
10	220.74	6.148841	68	0.34	0.05	0.00	140.00	300.00
13	220.74	5.996679	86	0.34	0.05	0.00	140.00	300.00
20	220.74	5.765754	126	0.32	0.05	0.00	140.00	300.00
30	220.74	5.541434	182	0.31	0.05	0.00	140.00	300.00
40	220.74	5.372315	236	0.30	0.05	0.00	140.00	300.00
50	220.74	5.238132	288	0.29	0.05	0.00	140.00	300.00
60	220.73	5.129399	339	0.29	0.05	0.00	140.00	300.00
70	220.73	5.03551	390	0.28	0.05	0.00	140.00	300.00
80	220.73	4.955087	439	0.28	0.05	0.00	140.00	300.00
90	220.73	4.885301	488	0.27	0.05	0.00	140.00	300.00
100	220.73	4.823865	536	0.27	0.05	0.00	140.00	300.00
110	220.73	4.769188	584	0.27	0.05	0.00	140.00	300.00
120	220.73	4.720105	631	0.26	0.05	0.00	140.00	300.00
130	220.73	4.675316	678	0.26	0.05	0.00	140.00	300.00
140	220.73	4.635048	724	0.26	0.05	0.00	140.00	300.00
150	220.73	4.597727	770	0.26	0.05	0.00	140.00	300.00
160	220.73	4.562986	816	0.26	0.05	0.00	140.00	300.00
170	220.73	4.531297	861	0.25	0.05	0.00	140.00	300.00
180	220.73	4.501526	906	0.25	0.05	0.00	140.00	300.00
190	220.73	4.473441	951	0.25	0.05	0.00	140.00	300.00
200	220.73	4.447532	995	0.25	0.05	0.00	140.00	300.00
210	220.73	4.422953	1040	0.25	0.05	0.00	140.00	300.00
240	220.73	4.359012	1170	0.24	0.05	0.00	140.00	300.00
310	220.73	4.24754	1468	0.24	0.05	0.00	140.00	300.00
410	220.73	4.129402	1881	0.23	0.05	0.00	140.00	300.00
510	220.74	4.037581	2284	0.23	0.05	0.00	140.00	300.00
610	220.75	3.963572	2681	0.22	0.05	0.00	140.00	300.00
710	220.75	3.902255	3071	0.22	0.05	0.00	140.00	300.00
810	220.76	3.850214	3456	0.22	0.05	0.00	140.00	300.00
910	220.77	3.805106	3836	0.21	0.05	0.00	140.00	300.00
1010	220.77	3.765307	4213	0.21	0.05	0.00	140.00	300.00
1110	220.78	3.73037	4586	0.21	0.05	0.00	140.00	300.00
1210	220.79	3.698667	4956	0.21	0.05	0.00	140.00	300.00
1310	220.80	3.66984	5323	0.21	0.05	0.00	140.00	300.00
1410	220.80	3.643523	5687	0.20	0.05	0.00	140.00	300.00
1510	220.81	3.619104	6049	0.20	0.05	0.00	140.00	300.00
1610	220.82	3.596333	6409	0.20	0.05	0.00	140.00	300.00
1710	220.82	3.575365	6766	0.20	0.05	0.00	140.00	300.00

1810	220.83	3.555675	7122	0.20	0.05	0.00	140.00	300.00
1910	220.84	3.537191	7476	0.20	0.05	0.00	140.00	300.00
2010	220.84	3.519656	7828	0.20	0.05	0.00	140.00	300.00
2110	220.85	3.503036	8178	0.20	0.05	0.00	140.00	300.00
2210	220.86	3.487162	8527	0.20	0.05	0.00	140.00	300.00
2310	220.86	3.472	8874	0.19	0.05	0.00	140.00	300.00
2410	220.87	3.457444	9220	0.19	0.05	0.00	140.00	300.00
2510	220.88	3.443459	9564	0.19	0.05	0.00	140.00	300.00
2610	220.88	3.429964	9907	0.19	0.05	0.00	140.00	300.00
2710	220.89	3.416941	10249	0.19	0.05	0.00	140.00	300.00
2810	220.89	3.404321	10589	0.19	0.05	0.00	140.00	300.00
2910	220.90	3.392099	10928	0.19	0.05	0.00	140.00	300.00
3010	220.91	3.380217	11266	0.19	0.05	0.00	140.00	300.00
3110	220.91	3.368671	11603	0.19	0.05	0.00	140.00	300.00
3210	220.92	3.35742	11939	0.19	0.05	0.00	140.00	300.00
3310	220.93	3.346455	12273	0.19	0.05	0.00	140.00	300.00
3410	220.93	3.335746	12607	0.19	0.05	0.00	140.00	300.00
3510	220.94	3.325291	12940	0.19	0.05	0.00	140.00	300.00
3610	220.94	3.31506	13271	0.19	0.05	0.00	140.00	300.00
3710	220.95	3.305053	13602	0.18	0.05	0.00	140.00	300.00
3810	220.95	3.295249	13931	0.18	0.05	0.00	140.00	300.00
3910	220.96	3.285643	14260	0.18	0.05	0.00	140.00	300.00
4010	220.97	3.276221	14587	0.18	0.05	0.00	140.00	300.00
4110	220.97	3.266981	14914	0.18	0.05	0.00	140.00	300.00
4210	220.98	3.257908	15240	0.18	0.05	0.00	140.00	300.00
4310	220.98	3.249	15565	0.18	0.05	0.00	140.00	300.00
4410	220.99	3.240246	15889	0.18	0.05	0.00	140.00	300.00
4510	220.99	3.231646	16212	0.18	0.05	0.00	140.00	300.00
4610	221.00	3.223188	16534	0.18	0.05	0.00	140.00	300.00
4710	221.01	3.214874	16856	0.18	0.05	0.00	140.00	300.00
4810	221.01	3.206692	17176	0.18	0.05	0.00	140.00	300.00
4910	221.02	3.198646	17496	0.18	0.05	0.00	140.00	300.00
5010	221.02	3.190723	17815	0.18	0.05	0.00	140.00	300.00
5110	221.03	3.182929	18134	0.18	0.05	0.00	140.00	300.00
5210	221.03	3.175251	18451	0.18	0.05	0.00	140.00	300.00
5310	221.04	3.167695	18768	0.18	0.05	0.00	140.00	300.00
5410	221.04	3.160249	19084	0.18	0.05	0.00	140.00	300.00
5510	221.05	3.15292	19399	0.18	0.05	0.00	140.00	300.00
5610	221.05	3.145694	19714	0.18	0.05	0.00	140.00	300.00
5710	221.06	3.13858	20028	0.18	0.05	0.00	140.00	300.00
5810	221.06	3.131564	20341	0.18	0.05	0.00	140.00	300.00
5910	221.07	3.124655	20653	0.17	0.05	0.00	140.00	300.00
6010	221.07	3.117842	20965	0.17	0.05	0.00	140.00	300.00
6110	221.08	3.11113	21276	0.17	0.05	0.00	140.00	300.00

6210	221.08	3.104509	21587	0.17	0.05	0.00	140.00	300.00
6310	221.09	3.097987	21896	0.17	0.05	0.00	140.00	300.00
6410	221.09	3.091553	22206	0.17	0.05	0.00	140.00	300.00
6510	221.10	3.085213	22514	0.17	0.05	0.00	140.00	300.00
6610	221.10	3.078961	22822	0.17	0.05	0.00	140.00	300.00
6710	221.11	3.072797	23129	0.17	0.05	0.00	140.00	300.00
6810	221.11	3.066721	23436	0.17	0.05	0.00	140.00	300.00
6910	221.12	3.060732	23742	0.17	0.05	0.00	140.00	300.00
7010	221.12	3.054826	24047	0.17	0.05	0.00	140.00	300.00
7110	221.13	3.049005	24352	0.17	0.05	0.00	140.00	300.00
7210	221.13	3.043266	24657	0.17	0.05	0.00	140.00	300.00
7310	221.14	3.037609	24960	0.17	0.05	0.00	140.00	300.00
7410	221.14	3.032032	25264	0.17	0.05	0.00	140.00	300.00
7510	221.15	3.026536	25566	0.17	0.05	0.00	140.00	300.00
7610	221.15	3.021118	25868	0.17	0.05	0.00	140.00	300.00
7710	221.16	3.015778	26170	0.17	0.05	0.00	140.00	300.00
7810	221.16	3.010515	26471	0.17	0.05	0.00	140.00	300.00
7910	221.17	3.005327	26772	0.17	0.05	0.00	140.00	300.00
8010	221.17	3.000215	27072	0.17	0.05	0.00	140.00	300.00
8110	221.17	2.995175	27371	0.17	0.05	0.00	140.00	300.00
8210	221.18	2.990211	27670	0.17	0.05	0.00	140.00	300.00
8310	221.18	2.985315	27969	0.17	0.05	0.00	140.00	300.00
8410	221.19	2.980494	28267	0.17	0.05	0.00	140.00	300.00
8510	221.19	2.975739	28564	0.17	0.05	0.00	140.00	300.00
8610	221.20	2.971057	28861	0.17	0.05	0.00	140.00	300.00
8710	221.20	2.96644	29158	0.17	0.05	0.00	140.00	300.00
8810	221.21	2.961894	29454	0.17	0.05	0.00	140.00	300.00
8910	221.21	2.95741	29750	0.17	0.05	0.00	140.00	300.00
9010	221.22	2.952996	30045	0.17	0.05	0.00	140.00	300.00
9110	221.22	2.948643	30340	0.17	0.05	0.00	140.00	300.00
9210	221.23	2.944358	30635	0.16	0.05	0.00	140.00	300.00
9310	221.23	2.940719	30929	0.16	0.05	0.00	140.00	300.00
9410	221.24	2.936081	31222	0.16	0.05	0.00	140.00	300.00
9510	221.24	2.932417	31516	0.16	0.05	0.00	140.00	300.00
9610	221.25	2.927888	31808	0.16	0.05	0.00	140.00	300.00
9710	221.25	2.924369	32101	0.16	0.05	0.00	140.00	300.00
9810	221.25	2.920365	32393	0.16	0.05	0.00	140.00	300.00
9910	221.26	2.916115	32684	0.16	0.05	0.00	140.00	300.00
10010	221.26	2.912722	32976	0.16	0.05	0.00	140.00	300.00
10110	221.27	2.908882	33267	0.16	0.05	0.00	140.00	300.00
10210	221.27	2.905209	33557	0.16	0.05	0.00	140.00	300.00
10310	221.28	2.901167	33847	0.16	0.05	0.00	140.00	300.00
10410	221.28	2.897954	34137	0.16	0.05	0.00	140.00	300.00
10510	221.29	2.89401	34426	0.16	0.05	0.00	140.00	300.00

10610	221.29	2.890891	34715	0.16	0.05	0.00	140.00	300.00
10710	221.30	2.88707	35004	0.16	0.05	0.00	140.00	300.00
10810	221.30	2.884049	35293	0.16	0.05	0.00	140.00	300.00
10910	221.31	2.880346	35581	0.16	0.05	0.00	140.00	300.00
11010	221.31	2.877415	35868	0.16	0.05	0.00	140.00	300.00
11110	221.32	2.873821	36156	0.16	0.05	0.00	140.00	300.00
11210	221.32	2.87098	36443	0.16	0.05	0.00	140.00	300.00
11310	221.33	2.867793	36730	0.16	0.05	0.00	140.00	300.00
11410	221.33	2.864404	37016	0.16	0.05	0.00	140.00	300.00
11510	221.34	2.861697	37302	0.16	0.05	0.00	140.00	300.00
11610	221.34	2.858363	37588	0.16	0.05	0.00	140.00	300.00
11710	221.35	2.855724	37874	0.16	0.05	0.00	140.00	300.00
11810	221.35	2.852497	38159	0.16	0.05	0.00	140.00	300.00
11910	221.36	2.849945	38444	0.16	0.05	0.00	140.00	300.00
12010	221.36	2.846818	38729	0.16	0.05	0.00	140.00	300.00
12110	221.37	2.844341	39013	0.16	0.05	0.00	140.00	300.00
12210	221.37	2.841307	39297	0.16	0.05	0.00	140.00	300.00
12310	221.38	2.838909	39581	0.16	0.05	0.00	140.00	300.00
12410	221.38	2.836218	39865	0.16	0.05	0.00	140.00	300.00
12510	221.38	2.833362	40148	0.16	0.05	0.00	140.00	300.00
12610	221.39	2.831076	40431	0.16	0.05	0.00	140.00	300.00
12710	221.39	2.828267	40714	0.16	0.05	0.00	140.00	300.00
12810	221.40	2.82604	40997	0.16	0.05	0.00	140.00	300.00
12910	221.40	2.823322	41279	0.16	0.05	0.00	140.00	300.00
13010	221.41	2.82117	41561	0.16	0.05	0.00	140.00	300.00
13110	221.41	2.818537	41843	0.16	0.05	0.00	140.00	300.00
13210	221.42	2.816449	42124	0.16	0.05	0.00	140.00	300.00
13310	221.42	2.813897	42406	0.16	0.05	0.00	140.00	300.00
13410	221.43	2.811877	42687	0.16	0.05	0.00	140.00	300.00
13510	221.43	2.809406	42968	0.16	0.05	0.00	140.00	300.00
13610	221.44	2.807447	43249	0.16	0.05	0.00	140.00	300.00
13710	221.44	2.805052	43529	0.16	0.05	0.00	140.00	300.00
13810	221.45	2.803156	43810	0.16	0.05	0.00	140.00	300.00
13910	221.45	2.800838	44090	0.16	0.05	0.00	140.00	300.00
14010	221.46	2.799	44370	0.16	0.05	0.00	140.00	300.00
14110	221.46	2.796752	44649	0.16	0.05	0.00	140.00	300.00
14210	221.47	2.794975	44929	0.16	0.05	0.00	140.00	300.00
14310	221.47	2.7928	45208	0.16	0.05	0.00	140.00	300.00
14410	221.48	2.791076	45487	0.16	0.05	0.00	140.00	300.00
14510	221.48	2.78897	45766	0.16	0.05	0.00	140.00	300.00
14610	221.49	2.787302	46045	0.16	0.05	0.00	140.00	300.00
14710	221.49	2.785264	46323	0.16	0.05	0.00	140.00	300.00
14810	221.50	2.783648	46602	0.16	0.05	0.00	140.00	300.00
14910	221.50	2.781674	46880	0.16	0.05	0.00	140.00	300.00

15010	221.51	2.780112	47158	0.16	0.05	0.00	140.00	300.00
15110	221.51	2.778202	47436	0.16	0.05	0.00	140.00	300.00
15210	221.52	2.776689	47713	0.16	0.05	0.00	140.00	300.00
15310	221.52	2.774995	47991	0.16	0.05	0.00	140.00	300.00
15410	221.53	2.773202	48268	0.16	0.05	0.00	140.00	300.00
15510	221.53	2.771763	48545	0.16	0.05	0.00	140.00	300.00
15610	221.54	2.77	48822	0.16	0.05	0.00	140.00	300.00
15710	221.54	2.768603	49099	0.15	0.05	0.00	140.00	300.00
15810	221.55	2.766903	49376	0.15	0.05	0.00	140.00	300.00
15910	221.55	2.765553	49652	0.15	0.05	0.00	140.00	300.00
16010	221.56	2.763907	49929	0.15	0.05	0.00	140.00	300.00
16110	221.56	2.762603	50205	0.15	0.05	0.00	140.00	300.00
16210	221.57	2.761012	50481	0.15	0.05	0.00	140.00	300.00
16310	221.57	2.75975	50757	0.15	0.05	0.00	140.00	300.00
16410	221.58	2.75834	51033	0.15	0.05	0.00	140.00	300.00
16510	221.58	2.75685	51309	0.15	0.05	0.00	140.00	300.00
16610	221.59	2.75565	51584	0.15	0.05	0.00	140.00	300.00
16710	221.59	2.754184	51860	0.15	0.05	0.00	140.00	300.00
16810	221.60	2.753023	52135	0.15	0.05	0.00	140.00	300.00
16910	221.60	2.751612	52410	0.15	0.05	0.00	140.00	300.00
17010	221.61	2.750489	52685	0.15	0.05	0.00	140.00	300.00
17110	221.61	2.749124	52960	0.15	0.05	0.00	140.00	300.00
17210	221.62	2.748042	53235	0.15	0.05	0.00	140.00	300.00
17310	221.62	2.746724	53510	0.15	0.05	0.00	140.00	300.00
17410	221.63	2.745677	53784	0.15	0.05	0.00	140.00	300.00
17510	221.63	2.744403	54059	0.15	0.05	0.00	140.00	300.00
17610	221.64	2.743393	54333	0.15	0.05	0.00	140.00	300.00
17710	221.64	2.742164	54607	0.15	0.05	0.00	140.00	300.00
17810	221.65	2.741188	54881	0.15	0.05	0.00	140.00	300.00
17910	221.65	2.740099	55155	0.15	0.05	0.00	140.00	300.00
18010	221.66	2.738951	55429	0.15	0.05	0.00	140.00	300.00
18110	221.66	2.738024	55703	0.15	0.05	0.00	140.00	300.00
18210	221.67	2.736896	55977	0.15	0.05	0.00	140.00	300.00
18310	221.67	2.736001	56250	0.15	0.05	0.00	140.00	300.00
18410	221.68	2.734916	56524	0.15	0.05	0.00	140.00	300.00
18510	221.68	2.734053	56797	0.15	0.05	0.00	140.00	300.00
18610	221.69	2.733005	57070	0.15	0.05	0.00	140.00	300.00
18710	221.69	2.732174	57344	0.15	0.05	0.00	140.00	300.00
18810	221.70	2.731164	57617	0.15	0.05	0.00	140.00	300.00
18910	221.70	2.730363	57890	0.15	0.05	0.00	140.00	300.00
19010	221.71	2.729468	58163	0.15	0.05	0.00	140.00	300.00
19110	221.71	2.728528	58436	0.15	0.05	0.00	140.00	300.00
19210	221.72	2.727767	58708	0.15	0.05	0.00	140.00	300.00
19310	221.72	2.726844	58981	0.15	0.05	0.00	140.00	300.00

19410	221.73	2.726112	59254	0.15	0.05	0.00	140.00	300.00
19510	221.73	2.725225	59526	0.15	0.05	0.00	140.00	300.00
19610	221.74	2.724519	59799	0.15	0.05	0.00	140.00	300.00
19710	221.74	2.723664	60071	0.15	0.05	0.00	140.00	300.00
19810	221.75	2.722986	60343	0.15	0.05	0.00	140.00	300.00
19910	221.75	2.722164	60615	0.15	0.05	0.00	140.00	300.00
20010	221.75	2.72151	60888	0.15	0.05	0.00	140.00	300.00
20110	221.76	2.720783	61160	0.15	0.05	0.00	140.00	300.00
20210	221.76	2.720019	61432	0.15	0.05	0.00	140.00	300.00